
UNIVERSITY OF LIVERPOOL

DOCTORAL THESIS

# Monitoring lava dome eruptions: a seismic, acoustic and experimental study

*Thesis submitted in accordance with the requirements of the University of Liverpool for the degree of Doctor of Philosophy*

*by*

Oliver D. Lamb

May 2017

# Declaration of Authorship

I declare that this thesis titled, "Monitoring lava dome eruptions: a seismic, acoustic and experimental study" and the work presented in it are my own work. The material contained in the thesis has not been presented, nor is currently being presented, either wholly or in part, for any other degree or qualification.

Signed:

_____

Oliver D. Lamb

4 May 2017

# Abstract

Lava dome eruptions are one of the most dangerous forms of volcanic activity. Geophysical, experimental, field or numerical investigations over the past few decades have improved our understanding of dynamic processes associated with these eruptions. In this thesis, I use multi-disciplinary approaches to analyse unrest at four different volcanoes: Volcán de Colima, Unzen, Santiaguito dome complex and Mt. Redoubt.

At Volcán de Colima, waveform correlation and seismic interferometry techniques are used to analyse seismic data collected prior to the November 1998 eruption. A decrease in seismic velocity is observed during pre-eruptive activity, consistent with rock failure caused by increased stress associated with the migration of magma towards the surface. This mechanism is confirmed by measurements during experimental Brazil tests on lava samples from the volcano. Furthermore, repetitive micro-cracking during the experiments suggest some repeating earthquakes detected at Volcán de Colima were produced by repeated tensile failure. At Unzen, I analyse seismic data collected during the formation of a lava spine during the last phase of the 1991-95 eruption. Two large groups of repeating earthquakes are identified and further analysis demonstrates how their sources migrated during their period of activation. Citing experimental and field observations, repeated slip motion along the margins of the spine are inferred as the source mechanisms for these earthquakes. Santiaguito dome complex is one of the most active volcanoes in the world, and here I present the first long-term seismo-acoustic dataset to be recorded at the volcano. The dataset captures a major transition in explosive activity that took place in 2015. Variations in energies and waveform arrival times are used to gain insights into the explosion source dynamics. During its eruption in 2009, Mt. Redoubt volcano erupted 19 times, at least 16 of which produced ash plumes tall enough to disrupt air traffic in the region. Using infrasound data recorded during two of these explosions and a three-dimensional plume rise model, I demonstrate how it is possible to efficiently and accurately estimate the ash plume height soon after an eruption begins.

These four case studies demonstrate how using a combination of geophysical, experimental, numerical, and field observations can provide more robust interpretations of dynamic processes prior to or during lava dome eruptions. Therefore, multi-disciplinary approaches to studying volcanic activity can have important implications for hazard assessments at active volcanoes worldwide.

# Contents

**Declaration of Authorship** **i**

**Abstract** **iii**

**List of Figures** **ix**

**List of Tables** **xi**

**List of Abbreviations** **xii**

**Acknowledgements** **xiii**

**About the author** **xv**

**1 Motivation** **1**
1.1 The importance of understanding volcanoes . . . 1
1.2 Aims and objectives . . . 2
1.3 Thesis structure . . . 3

**2 Monitoring and understanding eruptions** **7**
2.1 Volcano-seismology . . . 7
2.1.1 Volcano-tectonic events . . . 8
2.1.2 Long-period events . . . 9
2.1.3 Volcanic explosions . . . 12
2.1.4 Surficial events . . . 14
2.2 Infrasound . . . 15
2.3 Laboratory approaches to understanding volcanic processes . . . 17
2.3.1 Direct experimental observations . . . 17
2.3.2 Indirect observations in the laboratory . . . 20
2.4 Advantages of multi-disciplinary approaches . . . 21

**3 Lave domes and case study areas** **23**
3.1 Lava domes . . . 23
3.2 Dynamics of lava dome formation . . . 24
3.2.1 Petrology and magma ascent rates . . . 24
3.2.2 Magma rheology . . . 24
3.2.3 Permeability and porosity dynamics . . . 25
3.2.4 Cyclic magma ascent . . . 27
3.3 Current challenges for monitoring lava domes . . . 28
3.4 Case study lava domes . . . 30

**4 Seismic and experimental insights at Volcán de Colima** **35**
Paper abstract . . . 35
4.1 Introduction . . . 36
4.1.1 1998 eruption of Volcán de Colima . . . 37
4.2 Data and methods . . . 38
4.2.1 Seismic . . . 38
4.2.2 Experimental . . . 39
4.3 Results . . . 41
4.4 Discussion . . . 43
4.5 Conclusions . . . 47

**5 Repetitive fracturing during spine extrusion at Unzen volcano, Japan** **49**
Paper abstract . . . 49
5.1 Introduction . . . 50
5.1.1 Unzen eruption and spine extrusion . . . 51
5.2 Data and methodology . . . 52
5.2.1 Data source . . . 52
5.2.2 Automatic Event Detection . . . 53
5.2.3 Statistical Analysis . . . 54
5.2.4 Waveform Correlation . . . 55
5.2.5 Singular Value Decomposition . . . 56
5.2.6 Coda Wave Interferometry . . . 57
5.3 Results . . . 59
5.3.1 Single-station Detection . . . 59
5.3.2 Fast-Fourier Transform . . . 59
5.3.3 Waveform Correlation . . . 62
5.3.4 Cluster characteristics . . . 62
5.4 Discussion . . . 65
5.4.1 Cyclic variations in seismicity . . . 65
5.4.2 Repeating waveforms . . . 67
5.4.3 Source variations . . . 69
5.4.4 A conceptual model . . . 70
5.5 Conclusions . . . 71

**6 Long-term variations in explosion dynamics at Santiaguito dome complex** **73**
Manuscript abstract . . . 73
6.1 Introduction . . . 74
6.2 Santiaguito dome complex . . . 75
6.2.1 Instrument network . . . 75
6.3 2014-2016 eruptive sequence . . . 76
6.3.1 Pre-November 2014 . . . 76
6.3.2 November 2014 - December 2015 . . . 78
6.3.3 January 2016 - September 2016 . . . 78
6.3.4 October 2016 - ongoing . . . 79
6.4 Seismic and acoustic observations of explosions . . . 79
6.4.1 Methodology . . . 79
6.4.2 General observations . . . 81
6.4.3 Seismic and acoustic energies . . . 81
6.4.4 Change in arrival time differences . . . 83

6.5 Interpretation and discussion . . . 83
6.6 Summary . . . 86

**7 Using infrasound to constrain ash plume rise 89**
Paper abstract . . . 89
7.1 Background . . . 90
7.2 Data and methods . . . 91
7.2.1 Infrasound source velocity model . . . 92
7.2.2 Plume rise model . . . 93
7.3 Results . . . 94
7.4 Discussion . . . 95
7.5 Conclusions . . . 100

**8 Conclusions 101**
8.1 Response to project aims . . . 101
8.2 Study limitations and future directions . . . 102

**A Overview of seismic and infrasound analytical methods 105**
A.1 Seismic . . . 105
A.1.1 Event detection . . . 105
A.1.2 Pattern detection . . . 108
A.1.3 Repeating earthquakes . . . 110
A.1.4 Velocity changes . . . 110
A.2 Infrasound . . . 111
A.2.1 Ejection velocities . . . 111

**B Seismic and experimental insights into eruption precursors at Volcán de Colima - Supplementary figures 115**

**C Repetitive fracturing during spine extrusion - Supplementary figures 123**

**D Variations on explosion dynamics at Santiaguito - Supplementary Figures 131**

**Bibliography 135**

# List of Figures

1.1 Illustration of a volcano edifice to highlight the different chapters of this thesis. 4

2.1 Examples of volcanic earthquakes . . . . . 8
2.2 'Drumbeat' LP seismicity recorded at Mount St Helens during 2004-08 eruption 10
2.3 Cartoon from Tuffen and Dingwell (2005) illustrating stick-slip cycle . . . . . 12
2.4 Example of a gas-and-ash explosion recorded in seismic and acoustic waveforms at Santiaguito volcano . . . . . 13
2.5 Images of Strombolian and gas-and-ash explosions. . . . . 14
2.6 Examples of infrasound waveforms recorded at various volcanoes . . . . . 16
2.7 Examples of acoustic emissions recorded during experiments . . . . . 19
2.8 Two-phase fluid laboratory experiments of James et al. (2006) . . . . . 20
2.9 Joint geophysical observations from Santiaguito volcano collected by Johnson et al. (2014) . . . . . 22

3.1 Illustration of the glass transition in a time-reciprocal temperature space . . . 25
3.2 Illustration of a permeable fracture network induced by strain localisation in magma. . . . . 26
3.3 Cyclic seismic and tilt records from Soufrière Hills volcano in May 1997. . . . 28
3.4 Relative velocity changes in seismic data at Mount St Helens in 2004-2005 . . 29
3.5 Image and location map of Volcán de Colima . . . . . 31
3.6 Image and location map of Unzen volcano . . . . . 32
3.7 Image and location map of Santiaguito dome complex . . . . . 33
3.8 Image and location map of Mt. Redoubt volcano . . . . . 34

4.1 Map of Volcán de Colima with RESCO seismic stations marked as they were located in 1998. . . . . 37
4.2 Results of seismic analysis at Volcán de Colima in 1998. . . . . 42
4.3 Experimental results from Brazil tests on andesite samples from Volcán de Colima . . . . . 44
4.4 Two-stage illustration of our seismic and experimental observations for the 1998 eruption of Volcán de Colima. . . . . 46

5.1 Hourly event counts and STFT spectrogram from Unzen volcano . . . . . 60
5.2 MTM spectra of daily event counts of earthquakes at Unzen volcano . . . . . 61

5.3 Cluster occurrence at Unzen volcano from 1st October to 15th November 1994 63
5.4 Characteristics of clusters detected at Unzen volcano . . . . . 64
5.5 Results of CWI on clusters from Unzen volcano . . . . . 66
5.6 Conceptual model of processes occurring during spine extrusion at Unzen volcano in October/November 1994 . . . . . 72

6.1 Map of instrument network deployed at Santiaguito dome complex . . . . . 76
6.2 Timeline of activity at Santiaguito dome complex from November 2014 to December 2016 . . . . . 77
6.3 Network RSAM and Explosion rate at Santiaguito dome complex, 2014-16 . . 82
6.4 Seismic explosive energies plotted versus repose intervals and acoustic energies. 83
6.5 Examples of seismo-acoustic waveforms from explosions to illustrate differences in arrival times. . . . . 84
6.6 Distance between seismic and acoustic sources during explosions at Santiaguito dome complex . . . . . 86
6.7 Summary of activity sequence at Santiaguito dome complex over our period of study. . . . . 87

7.1 Infrasound signals and velocity profiles for explosions at Mt. Redoubt volcano in 2009. . . . . 91
7.2 Frequency spectra of infrasound signals for explosions at Mt. Redoubt volcano in 2009. . . . . 94
7.3 Estimated plume shape and height for event 2 at Mt. Redoubt volcano. . . . . 95
7.4 Estimated plume shape and height for event 17 at Mt. Redoubt volcano. . . . 96
7.5 Isomass contour map of deposits from the 2009 eruption of Mt. Redoubt volcano. . . . . 97

A.1 STA/LTA ratios calculated from seismic data . . . . . 107
A.2 Example of explosion waveform used for envelope detection . . . . . 108
A.3 Examples of STFT spectrograms calculated with different parameters . . . . . 109
A.4 Sketch illustrating the principle of seismic velocity change . . . . . 111
A.5 Acoustic pressures produced by ejection velocities from various source dynamics. . . . . 113

B.1 RSAM and velocity calculations from Volcán de Colima using various parameters . . . . . 116
B.2 Catalogue of repeating earthquakes using CCC of 0.7 . . . . . 117
B.3 MSNoise output plots at 0.5 to 1.1 Hz frequency . . . . . 118
B.4 Illustration of the set-up for the Brazil test experiments conducted during this research. . . . . 119
B.5 Compilation of experimental results from Volcán de Colima . . . . . 120

B.6 Change in velocity during the experiments, using the last pulse as the reference waveform. . . . . 121

C.1 STFT analysis of Unzen hourly counts without Butterworth filter or normalisation . . . . . 124
C.2 Unzen CWI with higher seismic velocities . . . . . 125
C.3 RSAM of seismic data from FG1 at Unzen . . . . . 125
C.4 Cluster lifespan plot for CC threshold of 0.6 and 2 or more events . . . . . 126
C.5 Cluster lifespan plot for CC threshold of 0.6 and 5 or more events . . . . . 127
C.6 Cluster lifespan plot for CC threshold of 0.7 and 2 or more events . . . . . 128
C.7 Cluster lifespan plot for CC threshold of 0.7 and 5 or more events . . . . . 129
C.8 Cluster lifespan plot for CC threshold of 0.8 and 2 or more events . . . . . 129
C.9 Cluster lifespan plot for CC threshold of 0.9 and 2 or more events . . . . . 130
C.10 Cluster lifespan plot for CC threshold of 0.9 and 5 or more events . . . . . 130

D.1 Availability of data from each station deployed around Santiaguito dome complex . . . . . 132
D.2 Calculated RSAM from each broadband station at Santiaguito dome complex. 133
D.3 Calculated RSAM from each short-period station at Santiaguito dome complex.134

# List of Tables

4.1 MSNoise parameters used for seismic data from Volcán de Colima . . . . . 40

5.1 STA/LTA parameters used in single-station event detection . . . . . 53
5.2 Extreme metric values used for single-station detection noise removal . . . . 53
5.3 Parameters used for waveform correlation at Unzen volcano . . . . . 56

6.1 Stations used, time periods covered, and reference waveforms used for explosion detection at Santiaguito dome complex . . . . . 80

7.1 Variables and values used for gas velocity and plume modelling at Mt. Redoubt volcano . . . . . 93

# List of Abbreviations

| | |
|---|---|
| **AE** | Acoustic emission |
| **CCC** | Cross-correlation coefficient |
| **CCF** | Cross-correlation function |
| **CWI** | Coda wave interferometry |
| **LP** | Long-period |
| **MTM** | Multi-taper Method |
| **PDC** | Pyroclastic density current |
| **PSD** | Power spectral density |
| **PZT** | Piezoelectric transducer |
| **RSAM** | Real-time seismic amplitude measurement |
| **SARA** | Seismic amplitude ratio analysis |
| **STA/LTA** | Short-term average/long-term average |
| **STFT** | Short-term Fourier Transform |
| **VASR** | Volcanic acoustic-seismic ratio |
| **VdC** | Volcán de Colima |
| **VLP** | Very Long Period |
| **VT** | Volcano-tectonic |

# Acknowledgements

Blimey, where do I begin...

I will be forever grateful to Yan, Silvio and Janine for taking me on as a postgraduate student and helping me realise my dream of studying volcanoes. I have gained so much through your supervision, advice, patience and passion during my time in Liverpool. I'm looking forward to working together with all three of you for many years to come.

This project would not have been possible without the financial support from ERC and NERC. Therefore, I thank these organisations for the grants which supported this project and various fieldwork campaigns, as well as conference workshop trips.

Various aspects of this project would not have been possible without the help of many collaborators around the world. I'm particularly grateful to Nick, who always made Colima in Mexico such a wonderful place to work. I'm also particularly grateful to Armando for his endless selflessness and friendship, and made working in Guatemala an absolute joy.

Back in Liverpool, I'm pretty sure I was part of the best research group in the world. Thank you to Jackie, Felix, Adrian, Steve C., Becky, Paul, James A., Guðjón, and Amy for the memories of working with a wonderful group of colleagues and friends. To Anthony, I sincerely hope neither of us end up again inside a very wet tent, on top of a volcano, in the middle of a lightning storm (Panama was fun though, right?).

Thank you to everyone who enriched every working day in the Department of Earth Sciences. I am grateful to Tom, Christina, Steve H., Lidong, Amaya, John, Mike, Ludo, James H., Julia and Caroline. To Pamela, thank you for your endless laughter and generous advice. To Simon, I couldn't have asked for a more friendly and supportive office companion. Playing board games long into the night won't be the same outside of Liverpool.

Of course, I would not be here without my amazing family. To Jonathan, thank for being the best big brother there is. To Angharad, thank you for knocking some sense into Jonathan. To my parents, thank you for giving me everything. Your love, support, advice, and inspiration is irreplaceable.

Finalement, a Cécile, ma superbe petite amie. Merci pour toute la joie que tu m'as donnée ces deux dernières années. Merci de m'avoir aidé dans mes moments les plus bas. Et merci de m'avoir fait découvrir le Pain Perdu! J'espère qu'un jour je pourrais te rembourser la dette pour tout ce que tu m'as donné. Voici l'espoir de plusieurs années de plus ensemble (avec du Pain Perdu!).

# About the author

Oliver D. Lamb graduated with a Master of Earth Sciences Degree (MEarthSci) from the University of Oxford in 2013. During this degree, he carried out two dissertations: a geology field mapping project in Scotland and a research project on statistical analysis of volcano-seismic data. In addition, Oliver volunteered for two months at the Colima Exchange and Research in Volcanology group at the University of Colima, Mexico. In October 2013, Oliver started his PhD project at the University of Liverpool, under the joint supervision of Prof. Yan Lavallée, Dr. Silvio de Angelis and Dr. Janine Kavanagh.

During his PhD, Oliver undertook fieldwork in Mexico and Guatemala to deploy geophysical instruments at active volcanoes. Oliver has also presented work at several international conferences, including the EGU General Assembly (four posters, one talk), the AGU Fall Meeting (two posters), and the IUGG General Assembly (one talk). He has also presented at several specialist workshops, including the inaugural 'Workshops on Volcanoes' held in Guatemala in January 2016, and a workshop on volcano-seismology held on Stromboli in September 2016.

In addition to the papers presented as part of this thesis, Oliver has first-authored an article entitled 'Multiple timescales of cyclical behaviour observed at two dome-forming eruptions', published in *Journal of Volcanology and Geothermal Research* in August 2014. This work formed from his MEarthSci dissertation, and was written up as a paper during his PhD studies. During this period, Oliver has also co-authored three articles. The first, authored by Adrian Hornby, was entitled 'Spine growth and seismogenic faulting at Mt. Unzen , Japan' and published in *Journal of Geophysical Research: Solid Earth* in May 2015. The second, authored by Jackie Kendrick, was entitled 'Blowing Off Steam: Tuffisite Formation As a Regulator for Lava Dome Eruptions' and published in *Frontiers in Earth Science* in April 2016. The third, authored by Silvio de Angelis, was entitled 'Characterization of moderate ash-and-gas explosions at Santiaguito volcano, Guatemala, from infrasound waveform inversion and thermal infrared' and published in *Geophysical Research Letters* in June 2016.

# Chapter 1

# Motivation

*"He also had one volcano that was extinct. But, as he said, 'One never knows!' So he cleaned out the extinct volcano, too. If they are well cleaned out, volcanoes burn slowly and steadily, without any eruptions. Volcanic eruptions are like fires in a chimney.*

*On our earth we are much too small to clean out our volcanoes. That is why they bring no end of trouble upon us."*

Antoine de Saint-Exupéry, *The Little Prince*

## 1.1 The importance of understanding volcanoes

Volcanoes are a spectacular and dangerous embodiment of the dynamic nature of our planet. Their eruptions have long enthralled the human race and have inspired countless legends and myths. A well-known example is Pele, the Hawaiian goddess of fire, lightning, wind, dance and volcanoes who is believed to reside in the Halemaumau crater at the summit of Kilauea, one of the world's most active volcanoes. One of the earliest accurate accounts of a volcanic eruption is credited to Pliny the Younger who witnessed the AD 79 cataclysm of Mount Vesuvius which killed his uncle, Pliny the Elder. The attention to detail in the accounts is so keen that modern day volcanology now describes these types of eruptions as "Plinian". It is not until 1883 and the eruption of Krakatoa that the field of volcanology was truly born. That eruption, one of the largest in historical times, was one of the first truly 'global' events due to the recent invention of the telegram. In response, the first compilation of the effects of volcanic activity was published in 1888 by the Royal Society of London (Symons, 1888). Today, an estimated >800 million people live within 100 km of a volcano that has erupted in the last 10,000 years (Brown et al., 2015). Year on year, that figure continues to grow, therefore the field of volcanology and how it contributes to volcano monitoring remains as important as ever.

Volcanologists focus on several key questions that can help us understand volcanoes. How does magma form and how does it move to the surface? What specific properties of the

magma, and the lithosphere through which it moves, control eruptive activity? How can we reduce the hazard and risk associated with different types of volcanic activity? To help answer these questions, the field of volcanology includes many different approaches such as field mapping, geochemistry, laboratory experiments, and geophysics. Several decades of advances in technology and scientific understanding have improved our capability of successfully assessing the hazard and risk of active volcanoes worldwide. Notable examples of successful evacuations of thousands of people include Pinatubo in 1991 (Philippines; Wolfe and Hoblitt, 1996) and Merapi in 2010 (Indonesia; Surono et al., 2012). However, the 2014 eruption of Mt. Ontake in Japan which claimed the lives of 57 climbers (Ogiso et al., 2015), is a grim reminder that there remain considerable challenges for volcanologists worldwide in understanding the processes underlying the differing behaviour between volcanoes.

Of all the styles of volcanic eruptions observed around the world, one of the most dangerous are lava dome eruptions. This style is characterised by the relatively slow effusion of lava onto the surface of the volcano, forming an unstable pile of blocks around the vent. It is this instability that makes this type of activity so dangerous: one moment the lava dome may seem calm and steady, the next moment it will suddenly and violently explode or collapse to produce pyroclastic density currents that directly threaten local populations. Indeed, a lava dome eruption was responsible for one of the deadliest volcanic disasters of the $20^{th}$ century when 27,000 people died during the 1902 eruption of Mount Pelée on the French island of Martinique (Tanguy, 1994). Lava dome volcanoes around the world continue to present a hazard to local populations therefore monitoring efforts remain an area of great importance.

## 1.2 Aims and objectives

The overarching aim of this thesis is to improve our understanding of a wide range of physical processes occurring during lava dome eruptions at several different case study volcanoes. The common link between each of these studies is the use of a multi-disciplinary approach, that is, combining the knowledge and ability of several different fields and datasets to produce a better understanding of the process under investigation. The key, specific aims of this thesis include:

- Relative velocity changes have been recorded prior to eruptions at several volcanoes, and thus, represent a potential tool for forecasting (e.g. Brenguier et al., 2008; Hotovec-Ellis et al., 2015). In addition, velocity changes have been observed in samples under stress in the laboratory (e.g. Heap et al., 2010; Blake et al., 2013). However, results from geophysics and rock mechanics are rarely combined in a single investigation. An investigation of the 1998 eruption of Volcán de Colima, Mexico, aims to demonstrate how experimental observations can be used to directly complement geophysical observations.

- Rhythmic earthquakes associated with spine extrusion are a well-documented phenomenon at a number of dome-forming volcanoes (e.g. Voight et al., 1999; Iverson et al., 2006; Neuberg et al., 2006; De Angelis, 2009). Building on the experimental work carried out and published in Hornby et al. (2015), I analyse the seismic data recorded during the emplacement of a lava spine at Unzen volcano, Japan. The aim is to demonstrate how the combination of geophysical, experimental and field investigations can help improve our models of shallow volcanic processes.
- The Santiaguito dome complex, Guatemala, is one of the most active volcanic centres in the world (Rose, 1987; Harris et al., 2003). Continuous and regular volcanic activity since 1922 has highlighted it as a laboratory volcano, where vital data can be collected for studying a range of processes. I analyse two years of seismic and infrasound data with the aim of describing and understand explosion dynamics during a major transition in activity over 2014-2016.
- Rapid growth of air traffic has prompted the scientific and engineering communities to increase our ability to detect and respond to ash clouds (Prata and Tupper, 2009). This need was highlighted by the 2010 eruption of Eyjafjallajökull, Iceland, which disrupted aviation across Europe (Sigmundsson et al., 2010). The aim of our work is to prove how infrasound data and 3D plume rise modelling can be combined to efficiently calculate the height and direction of propagation of an ash plume.

## 1.3 Thesis structure

The key research findings and contributions of this study (Chapters 4 to 7) are presented as peer-reviewed journal papers and this necessarily involves some repeating of material as key concepts are reintroduced in places. These chapters have their own abstract, introduction, results, discussion and conclusion. The chapters are ordered according to the volcanic process studied, from sub-surface magma movement to a study of ash plumes (Figure 1.1). Each chapter is preceded by a description of the publication status of the work and contributions made by co-authors. For conciseness, all references have been combined into a single bibliography at the end of the thesis.

After this introductory chapter, Chapter 2 reviews and discusses the fields of volcano monitoring and experimental volcanology. This is followed in Chapter 3 by an introduction to lava domes, their dynamic eruptive processes, and the volcanoes that are studied during this project.

Chapter 4 presents research carried out on the eruption of Volcán de Colima in 1998. By using seismic data collected during this period, a change in relative seismic velocity is observed prior to the eruption. Further work using experimental observations demonstrate

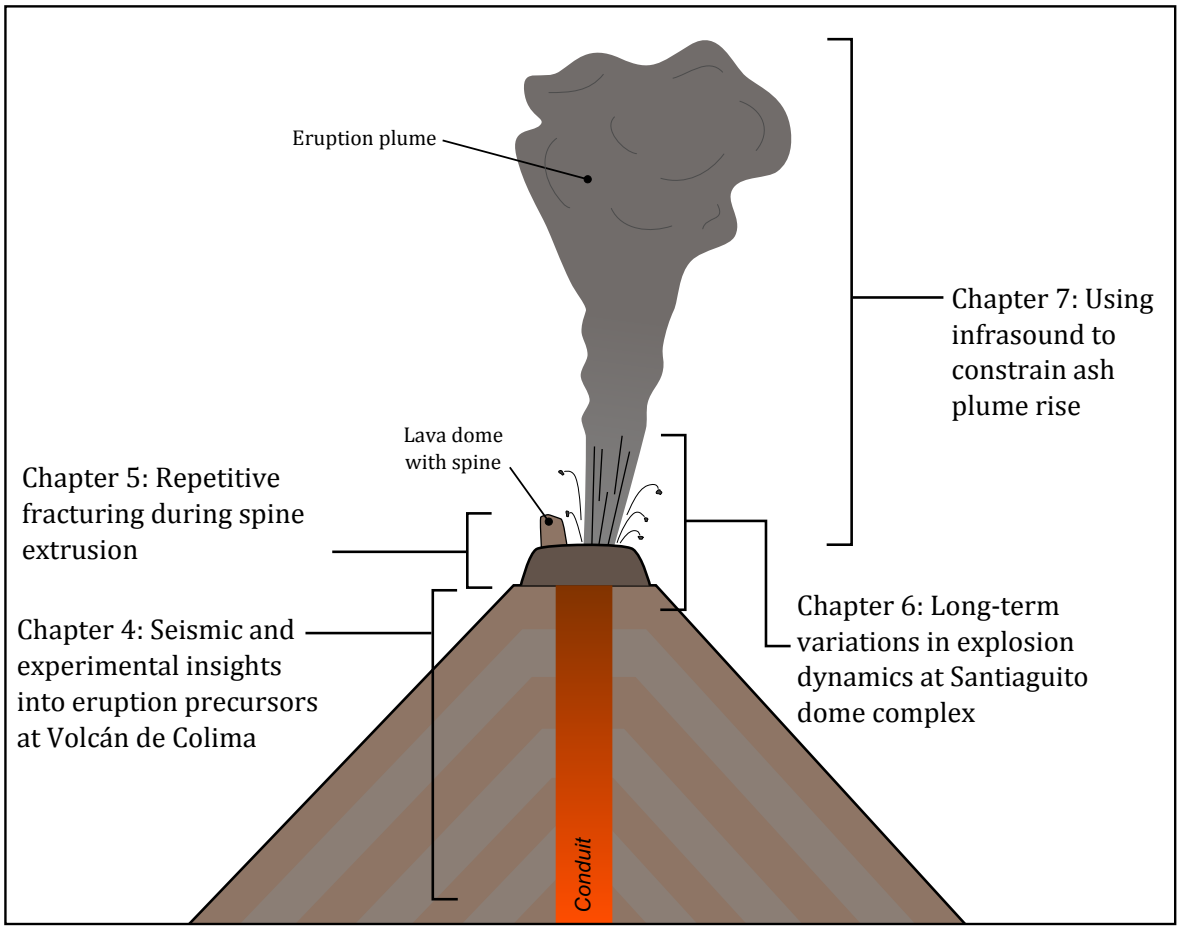


FIGURE 1.1: Illustration of a volcanic edifice showing a simplified view of the conduit which supplies magma and volatiles to produce the lava dome and explosions at the surface. The areas or processes that are the focus of Chapters 4 to 7 are highlighted.

how the material that makes up the edifice can produce these velocity changes due to magma ascent.

In Chapter 5 I analyse and interpret seismic data recorded during the last phase of the eruption of Unzen volcano, Japan, in 1994. One of the key observations made in this chapter is the presence of two significantly large groups of repeating earthquakes. Supported by analytical observations, and drawing on previous experimental work, these two groups are interpreted as the expression of faulting along the margin of the lava spine during its extrusion.

Chapter 6 details two years of seismic and infrasound data collected from Santiaguito dome complex, Guatemala. A key change in the style of activity during this period is observed and supported by seismo-acoustic data. Changes in energies and waveform arrival times illustrate the dynamics of the eruption sources in the conduits. This study highlights the importance of collecting and analysing long-term datasets for understanding the processes occurring during persistent lava-dome eruptions.

Chapter 7 presents a proof-of-concept workflow that incorporates the analysis of volcanic infrasound and numerical modelling of volcanic plume rise in a realistic atmosphere. Using infrasound data collected from Redoubt volcano, Alaska, during its 2009 eruption, I highlight the potential for infrasound measurements to be incorporated into ash dispersion modelling.

Finally in Chapter 8, the main conclusions of the project are presented, highlighting the contributions made towards understanding dynamic processes during eruptions at lava dome volcanoes. This is followed by a discussion of the limitations of the studies presented here, as well as potential future work directions in these fields of research.

This thesis also contains four appendix chapters. Appendix A details the key analytical methods used for our geophysical and experimental investigations in this project. Appendices B, C, and D hold the supplementary figures that accompanied the respective manuscripts for my studies on Volcán de Colima (Chapter 4), Unzen volcano (Chapter 5), and Santiaguito dome complex (Chapter 6).

# Chapter 2

# Monitoring and understanding eruptions

To ensure reliable and up-to-date hazard assessment, eruption forecasting, and risk assessment, many volcanoes are continuously monitored using geophysical techniques. Today, there are over 100 observatories worldwide who are responsible for monitoring active volcanoes and provide early warnings of anticipated volcanic activity to the authorities and the public (Loughlin et al., 2015). A number of geophysical parameters of a volcanic system are continuously or regularly monitored for signs of activity, including: ground deformation (e.g. Segall, 2013), gas emissions (e.g. Edmonds, 2008), optical and thermal imagery (e.g. Spampinato et al., 2011), infrasound (e.g. Fee and Matoza, 2013), and volcanic earthquakes (e.g. Chouet and Matoza, 2013). However, their potential to use the data to forecast the behaviour of volcanoes is constrained by a limited understanding of the underlying mechanisms within a wider volcanological context. This chapter will give an overview of the current understanding of seismic and acoustic (infrasound) signals recorded at volcanoes. I also present a brief overview of how recent experimental approaches have contributed towards understanding these processes. Finally, the last section will look at how combining these different approaches into a multi-disciplinary study can improve our understanding of volcanic processes.

## 2.1 Volcano-seismology

Volcano seismology is one of the most commonly used geophysical tools for monitoring the activity of a volcano. Its key advantages are its ability to monitor activity in real-time, and its practicality, as it can be done relatively cheaply and remotely without the necessity for entering potentially dangerous areas. An increase in seismic activity commonly heralds an impending eruption, but can also highlight the movement of hydrothermal fluids or magma beneath the volcano. A seismometer network around a volcano can record the occurrence of earthquakes, and also enables the location and possible source mechanism of each event to be described. Through the study of event rates, type, size, location, and migration of

seismic events, interpretations of sub-surface processes may be made and fed into hazard assessments.

Active volcanoes produce a great variety of seismic signals. Volcanic earthquakes have traditionally been classified based on the appearance and frequency content of the recorded waveform. General classification schemes include volcano-tectonic (VT), long-period (LP), explosion quakes, and surficial events. Examples of volcano-seismic events from the volcanoes in this study are given in Figure 2.1.

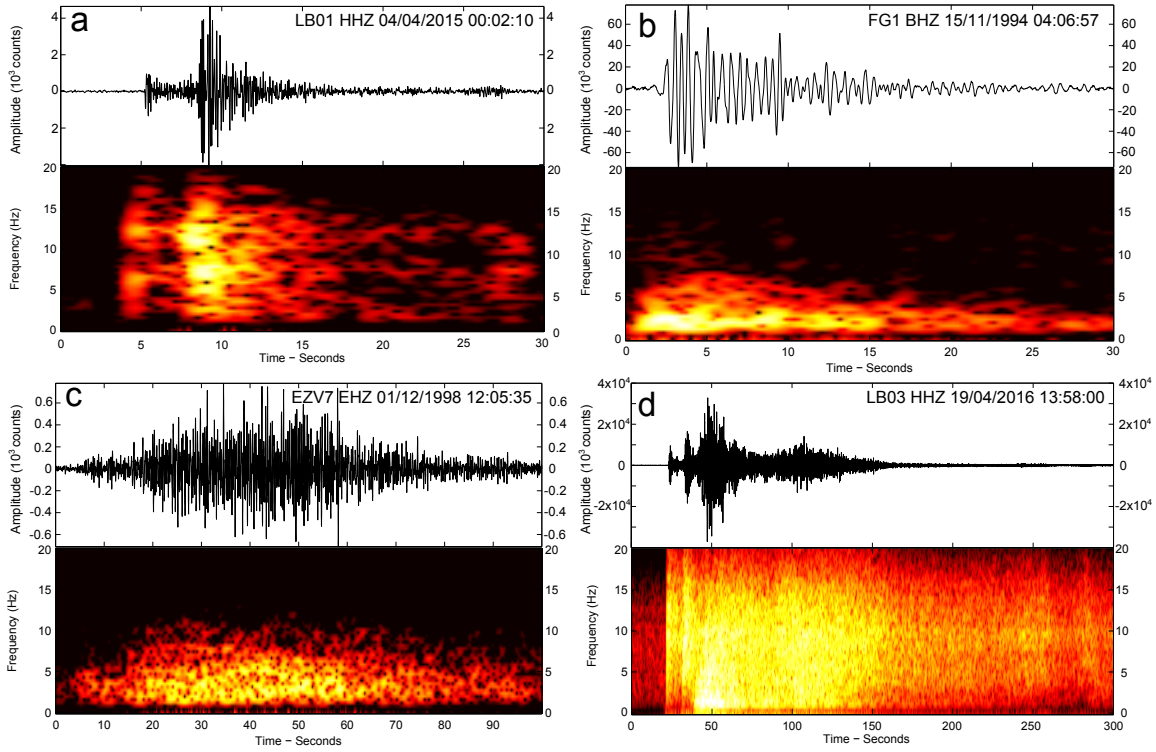


FIGURE 2.1: Example waveforms (top) and spectrograms (bottom) of volcanic seismicity: (a) Volcano-tectonic earthquake recorded at Santiaguito volcano. (b) Long-period earthquake recorded at Unzen volcano. (c) Rockfall recorded at Volcán de Colima. (d) Explosion followed by pyroclastic density current recorded at Santiaguito volcano. All signals are bandpass filtered between 1 and 15 Hz. Note different horizontal and vertical scales for each event. Station name, channel code, and event date and time (UTC) are given on each waveform.

### 2.1.1 Volcano-tectonic events

VT earthquakes, also known as high-frequency or A-type events, are the result of shear failure of rock inside the volcano edifice (Figure 2.1a). VT earthquakes are characterised by clear P- and S-wave onsets, with a broad spectrum extending up to 15 Hz (Lahr et al., 1994). They share similarities with tectonic earthquakes, but are driven by magmatic processes rather than large-scale tectonic movements (Chouet et al., 1994). They also differ from

the tectonic earthquakes in their typical magnitudes (M≤3; McNutt and Roman, 2015). VT events are usually interpreted as the result of stress perturbation due to magmatic intrusion (e.g. Wright et al., 2006; Sigmundsson et al., 2015; Ágústsdóttir et al., 2016) or by hydrothermal fluids expelled from a magmatic body (e.g. Hill, 1996; Shelly et al., 2013). Rather than mainshock-aftershock sequences that define major tectonic earthquakes, VTs often occur as intense swarms of events located beneath or near a volcano. A 'swarm' is defined as a group of many earthquakes clustered in space and time. One of the most recent and spectacular examples of a VT swarm occurred during magma movement prior to an eruption in central Iceland in 2014 (Sigmundsson et al., 2015; Ágústsdóttir et al., 2016). Over the course of two weeks, >30,000 earthquakes were detected as magma propagated laterally along a 48 km path from Bárðarbunga volcano to the eruptive site at Holuhraun. VT earthquakes have also been located up to 45 km away from the eruptive site, when stress from magmatic intrusions are enough to trigger earthquakes on tectonic fault structures (White and McCausland, 2016). These 'distal VT' swarms can occur years before an eventual eruption and can be used to estimate the intruded magma volume (White and McCausland, 2016), representing an important tool for anticipating eruptions at long-dormant (>25 years) volcanoes.

### 2.1.2 Long-period events

LP seismicity, also known as low-frequency or B-type events, are transient signals characterised by emergent P-waves and Rayleigh waves with a lack of distinct S-waves, with dominant frequencies from 0.5 to 5 Hz (Figure 2.1b; Chouet, 1996). These types of seismic waves are traditionally thought to be generated by resonating fluid-filled cavities responding to some type of trigger. LP seismicity also encompasses tremor and hybrid waves. The former is a more continuous ground vibration which may last up to years in duration (McNutt, 1992). In some seismic records, the repose interval between individual LP events have been observed to decrease, eventually merging to form a continuous tremor (e.g. Neuberg, 2011; Hotovec et al., 2013). However, tremor has been used to describe a wide variety of signals with different durations, signal amplitude and frequency content, indicating that a number of different mechanisms can produce this signal. Hybrid seismicity is used to describe waveforms that begin with the pronounced high frequency that characterise VT events, followed by a decaying harmonic coda that defines LP events. These types of events are generally interpreted as generated by brittle failure through a fluid-filled cavity or crack (Lahr et al., 1994). There are five broad groups of processes invoked for triggering LP seismicity: self-sustained oscillations, magma-hydrothermal interactions, slow-rupture failure, brittle failure of melt, and magmatic degassing. The latter group, described here as volcanic explosions, is covered in more detail in the next section.

Self-sustained oscillations in magma fluids have been suggested to produce tremor seismicity (Julian, 1994). In this model, elastic coupling of fluid and solid produces oscillations in

a viscous incompressible fluid flowing through a channel with compliant walls. If the fluid velocity increases, the fluid pressure will decrease due to the Bernoulli effect. This causes a cyclic motion as the channel walls move inward and constrict the flow, causing an increase in fluid pressure and forcing the walls out again. Further work has suggested that this mechanism is unlikely to explain most tremors, but it could occur during the rapid ($\geq$10 $ms^{-1}$) flow of hot, high pressure hydrothermal fluids (Rust et al., 2008).

One of the most important sources of shallow LP seismicity has been long-recognised as the interaction between magma and water (juvenile, meteoric, or a mixture; Latter, 1981; Chouet, 1985). Such interactions may occur via the boiling and depressurisation of groundwater (e.g. Matoza and Chouet, 2010), unsteady choking of a supersonic flow of magmatic steam (e.g. Chouet et al., 1994), or, most commonly, the cyclic collapse and recharge of pressurised hydrothermal cracks (e.g. Nishimura et al., 2000; Waite et al., 2008; Matoza et al., 2009b; Arciniega-Ceballos et al., 2012; Rodgers et al., 2013; Zecevic et al., 2013; Lyons et al., 2016). 'Drumbeat' seismic activity during the 2004-08 eruption of Mount St Helens (USA; Fig. 2.2) has been interpreted as this latter mechanism (Waite et al., 2008; Matoza et al., 2009b). Each 'drumbeat' was part of an extended sequence of millions of repetitive and regular LP events. Waite et al. (2008) inferred a water- or steam-filled crack where, intermittently, the fluid pressure exceeds the containment pressure, leading to its rapid collapse and resonance of the remaining fluid. In this model, the regular time spacing between each event corresponded to the time taken for pressure and temperature conditions to return to a critical state.

However, the 'drumbeats' recorded during the 2004-08 eruption of Mount St Helens remain a cause of general interest and debate regarding their source mechanics. The majority of the

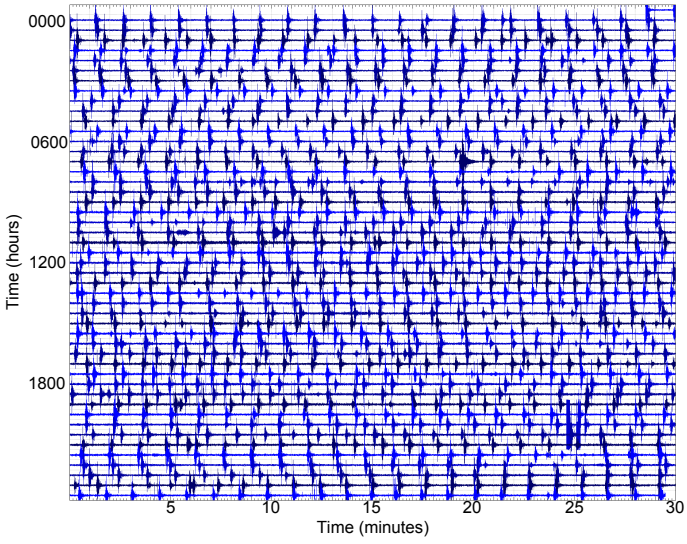


FIGURE 2.2: Example of a 24-hour seismogram illustrating the 'drumbeat' LP seismicity recorded at Mount St. Helens volcano during the 2004-2008 eruption. Graph shows data recorded at station YEL, located 1.5 km north of the eruptive vent. Time begins at 00:00 GMT on 3rd December 2005, and scrolls from left to right then top to bottom.

eruption was characterised by the extrusion of seven lava spines, mantled by gouge, pseudotachylyte, and slickensides aligned in the direction of motion (Pallister et al., 2008; Cashman et al., 2008; Kendrick et al., 2012; Pallister et al., 2013). The simultaneous occurrence of near-continuous spine extrusion with the highly regular 'drumbeat' seismicity led to the hypothesis that their source process involved slow-rupture failure of volcanic materials, in this case along the margin of a lava plug (Iverson et al., 2006; Iverson, 2008; Kendrick et al., 2012). This kind of failure along the margin of a plug has also been inferred for repetitive LP seismicity during eruptions at Augustine volcano (Power and Lalla, 2010) and Soufrière Hills volcano (De Angelis, 2009; Kendrick et al., 2014b). The mechanism, first proposed by Iverson et al. (2006), relates the repetitive LP seismicity to the dynamics of a solid plug forced upwards by a flux of molten and bubbly magma in the conduit. As well as the field observations of fault gouge and slickensides on the spines, this model is supported by experimental investigations on the frictional properties of the gouge and pseudotachylyte (Moran et al., 2008; Kendrick et al., 2012, 2014b). Furthermore, Harrington and Brodsky (2007) concluded that the 'drumbeat' events at Mount St. Helens could be explained by slow-rupture failure combined with path effects caused by loosely consolidated near-surface geology. These two processes have also been invoked to explain LP events at Etna and Turrialba volcanoes (Bean et al., 2013; Eyre et al., 2015; Zecevic et al., 2016). Bean et al. (2013) observed how pulse-like low-frequency events can transition into waveforms that appear as classic resonating LP signals at stations >500 m from the source. Ultimately, the LP waves at Turrialba and Etna are thought to be caused by shallow failure due to stress-driven edifice deformation and illustrates the importance of deploying seismic stations in close proximity to active volcanic vents (Bean et al., 2013; Eyre et al., 2015; Thun et al., 2015; Zecevic et al., 2016). At the start of this section, I defined LP events as those generated by fluid-filled resonators in response to an external trigger. Shallow failure around a plug or in the edifice does not meet this criterium, therefore should be viewed not as a trigger mechanism for LP seismicity but as an entirely different process that simultaneously triggers and produces low frequency waveforms.

An alternative mechanism for repeating LP events such as 'drumbeats' can take place deeper in the conduit in conditions where magma failure can occur. This is based on observations that the seismic source was not destructive (i.e. a similar trigger at a stationary location) and suggested that magma failure occurred when specific rheology and stress conditions were reached (e.g. Neuberg et al., 2006). This mechanism is supported by experimental observations of how viscous silicic melts behave under certain stress and strain conditions (Dingwell and Webb, 1989; Webb and Dingwell, 1990; Dingwell, 1996). At low strain-rates, the melts behave as Newtonian fluids, that is, the stresses arising from its flow are directly proportional to the local strain rate. At higher strain-rates the silicic melt exhibits non-Newtonian behaviour, where the viscosity of the melt decreases with higher-strain rates, and at high enough strain rates the melts can fail in a brittle manner. The transition from Newtonian to non-Newtonian behaviour is known as the brittle-ductile or glass transition (Dingwell

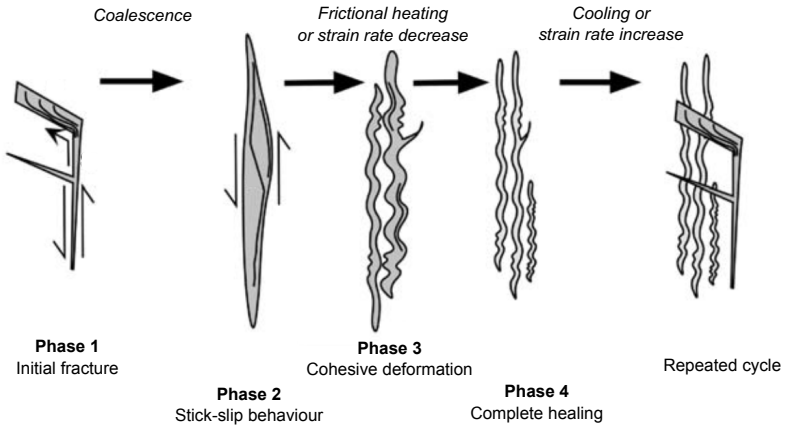


FIGURE 2.3: Cartoon illustrating the stick-slip cycle within rising magma as interpreted from field evidence. Adapted from Tuffen and Dingwell (2005).

and Webb, 1989; Webb and Dingwell, 1990). The temperature and strain rate at which the glass transition occurs is strongly affected by the melt composition, rheology (crystals and bubbles), and water content (Hess and Dingwell, 1996; Gonnermann and Manga, 2007). Further evidence for magma failure has come from observations of repeated shearing and welding of magma on the margins of exposed volcanic conduits (Tuffen et al., 2003; Tuffen and Dingwell, 2005). The conduit margins hold tuffisite veins filled by fragments of magma and phenocrysts; Tuffen et al. (2003) and Tuffen and Dingwell (2005) interpreted them as the product of repeated magmatic failure and healing (Fig. 2.3). This mechanism has been invoked to explain LP seismicity at Unzen (Goto, 1999), Soufrière Hills (Neuberg et al., 2006; Green and Neuberg, 2006; De Angelis and Henton, 2011) and Volcán de Colima (Varley et al., 2010). Goto (1999) and Neuberg et al. (2006) observed that these LP events generally come from stable locations, and proposed that the source is confined to a fixed depth range in the conduit where the stress and strain conditions for brittle failure of magma are met. Ascent of magma from below provides a supply of undeformed melt, and above this 'seismogenic window', the magma ascends as an aseismic plug. Alternatively, a geometrical constraint in the magma ascent path (e.g. a constriction or a bend), could provide a fixed source magma failure (Thomas and Neuberg, 2012).

### 2.1.3 Volcanic explosions

Due to their immediate and violent nature, the most dangerous hazard at volcanoes is explosions. Therefore, considerable research has gone into recording and analysing their seismic signals for the purpose of volcano monitoring and hazard assessment. Here I define volcanic explosions as the energetic release of magmatic gas at the surface that may also include a substantial fraction of ash or lava. Volcanic explosions can release a large amount of energy and a significant proportion of this is transferred through the ground via seismic energy (Figure 2.4a). Explosion earthquakes have generally been characterised by the single force model, describing how the force system of an eruption can be expressed by a vertical

downward single force (Kanamori and Given, 1983; Kanamori et al., 1984). This model has been one of the most widely adopted macroscopic source models for explosion earthquakes in the previous few decades. Further work on explosion earthquakes has focused on more microscopic source mechanisms, particularly on how the explosion is triggered.

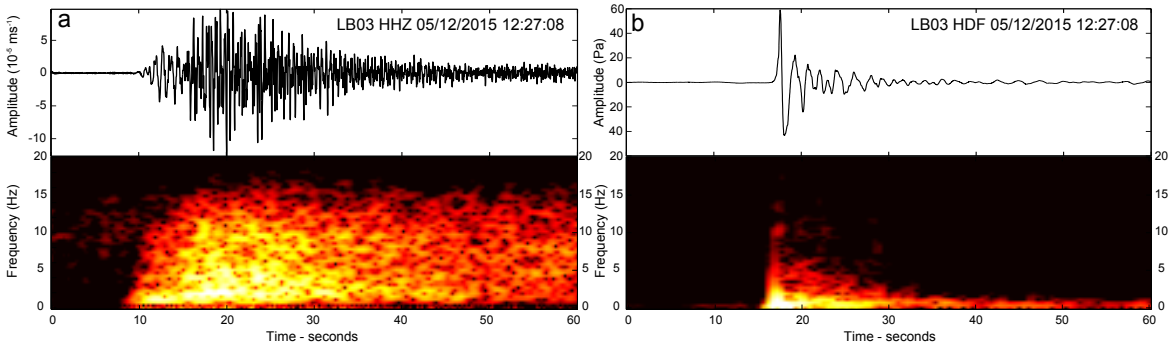


FIGURE 2.4: Seismic (a) and infrasound (b) waveforms (top) and spectrograms (bottom) of a gas-and-ash explosion recorded at Santiaguito volcano, Guatemala. The seismic and infrasound waveforms were bandpass filtered at 1-15 Hz and 0.1-10 Hz, respectively. Station name, channel code, and event date and time (UTC) are given on each waveform.

Strombolian explosions (Fig. 2.5a) are generally associated with LP or Very Long Period (VLP, <0.5 Hz) seismic events (e.g. Neuberg et al., 1994; Rowe et al., 1998; Petersen and McNutt, 2007; Aster et al., 2008). These waveforms are generally interpreted to reflect the rapid expansion of a gas slug in the magma conduit immediately prior to the explosion (Chouet et al., 2003). LP and VLP seismic signals have also been recorded during gas-and-ash (Fig. 2.4, 2.5b) or larger Vulcanian explosions (Chouet et al., 2005; Johnson et al., 2008; Sahetapy-Engel et al., 2008; Johnson et al., 2009; Dawson et al., 2011; Haney et al., 2013; Yamada et al., 2016). Similar to Strombolian explosions, these signals have been successfully modelled as explosive decompression within the conduit (Chouet et al., 2005; Dawson et al., 2011; Haney et al., 2013; Yamada et al., 2016). Alternatively, the same signals could be produced by shear-induced failure along the margins of a lava plug inside the vent (Johnson et al., 2008; Sahetapy-Engel et al., 2008; Lavallée et al., 2015b). Due to their rare occurrence, seismic records of Plinian and sub-Plinian eruptions are rarely described and analysed. The major eruption of Kelud volcano (Indonesia) in 2014 destroyed most of the monitoring equipment deployed near the vent, but remote seismic instruments up to 7000 km away were able to detect the eruption and help constrain the eruption chronology (Caudron et al., 2015b). Indeed, seismic signals are often used to monitor eruptive activity at volcanoes in remote regions (e.g. De Angelis et al., 2012a; Caudron et al., 2015b; Fee et al., 2016). Prejean and Brodsky (2011) used seismic waves and a simple mechanical model to calculate height of ash plumes during the eruptions of Kasatochi and Augustine volcanoes in Alaska.

A significant portion of the explosive energy is partitioned into the air as acoustic waves. These waves can manifest themselves in seismic records via air-to-ground coupling (e.g. Johnson and Aster, 2005; Marchetti et al., 2013). Variations in seismic and acoustic energy

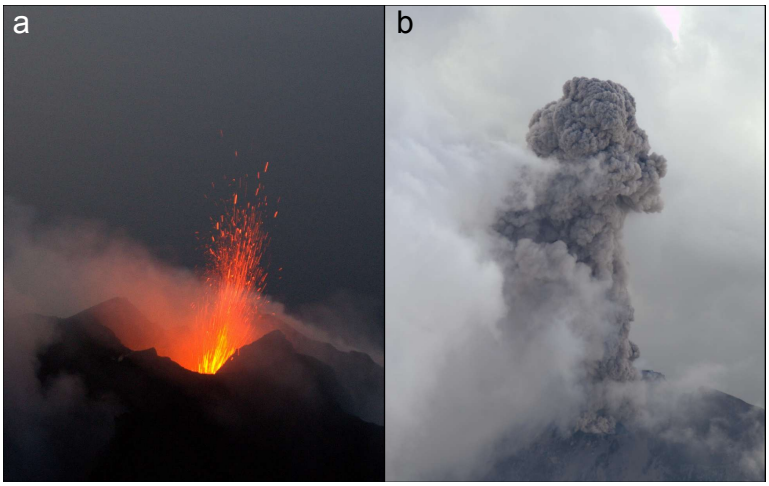


FIGURE 2.5: Examples of (a) Strombolian and (b) gas-and-ash explosions from Stromboli and Santiaguito volcanoes, respectively.

partitioning from explosions can be linked to the evolution of various conditions such as magma properties, conduit obstruction, or fragmentation depths (Johnson and Aster, 2005). Due to the smaller speed of sound compared to seismic velocities, the air-shock phase will appear at later stages in explosion waveforms recorded by seismometers at increasing distances from the source (e.g. Petersen and McNutt, 2007; De Angelis et al., 2012a). This phenomenon can be used to estimate the depth of explosive fragmentation within the conduit (Petersen and McNutt, 2007), or detect explosions at remote volcanoes when satellite observations have failed (De Angelis et al., 2012a).

### 2.1.4 Surficial events

Rockfalls are common during silicic eruptions forming lava domes or lava flows. The corresponding seismic signals are a manifestation of the rocks impacting onto the ground, and often last a minute or longer (Figure 2.1c). Studies of rockfall events can provide important information regarding the evolution of an eruptive process. For example, time-series of rockfall events may be used to track the effusion rate during lava dome eruptions (Mueller et al., 2013). Other volcanic events that may be recorded by seismometers include pyroclastic density currents (PDCs; Figure 2.1d) and lahars. These processes are respectively responsible for the two deadliest eruptions of the 20th century: Mount Pelée in 1902 (27,000 casualties; Tanguy, 1994) and Nevado del Ruiz in 1985 (25,000 casualties; Naranjo et al., 1986). Therefore, early detection and tracking of these events are particularly important for hazard mitigation. PDCs and lahars are commonly characterised as long-lasting, high-frequency continuous signals but often require acoustic or visual confirmation to distinguish between the two (e.g. Lavigne et al., 2000). A network of seismic instruments around a volcano can be used to locate the source of tremors from lahars, suggesting that real-time, automatic detection and tracking may be possible (Kumagai et al., 2009).

## 2.2 Infrasound

Volcanoes are one of the most dynamic sources of infrasound, defined as acoustic waves with a frequency below 20 Hz. The diverse nature of volcanic activity produces a wide variety of infrasonic signals, and nearly all types of active volcanism have been observed to produce infrasound waves. In addition, the relatively low atmospheric attenuation of infrasonic frequencies allows acoustic waves from large eruptions to propagate long distances and be recorded globally. Indeed, barometers around the world recorded low-frequency signals from the eruption of Krakatau Volcano, Indonesia, in 1883; acoustic-gravity waves continued to propagate around the world at least seven times (Strachey, 1888). Therefore, infrasound can provide information on volcanic activity at local (<15 km) to global (>350 km) distances.

Volcanic eruptions are traditionally divided into categories depending on eruption size, style, magma viscosity and tephra. Each of these eruption types (Strombolian, Vulcanian, Sub-plinian/Plinian and Hawaiian) could also be separated using their acoustic signals. Strombolian explosions are interpreted to result from over-pressurised 'slugs' of gas reaching the surface at the vent and subsequently bursting (Ripepe et al., 1996). The resulting acoustic signal is typically short-duration, consisting of a sharp compressional onset followed by a coda of up to tens of seconds (Fig. 2.6c; Fee and Matoza, 2013). However, a wide array of acoustic waveforms have been recorded from recognised Strombolian explosions which demonstrates the variety of shallow and surficial processes in effect during these events. For example, at Stromboli volcano, the type locale for these events, two principal signals have been described: a high amplitude, short duration signal, and a low amplitude signal with long, complex codas. The former is likely produced by simple bursting of the slug, while a more sustained gas flow can generate the latter (Ripepe et al., 1996).

Acoustic signals from Vulcanian explosions typically consist of an impulsive, high amplitude arrival followed by a coda lasting up to tens of minutes (Fig. 2.4b, 2.6d). The longer duration coda is linked to jetting at the source, tremor, or turbulence in the ash plume. Shock-waves have often been observed during Vulcanian explosions with a typical 'N-shape' waveform (Morrissey and Chouet, 1997). However, similar to Strombolian events, a wide variety of waveform signals has been observed from Vulcanian explosions at multiple volcanoes. For example, emergent acoustic signals have been recorded during Vulcanian explosions and are attributed to factors such as higher magma viscosity, impediments at the vent, variable depths of fragmentation, or partial dome collapse (Petersen et al., 2006; Fee and Matoza, 2013).

Due to their relative infrequency and associated hazard, studies of acoustic signals from sub-Plinian, Plinian and Hawaiian eruptions are relatively rare compared to Strombolian and Vulcanian. Sub-Plinian and Plinian eruptions can produce high-amplitude, long-lasting (up to hours) acoustic signals which are broadband in frequency. In addition, they can be

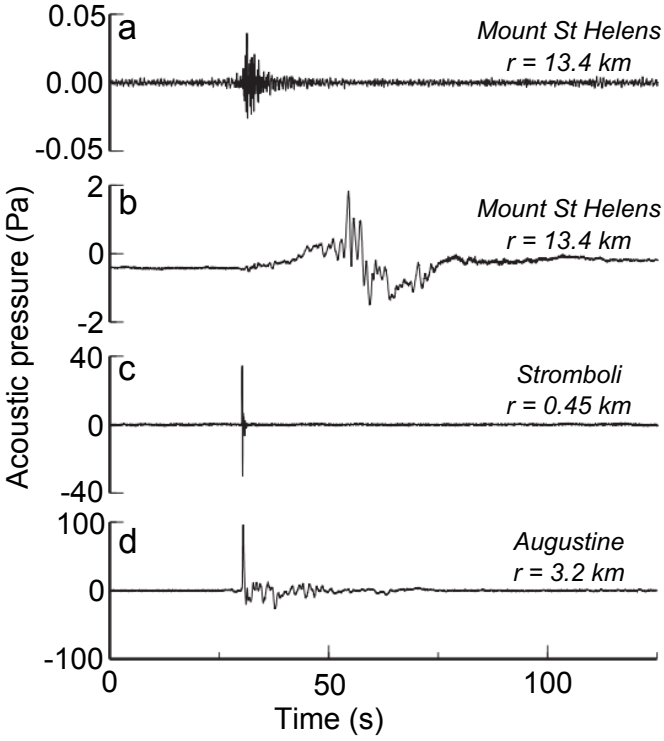


FIGURE 2.6: Examples of transient infrasound signals recorded at various volcanoes around the world (Adapted from Fee and Matoza, 2013). The respective distance between source and receiver ($r$) is listed to the right of the waveform. (a) Infrasound associated with LP seismic 'drumbeat' event at Mount St Helens (Matoza et al., 2009b). (b) Rockfall signal with very clear very-long-period (<0.5 Hz) frequencies present, recorded at Mount St Helens (Moran et al., 2008). (c) Typical infrasound waveform recorded during a Strombolian explosion at Stromboli, Italy (Ripepe and Marchetti, 2002). (d) Infrasound produced by a large, Vulcanian explosion from Augustine volcano, Alaska (Petersen et al., 2006).

recorded up to thousands of kilometres from the source and have proven useful for delineating the eruption chronology and the ash plume height (e.g. Caudron et al., 2015b). The broadband and complex nature of the acoustic signal from these high-energy events have been attributed to jet noise and turbulence generated by a sustained flux of material exiting the vent (e.g. Matoza et al., 2009a). Movement of eruptive activity along a Hawaiian style fissure eruption have been tracked using infrasound microphone arrays deployed at Mt. Etna and Kilauea volcano (Cannata et al., 2011; Fee et al., 2011). The vast majority of volcanic infrasound collected on Hawaii is caused by effusive activity or passive degassing. The characteristics of the acoustic signals are largely controlled by vents restricting gas escape to the atmosphere.

Multiple studies have documented infrasound signals accompanying shallow LP seismic signals at volcanoes (e.g. Petersen and McNutt, 2007). LP seismicity is typically attributed to the activity of magmatic and hydrothermal fluids in shallow subsurface cracks and conduits (Section 2.1.2). These studies have usually explained the acoustic signals be a gas-release mechanism accompanying the shallow seismicity. For example, Matoza et al. (2009b) proposed that rapid venting from a crack simultaneous with its collapse caused such signals recorded at Mount St Helens during the 2004-2008 eruption (Fig. 2.6a). Infrasound signals from PDCs, large rockfalls and lahars have also been recorded (Fig. 2.6b; e.g. Delle Donne et al., 2014; Johnson and Ronan, 2015; Johnson and Palma, 2015). It has been demonstrated that a single array of microphones can be used to track the location and speed of a PDC or a lahar (Delle Donne et al., 2014; Johnson and Palma, 2015). Although infrasound from PDCs

and rockfalls are relatively understudied compared to explosions, its potential for aiding in hazard mitigation has been proven.

## 2.3 Laboratory approaches to understanding volcanic processes

To improve our understanding of geophysical signals recorded during volcanic activity, many investigations have turned to laboratory experiments. Pertinent conditions such as temperature and pressure can be replicated in the laboratory and used to understand how volcanic materials may behave mechanically. Generally, there are two approaches for designing an experiment to understand volcanic geophysical signals: direct and indirect. Direct experiments use laboratory analogues of the natural signals under specific conditions to place strictures on how the latter are produced. Here, I will discuss how acoustic emissions and two-phase gas slug experiments are used to replicate volcano-seismic processes in the laboratory (Section 2.3.1). Indirect experiments look at the mechanical behaviour of volcanic materials to help understand whether the geophysical signals can be feasibly produced by them under specific conditions or processes that occur within a volcano. Examples would include friction experiments (e.g. Moore et al., 2008; Kendrick et al., 2014b; Hornby et al., 2015); this is covered in more detail in section 2.3.2.

### 2.3.1 Direct experimental observations

#### Acoustic emissions

The generation of cracks during experimental rock deformation has been studied intensely through the monitoring and analysis of acoustic emissions (AE; Wevers, 1997). AEs are transient elastic stress waves generated by the energy released when micro-cracking occurs in a material (e.g. Unnþórsson, 2013; Ishida et al., 2017). The micro-cracking can be generated by mechanical, thermal, and chemical stressing. Minute surface displacements associated with AEs can be measured using sensitive transducers, most commonly piezoelectric transducers, which can measure displacements on the order of picometres ($10^{-12}$ m). The output of the transducers is a 1D voltage-time representation of the displacement wave passing through the material. This is similar to how seismic deformation is recorded by a seismometer, therefore recording AE events during experiments enables us to relate the different conditions and mechanisms which might generate seismicity.

AEs are most commonly used to assess the mechanical properties of a material under various conditions (e.g. Lavallée et al., 2008; Tuffen et al., 2008; Smith et al., 2009; Heap et al., 2009; Heap et al., 2010; Kendrick et al., 2013; Farquharson et al., 2016). The seismogenic nature of non-Newtonian magma behaviour has also been investigated by recording AEs during high-temperature, high-pressure silicic sample deformation (Lavallée et al., 2008;

Tuffen et al., 2008; Smith et al., 2009). The increased release of AEs while sample failure is accompanied by a stress drop is taken as evidence that melt fracture can produce measurable seismic events in lava domes and along magma conduit margins. Smith et al. (2009) also observed an acceleration in AE before sample failure similar to that described for earthquakes before eruptions, supporting the use of laboratory data to interpret field observations. As an AE represents the elastic energy output of micro-cracking in the sample, it can be used as a proxy for 'crack damage' within the sample. AE behaviour during cyclic stressing of samples suggests that (at least at relatively fast strain rate) crack damage will only commence when stresses are higher than that during the previous cycle (Heap et al., 2009; Heap et al., 2010; Kendrick et al., 2013). This suggests that only stress episodes accompanied by volcano-seismicity will result in changes to the elastic moduli and seismic velocities. An increase in AE hit rate has been observed during experiments where pore pressure is increased within a sample, suggesting that such pore fluid induced brittle failure could contribute to the seismic record at volcanoes (Farquharson et al., 2016).

Other studies have compared the characteristics of seismic waveforms with AE waveforms produced during rock cracking under various conditions (Burlini et al., 2007; Benson et al., 2008, 2010; Harrington and Benson, 2011; Benson et al., 2014; Fazio et al., 2017). These experiments are designed to test hypotheses of how natural volcanic seismicity is induced. AE waveforms recorded during high temperature experiments can be qualitatively compared to natural volcanic earthquakes such as LPs and VTs (Burlini et al., 2007). Rapid decompression of a water-filled basalt sample triggered many low-frequency AE events, analogous to one mechanism for producing volcanic LP seismicity (Fig. 2.7; Benson et al., 2008). Similar experiments at higher temperatures produces notable shifts in frequency of the recorded AE, interpreted as an effect of changes in the fluid phases within the sample (Benson et al., 2014; Fazio et al., 2017). Further work by Benson et al. (2010), using a similar experimental set-up, described 'hybrid' AE events, where a high-frequency onset is followed by a low-frequency coda. In this set-up, these hybrid events were interpreted to be caused by a combination of crack-opening and the movement of high-pressure fluids. Estimating source characteristics using an empirical Green's function approach suggests that AE events occurring under dry or saturated conditions follow an expected scaling of moment and corner frequency for brittle-failure (Harrington and Benson, 2011). By comparing source scaling for AE events recorded during saturated experiments and the LP 'drumbeats' recorded at Mount St Helens, Harrington and Benson (2011) suggested that these earthquakes did not occur as a result of a fluid process. However, it must be noted that because AEs are typically recorded in voltages, it remains challenging to compare laboratory AEs with natural earthquakes. One approach is to use frequency-size scaling to match the experimental and natural waveforms, considering that dominant frequencies of earthquakes are inversely proportional to the source dimension (Aki and Richards, 1980; Burlini et al., 2007). In the field, increasingly sensitive accelerometers monitoring smaller volumes of rock have suggested an overlap between the characteristics of micro- and macro-cracking processes (e.g. Goodfellow and

Young, 2014). In the laboratory, where the challenge has been the reliable calibration of AE sensors, the source characteristics of laboratory earthquakes have been shown to be consistent with those of larger earthquakes (McLaskey and Kilgore, 2013).

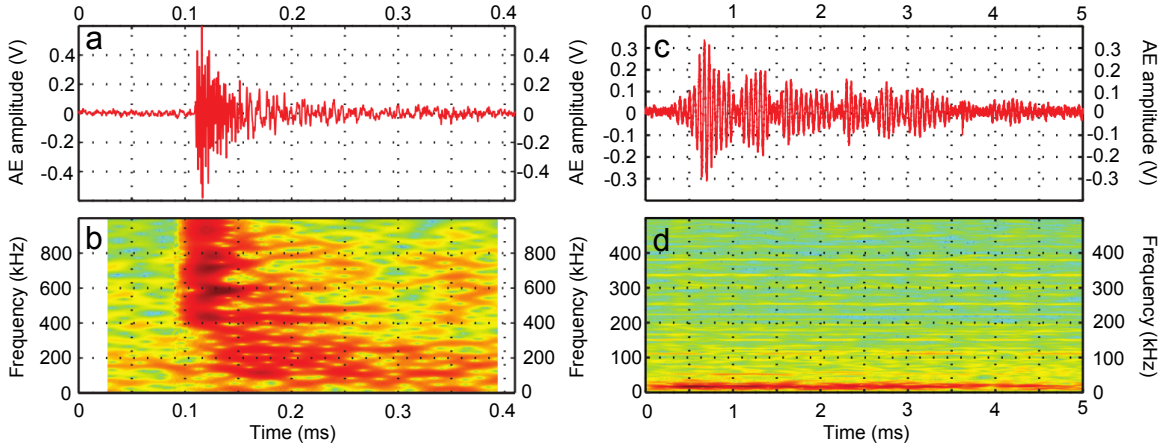


FIGURE 2.7: Waveforms (a,c) and frequency spectrograms (b,d) for high-frequency (a,b) and low-frequency (c,d) acoustic emissions recorded during an experiment on Basalt samples. Adapted from Benson et al. (2008).

### Two-phase experiments

To develop a better understanding of how fluid behaviour may produce LP or VLP seismic signals at volcanoes, laboratory experiments have been designed to explore the pressure changes caused by known flow processes (Lane et al., 2001; James et al., 2004; James et al., 2006). These experiments recorded pressure changes as gas slugs ascended buoyantly through a liquid-filled tube (Lane et al., 2001; James et al., 2004), with pressure oscillations used as an analogy for seismicity. These set-ups are a direct analogue of processes thought to be occurring in the conduit immediately prior to Strombolian explosions in low-viscosity magma systems (Section 2.1.3). The pressure oscillations measured during the gas slug rise display the characteristic properties that might be expected during the resonance of fluid flow (Lane et al., 2001; James et al., 2004). Furthermore, James et al. (2004) observed pressure oscillations during gas-slug burst at the top of the tube which shared characteristics with acoustic measurements from Strombolian explosions. Further experiments looked at how changes in the tube (i.e. conduit) geometry could induce LP or VLP seismicity during gas-slug rise (Fig. 2.8; James et al., 2006). Gas-slugs entering a tube section of significantly greater diameter induced pressure oscillations in the tube walls directly below the slug. This illustrated how changes in conduit geometry can produce LP and VLP seismicity during gas-slug rise in low-viscosity magma systems (James et al., 2006).

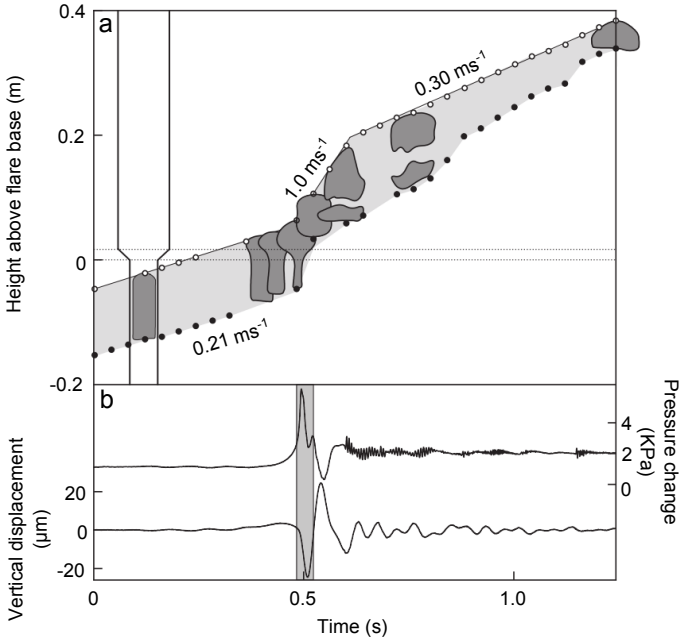


FIGURE 2.8: Slug ascent from small to large diameter tube in the laboratory experiments of James et al. (2006). (a) Position of the bubble (dark grey) in the tube shown on the left. White and black circles, respectively, mark the positions of the top and bottom of the bubble. Dotted lines mark position of the flare. (b) Pressure change (upper trace) and vertical displacement (lower trace) measured during slug ascent. The grey stripe represents the interval at which the slug tail passed through the flair. The fluid used is a 0.1 Pa s sugar solution. Adapted from James et al. (2006) via Chouet and Matoza (2013).

### 2.3.2 Indirect observations in the laboratory

Other experiments have been designed to help understand seismic sources without using AEs, such as friction experiments (Moore et al., 2008; Kennedy et al., 2009; Kendrick et al., 2012, 2014b; Hornby et al., 2015). Lava spines extruded during the 2004-2008 eruption of Mount St Helens were mantled by gouge layers, interpreted as the result of 'stick-slip' failure along the conduit margin that produced the 'drumbeat' seismicity (Fig. 2.2; Iverson et al., 2006; Cashman et al., 2008; Kendrick et al., 2012). Frictional experiments on gouge collected from the lava spines indicated that the material does satisfy the criteria needed to produce 'stick-slip' behaviour (Moore et al., 2008; Kennedy et al., 2009). Further work by Kennedy and Russell (2012) suggested an alternative 'fracture-slip' mechanism where rock fracture in undeformed dacite magma is followed by aseismic sliding within newly developed shear zones. Observations of pseudotachylytes within the gouge layers at Mount St Helens have been interpreted as evidence for frictional heating and melting taking place during the ascent of the lava spines (Kendrick et al., 2012). Using high velocity rotary shear experiments, Kendrick et al. (2014b) demonstrate how such frictional melt can be produced during seismogenic failure that produces the 'drumbeats' at Mount St Helens and Soufrière Hills volcano. At Unzen volcano, Japan, a combination of frictional experimental data, viscosity modelling, and seismic analysis show that frictional melt may commonly form and modify fault friction during the formation of a lava spine (Hornby et al., 2015).

## 2.4 Advantages of multi-disciplinary approaches

The methods described in this chapter each come with advantages and limitations. Seismic data is produced by processes which we cannot observe directly. We can use experimental investigations to constrain these processes (e.g. Burlini et al., 2007; Benson et al., 2008, 2010) but it remains unclear how to accurately scale from experimental to natural dimensions. Infrasound can be used to monitor eruptive activity at distances up to thousands of kilometres away (e.g. Caudron et al., 2015b), but often require visual observations of the processes to understand how the acoustic signal is generated. Multi-disciplinary studies using two or more approaches can reduce and/or help extract more information from the collected datasets. Recent reviews of volcano-seismicity (Chouet and Matoza, 2013) and volcanic infrasound (Fee and Matoza, 2013) each independently concluded that these fields are complementary for studying active volcanic processes. Indeed, many recent studies have used seismo-acoustic data to understand processes such as explosions (e.g. Johnson and Aster, 2005; Petersen and McNutt, 2007; De Angelis et al., 2012b; Gerst et al., 2013; Johnson et al., 2014; Palacios et al., 2016; Yamada et al., 2016; Fee et al., 2017), rockfalls (e.g. Johnson and Ronan, 2015), or shallow LP seismicity (Matoza et al., 2009b). Furthermore, as infrasound is largely generated by surficial processes it is readily compatible with other datasets such as gas, visual, and thermal (e.g. Delle Donne et al., 2014; De Angelis et al., 2016). A study by Johnson et al. (2014) provides a good illustration of the potential for integrating multiple datasets to understand eruptive processes. They collected acoustic, seismic, visual and deformation data during regular gas-and-ash explosions occurring at Santiaguito volcano, Guatemala, (see Section 3.4). Using this dataset, they were able to calculate gas fluxes, effusion rates, explosions source depths, and the ascent rate of volatiles through the conduit during an explosion. The analysis of this multi-parametric dataset had the ability to produce a detailed chronology and better understanding of explosion dynamics at an active volcano.

As our current understanding of lava dome behaviour develops, it becomes increasingly clear that the assessment of risks and hazards during ongoing and future eruptions requires integrated multi-disciplinary efforts. Due to the complexity of their eruptions, from the processes affecting magma ascent in the conduit, through to extrusion, emplacement, and destruction-related hazards, no two eruptions have behaved in the same manner, even at the same volcano. Therefore, the study of multiple examples of this type activity remains a key priority for modern volcanologists.

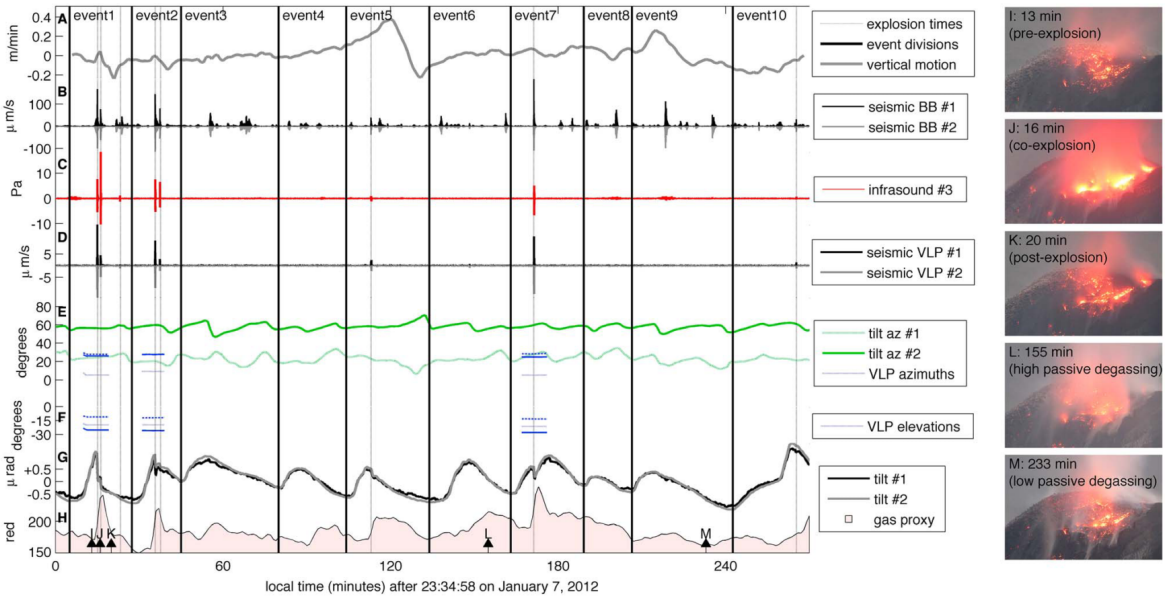


FIGURE 2.9: Joint geophysical observations of gas-and-ash explosions at Santiaguito volcano, Guatemala. (a) Average vertical velocity of the dome surface. (b) Broadband seismic signals indicating both explosion and rockfall signals. (c) Infrasound pressure transients showing the occurrence of gas-and-ash explosions (indicated by vertical grey lines). (d) Filtered seismic velocity records showing VLP signals associated with explosions. (e) Principal azimuths and (f) elevations of explosion sources as extracted from VLP signals. (g) Tilt records from two stations along with (h) gas flux proxy comparison. (i-m) Nighttime images of the active dome surface for indicated times. Adapted from Johnson et al. (2014).

# Chapter 3

# Lave domes and case study areas

## 3.1 Lava domes

Lava domes are defined as mounds of viscous lava and rocks that accumulate around a volcanic vent (Calder et al., 2015). They form as a result of cooled and degassed magma erupting onto the Earth's surface. Domes can form relatively rapidly in days to weeks, but can continue growing for years to decades, reaching diameters of a few kms and heights of up to 1 km. Hazards associated with growing domes include partial collapse, pyroclastic density currents, rockfall, moderate to major explosive activity, and lahars. The tendency for lava domes to undergo rapid transitions from effusive to explosive activity, to collapse with little warning, and to undertake protracted eruptive episodes, makes them a challenging type of activity for volcano observatories to manage. This type of volcanism is most commonly observed at convergent margin settings, and accounts for approximately 6% of eruptions worldwide (Calder et al., 2015). Therefore, an improved understanding of lava domes is vital for reducing the risks posed by such events.

The lava compositions of dome-forming eruptions are predominantly intermediate (andesite and dacitic) although they can also be basaltic or rhyolitic. All domes have high viscosities upon eruption, either through degassing-driven crystallisation (Sparks et al., 2000), or cooling and rheological stiffening of interstitial glass (Dingwell, 1996). Domes may form a range of morphologies, controlled by a combination of magma rheology, substrate topography, ascent dynamics and rate, and the mechanism of dome growth (i.e. endogenous or exogenous; Calder et al., 2015). Highly viscous lobate structures that are emplaced near the vent are classed as lava lobes. A number of different types can occur, from shear lobes, whalebacks, to pancake lobes (Calder et al., 2015). The most viscous magma can be extruded as a solid body called a spine, forming a massive columnar structure extruding along faults (e.g. Hornby et al., 2015). Spines are emplaced as coherent structures, but are rarely preserved due to their tendency to collapse as cooling and deformation continues.

## 3.2 Dynamics of lava dome formation

A wealth of data has emerged in recent decades to give us an increasingly complex description of the dynamic processes occurring during the eruption of silicic lava domes. This data has been collected in various ways: field observations from past and current eruptions (e.g. Tuffen et al., 2003), geophysical monitoring (e.g. Chouet et al., 1994; Neuberg et al., 2006), experimental efforts to replicate the processes in the lab (e.g. Kendrick et al., 2014b), as well as analogue and numerical modelling (e.g. Fink and Griffiths, 1998; Collinson and Neuberg, 2012). In this section, I will provide an overview of the most important processes that affect magma ascent and eruption dynamics during the formation of lava domes.

### 3.2.1 Petrology and magma ascent rates

The microtextural information present in eruptive material produced during dome eruptions are an important indicator of the physiochemical changes that can affect magma dynamics during its ascent in the conduit. Lava dome eruptions are generally driven by magma ascending at low rates (e.g. 10-50 m per day at Unzen volcano; Nakada et al., 1999). This results in magma having sufficient time to react to local changes in pressure and temperature conditions. As the magma rises and decompresses, gas bubbles form, microlites crystallise and water-rich minerals become unstable and react to recrystallise as anhydrous minerals (Cashman and Blundy, 2000). In rare occasions where silicic magma ascends at a high rate, it can skip these steps to quench and produce an obsidian-rich lava dome (e.g. eruption of Chaiten, Chile, in 2008-09; Pallister et al., 2013). Generally, the crystal and bubble content can be an important record of the magma decompression history, i.e. how quickly the magma ascended from the magma chamber to the surface (Cashman and Blundy, 2000). As I will describe in the next section, the crystal and bubble content of an ascending magma can have important implications for its rheology and, in turn, its eruptive dynamics.

### 3.2.2 Magma rheology

Rheology refers to the study of flow and deformation of materials. The rheology of magma is usually measured by its viscosity, which is a measure of a fluid's resistance to flow. Experiments have shown that viscosity has a first order control on deformation mechanisms and hence on magma ascent and extrusion (Lavallée et al., 2012a). Furthermore, analogue experiments have illustrated how, for example, changes in effusion rate can affect the morphology of the erupted lava dome (e.g. Fink and Griffiths, 1998).

Magma is a viscoelastic liquid, that is it shares the properties of a viscous body and an elastic body, separated in terms of strain rate and temperature. The divide, also known as the glass transition, marks either the ductile flow of magma or the onset of brittle failure

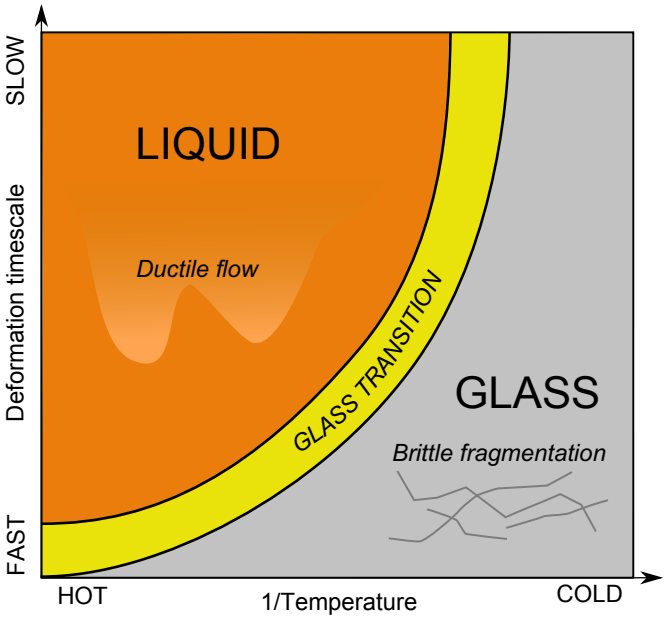


FIGURE 3.1: The glass transition in a time-reciprocal temperature space. Slow deformation would induce a relaxed, ductile flow in magma. Deformation at higher rates than the glass transition would induce elastic, brittle failure of magma. Adapted from Dingwell (1996).

(Fig. 3.1; Dingwell and Webb, 1989; Webb and Dingwell, 1990; Dingwell, 1996). Due to this property, lava dome behaviour can shift on short timescales in response to changes in strain rate. The addition of crystals and bubbles to magma can alter their rheological properties. An increase in the volume fraction of crystals causes an increase in viscosity (e.g. Lejeune and Richet, 1995; Costa et al., 2009), reducing the strain rate required for brittle failure (e.g. Gottsmann et al., 2009). The effect of bubbles on magma rheology depends on bubble size and strain rate, quantified as the capillary number (*Ca*; e.g. Llewellin and Manga, 2005). At low *Ca*, which means smaller bubbles and slower strain rates, the viscosity of the magma increases and therefore is more likely to fragment. With larger bubbles and higher strain rates, i.e. a high *Ca*, the viscosity decreases. At higher bubble fractions we expect see more shear-thinning behaviour. However, it is still not fully understood how the rheology of a bubbly suspension varies with different pressures; it may well be shear thinning or shear thickening depending on the conditions. Nevertheless, the volume fraction of crystals and bubbles is critical to whether the magma ascends to the surface as a fluid or as a lava plug, with strain localisation at the margins.

### 3.2.3 Permeability and porosity dynamics

Permeability is defined as the capacity of a material to transmit fluids. The permeability of rocks is generally positively correlated with porosity (e.g. Bourbié and Zinszner, 1985), defined as the fraction of voids in a volume of material. Vesicles, micro- and macro-cracks can contribute to overall porosity in volcanic rocks, resulting in complex permeable networks through the shallow volcanic edifice (e.g. Sparks, 1997; Heap et al., 2014; Farquharson et al., 2015). Furthermore, permeability can heavily depend on the orientation of the vesicles and

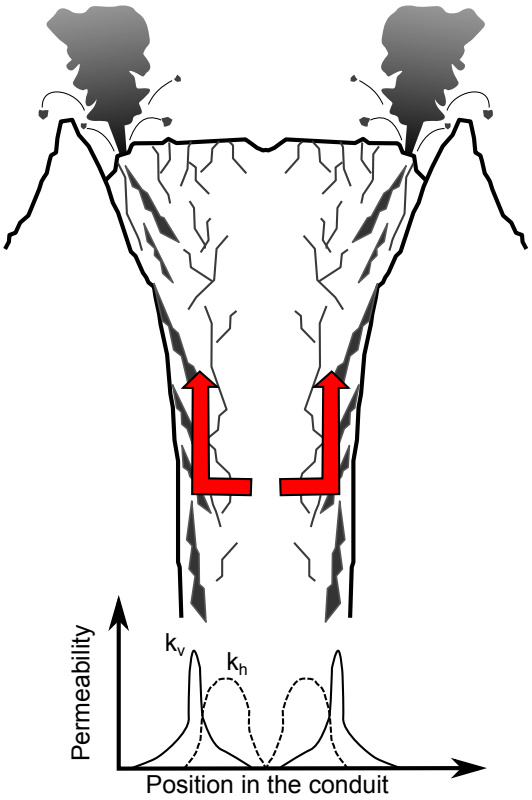


FIGURE 3.2: Localisation of strain induces an increase in permeability (k), promoting outward degassing (red arrows) towards the conduit margins, where magma is subjected to the highest strain rates. Vertical permeability ($k_v$) favours the ascent of gas over horizontal permeability ($k_h$). Adapted from Lavallée et al. (2013).

cracks; e.g. vertically orientated cracks would favour the vertical ascent of fluids (Fig. 3.2). As such, permeability can vary by up to four orders of magnitude for any given porosity (Farquharson et al., 2015). During lava dome eruptions, the development of a permeable network is critical as it affects outgassing and dome pressurisation and, thus, the likelihood of explosive activity (Sparks, 1997). For example, a low permeability plug in the vent may increase overpressure in the conduit, leading to explosive activity (e.g. Johnson et al., 2008; Lavallée et al., 2012a). The risk of explosions can be reduced by degassing via permeable networks through heavily fractured lava domes or country rock (e.g. Jaupart, 1998) and/or highly damaged conduit margin zones (Fig. 3.2; e.g. Lavallée et al., 2013; Gaunt et al., 2014). Therefore, understanding how permeability and porosity can change during a lava dome eruption is a fundamental element for describing transitions from effusive to explosive behaviour, and vice versa.

Recent investigations have illustrated how various processes can locally alter permeability throughout the lava dome (e.g. Lavallée et al., 2013; Kendrick et al., 2016). At depth, fractures are shut due to high normal stresses, and permeability is shut off (e.g. Heap et al., 2015a). Strain localisation near the conduit margin causes shear failure and constructs a permeable network, favouring outgassing towards the conduit margin followed by vertical fluxing (Fig. 3.2; Lavallée et al., 2013). Similarly, the brecciation of magma along the conduit margins can aid the degassing of ascending magma (e.g. Rust et al., 2004). Inspection

of rocks from lava domes have identified tuffisites as an important indicator for the state of permeability and pressurisation during the eruption. Tuffisites are veins of fine-grained pyroclastic material that have melted and deposited in cracks and voids in lavas, thought to be formed during gas-and-ash explosions (e.g. Tuffen et al., 2003; Castro et al., 2012). The tuffisite veins are generally several orders of magnitude more permeable than the lava rock, providing a network for degassing to occur, and reducing the risk of explosive activity (e.g. Kendrick et al., 2016). Active hydrothermal systems during dome eruptions may block degassing pathways through the precipitation of fluid-transported minerals into the voids (e.g. Horwell et al., 2013). Rodgers et al. (2015b) cite a similar mechanism to explain variations in seismic activity during persistent explosive activity at Telica volcano, Nicaragua.

### 3.2.4 Cyclic magma ascent

Multi-parametric datasets collected during lava dome eruptions have commonly highlighted their cyclic eruptive dynamics (e.g. Voight et al., 1999). These cycles can occur over a large range of timescales, from seconds (e.g. Iverson et al., 2006) to years (e.g. Barmin et al., 2002). Since the beginning of its eruption in 1997, Soufrière Hills volcano on Montserrat has produced cyclic activity across a wide range of timescales (Odbert et al., 2014). Over months to years, the lava dome eruption has undergone protracted episodes of dome growth in between periods of relative quiescence (Wadge et al., 2014). A commonly accepted conclusion is that the approximately 1-3 year extrusion cycles have been controlled by the recharging of a shallow magma chamber (top at circa 5 km) until it is ready to erupt again (e.g. Elsworth et al., 2008; Foroozan et al., 2011). Volcán de Colima is another example to display this type of cyclic behaviour since the beginning of its current activity in 1998 (section 3.4).

On shorter timescales, seismic and deformation records (Voight et al., 1998; Odbert et al., 2014) as well as $SO_2$ flux (Nicholson et al., 2013) at Soufrière Hills volcano have displayed cyclic activity with a $\sim$50 day period. This cycle has been interpreted as an effect of a dyke between the shallow magma chamber and a shallower cylindrical conduit (Costa et al., 2007a). The dyke acts like a volumetric capacitor with elastic walls, storing magma as pressure increases from the chamber, and releasing the magma into the conduit in a pulse of extrusion. Hautmann et al. (2009) used numerical modelling to demonstrate that such conduit geometry could explain the deformation data at Soufrière Hills volcano.

The dyke and conduit geometry has also been used to explain sub-daily cycles seen at Soufrière Hills (Costa et al., 2012). These cycles have been seen in seismic and tilt data overprinted onto the previously described $\sim$50 day cycles (Fig. 3.3; Voight et al., 1998; Voight et al., 1999; Neuberg et al., 2006). The deformation is interpreted as pressurisation in the shallow conduit due to the formation of a lava plug near the surface (Voight et al., 1999). When pressure reaches a critical threshold, the plug margins fail and move upwards, sometimes with vigorous ash ejection. The reduction of pressure beneath the repositioned plug

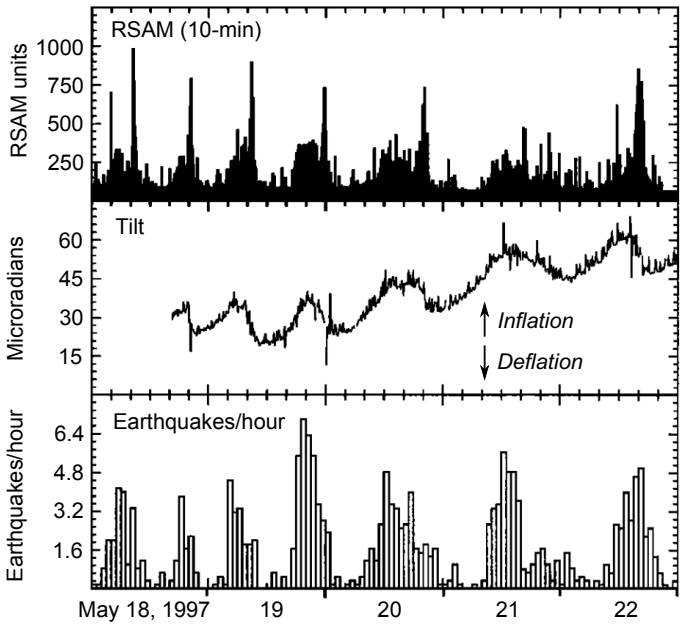


FIGURE 3.3: Comparison of cyclic seismic and tilt records from Soufrière Hills volcano in May 1997. The recorded earthquakes are dominated by hybrid events. The largest spikes in RSAM are rockfalls or pyroclastic flows. Adapted from Voight et al. (1998).

promotes magma degassing and the cycle continues. Magma fracturing and stick-slip flow during these cycles are interpreted as a trigger for LP earthquakes recorded during these cycles (Neuberg et al., 2006; De Angelis and Henton, 2011; Thomas and Neuberg, 2012). An alternative proposal for the sub-daily cycles cites regular fluxes of gas through the conduit to drive cyclic magma ascent (e.g. Michaut et al., 2013). Similar cycles, although with a much shorter ∼30 min period, have been described in seismic and deformation data at Santiaguito volcano, Guatemala (e.g. Johnson et al., 2014).

On a timescale of seconds to minutes, magma ascent can happen in repetitive, cyclic pulses of movement at rates of $mms^{-1}$ to $ms^{-1}$. This type of activity tends to be accompanied by repetitive LP seismicity, often described as 'drumbeats', and have been observed at Soufrière Hills volcano during periods of extrusion (De Angelis, 2009; Kendrick et al., 2014b). These repetitive earthquakes are interpreted as either the result of magma failure and stick-slip near the conduit margin, or the movement of hydrothermal fluids (section 2.1.2). They have also been observed at other volcano such as Mount St. Helens (Iverson et al., 2006; Iverson, 2008), Augustine (Power and Lalla, 2010), and Reventador volcanoes (Lees et al., 2008).

## 3.3 Current challenges for monitoring lava domes

Lava dome eruptions are an inherently complex type of volcanic activity with a wide range of dynamic processes affecting their behaviour. This presents a number of challenges for those analysing geophysical data collected prior to and/or during eruptions. For example, new eruptions are generally preceded by intense seismic activity beneath the volcano edifice

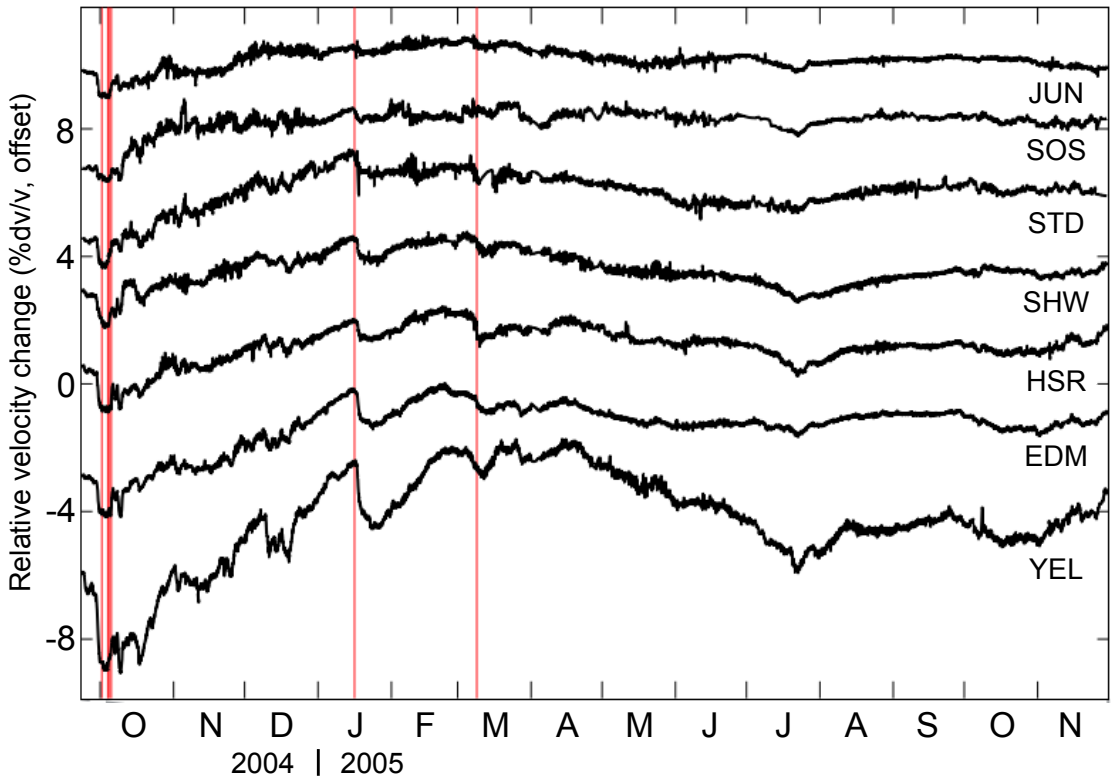


FIGURE 3.4: Relative velocity changes calculated from repeating earthquakes at Mount St Helens, plotted by distance from dome with closest station (YEL) at bottom. Vertical red lines mark explosions that occurred during the eruption. Adapted from Hotovec-Ellis et al. (2015).

due to magma movement (e.g. Nakada et al., 1999; Zobin et al., 2002a; White and McCausland, 2016). However, false alarms can be triggered by seismic activity produced by magma that never reaches the surface (e.g. White et al., 2011), or by hydrothermal fluid movement (e.g. Hill, 1996; Shelly et al., 2013). In some cases, eruptions can be preceded by very little seismic activity (e.g. Ogiso et al., 2015). Therefore, many investigations have tested new analytical tools to help improve short-term eruption forecasting (e.g. Bell et al., 2011; Brenguier et al., 2016). One example is calculating relative velocity changes in seismic data (Ratdomopurbo and Poupinet, 1995; Wegler et al., 2006; Brenguier et al., 2008; Duputel et al., 2009; Hotovec-Ellis et al., 2014). This uses the idea that stress changes from ascending magma would affect the velocity at which seismic waves can travel through the surrounding rock. Relative seismic velocity changes can be calculated from either repeating earthquakes (Fig. 3.4; Hotovec-Ellis et al., 2014, 2015) or ambient seismic noise (e.g. Brenguier et al., 2008), and have successfully detected significant signals related to eruptive activity (Brenguier et al., 2008; Hotovec-Ellis et al., 2015). Despite these successes, there are still limitations and potential for improving the technique. For example, very few investigations using this technique have directly verified their results using laboratory experiments, or tested the effect of different rock properties such as composition, porosity, and permeability.

The eruption of a lava dome can be accompanied by a wide range of volcano-seismic signals, from VT to explosive activity (section 2.1). Repetitive LP seismic signals have presented a particular challenge as they may be triggered by several different mechanisms (section 2.1.2). At Mount St Helens, repetitive 'drumbeats' have been interpreted as either the cyclic collapse and recharge of pressurised hydrothermal cracks (Waite et al., 2008; Matoza et al., 2009b) or stick-slip brittle failure along the margin of an ascending plug (Iverson et al., 2006; Kendrick et al., 2012). The debate continues to present day with both interpretations supported by geophysical, experimental and field investigations. What is clear, however, is that the observations from Mount St Helens have driven a lot of interest into using multidisciplinary approaches to understand the source mechanisms of repetitive LP events during dome eruptions.

One of the main challenges during monitoring lava domes is improving the system for timely and clear forecasting or eruption reports. Such reports may be used by private or governmental organisations to assess the hazard and take action to reduce the risk to the public. Air travel is one of the fastest growing industries in the world, but can be severely impacted by ash-rich volcanic eruptions. Aircraft engines can be badly damaged by airborne ash so timely and accurate reports of ash plumes into the atmosphere are of paramount importance for air travel companies (e.g. Prata and Tupper, 2009; Drexler et al., 2011). Currently, ash advisories are based on satellite imagery and numerical models of atmospheric ash dispersion (Mastin et al., 2009). While there might be a long wait for satellites to come overhead and image the plume, the numerical models rely on accurately known parameters regarding the eruption. Geophysical methods such as real-time GPS (Hreinsdóttir et al., 2014), seismic (Prejean and Brodsky, 2011), doppler radar (Schneider and Hoblitt, 2013) and infrasound (e.g. Caplan-Auerbach et al., 2010) all offer means for calculating these parameters. However, they can be limited by expense, requiring instruments dangerously close to the eruption vent, or by needing extensive networks around the volcano. Little work has been carried out to demonstrate how data from a single infrasound instrument, combined with newly developed numerical models, can efficiently and accurately predict the height of an ash plume from an eruption.

## 3.4 Case study lava domes

This study potentially has implications for monitoring efforts at many volcanoes worldwide, but will focus on the following as case studies: Volcán de Colima (Mexico), Unzen (Japan), Santiaguito dome complex (Guatemala), and Mt. Redoubt (USA). They were chosen due to the availability of datasets and materials to test out methods and ideas. This presented an interesting and unique opportunity to explore the similarities and differences between these and other silicic volcanoes, and to add to the understanding of the mechanics during silicic

eruptions which will hopefully feed into the hazard assessment processes by monitoring institutions.

**Volcán de Colima, Mexico**
***Composition: Andesite***
***Last eruption: 1998 - 2011, 2013 - ongoing***

Volcán de Colima, one of the most active volcanoes in North America, is located at the western end of the Trans-Mexico Volcanic Belt, approximately 30 km NNE of the city of Colima (Fig. 3.5). The andesitic stratovolcano has been active throughout historical time, broadly defined by ca. 100 year cycles of effusive activity culminating in major sub-Plinian or Plinian eruptions (Luhr and Carmichael, 1990; Breton Gonzalez et al., 2002; Luhr, 2002). The current eruptive episode began in November 1998 following a year of volcano-seismic swarms (Navarro-Ochoa et al., 2002; Zobin et al., 2002b). In a day, a new lava dome had filled the summit crater and lava was flowing over the SW rim (Navarro-Ochoa et al., 2002). Multiple pyroclastic flows originated from the repeated collapse of the flow front (Saucedo et al., 2002). This phase ended in February 1999 with an estimated total erupted lava volume of 0.039 $km^3$ (Zobin et al., 2002b) and the lava flow extending to a final length of 3.8 km (Navarro-Ochoa et al., 2002). Eruptive activity has been semi-continuous up to the present day, characterised by at least five more effusive episodes. Small gas-and-ash explosions of variable ash content have also occurred at a rate of <10 per day since March 2003. Large Vulcanian explosions in 2005, and a large dome collapse in 2015 represent the most intensive activity at the volcano since the last sub-Plinian eruption in 1913 (Varley et al., 2010; Reyes-Dávila et al., 2016). These phases of intense activity underscore the importance of a better understanding of the hazards posed to the local population.

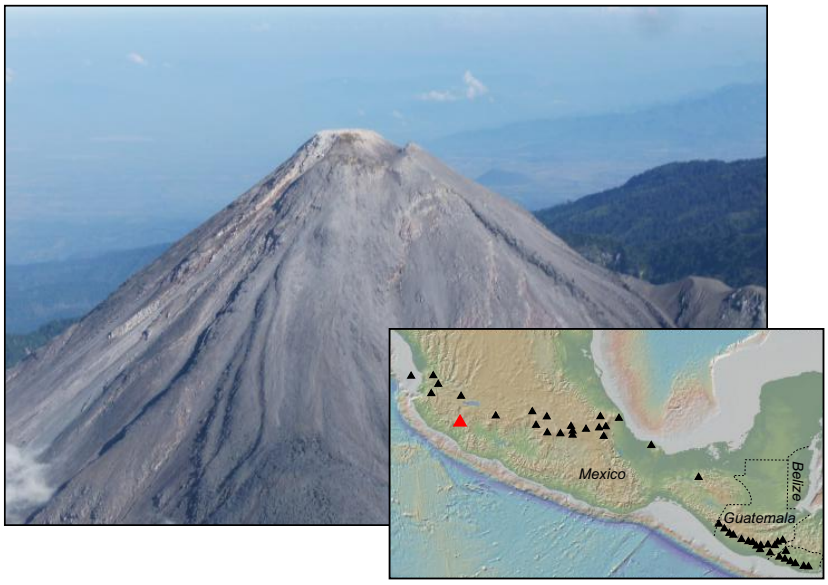


FIGURE 3.5: Volcán de Colima in May 2014. Inset: Location map of Volcán de Colima (red triangle). Also indicated are the location of other Holocene volcano centres in the region (black triangles), as identified by the Global Volcanism Program (Venzke, 2013).

**Unzen, Japan**
***Composition: Dacite***
***Last eruption: 1990 - 1995***

Unzen volcano, located on the Shimabara Peninsula in southern Japan, is a composite volcano with the volume of at least 35 $km^3$ consisting of multiple dacite to silicic andesite volcanic domes (Fig. 3.6; Nakada et al., 1999). It has grown within an active graben since ca. 500 ka and consists of lava flows or domes and their collapse debris (Nakada et al., 1999). A swarm of volcano-tectonic earthquakes to the west of the volcano in November 1989 heralded the first period of volcanic activity for 198 years (Nakada et al., 1999; Umakoshi et al., 2001). The hypocentral locations of the events moved progressively eastwards and towards the surface, culminating in phreatic explosions at Unzen in November 1990 (Nakada et al., 1999; Umakoshi et al., 2001). Phreatomagmatic eruptions followed in February 1991, which became larger over time, and evolved into an dacite dome eruption in May 1991 (Nakada et al., 1999). Dome growth began exogenically, with a brief phase of spine extrusion, followed by a series of 13 viscous lava lobes (Nakada et al., 1999). Vulcanian explosions occurred during initial dome eruption stages when the effusion rate was at its highest (Nakada et al., 1999). Due to its location on a topographic high the growing lava dome was structurally unstable, causing repeated partial collapses that generated pyroclastic density currents, forcing the evacuation of 10 000 local residents. Protracted spine growth defined the last 5 months of the eruption, beginning in mid-October 1994 (Nakada et al., 1999; Yamashina et al., 1999; Hornby et al., 2015). The eruption officially ended in February 1995, when lava effusion slowed to a halt and volcanic seismicity returned to pre-eruption levels (Nakada et al., 1999; Umakoshi et al., 2008).

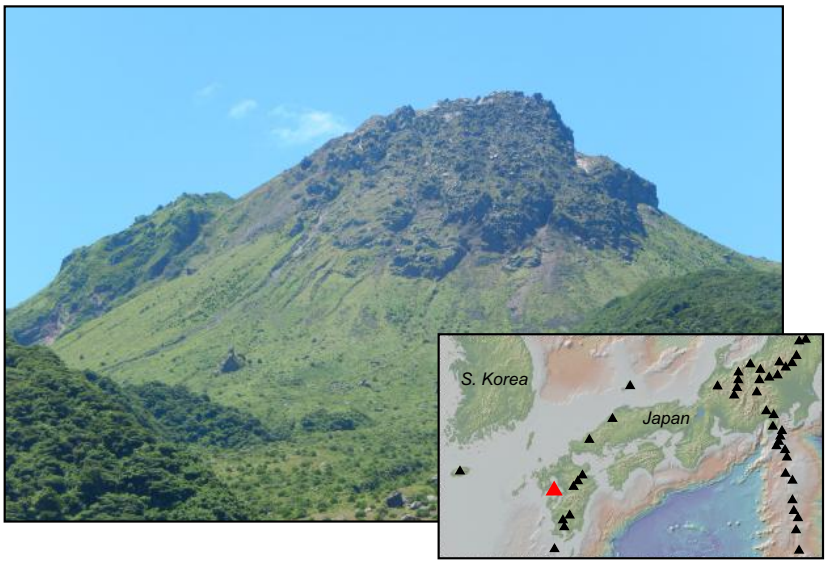


FIGURE 3.6: Unzen volcano in July 2013 (credit: Jackie Kendrick). Inset: Location map of Unzen volcano (red triangle). Also indicated are the location of other Holocene volcano centres in the region (black triangles), as identified by the Global Volcanism Program (Venzke, 2013).

**Santiaguito dome complex, Guatemala**
***Composition: Andesite - Dacite***
***Last eruption: 1922 - ongoing***

Santiaguito is a complex of dacitic lava domes and flows that grew at the base of the collapse scar formed by the 1902 eruption of Santa Maria, one of the largest of the twentieth century (Fig. 3.7; Bennett et al., 1992). Since its birth in 1922, eight cycles of extrusion from the El Caliente vent and three lateral vents (La Mitad, El Monje, and El Brujo) produced ~1.1 $km^3$ of lava (Rose, 1987; Harris et al., 2003). Since 1977, activity has been focused at the El Caliente vent and consists of semi-continuous extrusion of blocky lava flows interspersed by frequent gas-and-ash explosions, accompanied by occasional dome collapses and pyroclastic density currents (Rose, 1987; Harris et al., 2003; Harris et al., 2004). Explosions through the past decade have been of small-to-moderate size with volatile-rich, ash-poor plumes typically reaching 1-2 km above the vent (Yamamoto et al., 2008). Recent studies have shown a highly regular cycle of deformation associated with a source inferred at ~300 m below the El Caliente vent (Johnson et al., 2014). Petrological and geophysical work suggests the explosions are triggered by fragmentation that occurs along fault zones due to shear-induced thermal vesiculation (Lavallée et al., 2015b). Dome collapse has remained the greatest hazard throughout the eruption, causing thousands of deaths in 1929 (Rose, 1973), and continuing to threaten communities to the south. The most recent collapse took place in May 2014 and produced pyroclastic flows that ran for 10 km and destroyed some local infrastructure.

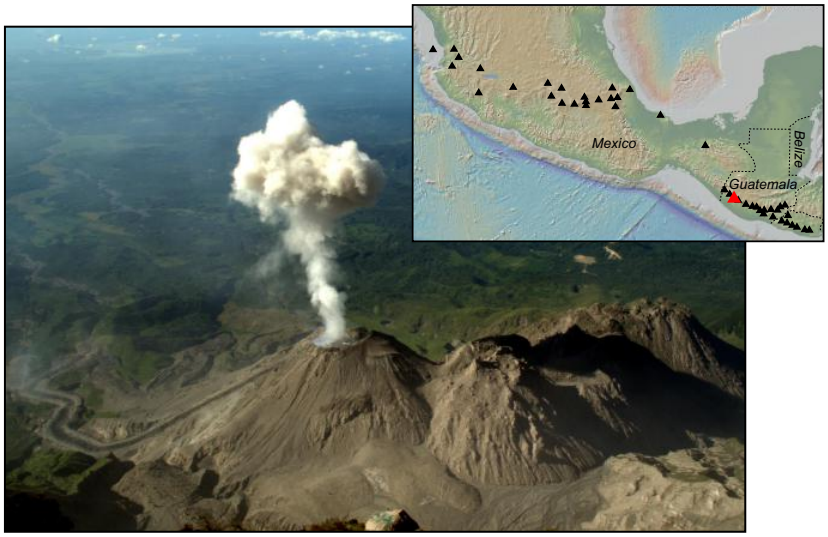


FIGURE 3.7: Santiaguito dome complex in November 2014. A small gas-and-ash explosion is exiting the active El Caliente vent. Inset: Location map of Santiaguito (red triangle). Also indicated are the location of other Holocene volcano centres in the region (black triangles), as identified by the Global Volcanism Program (Venzke, 2013).

**Mt. Redoubt volcano, USA**
***Composition: Basalt - Dacite***
***Last eruption: 2009***

Mt. Redoubt volcano is one of nearly 100 primarily andesitic volcanoes which lie along the Aleutian volcanic arc in Alaska, USA (Fig. 3.8). The volcano is located 170 km southwest of Anchorage, the largest population centre in the state, and is one of four historically active volcanoes that lie close to the area. The ice-covered edifice comprises of basaltic to dacitic pyroclastic density current deposits, block-and-ash flow deposits, and lava flows (Till et al., 1994). In March 2009, the volcano erupted for the first time since 1990, producing explosive and effusive activity. On March 15, a small phreatic explosion marked the onset of the eruption. This was followed by 19 explosions between March 23 and April 4, of which at least 16 produced ash plumes of 5-18 km height (Schneider and Hoblitt, 2013), disrupting international and domestic airspace over Alaska. During the same period, multiple pyroclastic density currents flowed to the north into glacial ravines, major lahars affected oil-storage infrastructure over 35 km away, and tephra fell on communities over 100 km away. On April 4, the eruption entered a phase of continuous lava extrusion at the summit before ending in July 2009.

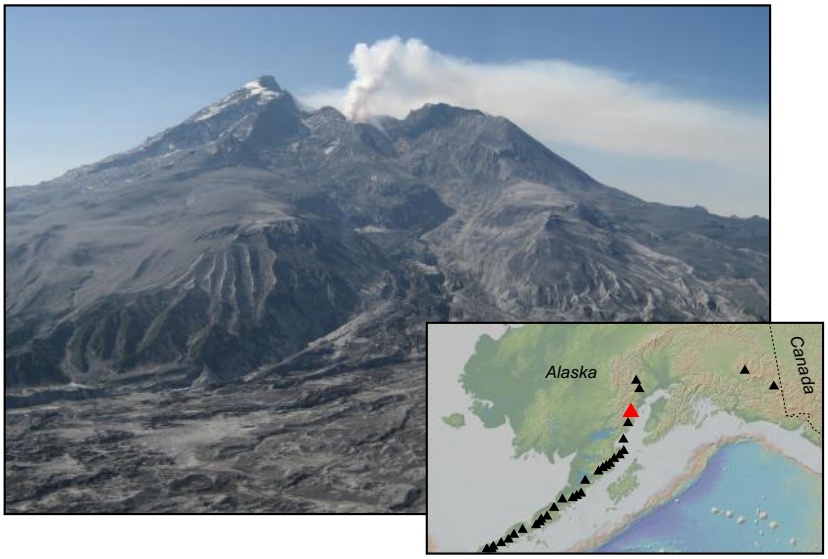


FIGURE 3.8: Mt. Redoubt in June 2009. (credit: AVO/UAF-GI) Inset: Location map of Mt. Redoubt (red triangle). Also indicated are the location of other Holocene volcano centres in the region (black triangles), as identified by the Global Volcanism Program (Venzke, 2013).

# Chapter 4

# Seismic and experimental insights into eruption precursors at Volcán de Colima

This chapter is derived from a manuscript accepted for publication in *Geophysical Research Letters* on 1 May 2017 and in press at the time of thesis submission. The authors of the manuscript are Oliver Lamb (main author), Silvio De Angelis, Richard J. Wall, Anthony Lamur, Nick R. Varley, Gabriel Reyes-Dávila, Raúl Arámbula-Mendoza, Adrian J. Hornby, Jackie E. Kendrick and Yan Lavallée. The aim of this study was to use a seismic and experimental approach to understand the pre-eruptive activity at Volcán de Colima in 1998. Silvio De Angelis participated in the seismic analysis. Richard J. Wall, Adrian Hornby and Anthony Lamur assisted with the experiments in the volcanology laboratory in the University of Liverpool. Nick R. Varley, Gabriel Reyes-Dávila, and Raúl Arámbula-Mendoza provided the seismic data analysed in this study. Jackie Kendrick collected the andesite samples used in the experiments. Yan Lavallée participated in the design of the study and experiments and helped draft the manuscript. All authors read and approved the submitted manuscript. The manuscript was accompanied by supplementary information which contained one table and four figures. The table has been incorporated into this chapter, and the figures can be found in Appendix B on page 115.

## Paper abstract

We combine geophysical and experimental observations to interpret pre-eruptive unrest at Volcán de Colima in 1998. 17,893 volcanic earthquakes were detected between 1 October and 31 December 1998, including 504 clusters. Using seismic ambient noise interferometry, we observe a drop in velocity prior to the eruption linked to damage accumulation during magma ascent. This is supported by experimental observations where static stress causes a velocity decrease prior to failure. Furthermore, we observe acoustic emission clusters during

the experiments, with lower porosity samples producing higher numbers of repeaters. This behaviour introduces tensile failure as an additional viable mechanism for clusters during magma ascent. The findings suggest pre-eruptive magma ascent may be monitored to variable degrees of accuracy via descriptions of damage accumulation and associated seismic velocity changes.

## 4.1 Introduction

An important aspect of volcano monitoring is assessing whether a period of unrest will portend an eruption. Recent studies have shown that seismic interferometry, using either the coda waves of repeating earthquakes or ambient noise, holds considerable potential as a tool for monitoring active volcanoes (e.g. Brenguier et al., 2008; Hotovec-Ellis et al., 2015). Seismic wave velocities are dependent on the physical properties of the material through which they travel, and velocity changes may be induced by property changes. Seismic velocity is frequently observed to decrease prior to eruption, and subsequently increase as the eruption ensues; a pattern often attributed to cycles of static stress due to magma movement (e.g. Ratdomopurbo and Poupinet, 1995; Wegler et al., 2006; Brenguier et al., 2008; Duputel et al., 2009; Hotovec-Ellis et al., 2015).

Laboratory experiments have enabled relative velocity changes to be recorded over a range of pressure and temperature conditions. The accumulation of fracture damage during loading under deviatoric stresses causes a elastic velocity decrease in the tested samples (e.g. Heap et al., 2010). During rock failure tests, individual micro-cracking events are recorded via acoustic emissions (AEs). AEs have been demonstrated to precede material failure under temperature and stress conditions typical of shallow volcanic conduits (e.g. Lavallée et al., 2008). Further investigations have used the characteristics of AEs under controlled conditions to decipher the source mechanisms of volcanic earthquakes (e.g. Benson et al., 2008; Smith et al., 2009). The recent advances in experimental rock mechanics have improved our understanding of field-scale volcanic processes.

Very few investigations on seismic velocity changes at volcanoes have sought to replicate their results in laboratory settings. In this paper we conduct a joint seismic and experimental investigation of the mechanical response of edifice rocks prior to the November 1998 effusive eruption of Volcán de Colima, Mexico. We utilise the ambient seismic noise method on seismic data collected during this period and replicate our observations via experimental tests on samples collected from Volcán de Colima. This dual approach enables us to build a more robust interpretation of the processes occurring during pre-eruptive magma ascent. Ultimately, we aim to demonstrate the potential of cross-disciplinary investigations between the fields of seismology, experimental volcanology and rock mechanics.

### 4.1.1 1998 eruption of Volcán de Colima

Volcán de Colima (VdC) is an andesitic stratovolcano located in western Mexico (Fig. 4.1). From 1998 to 2011, VdC experienced multiple phases of lava extrusion, interspersed by explosive activity accompanied by emplacement of pyroclastic flows and occasional dome collapses, providing a valuable opportunity to study a rapidly evolving volcanic system. The first phase of activity was preceded by five swarms of deep and shallow volcanic earthquakes over the course of a year (Zobin et al., 2002a). The final swarm in November 1998, located <3 km beneath the summit, heralded the appearance of the dome at the summit vent on 20 November (Zobin et al., 2002a). The dome rapidly filled the summit crater before spilling over the SW rim to form a lava flow. Rockfalls and multiple pyroclastic flows originated from the repeated collapse of the flow front. This phase of extrusion ended in February 1999 with a lava flow extending to a final length of 3.8 km.

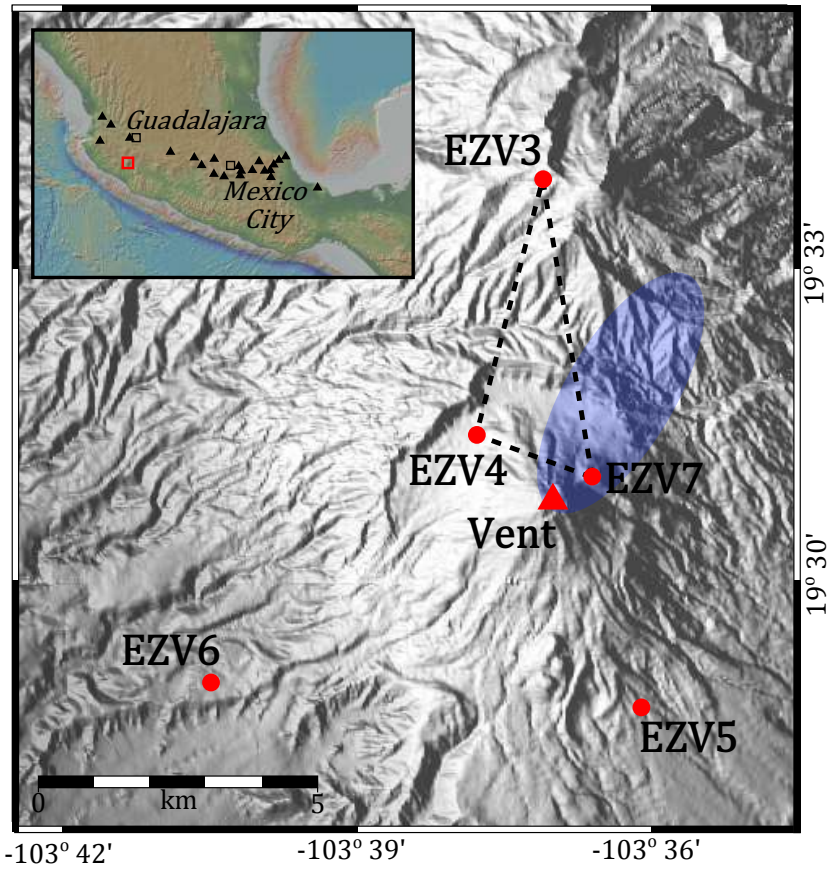


FIGURE 4.1: Map of VdC with the RESCO network of short-period stations marked as they were located in 1998. Blue ellipse marks where epicentres of November 1998 swarm were located by Zobin et al. (2002a). Dashed lines mark planes along which amplitude ratios and ambient noise analysis were calculated along. Insert: Map showing location of VdC in Mexico (red square), relative to the major cities of Mexico City and Guadalajara (black squares). Also indicated are the location of other Holocene volcanoes in central Mexico (triangles), as identified by the Smithsonian Global Volcanism Program.

## 4.2 Data and methods

### 4.2.1 Seismic

Seismic data used in this study were collected by the Colima Telemetric Seismic Network (Red Sísmica de Colima, RESCO), managed by Centro Universitario de Estudios e Investigaciones Vulcanologicas (CUIEV). In late 1998, this network consisted of five short-period seismometers (EZV3 - EZV7) located within 7 km of the volcano summit (Fig. 4.1). Signals were telemetered to CUIEV and were recorded with a sampling rate of 100 Hz. We applied multi-station earthquake detection from 1 October to 31 December 1998. Candidate trigger times were extracted from multiple stations using a short-term average/long-term average (STA/LTA) algorithm, on condition that an event was detected at three or more stations, assuming a reference seismic velocity of 2.5 km $s^{-1}$ (Nunez-Cornu et al., 2010). Seismic data were pre-processed with a bandpass filter between 1-7 Hz to improve signal-to-noise ratio.

Epicentres of 600 earthquakes prior to the eruption of VdC in 1998 were located generally NE of the summit vent (Fig. 4.1; Zobin et al., 2002a). The number and distribution of stations around VdC, as well as the emergent nature of most detected seismicity, does not enable accurate locations of more earthquakes. In order to track relative changes in the location of all seismicity prior to eruption at a higher temporal resolution, we employed the Seismic Amplitude Ratio Analysis method (SARA; Caudron et al., 2015a). This technique calculates the ratio of seismic intensity recorded at different seismic stations which are independent of seismic energy at the source. Since exceptional changes in attenuation are unlikely to occur at days-months timescales, temporal variations in the ratios must be explained by changes in source locations. Following a similar methodology to Caudron et al. (2015a), we calculated 10-min average Real-time Seismic Amplitudes (RSAM) for data from EZV3, EZV4 and EZV7 before using a 6-hour rolling median filter to smooth the data. Data from EZV5 and EZV6 were not used as they were contaminated by high levels of anthropogenic noise. Caudron et al. (2015a) noted that site effects, gains and sensitivity changes would correspond to a vertical shift in ratios, whereas changes in attenuation and wave regime would result in dilation or contraction. Therefore, we can use the relative changes rather than actual values that would require corrections (e.g., site effects).

Clusters, or groups of earthquakes with similar waveforms, are significant as they represent non-destructive sources at, generally, a fixed location (Iverson et al., 2006; Neuberg et al., 2006; Waite et al., 2008; Varley et al., 2010; Kendrick et al., 2014b; Lamb et al., 2015). We built a catalogue of clusters at VdC by applying waveform cross-correlation to our earthquake database. For each detected event, we use the first 5 s of the waveform; this time is sufficient as it includes the largest amplitudes of most waveforms whilst minimising the contribution of background noise. Seismograms from station EZV7 were used to build the catalogue, as

this station was closest to the summit vent (Fig. 4.1), and typically has the highest signal-to-noise ratio. All waveforms were filtered with a 0.5 - 20 Hz bandpass Butterworth filter to further increase the signal-to-noise ratio. The normalized cross-correlation coefficient (CCC) lies between 0 and 1, where 0 is unalike and 1 is identical, and was evaluated for every possible pair of earthquakes. A minimum CCC of 0.8 was used to define two or more earthquakes as a cluster. Using a CCC of 0.7 designates a higher proportion of earthquakes into clusters, but this is rejected as many of the clusters did not correlate visually (Fig. B.2).

Several studies have successfully used seismic ambient noise to detect small variations in seismic velocity prior to volcanic eruptions (e.g. Brenguier et al., 2008). The method uses repeated cross-correlations of seismic noise recorded at two seismic stations to assess the velocity properties of the sub-surface medium between them (Sens-Schönfelder and Wegler, 2006). A key advantage of this technique is that it bypasses the need for repeating earthquakes to assess the seismic velocity (e.g. Poupinet et al., 1984). For our calculations we used the MSNoise software, an open source python package for monitoring seismic velocity changes using ambient seismic noise (Lecocq et al., 2014). A cross-correlation function (CCF) was calculated from ambient noise seismic data from each individual pair of stations. Velocity variations were then calculated from different arrivals between individual CCFs and the reference CCF. Further details of the method and MSNoise program can be found in Lecocq et al. (2014). For our calculations, instrument responses were not removed because they were identical and constant in time at all stations. CCFs were calculated for time lags of $\pm$120 s within the frequency interval 0.5 - 1.1 Hz. This interval minimises the influence of volcanic earthquakes whose peak frequencies generally ranged from 1 - 10 Hz. We used a reference function stacked from noise recorded during October 1998, and calculated changes in velocity from stacks calculated over 5- and 10-day moving windows. A full list of the parameters used in MSNoise can be found in Table 4.1.

### 4.2.2 Experimental

In order to constrain the interpretation of seismological observations, we conducted deformation experiments to simulate the stressing conditions under which velocity change may be induced. We employed the Brazil test method to induce tensile failure (e.g. Li and Wong, 2013) in andesite lavas collected from the edifice of VdC. The tests involve the diametric compression of a sample disc (2:1 diameter:length aspect ratio), which induces tensional stresses in the orthogonal direction until the disc fails. This pseudo-tensile regime replicates, and can be used as a proxy for, the stress distribution associated with magma ascent prior to eruption. For our experiments, cylindrical samples of diameter 40 mm were drilled and then cut to a length of 20 mm, with the porosity of each disc measured using an Accupyc 1340 He pycnometer.

TABLE 4.1: Parameters used for calculating relative velocity change using the MSNoise ambient seismic noise package.

| **MSNoise configuration** | |
|---|---|
| **Parameter** | **Value** |
| Analysis duration (s) | 86400 |
| Cross-correlation sampling rate (Hz) | 20 |
| Resampling method | *Decimate* |
| Pre-process filter limits (Hz) | 0.01 - 8 |
| Maximum lag (s) | 120 |
| Correlation duration | 1800 |
| Overlap (%) | 50 |
| Windsorizing | 3 |
| Stacking method | *Linear* |
| Reference begin | 10/01/1998 |
| Reference end | 10/31/1998 |
| DTT Lag | *Static* |
| Lag window (s) | 10-40 |
| DTT sides | *Both* |
| Minimum coherence | 0.65 |
| Maximum DTT value | 0.08 |
| Maximum error | 0.1 |
| **Filter configuration** | |
| **Parameter** | **Value** |
| Whiten filter (Hz) | 0.5 - 1.1 |
| MWCS filter (Hz) | 0.5 - 1.1 |
| MWCS window length (s) | 12 |
| MWCS window step (s) | 4 |

The Brazil tests were carried out in a 100 kN Instron uniaxial press at room temperature and compressive deformation rate of 0.4 $\mu$m $s^{-1}$, corresponding to a diametral strain rate of $10^{-5}$ $s^{-1}$ (Fig. B.4). During the experiments, load was recorded by an Instron Dynacell 2527 load cell at 100 Hz, and tensile stress ($\sigma_t$) was calculated in real-time. Simultaneously, two ceramic piezoelectric transducers (PZT) attached to diametrically opposing faces of the disc (Fig. B.4) monitored AE data at a sampling rate of 1 MHz. The signals from each transducer were first fed through 20 dB amplifiers before reaching a PAC PCI-2 two channel recording system, with a bandwidth of 0.001-3 MHz and capable of simultaneous hit based collection and waveform streaming. For each experiment we tracked the hits per second and the energy of each hit; energy was calculated using the root-mean-square of the recorded waveform. AE clusters were identified using the a similar approach to that used to identify seismic clusters (previous section); but, no bandpass filter was used. To calculate elastic velocity properties of the sample, one PZT was set to produce 'pulses' for the entire experiment duration while the other PZT recorded the pulses after they travelled through the sample.

During the experiment, bursts of five pulses, each spaced 0.5 s apart, were triggered every 5 s. Each received pulse 'burst' was stacked to increase the signal-to-noise ratio before using coda wave interferometry (CWI) to calculate change in velocity during the experiment. CWI uses the degree of correlation of the coda waves for two waves from different time intervals to calculate the variance in travel time perturbation. In particular, the correlation coefficient, $R$, is related to the variance of the travel-time perturbation, $\sigma_\tau$, and to the frequency, $\overline{\omega}^2$, according to the following relationship (Snieder et al., 2002):

$$R = 1 - \frac{1}{2}\overline{\omega}^2\sigma_\tau^2 \tag{4.1}$$

The frequency, $\overline{\omega}^2$, can be calculated from the seismogram data, $u(t)$:

$$\overline{\omega}^2 = \frac{\int_{t-T}^{t+T} \dot{u}^2(t')dt'}{\int_{t-T}^{t+T} u^2(t')dt'} \tag{4.2}$$

where the integral is performed over a window of length $2T$ centred at time $t$. The velocity change follows from the travel time perturbation:

$$\frac{\delta v}{v} = -\sigma_\tau^2 \tag{4.3}$$

For our reference waveform, we used the stacked waveform from the first 'burst'. $\delta v/v$ was then calculated against this reference at the time of each of the following 'burst' in the experiment. Grêt et al. (2006) used a similar method to track changes in rock properties in response to changes in stress, temperature and water saturation.

## 4.3 Results

From 1 October to 31 December 1998, a total of 17,893 earthquakes were detected using our multi-station detection method on data from the RESCO network (Fig. 4.2a). We observe a gradual and steady rise in the number of seismic events detected per hour in the period 1-20 November 1998. Simultaneously, we observe an unsteady rise in the amplitude ratios of EZV4/EZV3 and EZV7/EZV3 that indicates the relative movement of earthquake sources towards stations EZV4 and EZV7 prior to the eruption on 20 November (Fig. 4.2b). We also observe that amplitude ratios for EZV4 are higher than that of EZV7, even though the latter is closer to the summit vent (Fig. 4.1). After 20 November, the seismic record is dominated by rockfalls originating from the lava flow on the western flank of VdC, thus explaining the larger EZV4/EZV3 ratio in the second half of our period of analysis. A total of 1,313 earthquakes were defined as repeating events, representing 7.3% of the catalogue, and spread

across 504 clusters containing between 2-22 events (Fig. 4.2c). 355 clusters were active during the 1 - 20 November earthquake swarm, of which <10 continue after this period. Using the ambient seismic noise during this period, we observe a ~0.2% decrease in seismic velocity from mid-October to 20 November (Fig. 4.2a). This is followed by what appears to be a sharp recovery of 0.2% shortly after the beginning of the eruption, but low coherence and large errors in measurements prevent consistent calculations during the second half of our period of analysis (Fig. B.3).

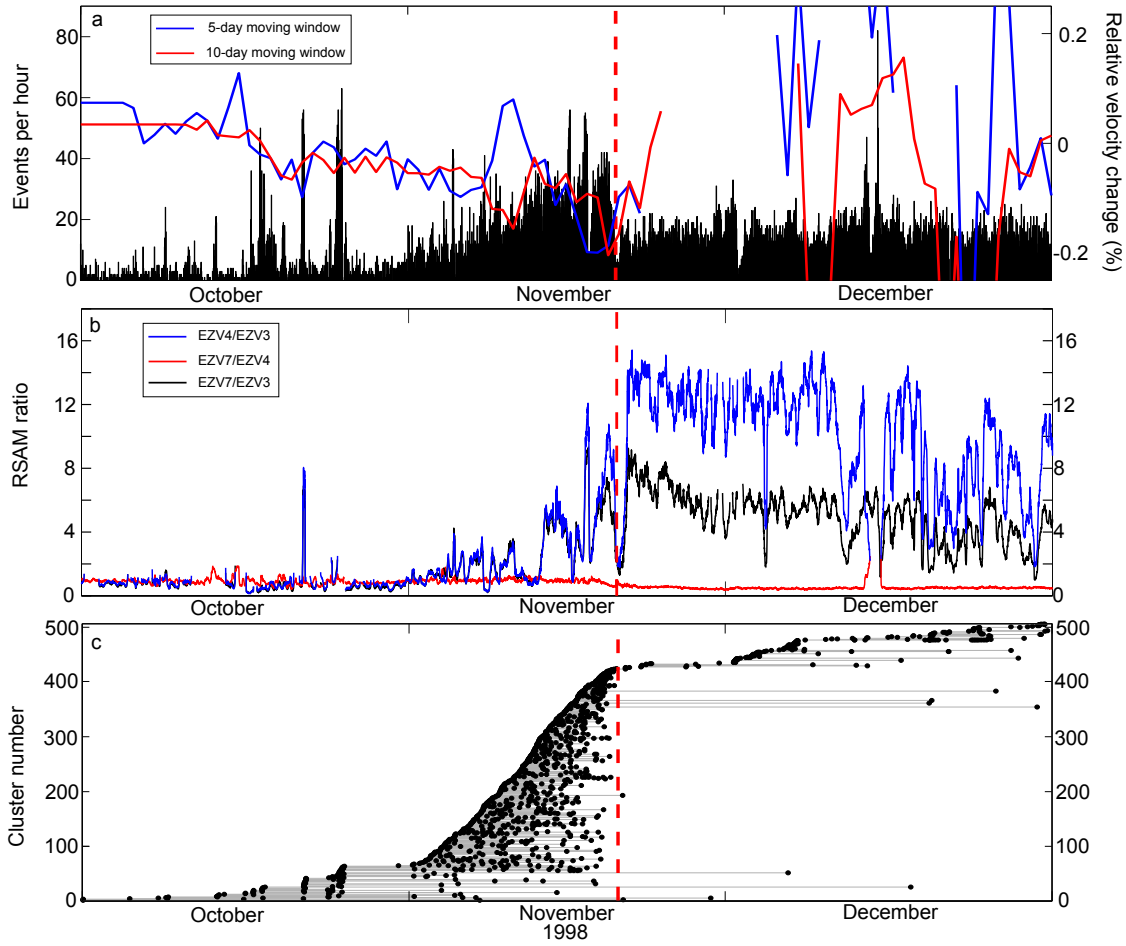


FIGURE 4.2: (a) Events per hour (black bars) from 1 October to 31 December 1998. Also plotted are the variations in seismic velocity calculated from 5-day (blue line) and 10-day (red) moving windows using seismic ambient noise. Gaps in lines represent periods where low coherence and large errors prevented viable calculations. (b) Intensity ratios calculated from 10-min RSAM for EZV3, EZV4 and EZV7 stations, smoothed using a 6-hour median filter. The original RSAM values are plotted in Figure S1. (c) Catalogue of repeating earthquakes (black dots and grey lines) in our dataset from 1 October to 31 December 1998. Each plotted point represents an individual earthquake, and each line joins groups of repeating events. The red dashed line in all plots represents the beginning of the effusive eruption at VdC on 20 November 1998.

Ten Brazil tests were conducted on samples with a porosity constrained at 0.07±0.02 (COL216), 0.15±0.01 (COLP2), and 0.22±0.02 (COLP21). The tensile strength of the samples was inversely proportional to the porosity, ranging between 7-22 MPa (Fig. B.5a). AE hit rate and cumulative AE energy showed an exponential increase prior to sample failure (Fig. 4.3a,b). Calculated relative velocity changes during the experiments showed a consistent decrease in measurements through all samples, with no apparent relation to sample porosity (Fig. 4.3c). We see very similar results when repeating these calculations but using the last pulse as a reference instead (Fig. B.6). We successfully detected AE clusters by cross-correlating waveforms collected during one test from each sample (Fig. 4.3d,e,f). The proportion of AE clusters was higher in samples of lower porosity. For COL216, 685 groups of repeating events were detected, containing 1657 hits (5.2% of all AEs detected), COLP2 had 152 groups with 337 hits (2.3%), and COLP21 had 25 groups with 56 hits (0.37%).

## 4.4 Discussion

By conducting a joint seismic and experimental investigation of the 1998 eruption of VdC, we aimed to establish the potential for using multi-disciplinary approaches to understand pre-eruptive seismic activity. The transport and eventual eruption of magma requires the formation of a pathway, and in the process, rocks fracture seismogenically, providing a key proxy to forecast the eruption onset (Smith et al., 2009). Indeed, this was inferred by previous analysis of the pre-eruptive volcano-seismic swarms of 1997-98 (Zobin et al., 2002a), and is also clearly seen in the seismic observations here (Fig. 4.2a). Using SARA on seismic data from EZV3, EZV4 and EZV7 stations, we found that the sources of the seismic activity tended to drift towards the stations closest to the vent during this period (Fig. 4.2b). Amplitude ratios at EZV4 tended to be higher than that of EZV7, even though the latter was located closer to the summit vent. This is likely an effect of the pyroclastic deposits where EZV4 is located, compared to the lava dome directly beneath EZV7.

Relative velocity changes measured over this period indicate a decrease of ∼0.2% prior to eruption. Low coherence and large errors in calculation prevent velocity calculations after the eruption from being well resolved. However, repeating the calculations with reference waveforms stacked from the whole period or December alone consistently calculates a slow velocity recovery following the eruption (Fig. B.1b, d). This cycle of decrease-increase around volcanic eruptions is similar in magnitude to those seen at other volcanoes (e.g. Ratdomopurbo and Poupinet, 1995; Wegler et al., 2006; Brenguier et al., 2008; Duputel et al., 2009; Hotovec-Ellis et al., 2015). However, it does not agree with previous observations from VdC using a similar methodology (Lesage et al., 2014). Their measurements of seismic velocity from ambient noise covered a much larger period of 1998 to 2013 and observed no marked changes in relation to eruptive activity, including 1998. However, their reference cross-correlation function was stacked from over the whole period. While this step would

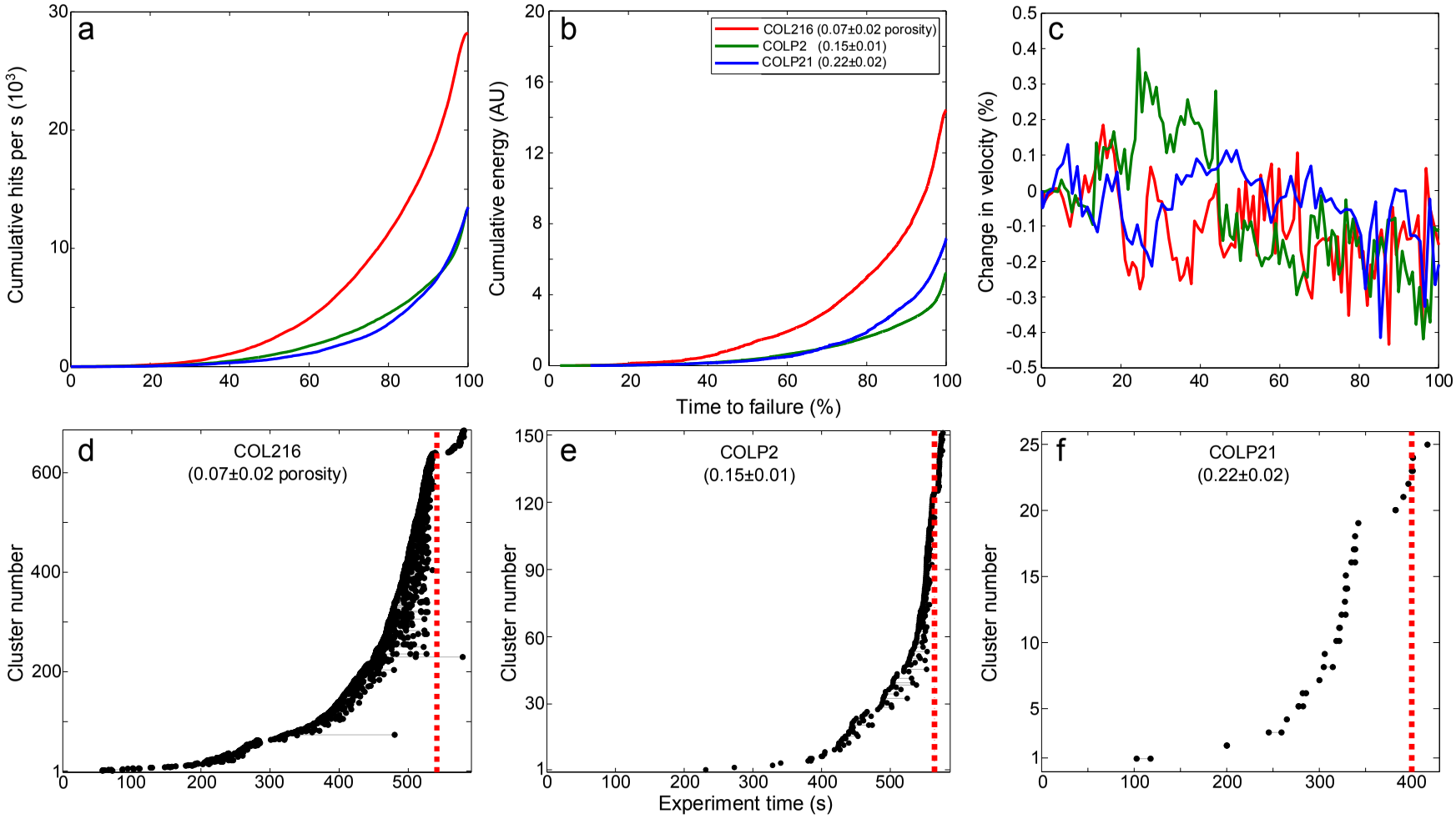


FIGURE 4.3: Example results for a Brazil test on discs from COL216, COLP2 and COLP21 samples. (a) Cumulative number of AEs recorded per second during experiments. (b) Cumulative energy of the recorded AE (c) The change on velocity recorded during the experiment. (Results from all other experiments are plotted in Fig. S4.) Catalogues of repeating AEs in datasets recorded during a Brazil test for (d) COL216 , (e) COLP2 and (f) COLP21 samples. Each black plotted point represents an individual AE, and each grey line joins groups of repeating events (i.e. clusters). The dashed red line marks the time at which the sample failed.

result in a cleaner reference function, it would also dampen the effect of eruptive activity on velocity properties. In addition, Lesage et al. (2014) used a broader frequency range of 0.125-2 Hz as opposed to the 0.5-1.1 Hz used here. Repeating our measurements using a reference waveform stacked from the whole period of study produces dampened velocity change decrease prior to the eruption (Fig. B.1b). Furthermore, using the wider frequency range produces erratic measurements that are consistent with our assertion that the volcanic earthquakes would influence the velocity change calculations (Fig. B.1b-d).

Pre-eruptive velocity changes at other volcanoes have been linked to changes in stress in the volcano edifice. These changes may be induced by the expansion of pore spaces or cavities due to fluid saturation (Grêt et al., 2006; Sens-Schönfelder and Wegler, 2006), stress changes imposed by passing seismic waves (Battaglia et al., 2012; Hotovec-Ellis et al., 2014; Lesage et al., 2014), changes in surface snow load (Hotovec-Ellis et al., 2014), or magma propagating through the host rock (Wegler et al., 2006; Brenguier et al., 2008; Hotovec-Ellis et al., 2015). Since the region had entered the dry season during our period of analysis, and no M5+ earthquakes were recorded within 800 km, we interpret our velocity change as a result of ascending magma. Our observations from Brazil tensile tests on samples from VdC lend support to this interpretation. Here, failure of the sample is analogous to the failure of host rock during magma ascent prior to the eruption at VdC on 20 November (Fig. 4.4). The measured porosities of our samples fall well within previously measured values on samples at VdC (Lavallée et al., 2012a), and are therefore representative of the materials making up the volcanic edifice (Mueller et al., 2011). The AE hit rate (Fig. 4.3a,b, B.5) show similar trends to those seen during the November 1998 swarm (Fig. 4.2a). We observe a drop in the velocity of elastic waves travelling across the sample during the experiment (Fig. 4.3c), replicating the velocity changes seen in ambient seismic noise (Fig. 4.2c). This is indicative of fracture damage accumulation in the samples during loading (e.g. Heap et al., 2010). However, it must be noted that our experiments do not replicate the pressure and temperature conditions found at shallow depths in the volcanic edifice. Thus, the results can only be taken as a first order approximation of velocity changes associated with damage accumulation leading to tensile failure. A recent investigation concluded that higher confining (isostatic) pressures, analogous to greater depths in the crust, would dampen the reduction in elastic velocities due to crack opening (Blake et al., 2013).

Clusters had previously been described prior to eruptions at VdC (Varley et al., 2010) and other active volcanoes (e.g. Hotovec-Ellis et al., 2015). Waveform correlation of all the earthquakes from October to December 1998 identified 504 clusters, with a vast majority occurring during the November swarm (Fig. 4.2c). The number of short-lived clusters indicate that multiple sources were repeatedly triggered during magma ascent (Fig. 4.4b). Several source mechanisms have been inferred for clusters: 'stick-slip' failure on the margins of an ascending plug (e.g. Iverson et al., 2006; Kendrick et al., 2014b; Lamb et al., 2015), brittle failure of silicic magma on the conduit margins (e.g. Neuberg et al., 2006; Varley et al., 2010),

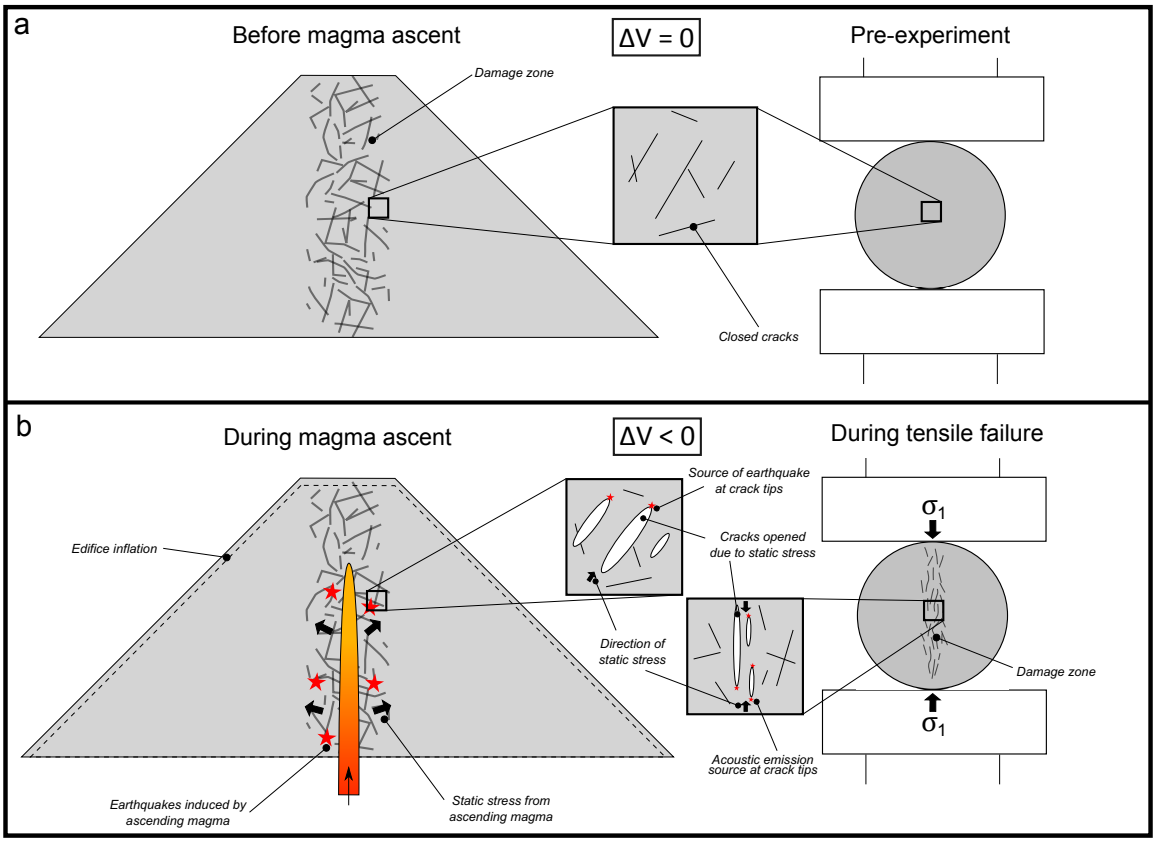


FIGURE 4.4: Two-stage illustration of our seismic and experimental observations for the 1998 eruption of VdC: (a) Before magma ascent or experiment initiation and (b) during magma ascent or sample tensile failure. For further description of the model, please see the text.

and hydrothermal fluid motion (e.g. Waite et al., 2008). No lava plug was observed at the beginning of the eruption (Zobin et al., 2002b), therefore the 'stick-slip' mechanism is unlikely to have occurred. The low percentile of repeating events in the catalogue (7.3%) suggests the occurrence of a relatively low-viscosity magma, no lava plug, and a high extrusion rate (Thelen et al., 2011); this agrees with observations during the eruption (e.g the extrusion rate of 4.4 $m^3s^{-1}$, and new lava flow; Zobin et al., 2002b). We also detected AE clusters during our experiments to indicate repeated micro-cracking occurred prior to sample failure (Fig. 4.3d, e, f). We noticed an inverse correlation between the sample porosity and the number of AE clusters. This conforms with previous observations that increased porosity may act to inhibit dynamic fracture by crack arrest and/or by introducing a more heterogeneous stress field (Kierfeld and Vinokur, 2006; Ramos et al., 2013). We interpret the repeating events as the output of tensile, dynamic opening of new or existing fractures within the sample (Fig. 4.4b). This suggests that tensile opening of cracks in the country rock due to static stress from propagating magma could also produce short-lived clusters. Further work with rigorous testing of how sample heterogeneity may affect repetitive cracking and/or changes in velocity is required.

The velocity changes and the clusters at VdC during November 1998 may have been assisted by the presence of a 'damage zone' surrounding the central volcanic conduit (Fig. 4.4). The edifice at VdC is likely to be highly fractured and heterogeneous owing to the persistence of volcanic activity in recent centuries (Breton Gonzalez et al., 2002). Damage is observed at micro- to macro-scopic scales in the proximal deposits observed at VdC (e.g. Lavallée et al., 2012a). This is supported by modelling at other dome-forming volcanoes, for example the existence of an intensely fractured damage zone surrounding the conduit can explain syn-eruptive strain data recorded at Soufrière Hills volcano (Young and Gottsmann, 2015). As demonstrated by our Brazil test experiments, static stress from the ascending magma can open pre-existing or new fractures which reduces the velocity properties of the host rock (Fig. 4.4b). Inflation and deflation of the volcanic edifice was observed around the 20 November 1998 eruption (Ramírez-Ruiz et al., 2002), illustrating the cycle of static stress caused by the ascent and eruption of magma through the edifice. In some cases, repeated activation can occur at the tips of the fractures as they open (Fig. 4.4b). Tracking AE clusters during experiments on samples of different porosity demonstrates how the heterogeneity may also hinder further reactivation of earthquake sources. The recovery of seismic velocity and cessation of clusters at VdC can be explained by the release of static stress after the beginning of the eruption.

Here, a combined field and laboratory investigation of seismic velocity changes associated with magma ascent has shown that velocity changes calculated via ambient seismic noise can be successfully used to assess eruption onset at Volcán de Colima. Furthermore, we have described evidence for dynamic crack propagation producing repetitive earthquakes that may have implications for future descriptions of pre-eruptive seismic activity. The study highlights the need for multi-disciplinary investigative approaches for interpreting shallow processes associated with volcanic unrest.

## 4.5 Conclusions

A multi-disciplinary approach was employed to investigate the seismic activity prior to the 20 November 1998 effusive eruption at Volcán de Colima, Mexico. Using seismic data recorded by the RESCO network of short-period seismometers, we constructed a database of 17,893 earthquakes during this period. From this database, we identified 504 clusters using waveform correlation. Velocity changes during this period were measured using ambient seismic noise and indicate a $\sim$0.2% decrease prior to the eruption. We analysed natural and artificial acoustic emissions recorded during Brazil tensile tests on andesite from Volcán de Colima. We observed a decrease in elastic wave velocity prior to sample failure, independent of sample porosity, which suggests that static stress due to ascending magma at Volcán de Colima was enough to induce velocity changes in the seismic data. We also observe a similarity in the pattern of clusters in the seismic and acoustic emission data, suggesting

that tensile failure at crack tips is an additional viable source mechanism for clusters. This study highlights how using a multi-disciplinary approach to understanding geophysical signals can help future interpretations of volcanic unrest and constrain eruption onset.

# Chapter 5

# Repetitive fracturing during spine extrusion at Unzen volcano, Japan

This chapter is derived from a paper published in *Solid Earth*, accepted for publication on 20 November 2015 and published on 7 December 2015. Authors of the manuscript are Oliver Lamb (main author), Silvio De Angelis, Kodo Umakoshi, Adrian Hornby, Jackie Kendrick, and Yan Lavallée. The aim of this study was to understand trends in seismic activity during spine extrusion and relate them to experimental observations such as those by Hornby et al. (2015). Silvio De Angelis participated in the analysis, and helped draft the manuscript. Kodo Umakoshi provided the seismic data analysed in this study. Jackie Kendrick, Adrian Hornby, and Yan Lavallée participated in the design of the study and helped draft the manuscript. All authors read and approved the final manuscript. The appendices of the paper have been incorporated into the main body of this chapter, and the supplementary figures can be found in Appendix C on page 123.

## Paper abstract

Rhythmic seismicity associated with spine extrusion is a well-documented phenomenon at a number of dome-forming volcanic systems. At Unzen volcano, Japan, a four year dome-forming eruption concluded with the emplacement of a spine from October 1994 to February 1995, offering a valuable opportunity to further investigate seismogenic processes at dome-forming volcanoes. Using continuous data recorded at a seismic station located close to the dome, this study explores trends in the seismic activity during the extrusion of the spine. We identify a total of 12,208 volcano-seismic events in the period between October 1994 and February 1995. Hourly event counts indicate cyclic activity with periods of ∼40- to ∼100-hours, attributed to pulsatory ascent defined by strain localisation and faulting at the conduit margins. Waveform correlation revealed two strong clusters (a.k.a. multiplets, families) which are attributed to fracturing along the margins of the shallow, ascending spine. Further analysis indicates variable seismic velocities during the spine extrusion, as well as migration of the cluster sources along the spine margins. Our interpretation of the results

from seismic data analyses is supported by previously published field and experimental observations, suggesting that the spine was extruded along an inclined conduit with brittle and ductile deformation occurring along the margins. We infer that changes in stress conditions acting on the upper and lower spine margins led to deepening and shallowing of the faulting sources, respectively. We demonstrate that the combination of geophysical, field and experimental evidence can help improve physical models of shallow conduit processes.

## 5.1 Introduction

Lava dome growth and collapse represent a major volcanic hazard globally (Sparks, 1997). The transition from effusive to explosive activity of a dome may be rapid and can generate destructive pyroclastic flows (Calder et al., 2002). This range of behaviour presents a significant challenge for forecasting and hazard mitigation; for example, the 1991-1995 eruption at Unzen, Japan (see Sect. 5.1.1). Continuous monitoring of growing and unstable lava domes is thus central to risk mitigation. The movement of magma during dome-building eruptions is a rich source of geophysical signals, particularly earthquakes. Analysis of shallow (<3 km) volcanic-earthquakes has highlighted the importance of discerning their characteristics for the purpose of hazard assessment (Neuberg, 2000; Chouet and Matoza, 2013).

Volcanic earthquakes are conventionally classified as either high-frequency or low-frequency. High-frequency signals, or Volcano-Tectonic events, are typical earthquakes within a volcanic edifice or in the crust beneath it (Chouet et al., 1994; Lahr et al., 1994; Chouet and Matoza, 2013). Their occurrence may be related to the movement of magma (e.g. Wright et al., 2006) or gas (e.g. Hill, 1996), or can be the result of local-regional stress interactions (e.g. Roman et al., 2008). Despite extensive research into low-frequency volcanic seismicity, the interpretation of its source mechanisms and propagation effects is still controversial. Typical low-frequency events (1-4 Hz) are ascribed to volumetric sources involving motion of fluids within resonating volcanic conduits and dykes (Chouet, 1996). Earthquakes characterised by high-frequency and impulsive onsets with a low-frequency coda, known as hybrids, are often considered part of the low-frequency family of events (Green and Neuberg, 2006). Neuberg et al. (2006) suggested that the long ringing coda of these signals are generated by conduit resonance triggered by brittle fracturing of magma, a process that can be preserved in a conduit margin (Tuffen and Dingwell, 2005; Kennedy et al., 2009; Kendrick et al., 2012, 2014a). Repeating low-frequency events have been interpreted as the result of stick-slip motion along the margins of a viscous magma plug forced upwards by ascending magma (Iverson et al., 2006; Lensky et al., 2008; Iverson, 2008; De Angelis, 2009; Power and Lalla, 2010; Varley et al., 2010; De Angelis and Henton, 2011), and possibly regulated by frictional melting (Kendrick et al., 2014b). Harrington and Brodsky (2007) noted that Hybrid events recorded at different volcanic systems all exhibit corner frequencies and magnitudes consistent with brittle-failure sources. A recent study by Bean et al. (2013), employing a more

proximal instrument network (<500 m from volcanic vent), proposed that slow-rupture failure of weak volcanic materials can produce low-frequency events.

Cyclic behaviour has been commonly observed in volcano-seismicity during dome-forming eruptions (e.g. Voight et al., 1999; Lachowycz et al., 2013; Lamb et al., 2014). Various physical parameters may contribute to short-term cyclicity, including: wall-rock elasticity (Maeda, 2000; Costa et al., 2007b, 2012), outgassing pulses (Voight et al., 1999; Waite et al., 2008; Massol and Jaupart, 2009; Collinson and Neuberg, 2012; Michaut et al., 2013), and magma failure and frictional slip (Lavallée et al., 2008; De Angelis and Henton, 2011; Lavallée et al., 2012b; Thomas and Neuberg, 2012; Chouet and Matoza, 2013; Kendrick et al., 2014a,b; Okumura et al., 2015). Indeed, it is believed that it is frictional properties that control the final part of magma ascent (Kendrick et al., 2014b; Hornby et al., 2015; Lavallée et al., 2015a), which is driven by buoyancy. In tectonic settings, variations in fault-normal stresses can produce wide-ranging fault products, such as gouge, cataclasite, pseudotachylyte, and mylonite (Ben-Zion and Sammis, 2003). In volcanic settings, it is challenging to understand the conditions which result in failure and particularly the influence of faulted rocks on slip behaviour (Kendrick et al., 2014b). Frictional sliding is velocity dependent and may be velocity strengthening, which promotes stable aseismic slip, or velocity weakening (i.e. likely to produce earthquake instabilities; Dieterich, 1979). Comminution during slip produces fault gouge, which results in a reduction in friction with increasing slip velocity, as determined experimentally for ash gouge by Lavallée et al. (2014). Gouge may be fluidised by dilation during rupture and form cataclasites, which have been observed in volcanic settings (Tuffen and Dingwell, 2005; Cashman et al., 2008; Kennedy et al., 2009; Kendrick et al., 2012, 2014a; Gaunt et al., 2014; Plail et al., 2014).

In this study, we present a detailed characterisation of the seismicity associated with the extrusion of a spine during the late stage of the 1991-95 dome-building eruption at Unzen volcano, Japan. We use the results from our methods, together with previously published field and experimental constraints, to develop a conceptual model of the processes occurring during the magma ascent and spine extrusion.

### 5.1.1 Unzen eruption and spine extrusion

Following almost 200 years of dormancy at Unzen volcano, Japan, a new period of activity began with a swarm of Volcano-Tectonic earthquakes to the west of the volcano in November 1989 (Nakada et al., 1999; Umakoshi et al., 2001). The hypocentral distribution of Volcano-Tectonic events subsequently progressively evolved eastwards, towards the volcano at the surface (Umakoshi et al., 2001). Eventually, eruptive activity at the surface began in November 1990, with the first months dominated by phreatic and phreatomagmatic activity as magma approached the surface (Nakada et al., 1999). In May 1991 exogenic dome growth began, with a brief phase of spine extrusion, followed by a series of 13 viscous,

dacitic lava lobes (Nakada et al., 1999). Vulcanian explosions occurred during the initial dome eruption stages in June and August 1991, when the effusion rate was at its highest (Nakada et al., 1999). The growing lava dome was structurally unstable and experienced repeated partial collapses that generated pyroclastic density currents, forcing the evacuation of over 10,000 local residents. This activity continued until February 1995, by which point effusion had ceased and seismicity returned to background levels (Nakada et al., 1999; Umakoshi et al., 2008).

Protracted spine growth defined the last five months of the eruption, beginning in mid-October 1994 and growing at an average rate of 0.8 m per day in November (Nakada et al., 1999; Yamashina et al., 1999; Hornby et al., 2015). Extrusion proceeded obliquely, with the spine inclined at an angle of 45° towards the east-south-east (Kohno et al., 2008). The final dimensions of the spine were 150 m long, 30 m wide, and 60 m high (Nakada et al., 1999), with a record of ductile and brittle deformation preserved along the spine margins (Smith et al., 2001). The exposed shear zone bounding the upper margins of the inclined spine was up to 10 metres thick and comprised of sheared dacite, cataclasite and breccias (Hornby et al., 2015), whereas the underside has less pervasive damage and shows slickensides on the surface (Calder et al., 2015). Seismic activity during the spine extrusion was relatively low and shallow (<0.5 km; Umakoshi et al., 2008) but periodic increases in event output were observed synchronous with tilt oscillation on the volcanic edifice (Yamashina et al., 1999), constrained to originate from a fluctuating pressure source at 0.7-1.3 km depth (Kohno et al., 2008).

## 5.2 Data and methodology

### 5.2.1 Data source

The seismic data used for this investigation was collected by the Shimabara Earthquake and Volcano Observatory (SEVO[1]; Shimizu et al., 1992). Three stations were installed <1 km from where the dome would eventually emerge and all were equipped with a 1 Hz vertical component seismometer (see Figure 3 in Umakoshi et al., 2008). Signals were telemetered to SEVO and recorded continuously with a sampling rate of 100 Hz. For the last five months of the eruption, the most complete dataset was recorded by station FG1. The station also lies close to the spine (∼600 m) and was positioned in line with the direction of spine inclination. Here we analysed the complete high-resolution dataset from station FG1 for our investigation.

[1]Now known as the Institute of Seismology and Volcanology, Faculty of Sciences, Kyushu University.

### 5.2.2 Automatic Event Detection

Single station detection was performed from October 1st 1994 to February 28th 1995 to extract all types of seismic events from continuous vertical channel data using a conventional short-term average, long-term average (STA/LTA) algorithm (Allen, 1978). Using a single station improves the chronology of the progression of seismic events as it includes those not large enough to be detected at multiple stations. However, it is well known that the STA/LTA technique is prone to false alarms or missed events, depending on the choice of parameters. To help alleviate this issue, we tested different STA/LTA parameters on a 24 hour period of the seismic record. Once triggers were identified, we used a multi-parametric filter to remove false triggers from the record. A complete list of the parameters used for the Short-term Average, Long-term Average (STA/LTA) algorithm used in single-station detection is provided in Table 5.1. Events associated with noise and low signal-to-noise ratio were stripped from the overall event set; Table 5.2 lists the metric threshold values used. The metric values were chosen after characterisation of noise manually picked from the data. Of the 18,292 events originally detected, 6084 of these were removed by filtering.The STA/LTA calculation and waveform correlation below were implemented within the framework of a Matlab toolbox tailored for large datasets (GISMO; Reyes and West, 2011). The STA/LTA algorithm is widely used for automatic detection of volcanic earthquakes from a large dataset (e.g. Matoza et al., 2009b; Thelen et al., 2010; De Angelis and Henton, 2011; Ketner and Power, 2013). Amongst others, the single-station detection approach was successfully employed for the analysis of continuous seismic data recorded during the 2009 eruption of Mt. Redoubt volcano, USA, where it allowed a fine-scale view of variations in seismic behaviour as potential indicators of impending explosions (Ketner and Power, 2013).

TABLE 5.1: STA/LTA parameters used in single-station event detection

| Variable | Value | Description |
|---|---|---|
| $L_{STA}$ | 0.8 s | Length of short-term window |
| $L_{LTA}$ | 7 s | Length of long-term window |
| $t_{on}$ | 1.5 | Trigger-on threshold |
| $t_{off}$ | 1 | Trigger-off threshold |

TABLE 5.2: Extreme metric values used for single-station detection noise removal. P2P refers to peak-to-peak amplitude.

| Metric | Limits |
|---|---|
| Frequency Index | $> 0.5$ |
| Root-mean square amplitude (RMSA) | $< 50$ counts |
| P2P/RMSA | $> 20$ |
| Duration | $< 2$ s |
| Centre Frequency | $< 1$ Hz, $> 50$ Hz |

### 5.2.3 Statistical Analysis

Volcanic time-series are inherently non-linear and can show cyclicity over a range of timescales (e.g. Odbert et al., 2014). Superposition of multiple cycles within a dataset can make it difficult to observe and interpret individual signals. The Fast-Fourier Transform (FFT) offers an efficient means of examining the characteristics of a time-series (Danielson and Lanczos, 1942) via the Power Spectral Density estimate, which highlights the strength of periodic components in the signal (Percival and Walden, 1993). Here the Power Spectral Density is estimated using the Multitaper Method (MTM), demonstrated to be the most robust method when there is no prior knowledge of the signal-generating source (Thomson, 1982). The SSA-MTM Toolkit presented by Ghil et al. (2002) was used to perform the spectral analyses. A detrending correction was used to prepare the data by rendering the time-series approximately stationary, then either padded with zeroes at either end or truncated to a length of $n^2$, for integer $n$, as required for FFT. The significance of spectral peaks were assessed against a statistical Red Noise Model (Mann and Lees, 1996), considered appropriate for systems with background noise heavily influenced by long-term processes. It is impossible to completely characterise the nature of the noise without prior knowledge of the source, therefore the red noise model acts only as a guide to interpretation. Here only peaks above the 99% confidence threshold are considered significant for discussion.

MTM analysis requires statistical stationarity over the whole data window, which is not a common feature of many geophysical systems and can result in spectra which are difficult to interpret. Short-term Fourier Transform (STFT) analysis calculates a series of Power Spectral Density estimates using a moving window of specified length with results illustrated using spectrograms. An assumption of stationarity is only required within an individual sample window, therefore spectrograms are useful for tracking changes in the spectral content of a time-series (Odbert and Wadge, 2009). In other words, the STFT spectrogram is a series of PSD estimates overlapping each other, instead of a single PSD estimate as produced by MTM analysis. The choice of parameters (window length and overlap) is critical and has been optimised for our analysis. A window length of 336 hours (14 days) with 99% overlap provided the best compromise between achieving sufficient temporal resolution and maintaining a long-enough window for robust analysis. The frequency distribution of each window was normalised to unity in order to remove the influence of changes to absolute spectral power, thereby allowing direct comparison of the relative frequency distributions between contiguous windows. For the analysis, a high-pass Butterworth filter with a cut-off of 672 hours was applied to the time-series to enhance the clarity of shorter period cycles of interest in the final spectrogram. Comparison between spectrograms generated from both non-filtered (Fig. C.1) and filtered data indicated that the use of the filter did not affect either the timing or the frequency of spectral peaks. This combination of methods has not been previously used at Unzen volcano but has been successfully applied to geophysical datasets from other volcanic systems (Odbert and Wadge, 2009; Nicholson et al., 2013; Lamb et al., 2014). At

Soufrière Hills volcano (Montserrat), this combination of methods identified cyclic patterns in tiltmeter displacement (Odbert and Wadge, 2009), $SO_2$ flux (Nicholson et al., 2013) and seismic event rates (Lamb et al., 2014). Lamb et al. (2014) also described similar sub-annual cyclic patterns in a dataset from Volcán de Colima (Mexico), attributed to cyclic motion of magma within the system and expansion and contraction of a feeder dyke.

### 5.2.4 Waveform Correlation

Assessment of waveform similarity is useful for investigating trends in earthquake activity within large datasets. Repeating waveforms are significant because they represent the product of earthquakes generated by the same source in the same location. Small, impulsive earthquakes that accompanied spine extrusion at Mount St Helens from 2004 to 2008 were dubbed 'drumbeats' due to their rhythmic occurrence (Iverson et al., 2006; Iverson, 2008). These waveforms were hypothesised to derive from 'stick-slip' motion of the magma plug as it was forced upwards (Iverson et al., 2006; Iverson, 2008). The margins of this magma plug experienced strain localisation, and the surface textures (deformation features) of the extruded spine can provide the key to sub-surface deformation that may help regulate magma ascent (Kennedy et al., 2009; Kendrick et al., 2012). Here we explore the role of repeating earthquakes as an indicator of the conditions along the margins of the spine at Unzen.

We use cross-correlation to measure the similarity of waveforms in the event catalogue constructed using the single-station detection method (Sect. 5.2.2). To calculate waveform cross-correlation, we extract a 5-second window of data beginning at the picked arrival time. All waveforms are filtered with a 0.5 to 20 Hz passband Butterworth filter to minimise background noise and increase the signal-to-noise ratio. Five seconds of data following the arrival is sufficient to include the largest amplitude section of most waveforms while minimizing the effect of background noise. Changes in window length of a few seconds has a minor influence on the calculated correlation coefficient (not shown here). In the chosen period of analysis, each waveform is compared to every other waveform and the pair is designated a correlation value between 0 and 1; *i.e.* a value of similarity where 0 is completely different and 1 is identical. We identify clusters (repeating earthquakes, a.k.a. families, multiplets) using a hierarchial clustering method similar to that used by Buurman and West (2010). Based on visual inspection of the cluster tree, we choose a correlation threshold of 0.8 and a minimum number of five events to define clusters. The value is equal to or higher than in comparable studies (e.g. Green and Neuberg, 2006; Buurman and West, 2010; Rodgers et al., 2013). The choice of parameters for waveform correlation can affect the resulting clusters and their characteristics. Table 5.3 lists the different output results for various parameters that could be used for waveform correlation. Figures C.4 - C.10 contain the cluster lifespan plots for the parameters not used. From 1st October to 15th November, our chosen

values assign 16% of all events to a cluster (Table 5.3). This lies inside the range of values reported in previous publications (10% to 25%; Thelen et al., 2011; Rodgers et al., 2013, 2015a). Therefore our parameters, while strict, do not exclude an unusual amount of events from clusters. One exception is Green and Neuberg (2006) who assigned 50% of a particular type of low-frequency seismic events at Soufrière Hills volcano during a specific period of time. As this is an analysis of a particular type of event, therefore it cannot be directly compared to our values. Previously, waveform correlation has detected low-frequency clusters during swarms at Soufrière Hills volcano which were linked to a fixed shallow conduit source in the volcanic system (Green and Neuberg, 2006). Buurman and West (2010) found clusters of waveforms closely tied to explosions at Augustine volcano (USA) and proposed that the method has considerable potential as an automated real-time volcanic explosion monitoring tool.

TABLE 5.3: Parameters used for waveform correlation and their output values using the 5,738 events detected from 1st October to 15th November 1994. CC stands for correlation coefficient.

| Parameters | | Outputs | | |
|---|---|---|---|---|
| No. of events limit | CC threshold | Number of clusters | Size of largest cluster | % of all events in clusters |
| $\geq 2$ | 0.6 | 762 | 514 | 69 |
| | 0.7 | 579 | 505 | 46 |
| | 0.8 | 275 | 487 | 26 |
| | 0.9 | 90 | 372 | 14 |
| $\geq 5$ | 0.6 | 144 | 514 | 43 |
| | 0.7 | 85 | 505 | 26 |
| | 0.8 | 29 | 487 | 16 |
| | 0.9 | 18 | 372 | 11 |

### 5.2.5 Singular Value Decomposition

Since the original dataset is derived from only three seismic stations, it is not possible to accurately calculate locations, and thus, absolute magnitudes and earthquake energies. However, we can assess the relative magnitudes between events of a cluster because the entire cluster must derive from the same source (e.g. Green and Neuberg, 2006). To determine the relative earthquake amplitudes and relative time lags within the two largest clusters we apply a method based on standard matrix factorization; the singular value decomposition (SVD). The method was proposed by Rubinstein and Ellsworth (2010) and used on clusters located around Parkfield, Northern California. SVD estimates relative earthquake size for repeating earthquakes by taking advantage of the waveform similarity of all the events within the sequence. The method uses the entire waveform, which reduces the uncertainty in earthquake size and produces a measurement which is consistent from event to event within a cluster. The technique robustly computes earthquake size while exploiting

the information from the whole waveform, unlike the parametric information used in most standard magnitude estimation methods. The SVD can be used to describe a matrix $M$ (i.e. a group of horizontal vectors) in terms of two sets of basic vectors (input $U$ and output $V$) and set of nonnegative singular values $\sum$ ascribed to the weight of the output-basis vector, as in the following relationship:

$$M = U \sum V' \tag{5.1}$$

$U$ is a matrix that maps the weight applied to each output-basis vector for each data vector. Each column $\overrightarrow{U}_{\mathrm{i}}$ of $U$ gives the relative amplitude of the associated output-basis vector ($\overrightarrow{V}_{\mathrm{i}}$) for each data vector. When the input data consists of repeating events, the similarity of their waveforms means that most of the data's power is explained by the first output basis vector (a.k.a. the first principal component). If we assume that all variables except size and arrival times are exactly the same, the other output-basis vectors will only be describing background noise. This means that the relative amplitude, and therefore moment, of the seismograms is described by the first input-basis vector. However, this can only be true when the SVD is applied to seismograms filtered such that the frequency content is below the corner frequency of the event that is being examined. Rubinstein and Ellsworth (2010) demonstrate that estimating the moment using SVD has much less uncertainty than the whole-network estimates of moment based on coda duration. A more detailed methodology, and a discussion of the associated errors and pitfalls of the method is presented in Rubinstein and Ellsworth (2010).

To find the relative time lags of the earthquakes in each cluster, we employed a cross-correlation method using the first output-basis vector calculated by SVD as a reference. That is, all waveforms in each cluster are cross-correlated with the first-output basis vector, under the assumption that the first output-basis vector is effectively the mean waveform and representative of an unperturbed background state. The results of this method should reflect temporal variations in velocity relative to such unperturbed background levels.

### 5.2.6 Coda Wave Interferometry

While it is not possible to calculate source locations, coda wave interferometry (CWI) has the advantage in using repeating waveforms from a single station to provide an estimate of source separation. By exploiting the cross-correlation properties of the repeating waveforms with the use of CWI, it is possible to separate temporal changes of the material and source properties from the spatial variation of the earthquake source. The migration of a seismic source results in a change in distance to scatterers in the surrounding medium, affecting the arrival times of the waves that interfere to produce the seismic coda. De Angelis (2009) used this method to infer a source migration of 235 m over 24 hours for repetitive low-frequency earthquakes at Soufrière Hills volcano. The correlation coefficient, $R$, is related to the variance of the travel-time pertubation, $\sigma_\tau$, and to the frequency, $\overline{\omega}^2$, according to the

following relationship (Snieder, 2003):

$$R = 1 - \frac{1}{2}\overline{\omega}^2\sigma_\tau^2 \tag{5.2}$$

The frequency can be calculated from the seismogram data, *u(t)*:

$$\overline{\omega}^2 = \frac{\int_{t-T}^{t+T} \dot{u}^2(t')dt'}{\int_{t-T}^{t+T} u^2(t')dt'} \tag{5.3}$$

where the integral is performed over a window of length $2T$ centred at time $t$. The relationship between the variance of the travel time-pertubation and inferred source migration depends on the source mechanism. Snieder and Vrijlandt (2005) have demonstrated this relationship for different types of source such as a explosive, point or fault plane. If displacement occurs, for instance, along the fault plane, the source dislocation, $\delta$ is given by:

$$\delta = \left[7\left(\frac{2}{v_p^6} + \frac{3}{v_s^6}\right) / \left(\frac{6}{v_p^8} + \frac{7}{v_s^8}\right)\right]^{\frac{1}{2}} \sigma_\tau \tag{5.4}$$

where $v_p$ and $v_s$ are *P*- and *S*-wave velocities in the medium.

We applied equation (5.4) to 36-hour waveform stacks from clusters identified by waveform correlation (Sect. 5.2.4), to maximise temporal resolution and reduce the computing power required. Waveform stacking also improves the signal-to-noise ratio and improves correlation. The correlation coefficient was calculated for different frequency bands (1-5 Hz, 1-10 Hz) and time windows (1-5 s, 7-11 s) between each waveform stack and the first stack, and converted to source displacement. The calculations were based on a *P*-wave velocity of 4.5 km $s^{-1}$ and *S*-wave velocity of 2.6 km $s^{-1}$, consistent with measured velocities during the Unzen Scientific Drilling Project (Ikeda et al., 2008). These velocities are smaller than these measured in laboratory samples from Unzen (Scheu et al., 2006) and passive seismic source experiments at Unzen (Ohmi and Lees, 1995). They are also higher than those inferred during an active seismic source experiment deployed a few kilometres to the west of Unzen (Matsumoto et al., 2012); our chosen values represent a compromise between these measurements. However, it must be noted that these velocities do not account for macroscale fractures and fracture density along the seismicity pathways. Therefore our velocity values represent the upper limit of the range of actual velocities. To test the sensitivity of the equations, we used the higher velocities of Ohmi and Lees (1995) and find they do not change the results significantly (Figure C.2). Therefore equation (4) is sensitive to the seismic velocities employed but uncertainties do not appear to affect the results dramatically. The velocities represent a second-order effect in comparison to the scarce knowledge of the source dynamics. The CWI method relies on a series of simplifying assumptions: the velocity field is considered isotropic and the medium locally homogenous, mode conversion at the surface

is ignored and the source separation must be less than a wavelength; a full discussion of the limitations of the method is presented by Snieder and Vrijlandt (2005). However, results from its application have been validated by comparison with other techniques such as the double-difference relocation method (Snieder and Vrijlandt, 2005).

## 5.3 Results

### 5.3.1 Single-station Detection

After filtering out false triggers, a total of 12,208 seismic events were detected; hourly event counts are plotted in Fig. 5.1. Two key observations of the dataset are:

1. The event rate for all types of events begins with peaks of 10-20 events per hour in October 1994, and decreases to less than 5 events per hour by the end of the eruption in February 1995.
2. Peaks at regular time intervals in October and November 1994 indicate cyclic activity during this period. This type of activity is the focus of the analysis using FFT techniques (Sect. 5.2.3, 5.3.2).

### 5.3.2 Fast-Fourier Transform

MTM analysis was carried out on the complete record of hourly event counts from single-station detection analysis to provide a first-pass assessment of the cyclic character of the dataset (Fig. 5.2A). The Power Spectral Density estimate reveals two peaks that appear significant above the 99% noise confidence threshold: 40- and 24-hours. However, analysis of the first and last four weeks of the dataset (Fig. 5.2B, C) reveals the cyclic components are not wholly persistent throughout the dataset. The 40-hour cyclic component does not appear in the Power Spectral Density estimate for the last four weeks of the dataset (Fig. 5.2C). Although this cyclic instability brings into question the assumption of statistical stationarity (required by definition of MTM spectral analysis), STFT analysis only requires the time-series to remain stationary within each window (described in Sect. 5.2.3). We therefore used the STFT method to explore the temporal variability of the hourly event count in more detail.

Inspection of the spectrogram from the hourly event count (Fig. 5.1B) highlights the following key observations:

1. Mid-October to mid-November 1994 is dominated by a strong $\sim$40-hour cyclicity. This behaviour does not appear again in any other part of the time-series.
2. From December to the end of January the cycle period 'glides' from $\sim$50-hours to $\sim$100-hours.

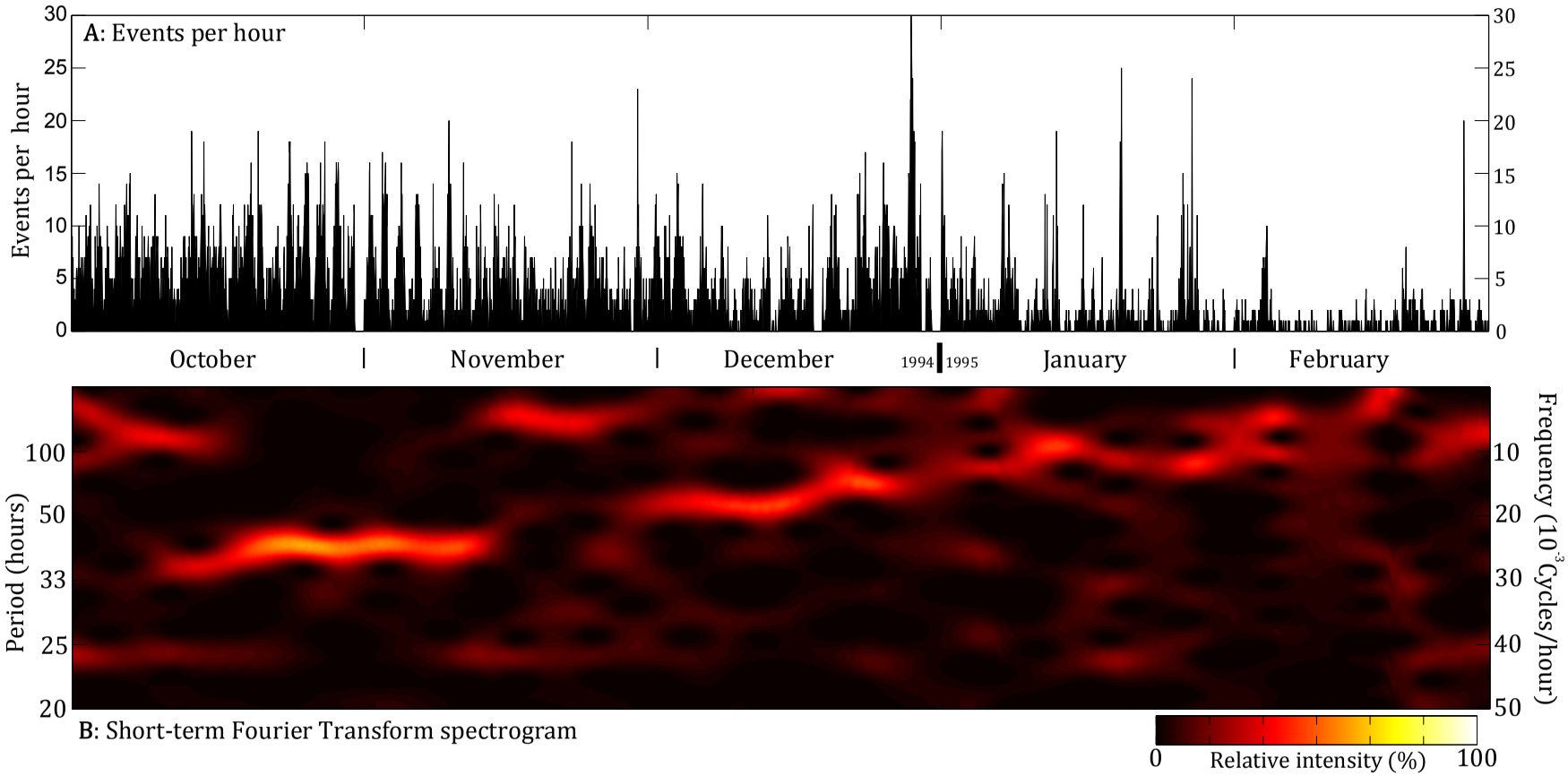


FIGURE 5.1: (A) The hourly event record of events detected from continuous data recorded at station FG1 at Unzen from 1st October 1994 to 28th February 1995. (B) The STFT spectrogram for the hourly event count time-series plotted in (A). Spectrograms are plotted from 20- to 672-hour (4 weeks) cycle periods; the maximum defined by the high-pass Butterworth filter. The Power Spectral Density of each window has been normalised to unity. The last two weeks of November 1994 is dominated by a peak cyclicity whose period (>100 hours) lies close to the size of the moving window (336 hours); it is therefore considered a methodological artefact.

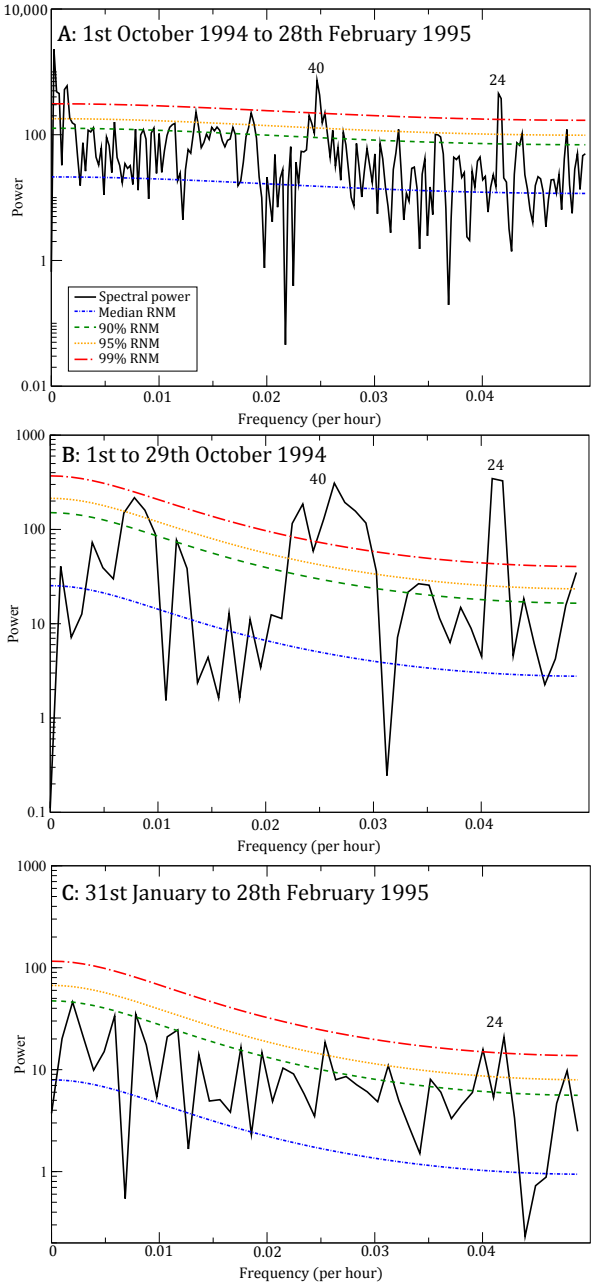


FIGURE 5.2: MTM spectra showing time-series Power Spectral Density of the daily event counts of (A) the whole hourly event count time-series (01/10/94 - 28/02/95), (B) the first four weeks (01/10/94 - 29/10/94), and (C) the last four weeks of the time-series (31/01/95 - 28/02/95). The Power Spectral Density is plotted against various confidence levels of the Red Noise Model. Peaks exceeding at least the 99% confidence level are annotated with corresponding cycle period in hours.

3. The 24-hour periodicity noted in the MTM analysis (Fig. 5.2) is present in the spectrogram, but is not clear against the background noise.

### 5.3.3 Waveform Correlation

For waveform correlation, we focused on 5,738 events detected during the period of 1$^{st}$ October to 15$^{th}$ November 1994 to explore the emergence of the spine and its strong 40-hour pulsatory extrusion (Fig. 5.3A). The key observations are:

1. Two large clusters dominate the results of the waveform correlation. The clusters, henceforth known as cluster 1 and 2, are highlighted and their waveforms contain a strong low-frequency component (Fig. 5.3A, B and C).
2. Waveform stacks for clusters 1 and 2 show opposite arrival polarities (Fig. 5.3B, C).
3. Cluster 1 (487 events) and 2 (181 events) are significantly larger than the other 27 clusters detected during this period; by comparison the third largest cluster has 32 events.
4. The occurrence of both clusters also shows strong cyclicity, corresponding to the approximately 40-hour cycles identified in the STFT analysis of the hourly event counts (Sect. 5.3.2).
5. 84% of events in this period (01/10/94 - 15/11/94) did not fall under our criteria of being part of a cluster, thus the clusters represent a fraction of the seismic record (Fig. 5.3D).

### 5.3.4 Cluster characteristics

For each cluster, the frequency index for each waveform (calculated for single-station detection filtering; Sect. 5.2.2) is plotted over time (Fig. 5.4A). There is a clear division in the frequency component of clusters 1 and 2, with the latter containing waveforms with more low-frequency components. SVD of the waveforms in cluster 1 and 2 show that during their lifetimes, the relative amplitudes (and by extension, relative moment) remain substantially unchanged (Fig. 5.4B). In contrast, relative time differences for each cluster show opposite trends (Fig. 5.4C). Cluster 1 has a positive trend, indicating that the events are arriving sooner relative to the mean cluster waveform; whereas for cluster 2, a negative trend indicates that the events are arriving later relative to the mean waveform (Fig. 5.4C).

CWI was applied to the bandpass-filtered stacked waveforms from each cluster. Displacements calculated in the 1-5 s window of the waveforms, filtered at 1-5 Hz, are relatively stable during the early stages of both clusters (Fig. 5.5B, E). However, the last week of each cluster is defined by displacements of over 100 m. The displacements calculated after the 5-10 Hz filter show greater scattering but smaller displacements (Fig. 5.5C, F). The codas

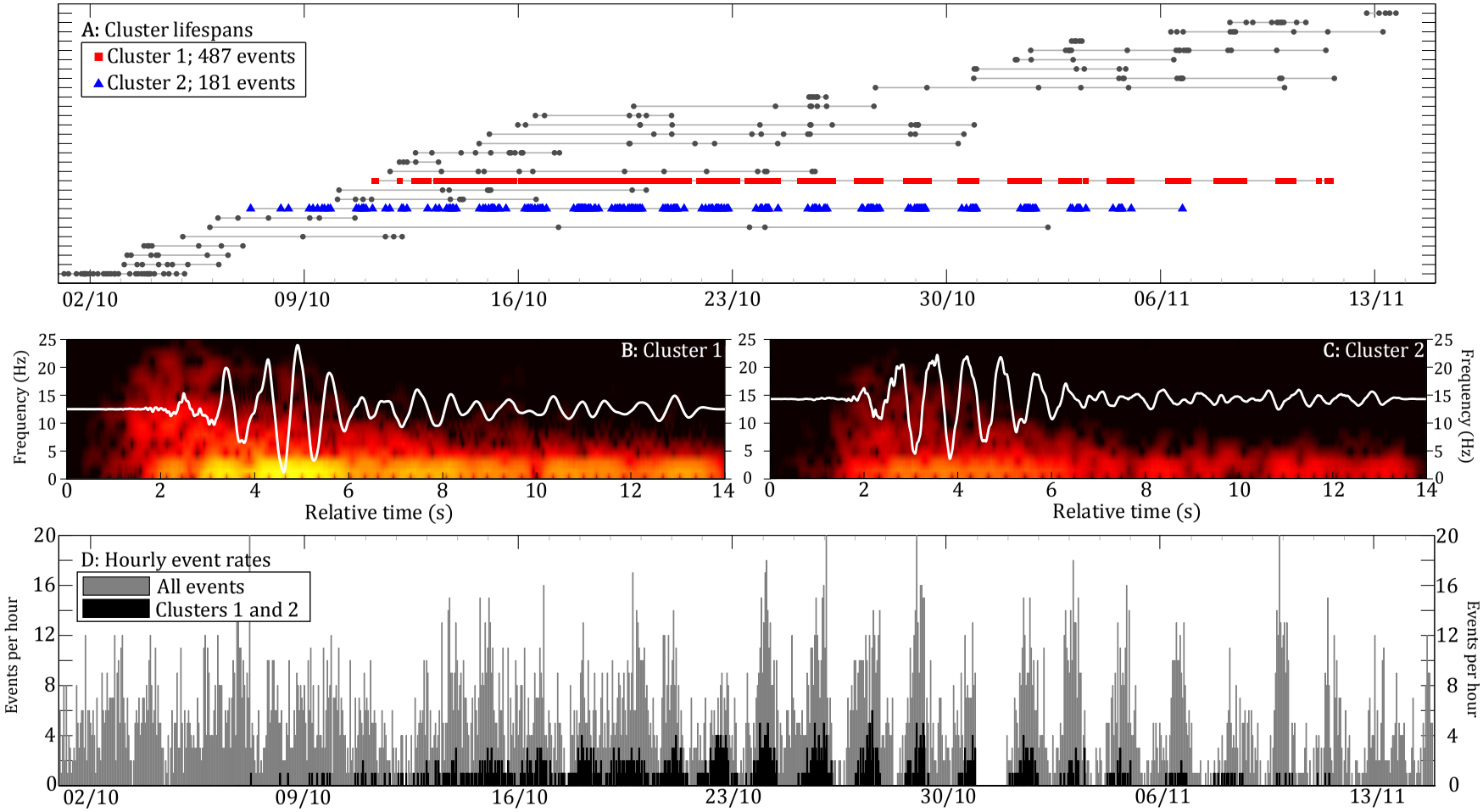


FIGURE 5.3: (A) Catalogue of cluster occurrence in our dataset from 1st October to 15th November 1994. Each plotted point represents an earthquake, and earthquakes on the same line are part of the same cluster. Only clusters with 5 or more events are shown. The two largest clusters, clusters 1 and 2, are plotted with red squares and blue triangles respectively. (B) The waveform stack of all events in cluster 1, overlain on a frequency spectrogram of the stack. (C) The waveform stack of all events in cluster 2, overlain on a frequency spectrogram of the stack.(D) Hourly event rates for all events (grey) and events in clusters 1 and 2 (black) during the period of 1st October to 15th November 1994.

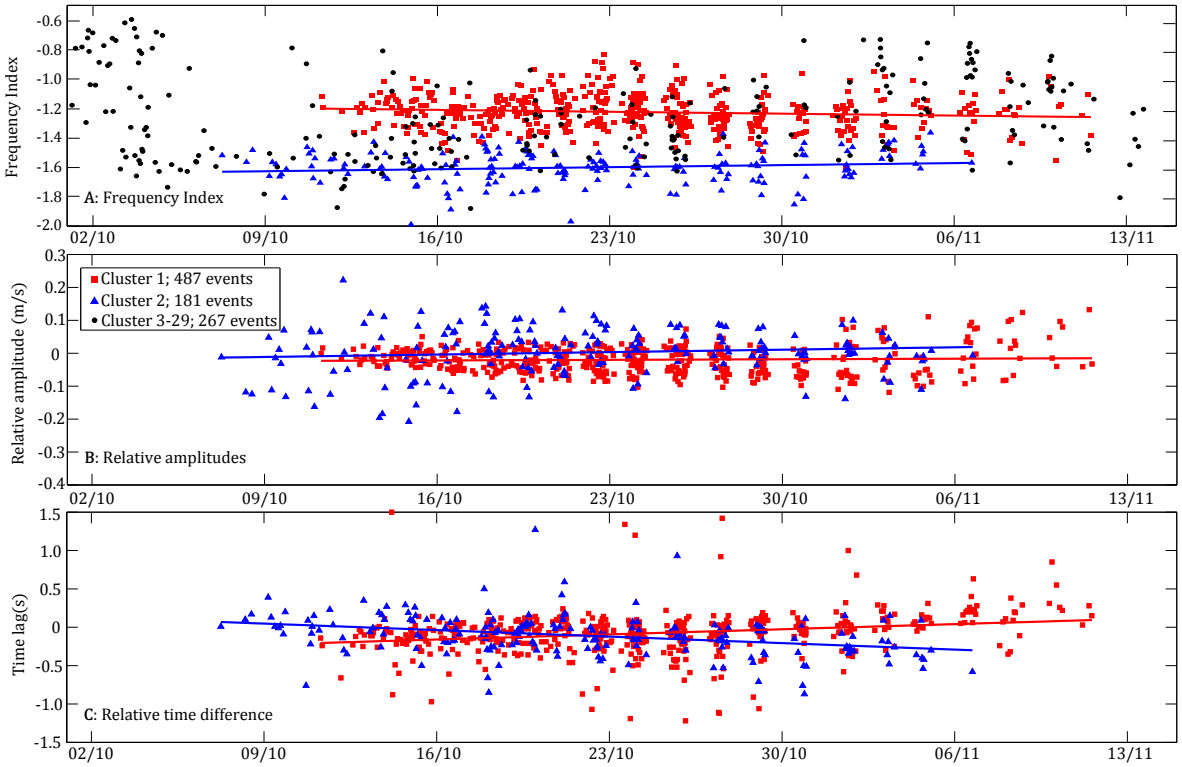


FIGURE 5.4: (A) The frequency index of earthquakes in clusters 1, 2, and 3-29. (B) Relative amplitudes of earthquakes in clusters 1 and 2, as measured using singular value decomposition. (C) The relative time difference (i.e. time lag) of each earthquake in clusters 1 and 2, as measured using cross-correlation against the first principal component. In each panel the linear best fit for each cluster are plotted. Relative amplitudes and time differences were not calculated for clusters 3-29.

(5-9 s) in both bandpass filters do not reflect these changes, with relatively stable movement throughout each cluster's lifetime (Fig 5.5B, C, E, and F). This indicates little or no motion of the scatterers in the source-receiver path.

## 5.4 Discussion

### 5.4.1 Cyclic variations in seismicity

Single-station detection with a STA/LTA algorithm detected a total of 12,208 volcano-seismic events between 1$^{st}$ October 1994 and 28$^{th}$ February 1995 at Unzen volcano (Fig. 5.1A). Our count is in good agreement with previous results published by Nakada et al. (1999) and Umakoshi et al. (2008). Furthermore, good visual correlation between the temporal pattern of earthquake rates and real-time seismic amplitude measurements reinforces our confidence in the results of the detection algorithm (Figure C.3). However, our rates are much higher than those of Yamashina et al. (1999), who used data recorded 5 km south-west of the vent and which likely did not detect many smaller events during the activity. A combination of MTM and STFT analysis on hourly event counts revealed a strong ∼40-hour cyclicity during the extrusion of a spine (Fig. 5.1B). We also see a 'gliding' in the cycle period from ∼40-hours in mid-November up to ∼100-hours at the end of January 1995. The ∼40-hour periodicity is very similar to that previously described in seismicity and tilt data (Nakada et al., 1999; Yamashina et al., 1999). However, the ∼100-hour cycle at the end of January 1995 is longer than the ∼60-hour period described by Nakada et al. (1999).

Numerous studies of seismicity during dome-forming eruptions have described characteristic sequences of earthquakes that correlate with changes in surface activity (e.g. Chouet, 1996; Iverson et al., 2006; Neuberg et al., 2006; Buurman and West, 2010; Ketner and Power, 2013; Johnson et al., 2014). This has been modelled to reflect frictional processes along conduit walls as the ascending magma releases accumulated energy by faulting and/or pulsatory ascent (Denlinger and Hoblitt, 1999; Voight et al., 1999; Iverson et al., 2006; Neuberg et al., 2006; Iverson, 2008; Lensky et al., 2008; Moore et al., 2008; Kennedy et al., 2009; Kendrick et al., 2012; Pallister et al., 2013; Kendrick et al., 2014b; Scharff et al., 2014). Yamashina et al. (1999) proposed a cyclic upward movement of the Unzen spine due to periodic variations in pressure in the conduit and Umakoshi et al. (2011) invoked a similar model to explain a short period 1-2 hour cycle during an earlier phase of the eruption in May 1991. The increase in observed cycle periods between May 1991 and November 1994 is likely due to a decrease in the effusion rate from >2 to <0.3 $m^3d^{-1}$ through the same period (Nakada et al., 1999). This is a similar mechanism to that inferred by Voight et al. (1999) to explain cycles of a similar periodicity at Soufrière Hills volcano, and later successfully modelled by Costa et al. (2012). The gradual decline and eventual halting of effusion by February 1995 would also explain the observed 'gliding' of the cycle periodicity. The short-term cyclicity at Unzen could also

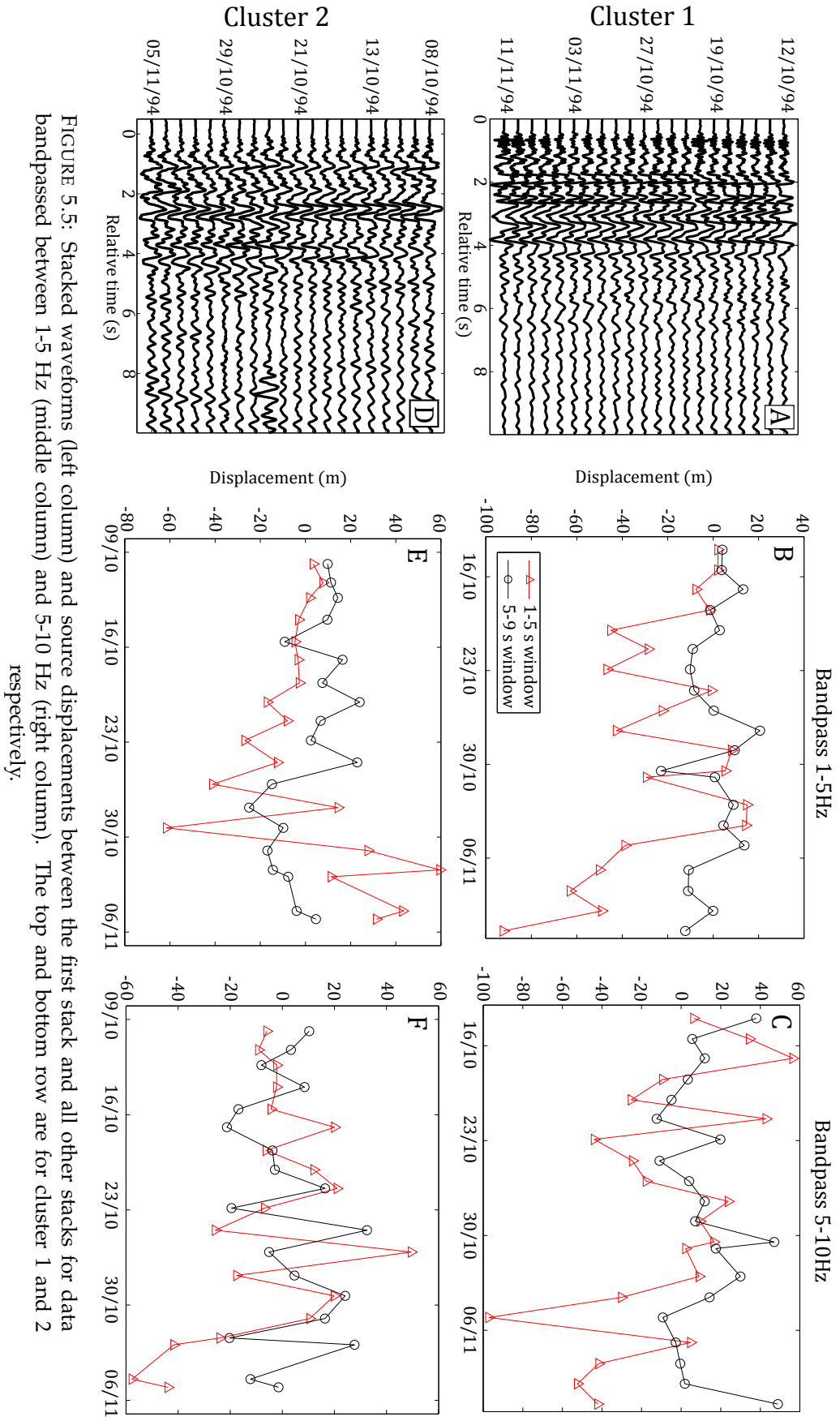


FIGURE 5.5: Stacked waveforms (left column) and source displacements between the first stack and all other stacks for data bandpassed between 1-5 Hz (middle column) and 5-10 Hz (right column). The top and bottom row are for cluster 1 and 2 respectively.

be explained by the presence of an elastic-walled dyke (e.g. Costa et al., 2007b); indeed, a dyke was emplaced beneath the dome in the early stages of the eruption (Yamashina and Shimizu, 1999; Umakoshi et al., 2011). However, the calculated thickness of the dyke (13 m; Yamashina and Shimizu, 1999), coupled with the low extrusion rate in November 1994, would not be able to account for the cycle period observed here (see Figure 6 in Costa et al., 2007b).

Given the high ambient temperatures in the shallow magma column, local temperature increases during slip events are likely to produce pseudotachylyte (e.g. Kendrick et al., 2012, 2014a,b), greatly altering fault properties (Otsuki, 2003; Di Toro et al., 2006; Nielsen et al., 2010; Hornby et al., 2015; Lavallée et al., 2015a). A recent study has shown that slip velocities as little as 0.1 $m.s^{-1}$ are sufficient to induce frictional melting (Kendrick et al., 2014a) - a threshold regularly met during faulting in the seismic events related to the spine extrusion at Unzen volcano (Hornby et al., 2015). However, it is difficult to infer the importance of mechanical contributions to the cyclicity detected above, as our description of these signal's trigger mechanisms remains incomplete. Here, using a combination of waveform correlation, SVD and CWI we have attempted to get a better understanding of this problem.

### 5.4.2 Repeating waveforms

Waveform correlation was carried out on the period around the extrusion of the spine instead of the entire period to focus on repetitive events related to its upward movement. 29 clusters were detected between 1$^{st}$ October and 15$^{th}$ November 1994 (Fig. 5.3B). The two largest clusters, which emerge coincidentally with the first observation of the spine (Yamashina et al., 1999), also feature a strong $\sim$40-hour periodicity similar to that detected in our FFT analysis (Sect. 5.3.2). The similar cluster waveforms (Fig. 5.3B, C) and the cyclic, non-destructive source character of the seismicity suggests a common process occurring within a similar setting. In addition, the opposing arrival polarities of each stacked cluster waveform (Fig. 5.3B,C) indicates opposite failure directions. Therefore, we propose that each cluster of low-frequency events derive from brittle shear failure on opposite sides of the ascending magma plug at Unzen volcano.

It is the rheology of magma that helps drive this process; during ascent magma becomes increasingly brittle as it both vesiculates and outgasses (Caricchi et al., 2007). This behaviour, on short timescales in the upper conduit, provides exceptionally dynamic rheological conditions that favour strain localisation and failure (Lavallée et al., 2008); providing a hypothesised source for repeating volcanic earthquakes during the delicate interplay of magma across the glass transition (e.g., Neuberg et al., 2006). As magma undergoes a similar pressure temperature path through time, the conditions of failure would remain constant and failure would be achieved at a similar depth in the conduit, thereby generating seismicity

from a recurring source (Thomas and Neuberg, 2012). Field examination of eruptive products elsewhere have exposed the importance of multiple fault processes (Tuffen et al., 2003; Tuffen and Dingwell, 2005; Kendrick et al., 2012, 2014b; Plail et al., 2014), where magma fracture is followed by friction, inducing comminution, brecciation, cataclasis (Kennedy et al., 2009), frictional melting and viscous remobilisation near the conduit margin (Kendrick et al., 2014a). These findings support the view that the bulk of the magma is able to ascend as a plug, where brittle fracturing along the margins of the ascending spine is responsible for seismicity, including the repetitive 'drumbeats' observed during the 2004-08 eruption at Mount St Helens (Iverson et al., 2006; Iverson, 2008; Kendrick et al., 2012). These mechanisms have been observed or, in some instances, inferred at other volcanic systems such as Augustine (Power and Lalla, 2010), Volcán de Colima (Varley et al., 2010) and Soufrière Hills volcano (Green and Neuberg, 2006; Neuberg et al., 2006; Lensky et al., 2008; Hammer and Neuberg, 2009; De Angelis, 2009; De Angelis and Henton, 2011; Kendrick et al., 2014a).

At Unzen, the gas flux scaled relatively consistently with magma extrusion rate throughout the eruption, with no marked increase during spine growth (e.g. Hirabayashi et al., 1995), therefore we exclude the movement of hydrothermal fluids as a source for the repetitive seismicity at Unzen (see e.g., Waite et al., 2008; Matoza and Chouet, 2010). In contrast, evidence of brittle failure along the spine margins at Unzen is present in field observations and laboratory measurements. Parallel-plate viscometry experiments have indicated that under the temperature and stress conditions in the conduit at Unzen, the magma's rheology would have induced brittle failure in regions of high strain rate (Goto, 1999; Cordonnier et al., 2009). Indeed, the brittle failure of magma at high temperature is integral to magma discharge (Lavallée et al., 2008; Tuffen et al., 2008; Smith et al., 2011) and occurs when the strain-rate surpasses the melt's timescale of relaxation (Webb and Dingwell, 1990). In the crystal-rich Unzen magma (56% crystal content; Cordonnier et al., 2009) there is a wide transitional area between viscous flow and brittle failure, where cracks nucleate, propagate and coalesce as catastrophic failure is approached (Cordonnier et al., 2012). In the conduit this shear failure occurs at the margins (Lavallée et al., 2012c), creating a marginal damage zone that enhances permeability and hence the outgassing capability of the magma column (Watts et al., 2002; Gaunt et al., 2014; Kendrick et al., 2014b; Plail et al., 2014). It is thought that lava domes may evolve from endogenous to exogenous growth through the development of such damage zones (Hale and Wadge, 2008; Cordonnier et al., 2009); and indeed, sheet-like layers of different porosities were described in rocks within the Unzen spine (Kueppers et al., 2005) along with a variety of cataclastic and brecciated fault rocks that preserve a record of brittle and ductile deformation along the margins of the spine (Smith et al., 2001; Calder et al., 2015; Hornby et al., 2015).

### 5.4.3 Source variations

Since our dataset only includes data from three stations, it is not possible to calculate the location of each earthquake in the record, which would aid our understanding of the source processes for the clusters. Instead, we employed the SVD method (Rubinstein and Ellsworth, 2010) to calculate relative amplitudes (and by extension, relative moments) and relative time differences (Fig. 5.4). While relative amplitudes for both clusters remain the same throughout each lifespan (Fig. 5.4B), the relative time differences have positive and negative trends for cluster 1 and 2, respectively (Fig. 5.4C). This suggests changes in either seismic velocity or source-receiver distance. The presence of a cluster generally implies a relatively stable source volume for the earthquakes, allowing for displacement within a quarter-wavelength (Geller and Mueller, 1980). However, De Angelis (2009) used CWI to estimate a source migration of 235 m for a cluster at Soufrière Hills volcano, Montserrat. Determining relative relocation for the cluster events at Unzen volcano is difficult due to the low number of stations available, but published locations have shown that the vast majority of earthquakes during our period of analysis occurred in the shallow subsurface (<1 km below summit; Nakada et al., 1999; Umakoshi et al., 2008).

Using CWI, we analysed the stacked waveforms from cluster 1 and 2 to assess changes in relative source locations (Fig. 5.5). We measured displacements of up to 100 m from the original position towards the end of each cluster's lifetime. However, displacements measured in the codas are relatively small, remaining close to zero. This shows that the position of scatterers remained relatively fixed during this period. Additionally, the calculated displacements are sensitive to which bandpass filter is used (Fig. 5.5B, C, E and F). However, as each waveform stack indicates a low-frequency nature (1-5 Hz, Fig. 5.3B, C) we do not consider displacements in the higher bandpass filter as relevant. The results presented in Figure 5.5 do not account for errors that are due to the choice of source models and seismic velocities (see Sect. 5.2.6). For the former, it is reasonable to expect the displacement occurs along a fault plane rather than an explosive or point source; no explosions were reported at Unzen during the spine formation (Nakada et al., 1999). Using seismic velocities consistent with those measured during the Unzen Scientific Drilling Project (see Sect. 5.2.6 here; Ikeda et al., 2008) we estimate that these displacements cannot explain the entire relative time difference trend seen in Fig. 5.4C. Therefore, we ascribe the relative time differences in both clusters (Fig.5.4C) to source displacements and an increase and decrease in seismic velocities for Cluster 1 and 2, respectively. Such characteristic opposite trends must derive from a common phenomenon with different conditions, as described by our conceptual model (Sect. 5.4.4).

### 5.4.4 A conceptual model

The displacement in the cluster sources and changes in seismic velocity at the source requires a mechanistic understanding. There are multiple processes by which the seismic velocity in a volcanic edifice can change: damage in and close to the volcanic conduit, the presence of hydrothermal fluids, or changes in stress and temperature conditions (e.g., Scheu et al., 2006; Heap et al., 2015b). Damage around the margins of spines is reported at Mount St Helens (Kennedy et al., 2009; Kendrick et al., 2012; Pallister et al., 2013) and Unzen volcano (Smith et al., 2001; Hornby et al., 2015). It is highly unlikely that the source location for Cluster 1 was becoming less damaged during the cluster lifespan, but variable loading of damaged rocks may affect material response, for example as fractures perpendicular to the principal stress close, seismic velocity can be increased (e.g., O'Connell and Budiansky, 1974; Heap et al., 2014). On the other hand, it is likely that the source location for cluster 2 was becoming increasingly damaged by both the thermal and cyclic stressing associated with the eruption (Kendrick et al., 2013; Schaefer et al., 2015). The frequency content of each cluster suggests the presence of fluids around the source regions, with higher fluid content around the source for cluster 2 (Fig. 5.4A), despite no reports of significant changes in the flow of hydrothermal fluids towards the end of the eruption (Hirabayashi et al., 1995). However, we do not believe it can explain the observed opposite trends in time lag for the events in clusters 1 and 2, though hydrothermal fluids may contribute towards mechanical weakening of the rocks (e.g., Heap et al., 2015b). We therefore propose a model where the extrusion of an inclined spine can lead to both variations in seismic velocities at the cluster sources and migration of each source (Fig. 5.6). In this model the source regions for each low-frequency cluster are located on the eastern and western margins of the spine, for cluster 1 and 2 respectively. The spine, rising in a pulsatory manner, undergoes volatile exsolution leading to densification and a loss in buoyancy. The dense, eastward-inclined spine then exerts an increasing amount of normal stress on the eastern, lower margin, and a decreasing amount on the western, upper margin. The inclination of the spine is evident from the inclined distribution of seismic hypocentres (Umakoshi et al., 2001) and pressure sources beneath the volcano (Kohno et al., 2008). Experimental work on Unzen dome samples by Scheu et al. (2006) has shown that under isothermal conditions, an increase in normal stress increases the *P*- and *S*-wave velocities. Each seismic event in the cluster is the result of a shear stress increase above the material strength or the frictional resistance on the surface of the spine, which are equally affected by normal stress (Byerlee, 1978). On the eastern, lower margin of the spine, an increase in the normal stress occurred throughout extrusion and cooling and densification resulted in a shallowing of the cluster source as the failure criteria was met at the same stress conditions at increasingly shallower depth. On the western, upper margin the opposite effect is seen, the source deepened to where failure conditions were met as the spine sunk away from the contact, unloading it from below and decreasing normal stress.

Furthermore, a reduction in normal stress across the western margin could introduce a degree of aseismic slip, causing cluster 2 to cease first. Therefore, the response of the magma subjected to differing stress-strain conditions on the upper and lower spine margin could in-part explain the difference in occurrence times and rates between clusters 1 and 2. Additionally, the locations of each cluster source on opposite sides of the plug explains the opposite arrival polarities seen in the cluster waveform stacks (Fig. 5.3B, C). The lower frequency content in the waveforms from cluster 2 (Fig. 5.4A) could result from greater fluid saturation due to degassing of the magma through the upper surface of the spine as the failure point propagates ever deeper towards the base of the magma plug. These stress variations form a minor contribution to the variations in seismic velocity in the source region for cluster 2, dominated by the decreasing normal stress due to the inclined spine.

## 5.5 Conclusions

We have characterised the seismicity of spine extrusion during the last stage of the 1991-1995 dome-forming eruption at Unzen volcano, Japan. Using a single-station detection approach, we identified 12,208 seismic events between October 1994 and February 1995. Two Fast-Fourier Transform analysis methods (Multitaper Method and Short-term Fourier Transform) revealed strong ∼40-hour cycles in hourly counts during the emergence of the spine. By the end of January 1995, the cycle 'glided' to a ∼100-hour period. The cycles are linked to pulsatory extrusion of the spine, in-part governed by the frictional properties of the magma plug and driven by magma supply from below. Waveform correlation of the dataset revealed two strong cyclic clusters of low-frequency volcano-seismic events during the spine extrusion, interpreted as repeated fracturing events at the spine margins. A combination of singular value decomposition and coda wave interferometry revealed changes in seismic velocities in the Unzen edifice during the extrusion. Our conceptual model proposes that late-stage densification of the inclined magma spine resulted in increasing normal stresses on the lower margin, serving to close preferentially aligned fractures, and the opposite effect on the upper margin, where pervasive damage resulted from unloading from below as the spine slumped. This results in increasing and decreasing seismic velocities respectively, as well as a migration of the source regions along the conduit walls as failure criteria are met. This study highlights the application of single-station detection, statistical analysis, waveform correlation, singular value decomposition, and coda wave interferometry to deduce subtle variations during eruptions. We anticipate that the application of such mechanism-based interpretation of geophysical signals, combined with field and experimental evidence, will help improve physical models needed to inform future assessment of hazards during lava dome eruptions.

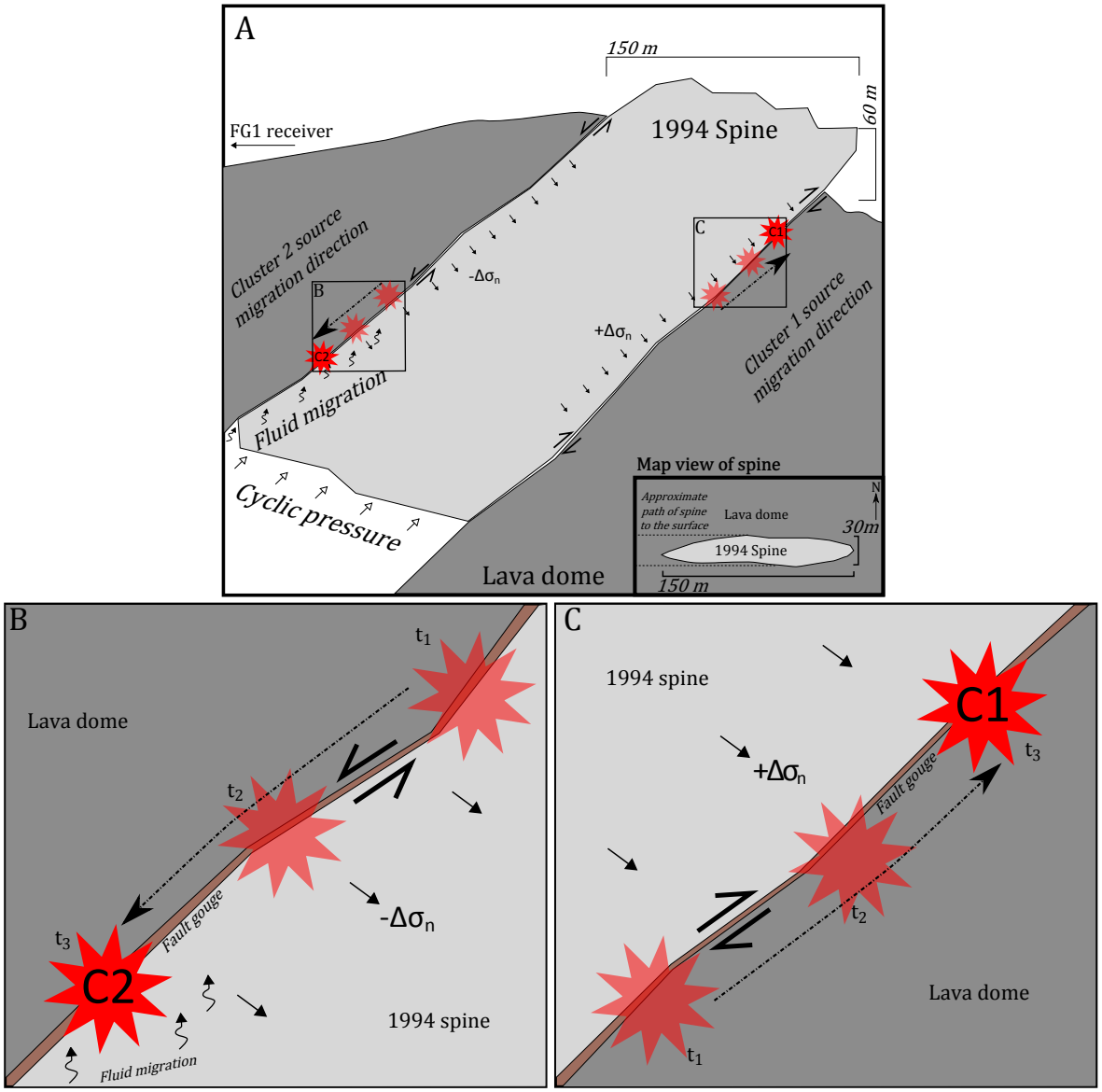


FIGURE 5.6: (A) An E-W cross-section of the conceptual model for spine extrusion and cluster source locations at Unzen volcano in October/November 1994, looking North. The inset shows a map-view of the spine at the surface of the lava dome. Squares indicate the locations for Panels B and C. (B) Detailed view of the source region for cluster 2, showing how it moves progressively deeper over time (t1,t2,t3) in response to the decrease in normal stress. (C) Detailed view of the source region for cluster 1, showing how it moves progressively shallower over time (t1,t2,t3) in response to the increase in normal stress. Please see Sect. 5.4.4 for more details and explanations.

# Chapter 6

# Long-term variations in explosion dynamics at Santiaguito dome complex

This chapter is derived from a manuscript currently under preparation for submission to *Journal of Volcanology and Geothermal Research*. The authors of the manuscript are currently Oliver Lamb (main author), Alejandro Diaz Moreno, Silvio De Angelis, Gustavo Chigna, Yan Lavallée and Andreas Rietbrock. This manuscript is a product of an ongoing project centred on Santiaguito dome complex, Guatemala. Silvio de Angelis, Yan Lavallée, and Andreas Rietbrock are the primary investigators of the project. Gustavo Chigna assisted the project during fieldwork in Guatemala. Alejandro Diaz Moreno assisted with analysing the seismo-acoustic dataset. The manuscript will be accompanied by at least three supplementary figures, which are included in Appendix D on page 131.

## Abstract

Investigations using multi-parameter and long-term datasets have been identified as particularly valuable for providing insights into the processes governing explosive activity during lava dome eruptions. Here, I present and describe a nearly two-year long seismo-acoustic dataset recorded at Santiaguito dome complex, Guatemala. Santiaguito has been continuously active for nearly 100 years and has experienced regular, gas-rich explosions since the 1970s. The dataset covers a period of heightened activity observed between November 2014 and September 2016. Before June 2015, activity was characterised by regular, gas-rich explosions that have been extensively described by previous investigations. However, from July 2015 to October 2016, the volcano experienced more irregular and energetic explosive activity, sometimes accompanied by pyroclastic density currents. This phase included lower explosion rates and higher energies recorded in the seismo-acoustic dataset. No correlation exists between the repose intervals between explosions, and subsequent explosive energy,

suggesting a complex trigger mechanism. Calculated ratios between seismic and acoustic energies illustrate how the conduit geometry had a major impact on the energy partitioning during explosions. A small fraction of events are accompanied by a large delay between the arrival of seismic and acoustic waveforms, suggesting these explosions originated at a greater depth in the conduit. Ultimately, this study has highlighted how long-term deployments of instruments will be highly valuable for future hazard and risk assessments around persistently active volcanoes.

## 6.1 Introduction

Lava dome eruptions are characterised by the relatively slow extrusion of highly viscous, degassed magma that accumulates on or near the vent and can eventually form voluminous edifices (>1 $km^3$). These eruptions can occur over a range of timescales, from weeks to decades, and often involve multiple episodes of explosive activity and/or collapses (Calder et al., 2015). This behaviour presents a significant challenge for monitoring and hazard assessment, particularly as transitions from effusive to explosive, and vice versa, can be rapid (e.g. 2010 eruption of Merapi, Indonesia; Surono et al., 2012). To this end, investigations using multi-parameter and long-term datasets are of particular value for providing insights into the processes governing these rapid transitions in behaviour, and reduce the hazard from lava dome eruptions.

Santiaguito dome complex in Guatemala is a lava dome eruption that has produced many effusive/explosive transitions throughout it's history. A network of seismometers and infrasound microphones was deployed around the vent and recorded eruptive activity from November 2014 to September 2016. The deployment was motivated by the need to build a long-term dataset to understand explosion dynamics at Santiaguito, as previous investigations had focused only on short periods of activity (e.g. Sahetapy-Engel et al., 2008; Johnson et al., 2014). Our period of study covers two major shifts in activity at the volcano, with a change to more explosive activity in mid-2015 followed by a return to effusive activity in October 2016.

Seismo-acoustic datasets have been increasingly used to understand the source dynamics of regular explosions during eruptions (e.g. Johnson and Aster, 2005; Petersen and McNutt, 2007; Sahetapy-Engel et al., 2008; Johnson et al., 2009, 2014). Johnson and Aster (2005) proposed using a ratio between estimates of acoustic and seismic energy from each individual explosion to characterise the relative partitioning of elastic energy into the atmosphere and the solid earth. The ratio, dubbed the volcanic acoustic-seismic ratio (VASR), may provide insight into the evolving eruption source, the magma properties, or the conduit geometry (Johnson and Aster, 2005). Furthermore, acoustic and seismic waves recorded at co-located instruments can be used to estimate the depths of the explosion source in the conduit (e.g.

Petersen and McNutt, 2007). At Santiaguito dome complex, seismo-acoustic datasets have been combined with thermal, visual and/or deformation datasets to constrain the source dynamics of regular gas-and-ash explosions (e.g. Johnson et al., 2009, 2014). Deformation cycles recorded during the explosion sequences have been interpreted as steady gas exsolution and accumulation beneath a lava plug in the conduit (Johnson et al., 2014). However, this needs to be reconciled with gas, field, and experimental data that suggests brittle failure of magma along the conduit margin is synchronous with explosions (Holland et al., 2011) and perhaps acts as a trigger via thermal vesiculation (Lavallée et al., 2015b).

We begin this article with a short description of Santiaguito dome complex and its eruptive history, and detail the network of instruments deployed around the area since November 2014. This is followed by a summary of the reported activity from the volcano since 2014. Observations of this activity from the seismo-acoustic datasets are summarised before a brief discussion of their implications.

## 6.2 Santiaguito dome complex

Santiaguito is a $\sim$1.1 km$^3$ active complex of lava domes located 110 km west and 11 km south of the cities of Guatemala City and Quetzaltenango, respectively (Harris et al., 2003). The dome complex first began extruding in 1922 into the centre of an eruption crater on the southwestern flank of Santa Maria volcano (Rose, 1973). The crater formed during the October 1902 eruption of Santa Maria, one of the largest of the twentieth century, erupting 8.3 km$^3$ of dacite over an area of 1.2 x 10$^6$ km$^2$ and resulted in thousands of deaths (Williams and Self, 1983). Since 1922 up to present day, the dome complex has been continuously active from the El Caliente vent and three lateral vents (La Mitad, El Monje and El Brujo; Rose, 1973). Extrusion rates have shown a distinctly cyclic nature, with at least eight cycles identified with periods of 7-15 years length (Harris et al., 2003). Since 1977, activity has been focused at the El Caliente vent and consists of semi-continuous extrusion of blocky lava flows interspersed by frequent gas-and-ash explosions, accompanied by occasional dome collapse and pyroclastic flows (Rose, 1987; Harris et al., 2003). Since 2000, explosions have generally been of small to moderate size with volatile-rich, ash-poor plumes typically reaching 1-2 km above the vent (Sahetapy-Engel et al., 2008; Johnson et al., 2014; De Angelis et al., 2016). Throughout the course of the eruption, the erupted lava has become progressively less evolved over time, with a $\sim$4 wt.% decrease in bulk $SiO_2$ from 1922 to 2002 (Scott et al., 2013).

### 6.2.1 Instrument network

The temporary network deployed in November 2014 consisted of eleven seismometers and five acoustic microphones capable of recording infrasound. The seismometers consisted

of five Nanometrics Trillium Compact three-component broadband instruments and six Lennartz LE-3Dlite three-component short-period instruments. The microphones were iTem prs100 instruments and were co-located with the broadband seismometers. The stations were strategically deployed around Santiaguito dome complex to minimise the largest azimuthal gap between two stations (Fig. 6.1). These stations stored data internally at a rate of 100 Hz and are powered by 12 V batteries charged by solar panels, if possible. Periods of station operation are shown in supplementary Figure D.1.

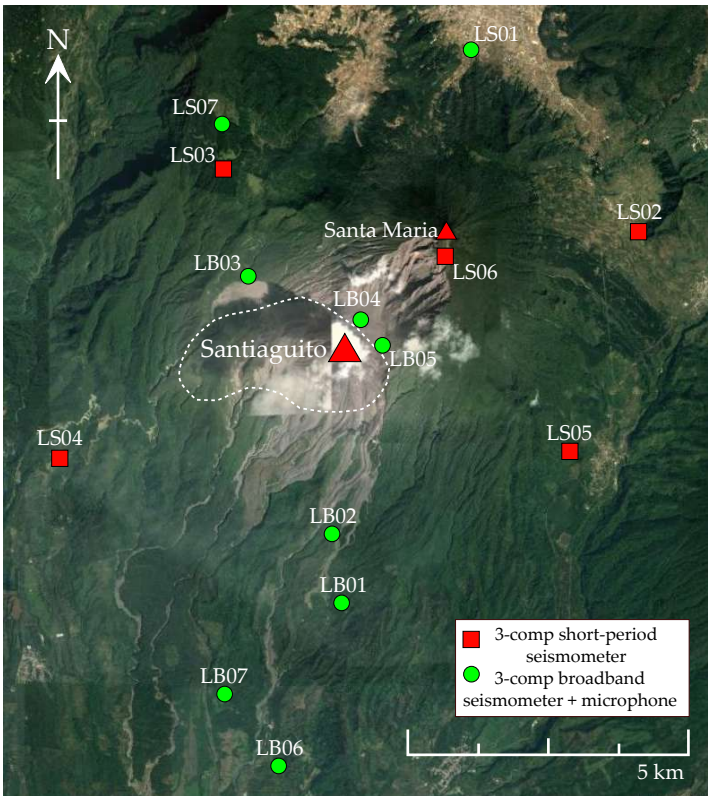


FIGURE 6.1: Map of the instrument network deployed around the Santiaguito dome complex, Guatemala. Green circles indicate stations that were co-deployed with an acoustic microphone. Dashed line indicates the extent of the Santiaguito dome complex.

## 6.3 2014-2016 eruptive sequence

The following chronology is based on a combination of observations compiled by the authors from several field campaigns in 2014, 2015, 2016 and 2017. Further details are derived from INSIVUMEH reports, personal communications, and the Bulletin of the Global Volcanism Network, published on the Global Volcanism Program website (Venzke, 2013).

### 6.3.1 Pre-November 2014

Activity at Santiaguito in 2014 was characterised by a major dome collapse followed by the emplacement of an extensive lava flow. The collapse, which occurred on 9$^{th}$ May 2014,

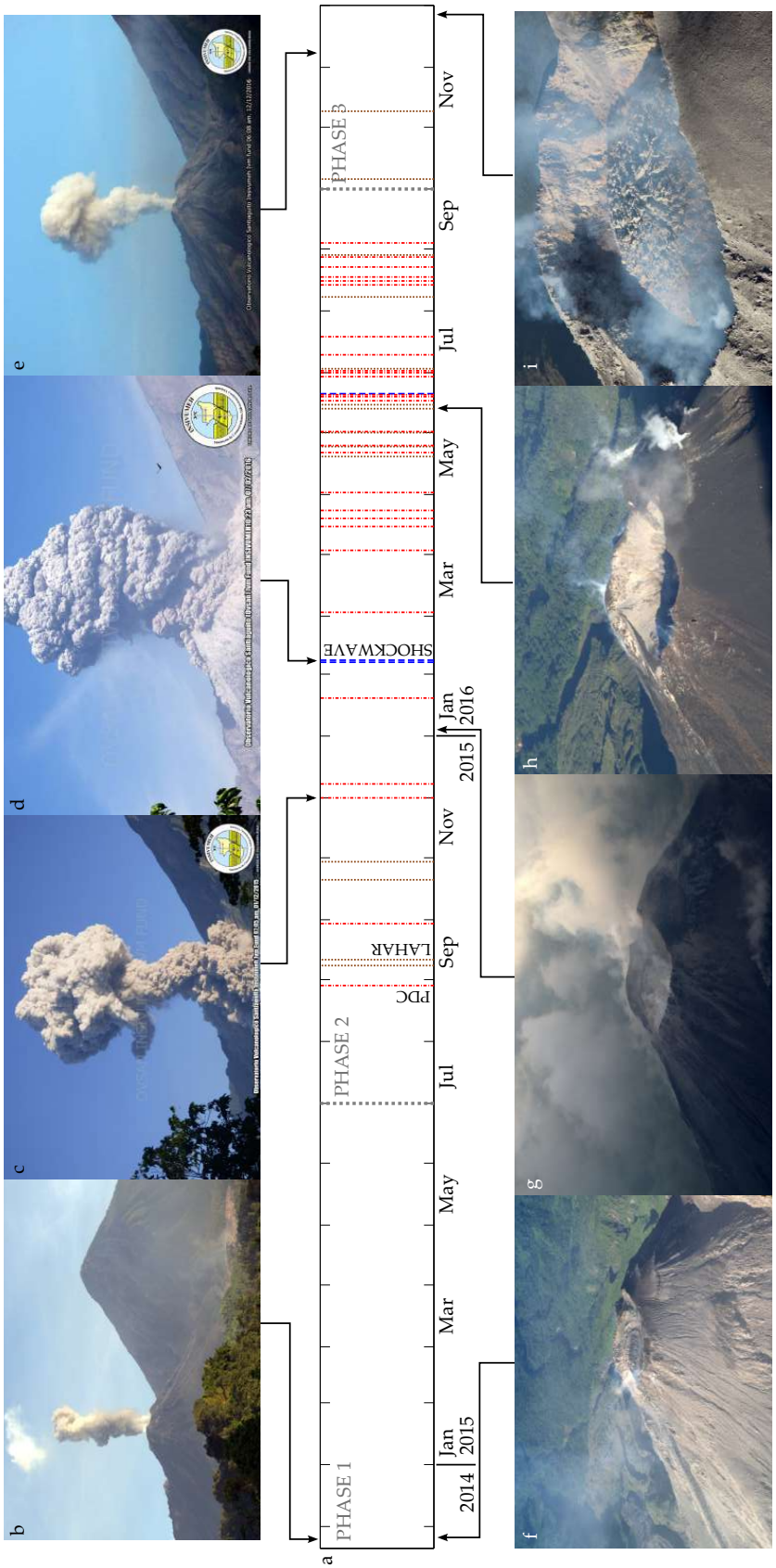


FIGURE 6.2: (a) Timeline of significant activity at Santiaguito dome complex from November 2014 to December 2016. Red dashed lines indicate explosions accompanied by pyroclastic density currents. Brown dashed lines indicate days when lahars occurred. (b-e) Images of explosions from different phases during the period of study. Images (c-e) are courtesy of INSIVUMEH. (f-i) Images of the evolution of the El Caliente vent during our period of study. Image (i) is courtesy of Armando Pineda.

removed a significant section of the eastern flank of El Caliente vent and produced a pyroclastic density current that travelled ∼7 km to the south, depositing 1x$10^6$ $m^3$ of tephra. This was followed by a series of lahars in the next two weeks, including two major events on 6$^{th}$ June and 15$^{th}$ July that damaged local infrastructure and forced temporary evacuations. Shortly after the 9$^{th}$ May collapse, a lava flow was observed descending the collapse scar and generating incandescent rockfalls. The flow continued along two lobes for the rest of 2014, eventually stopping in December at a length of 3.5 km (Global Volcanism Program, 2015). Throughout this period of activity, repeated small gas-and-ash explosions continued to occur at regular intervals from the active El Caliente vent, forming ash plumes up to 1 km high.

### 6.3.2 November 2014 - December 2015

During the deployment of the instrument network in November/December 2014, regular gas-and-ash explosions continued to occur from the El Caliente vent (Fig. 6.2b). Previous analysis has found that these explosions only carried minor ash fractions suggesting no extensive magma fragmentation was occurring in the conduit (De Angelis et al., 2016). Incandescence was observed from the active vent, although lava effusion was negligible or halted. This activity continued until July/August 2015, at which point a phase of heightened explosivity began. Explosions became less regular and occasionally much more energetic, sometimes accompanied by pyroclastic density currents (Fig. 6.2c). The largest group of explosions in 2015 were observed in December, producing 7 km high ash plumes and further pyroclastic density currents. Fine ashfall fell at least 10 km from the vent in all directions, and ash was tracked by the Washington VAAC for 280 km before dissipating. During this phase, heavy rainfall triggered hot lahars that descended river drainages to the south on 8$^{th}$ September, 11$^{th}$ September, 21$^{st}$ October and 30$^{th}$ October (Global Volcanism Program, 2016a).

### 6.3.3 January 2016 - September 2016

From January to June 2016, major ash-rich explosions and pyroclastic density currents continued to occur at irregular intervals with smaller gas-rich explosions in between. Plumes rose to 5 km altitude with ash regularly falling on villages up to 20 km from the vent. Two explosions in February, and one in June, were accompanied by acoustic shockwaves that were heard up to 25 km away from the volcano (Fig. 6.2d). The largest explosions of the entire 2-year period were observed in March to May 2016, ejected 2-3 m diameter blocks up to 3 km away from the vent, and excavated the summit vent to a ∼150 m depth crater (Fig. 6.2h). Heavy rainfall triggered two lahars in May and a further five lahars in June (Global Volcanism Program, 2016b). The irregular and large explosions with occasional pyroclastic

density currents continued to occur at Santiaguito through July, August and into September, with smaller gas-rich explosions in between.

### 6.3.4 October 2016 - ongoing

In October 2016, a new phase of activity began, characterised by the extrusion of lava into the summit crater of El Caliente (Fig. 6.2i). By February 2017, this new lava extrusion had filled most of the summit crater, extruding at an approximate rate of $< 0.6$ $m^3s^{-1}$. Small, gas-rich emission events continued to erupt from the active vent (Fig. 6.2e), but no large explosions have been reported since September 2016. Hot lahars were occasionally triggered by rainfall throughout this period.

## 6.4 Seismic and acoustic observations of explosions

In this section, I will provide an overview of the seismic and acoustic observations of the activity during our period of study. Also included are subsections that describe and discuss the energy dynamics of the explosions at Santiaguito (section 6.4.3), as well as describe the change in arrival time-differences between seismic and acoustic waveforms from the explosions (section 6.4.4).

### 6.4.1 Methodology

To get a general overview of the activity taking place from November 2014 to September 2016, the real-time seismic amplitude (RSAM), explosion counts and explosion energies are calculated. However, due to technical issues in the network of instruments, no single station covers the entire period of study (Fig. D.1). Therefore, a network RSAM time-series was constructed by combining the individual station RSAM time-series (Fig. D.2, D.3). Each individual RSAM time-series was calculated from the average amplitude within successive 10 minute windows across the recorded seismic time-series. Before combining into the network RSAM, the individual time-series were calibrated and corrected for site amplification. Site amplification factors were calculated from the ratio of seismic noise amplitudes at each station relative to seismic noise recorded at a reference station, which we chose to be LB01. Amplification factors calculated using explosion amplitudes produced similar values. Following these steps, the network RSAM was calculated using the average of all stations available within each 10 minute window.

The lack of a single, consistent time-series through the entire study period also affected the methodology for detecting explosions. To automatically pick explosions from the dataset, an envelope detection method was used. This approach uses the envelope of a chosen seismic

waveform and scans through the recorded time-series to find other waveforms that reach a certain threshold of similarity (i.e. cross-correlation coefficient, CCC). This method was chosen as it can filter out other types of volcanic seismicity and bypasses the variability in frequency content between explosions. For Santiaguito, a CCC of 0.8 is used and a minimum of 60 s was required between explosions. Each 60 s long reference waveform, and the seismic time-series, was bandpass filtered at 0.01 - 1.8 Hz before envelope detection was carried out. This frequency band was chosen as it filtered out false triggers from rockfalls or anthropogenic noise. As no single station covers the whole study period, the explosion detection was used on different stations depending on their availability and signal-to-noise ratio; stations with a higher ratio were favoured. Table 6.1 lists the stations used, the time periods covered, and the time of the reference waveforms used.

TABLE 6.1: Stations used, time periods covered, and reference waveforms used for explosion detection at Santiaguito dome complex from 23 November 2014 to 06 September 2016.

| Station | Time period covered | Reference waveform (UTC) |
|---|---|---|
| LB01 | 23/11/2014 - 18/09/2015 | 05/06/2015 04:46:45 |
| LS06 | 18/09/2015 - 27/10/2015 | 04/10/2015 07:12:10 |
| | *Network data loss* | |
| LB03 | 01/12/2015 - 26/12/2015 | 02/12/2015 09:24:05 |
| LS04 | 26/12/2015 - 03/01/2016 | 27/05/2016 05:46:10 |
| LB02 | 03/01/2016 - 20/02/2016 | 06/01/2016 10:44:04 |
| LS04 | 20/02/2016 - 18/03/2016 | 27/05/2016 05:46:10 |
| LB03 | 18/03/2016 - 26/04/2016 | 02/12/2015 09:24:05 |
| LS04 | 26/04/2016 - 20/06/2016 | 27/05/2016 05:46:10 |
| LS06 | 21/06/2016 - 06/09/2016 | 01/07/2016 09:50:31 |

Once an explosion catalogue was compiled, the energy of each explosion was calculated from the seismic and, where available, acoustic waveforms. Following Johnson and Aster (2005), a standardised method for comparing discrete explosive energies was adopted. Explosive seismic energy is calculated using an approach that assumes velocity waveforms are representative of the seismic kinetic energy density at a specific location on the volcano. Due to equipartitioning, potential energy density is equivalent to the kinetic energy density. Thus, for an isotropic source located at the top of a homogenous half space, seismic energy ($E_{seismic}$) can be written as (e.g. Boatwright, 1980):

$$E_{seismic} = 2\pi r^2 \rho_{earth} c_{earth} \frac{1}{A} \int S^2 U(t)^2 dt \tag{6.1}$$

where $r$ is source-to-receiver distance, $\rho_{earth}$ is rock density, $c_{earth}$ is seismic velocity (2150 ms$^{-1}$), $A$ is attenuation, $S$ is the seismic site response, and $U$ is the particle velocity. For each explosion, we integrate over a time window that corresponds to the entire duration of the waveform. The integral is thus calculated from the signal onset until seismicity returns to background levels. In contrast, acoustic energy radiated during volcanic explosions is

relatively simple to evaluate from pressure records. Assuming isotropic radiation from a point source, it is possible to space-time integrate over a hemispherical surface to estimate the acoustic energy ($E_{acoustic}$) radiated into the atmosphere (e.g. Pierce, 1981; Johnson and Aster, 2005):

$$E_{acoustic} = \frac{2\pi r^2}{\rho_{atmos} c_{atmos}} \int \Delta P(t)^2 dt \tag{6.2}$$

where $\rho_{atmos}$ is the air density, $c_{atmos}$ is the speed of sound (325 ms$^{-1}$; De Angelis et al., 2016), and $\Delta P$ is the excess pressure recorded by the microphone. Similar to seismic energy, we integrate over a time window spanning the entire duration of the acoustic waveform. It is important to note that Eq. 6.2 assumes linear sound propagation and a monopole source. Non-linear sound propagation may result in an underestimation of the explosive energy during intense events. Non-monopole or multipole sources have been proposed for volcanic explosions (e.g. Woulff and McGetchin, 1976; Kim et al., 2012).

### 6.4.2 General observations

Generally, the network RSAM remains relatively low throughout and is only punctuated by spikes of energy associated with larger explosions, pyroclastic density currents and/or lahars (Fig. 6.3a). The frequency and size of these energy spikes does slightly increase from December 2015 onwards, reflecting the relative increase in energy of explosions during this period (section 6.3.3). The change in explosive activity mid-2015 (section 6.3.2) is immediately clearer when plotting the rate of explosions per day over our period of study (Fig. 6.3b). Between November 2014 to June 2015, explosions occurred at an average rate of 13.5 explosions per day, reaching a maximum of 40 explosions on 5$^{th}$ March 2015. After mid-2015, the rate of explosions per day continues at a much reduced pace, with an average 1.9 explosions per day; this includes some days when no explosions are detected (e.g. February 2016).

### 6.4.3 Seismic and acoustic energies

From November 2014 to June 2015, explosive energy remains relatively constant (Fig. 6.3c, d). This is also clear from the steadily rising cumulative energy during this period (Fig. 6.3b). From June 2015 onwards, the energy of a portion of the explosions increases by several orders of magnitude. The largest explosions took place during March to May 2016, consistent with the reported increase in activity at the time (section 6.3.3). This is clearly seen in the cumulative energy curve where large jumps are observed during this period.

Repose intervals are defined as the time periods between two particular events. Plotting the seismic energy of the explosions versus their repose interval since the last event reveals

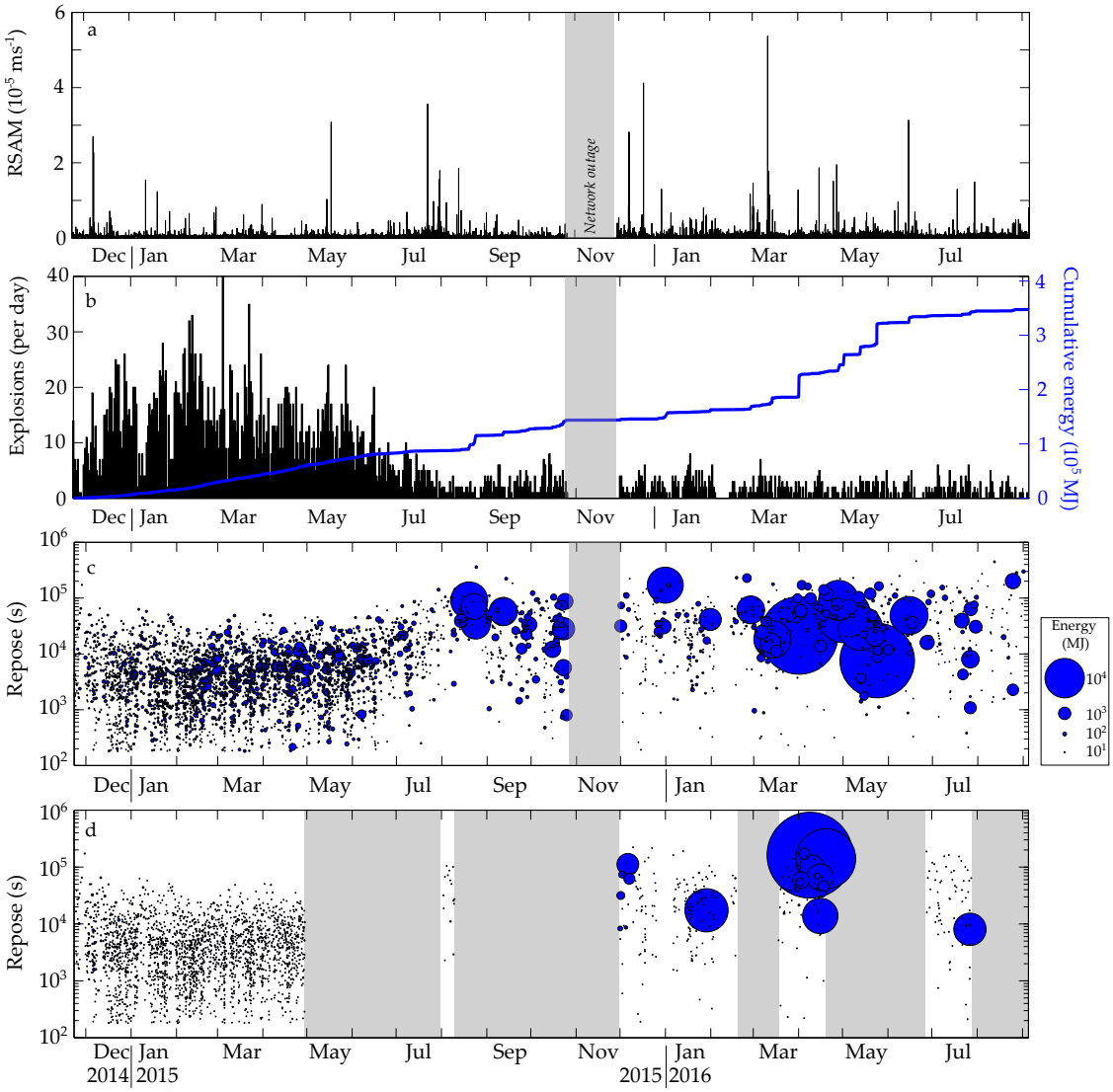


FIGURE 6.3: (a) Network RSAM recorded across the instrument network deployed at Santiaguito dome complex. (b) Explosions per day (black bars) and cumulative energy of the explosions (blue line) during our period of study. (c) The repose interval of each explosion since the previous event, with the point scaled by the energy of the recorded seismic waveform. (d) The repose interval of each explosion since the previous event, with the point scaled by the energy of the recorded infrasound waveform. Grey areas in all plots mark time periods where no data was recorded due to technical issues.

no significant correlation (Fig. 6.4a). In Fig. 6.4b we have plotted the seismic energy as a function of acoustic energy for each explosion (when both data types are available). The results reveals a clear difference between the phases of activity occurring during the period of study. Explosions pre-June 2015 are well grouped together and generally have a low VASR. Explosions after this date are more disperse, and display a wide range of VASR values.

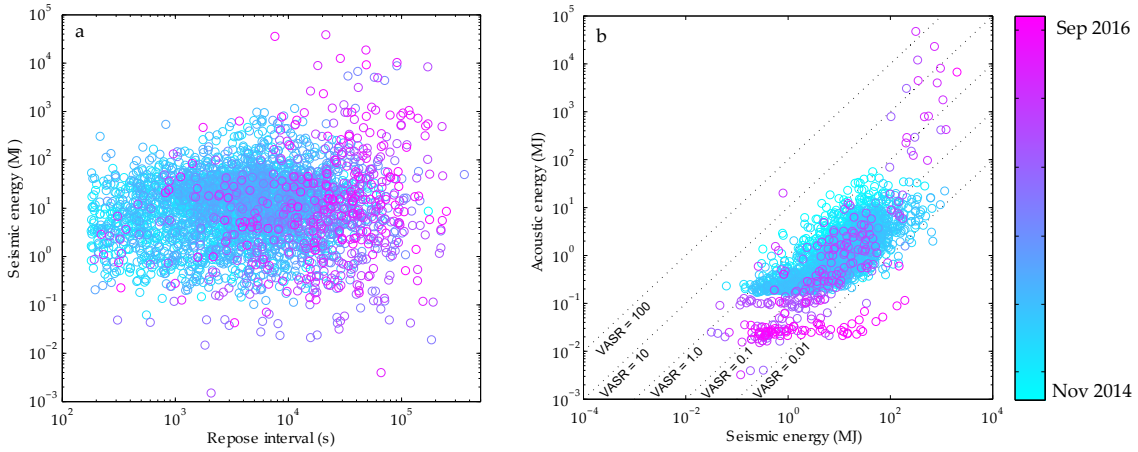


FIGURE 6.4: (a) Seismic energy plotted as a function of the repose interval since the previous explosion. (b) Acoustic versus seismic energy for each explosion at Santiaguito dome complex. The dotted lines indicate the VASR boundaries.

### 6.4.4 Change in arrival time differences

Arrival times of seismic and acoustic waves at the same station can give an indication of the source location of each explosion. For explosions pre-June 2015, the travel-time difference at a single station generally remained stable (e.g. ∼6 s at LB03, 2.5 km from vent; Fig. 6.5a, c). Post-June 2015, the travel-time differences became more variable with some explosions seemingly producing 'slow' acoustic waveforms (e.g. ∼20 s at LB03; Fig. 6.5b, d). To constrain the proportion of explosions with 'slow' acoustic waveforms, the arrival times were manually picked for selected explosions at regular intervals; 3-day pre-June 2015, 1-day post-June 2015. Assuming the distance travelled by the acoustic and seismic waveforms are approximately equal, the time for materials to travel between the seismic source within the conduit and the acoustic source at the vent surface can be calculated. Using an acoustic velocity of 325 $ms^{-1}$ (De Angelis et al., 2016), and a seismic velocity of 2150 $ms^{-1}$, the conduit travel times range from 0 to nearly 16 s (Fig. 6.5e). Only a small fraction of explosions post-June 2015 have a large conduit travel time. Most explosions throughout the period of study have travel times of $\leq$6 s. Some conduit travel times are negative due to the assumptions that acoustic and seismic velocities remain fixed, and that the effects of source dynamics and topography are negligible.

## 6.5 Interpretation and discussion

The long-term seismo-acoustic dataset recorded at Santiaguito dome complex from November 2014 to September 2016 has captured multiple phases of activity (section 6.3), each characterised by different explosion rates and energies (Fig. 6.3). Analysis of the temporal

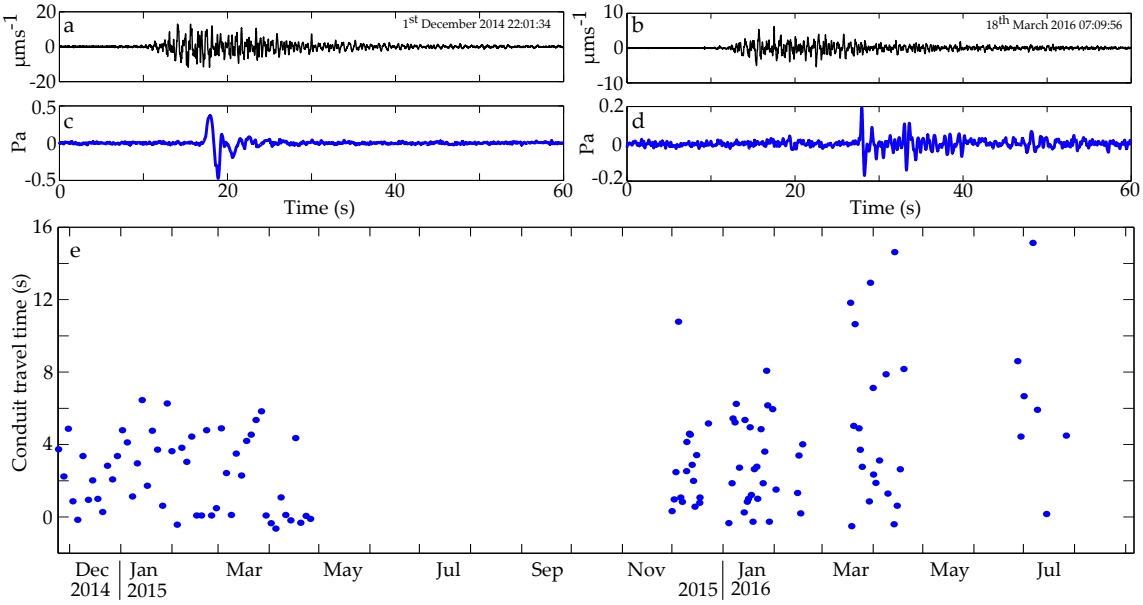


FIGURE 6.5: Examples of seismic (a, b) and acoustic (c, d) waveforms from two explosions illustrating the changes in arrival time differences (recorded at station LB03). The event in December 2014 (a, c) has 6 seconds between seismic and acoustic waves arriving; the event in March 2016 (b, d) has 17 second time difference. (e) Calculated conduit travel time for selected explosions through our period of study.

trends in explosions energies and seismic-acoustic waveform arrival times have revealed a dynamic system during our period of analysis (Figs. 6.3, 6.4, 6.5). In this section is the interpretation and discussion of the observations described in section 6.4.

Plotting the seismic energy of explosions versus the time interval since the previous event reveals no correlation between the two values (Fig. 6.4a). If such a correlation was observed, this would suggest that explosions are a result of pressure build-up in the conduit and longer intervals between events would produce more energetic explosions (e.g. Roman et al., 2016). Therefore, the explosion source process at Santiaguito dome complex throughout our period of study is likely a more complicated process. For example, based on gas flux and experimental observations, brittle failure of magma has been proposed as a trigger process for explosions (Holland et al., 2011; Lavallée et al., 2015b). However, more analysis is required before ruling out the role of gas accumulation beneath a lava plug (Johnson et al., 2014). The ratios between the seismic and acoustic energies (VASR) for explosions display a wide range of values (Fig. 6.4b). A low VASR suggests that the explosion initiated relatively deeper in the conduit, and/or acoustic waveforms were dampened by material in the conduit. A high VASR would suggest the opposite, that is, a shallow explosion initiation point and/or little dampening of the acoustic waveforms between the source and the atmosphere (Johnson and Aster, 2005). Explosions recorded pre-June 2015 generally have a low VASR, which agrees with a vent filled with lava and ash (Fig. 6.2f). Post-June 2015,

some explosions were associated with larger VASR values which corresponds to the erosion of the crater vent in 2016 (Fig. 6.2h). However, most explosions are still of a low VASR value suggesting there may have still been enough material in the vent to dampen the acoustic waveforms, or explosions were initiating at greater depths.

To verify this, the temporal variation in arrival time differences recorded for selected explosions over our period of study may be used (section 6.4.4; Fig. 6.5). A small portion of explosions recorded post-June 2015 were accompanied by a larger time difference between the arrival of seismic and acoustic waveforms (Fig. 6.5). This corresponds to a larger travel time for gas-and-ash between the initiation point (i.e. the seismic source) and the vent surface, where the ejected material disturb the atmosphere to produce acoustic waves (Fig. 6.5e). Thus, explosions with a larger travel time difference between seismic and acoustic waveforms have likely initiated at a greater depth. Following a similar approach by Petersen and McNutt (2007), a simple model can be used to calculate the approximate depths of the explosions (Fig. 6.6, inset). We assume the seismic and acoustic sources are separated by a vertical distance $h$ in the conduit. Additionally, the distance ($x$) travelled by the acoustic and seismic waves are assumed approximately equal. For velocities, we use $V_{seis}$ = 2150 ms$^{-1}$, $V_{air}$ = 325 ms$^{-1}$ (De Angelis et al., 2016), and $V_{con}$ = 50 ms$^{-1}$ (Johnson et al., 2014). Our chosen value for $V_{con}$ agrees well with material ejection velocities of 20-30 ms$^{-1}$ measured using doppler radar and infrasound techniques (Scharff et al., 2014; De Angelis et al., 2016). Pre-June 2015, explosions remain relatively shallow in the conduit (<300 m; Fig. 6.6). Post-June 2015, the range in depths extend down to <800 m in the conduit, representing a change of >500 m. VASR values for these explosions suggest no correlation to their initiation depths, implying that material in the conduit is the major factor affecting the partitioning of acoustic and seismic energies. However, these calculations heavily rely on $V_{con}$ which is unlikely to be fixed over our period of analysis. Visual observations of explosions post-June 2015 and reports of shockwaves during some explosions (section 6.3.3) suggests that gas and ash were moving through the conduit at a much higher rate. Therefore, the 50 ms$^{-1}$ value calculated by Johnson et al. (2014) likely represents a minimum value and by extension, these depth calculations as well. Further work is needed to constrain the velocity of the material moving through the conduit, as well as constrain the effect of topography and atmospheric conditions on the acoustic waveforms, in order to advance our models based on seismo-acoustic monitoring datasets.

However, our dataset cannot shed light on what process may have triggered this sequence of activity at Santiaguito dome complex. Previous investigations on transitions to more vigorous explosive activity have generally inferred processes occurring at depth in the magmatic system as trigger mechanisms (Tait et al., 1989; Murphy et al., 2000; Cashman and Sparks, 2013; Christopher et al., 2015). There are several scenarios which may have triggered the increased activity observed at Santiaguito: melt recharge into the reservoir may have mobilised partially crystalline magma (Fig. 6.7; e.g. Murphy et al., 2000), evolved melt

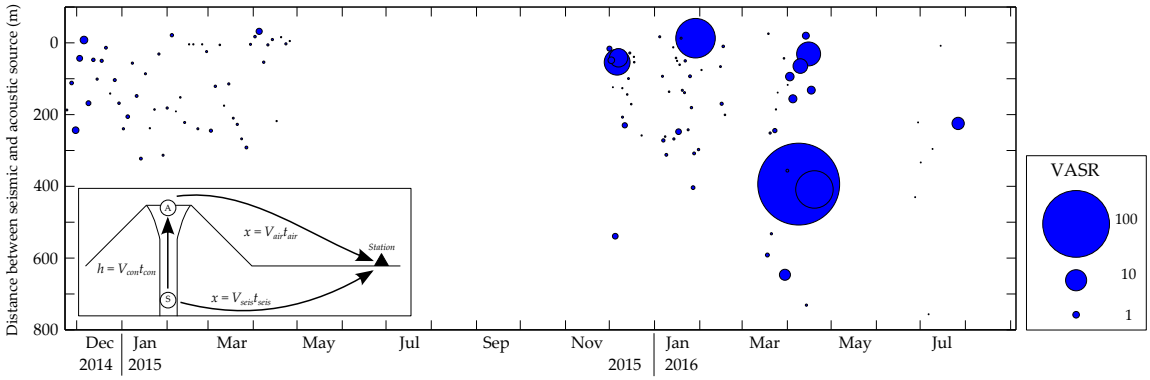


FIGURE 6.6: Distance between the seismic and acoustic sources during explosions at Santiaguito dome complex. Each point has been scaled by the calculated VASR for the corresponding explosion. Inset: Schematic of the simple model used to calculate the distances. $x$ is the distance from source to station. $h$ is distance between seismic and acoustic sources. $t$ is the travel time for acoustic waves (air), seismic waves (seis) and gas/ash material (con), $V$ are their velocities.

may have efficiently moved into shallower storage regions (e.g. Cashman and Sparks, 2013; Christopher et al., 2015), or pressure was released from water-supersaturated magma (Tait et al., 1989). Previous investigations of the eruptive products have described evidence that the 1902 eruption of Santa Maria was triggered by magma mixing in the magmatic system (Scott et al., 2013). However, since the 1940's the lava extruded from Santiaguito have shown little evidence for mixing and instead suggests a progressive tapping of less evolved parts of a stratified magmatic system (Scott et al., 2013). This suggests that either magma recharge or evolved melt movement could have triggered the 2015-2016 activity at Santiaguito dome complex. Geochemical and petrological analysis of ash and lava from the recent activity should help differentiate which process was the major factor in triggering the sequence of activity.

Ultimately, the seismo-acoustic dataset described here has captured an unprecedented sequence of activity at Santiaguito dome complex, switching from mild, regular explosive activity, followed by irregular, sometimes vigorous explosions, and concluding with effusive activity. Datasets recorded on shorter timescales (e.g. weeks to months) would likely have failed to capture the whole sequence. Therefore, long-term deployments of seismic and acoustic instruments around persistently active volcanoes are required before general interpretations of the volcanic system can be made.

## 6.6 Summary

Seismo-acoustic datasets can provide important insights into the dynamics of explosions during lava dome eruptions. Here, I have presented the first long-term seismo-acoustic

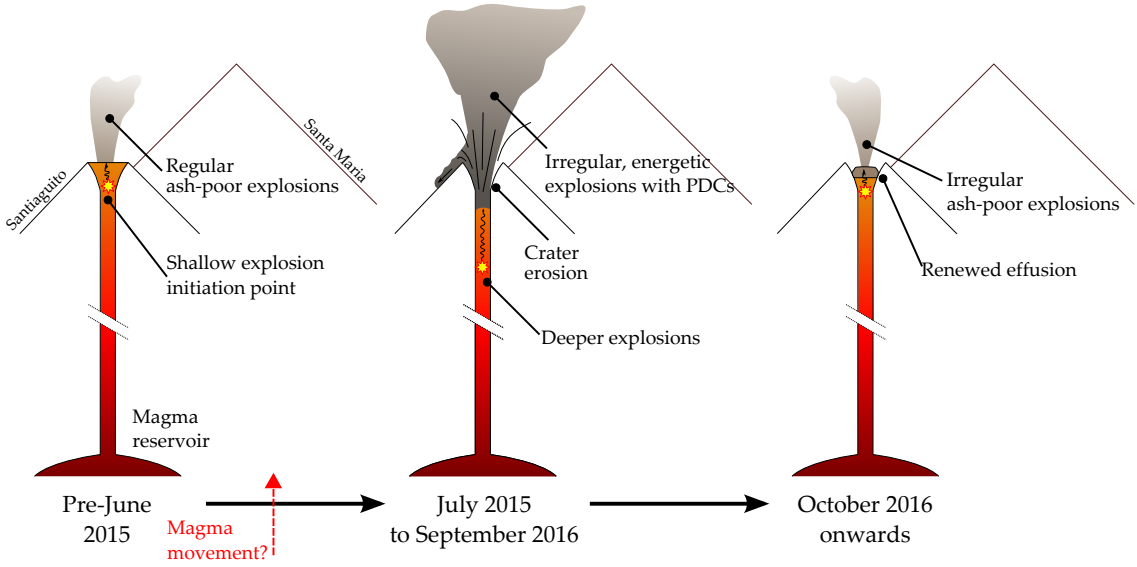


FIGURE 6.7: Summary of the activity sequence at Santiaguito dome complex over our period of study.

dataset to be recorded at Santiaguito dome complex, Guatemala. The dataset covers activity at the volcano from November 2014 to September 2016. This period includes an unprecedented change in activity, where regular, gas-rich explosions were replaced with irregular, ash-rich, sometimes energetic explosions with pyroclastic density currents. This sequence in activity is highlighted by tracking the changes in energies over the whole time periods. The ratio of acoustic to seismic energy has highlighted how the presence of material in the conduit is a major factor affecting the energy of acoustic waveforms from explosions. Variations in the arrival times of seismic and acoustic waveforms has suggested that a small fraction of the recorded explosions have originated from a greater depth in the conduit. Ultimately, this study has highlighted how long-term deployments of instruments, combined with other approaches such as geochemistry, will be imperative for future hazard and risk assessments around volcanoes such as Santiaguito dome complex.

# Chapter 7

# Using infrasound to constrain ash plume rise

This chapter is derived from a paper published in *Journal of Applied Volcanology*, accepted for publication on 3 November 2015 and published on 19 November 2015. Authors of the manuscript are Oliver Lamb (main author), Silvio De Angelis and Yan Lavallée. The aim of this study was to produce and test an efficient workflow that can quickly use infrasound recordings to measure the height of an explosion ash plume. Silvio De Angelis participated in the analysis, and helped draft the manuscript. Yan Lavallée participated in the design of the study and helped draft the manuscript. All authors read and approved the final manuscript.

## Paper abstract

Airborne volcanic ash advisories are currently based on analyses of satellite imagery with relatively low temporal resolution, and numerical simulations of atmospheric plume dispersion. These simulations rely on key input parameters such as the maximum height of eruption plumes and the mass eruption rate at the vent, which remain loosely constrained. In this study, we present a proof-of-concept workflow that incorporates the analysis of volcanic infrasound with numerical modelling of volcanic plume rise in a realistic atmosphere. We analyse acoustic infrasound records from two explosions during the 2009 eruption of Mt. Redoubt, USA, that produced plumes reaching heights of 12-14 km. We model the infrasonic radiation at the source under the assumptions of linear acoustic theory and calculate variations in mass ejection velocity at the vent. The estimated eruption velocities serve as the input for numerical models of plume rise. The encouraging results highlight the potential for infrasound measurements to be incorporated into numerical modelling of ash dispersion, and confirm their value for volcano monitoring operations.

## 7.1 Background

Mt. Redoubt, a dome-building volcano located 170 km south-west of Anchorage, Alaska, erupted in March 2009 after approximately 20 years of quiescence. On March 15, a small phreatic explosion marked the onset of the eruption. This was followed by 19 eruptive events between March 23 and April 4, of which at least 16 generated ash plumes with heights of 5-18 km (Schneider and Hoblitt, 2013), forcing the grounding of aircraft at Anchorage airport. On April 4, the eruption entered a phase of continuous lava extrusion and dome building at the summit before ending in July 2009.

Mt. Redoubt is one of 50 historically active Alaskan volcanoes located on the busy North Pacific and Far East Russia air traffic corridors along which at least 70 aircraft, collectively carrying approximately 10,000 passengers, fly daily. Between 1953 and 2009, 129 encounters of aircraft with volcanic ash clouds have been documented (Guffanti et al., 2010), including an incident at Mt. Redoubt in 1989 (Casadevall, 1994). Rapid growth in air traffic has pushed the scientific and engineering community to increase our ability to detect ash clouds (Prata and Tupper, 2009) and constrain the melting characteristics of ash (Song et al., 2014) in order to improve the design of jet engines and mitigate risk (e.g. Drexler et al., 2011). Currently, nine Volcanic Ash Advisory Centers (VAAC) are responsible for issuing warnings of airborne volcanic ash. Advisories are based on satellite imagery and numerical models of atmospheric ash dispersion (Mastin et al., 2009). Whilst numerical models can provide accurate forecasts of atmospheric ash dispersion patterns, they rely on precise knowledge of key eruption parameters such as maximum plume height and mass ejection rates at the vent, which remain loosely constrained.

In recent years the use of acoustic infrasound technology has become commonplace at volcano observatories, in particular to detect eruptions in remote locations (e.g. Caplan-Auerbach and McNutt, 2003; Petersen et al., 2006; De Angelis et al., 2012a) and to measure parameters such as mass eruption rates and plume height (Caplan-Auerbach et al., 2010; Ripepe et al., 2013). A number of studies have focused on estimating gas bubble sizes and gas outflux at the vent during Strombolian-type eruptions (Firstov and Kravchenko, 1996; Ripepe et al., 1996; Johnson, 2003; Vergniolle and Caplan-Auerbach, 2006; Delle Donne and Ripepe, 2012; Gerst et al., 2013; Kremers et al., 2013). In contrast, only a handful of eruptions accompanied by atmospheric injection of vigorous, ash-rich plumes have been investigated to date (e.g. Caplan-Auerbach et al., 2010; Fee et al., 2013; Mastin et al., 2013; McNutt et al., 2013; Ripepe et al., 2013; Matoza and Fee, 2014).

In this paper we combine analyses of infrasound observations with numerical modelling of volcanic plume rise in a realistic atmosphere in order to characterize airborne ash injection during the 2009 eruption of Mt. Redoubt. Our results are confirmed by estimates of plume height obtained from Doppler radar measurements (Schneider and Hoblitt, 2013),

satellite imagery (Webley et al., 2013), and further validated by field observations of tephra fall deposits (Wallace et al., 2013).

## 7.2 Data and methods

Mt. Redoubt is monitored by the Alaska Volcano Observatory (AVO) with a permanent network of eleven seismometers. In addition, one infrasonic microphone, a Chaparral Physics Model 25V (flat response between 0.1-200 Hz), is located 12.2 km NNE of the active vent (McNutt et al., 2013). In March 2009, with an eruption considered imminent, AVO deployed a portable radar system (Electronics Corporation MiniMax-250C Doppler radar) on the Kenai Peninsula, 82 km east of Mt. Redoubt (giving a beamwidth of 2.6 km), in order to monitor eventual ash plumes from the volcano (Schneider and Hoblitt, 2013). The Doppler radar captured all major explosions at Mt. Redoubt, providing unprecedented, high-resolution, images of the associated plumes. A detailed description of the radar scanning strategy can be found in Schneider and Hoblitt (2013). All the explosive events during this eruption were also recorded and measured with low-spatial resolution thermal infrared, mid-infrared, and ultraviolet satellite remote sensing data (Webley et al., 2013). In this study we complement this dataset with an analysis of the infrasound record of two explosions during the 2009 eruption of Mt. Redoubt (Figure 7.1a, c).

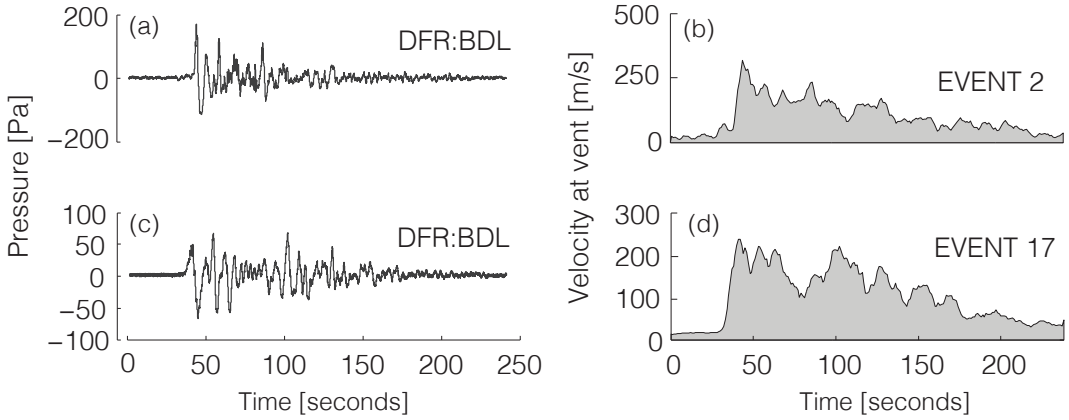


FIGURE 7.1: The recorded infrasound signals, de-trended and high-pass filtered (0.1 Hz) for removal of very long-period noise/drift (left column), and calculated mass velocity profiles (right column) for event 2 (top row), and event 17 (bottom row).

### 7.2.1 Infrasound source velocity model

Fluctuations in air pressure recorded at a distance from a volcanic vent are directly related to acoustic power that, in turn, depends on mass outflux at the source (Woulff and McGetchin, 1976; Caplan-Auerbach et al., 2010). The relationship between acoustic power and eruptive flux, however, is complicated by uncertainties in the source dynamics. Woulff and McGetchin (1976) introduced, within the framework of linear acoustic theory, relationships between velocity and power for three source types: monopole, dipole, and quadrupole. A monopole source is one in which variations in pressure are due entirely to the rate of change of mass flux, and can be envisioned as an isotropically expanding source. A dipole is often used to describe a directional jet or gas flux that interacts with solid walls. A quadrupole best represents a gas source that generates noise through turbulence, such as a jet engine.

For a source that radiates sound as a hemisphere of radius $r$, the relation between recorded pressure $p$ and acoustic power $\Pi$ is given by:

$$\Pi = \frac{\pi r^2 \Delta p^2}{\rho_{air} c} \tag{7.1}$$

where $\rho_{air}$ is air density, $c$ is the speed of sound and $\Delta p$ is the excess pressure. The modelled acoustic power depends strongly on the radiation mechanisms at the source (monopole, dipole, or quadrupole) and is given by one of the following equations:

$$\Pi_m = K_m \frac{4\pi R^2 u^4 \rho_{atm}}{c} \tag{7.2}$$

$$\Pi_d = K_d \frac{\pi R^2 u^6 \rho_{atm}}{c^3} \tag{7.3}$$

$$\Pi_q = K_q \frac{\pi R^2 u^8 \rho_{atm}}{c^5} \tag{7.4}$$

where $K_m$, $K_d$, and $K_q$ are empirically derived constants for specific radiation mechanisms (monopole, dipole, and quadrupole respectively), $R$ is the source radius (i.e. volcanic vent radius), $u$ is the velocity of the material at the source, and $c$ is the speed of sound in air. The value of $K_m$ is of the order of 1, while $K_d$ and $K_q$ are approximately $10^{-2}$ and $10^{-5}$, respectively (Woulff and McGetchin, 1976).

Following Caplan-Auerbach et al. (2010) we favour a dipole source for the explosions at Mt. Redoubt. The presence of conduit walls exerting a force on the erupting gas, the interaction of gas with solid particles within the flow, and the interaction of the infrasound waves with the crater walls around the vent (Bull and Buurman, 2013) can be approximated by a dipole radiation model. In our calculation of acoustic power we consider the speed of sound in air to be 320 m $s^{-1}$ (Table 7.1; McNutt et al., 2013).

For each of the eruptive events considered the infrasound records are pre-filtered between 0.1 and 25 Hz, above the low frequency cut-off of the sensor and in a frequency band that includes the dominant energy of the signal (Figure 7.2). Piecewise linear detrending is also applied in order to remove undesirable effects of very long-period instrument drift (Johnson and Miller, 2014). We then calculate a 2-second average of the acoustic power from the infrasound time series using eq. 7.1 and invert eq. 7.3 to retrieve the time-history of mass velocity at the vent. The peak value of velocity provides the input for a numerical model of plume rise.

TABLE 7.1: Variables and values used in calculations for gas velocity and plume modelling for the explosions recorded at Mt. Redoubt volcano in 2009.

| **Gas velocity modelling** | | | |
|---|---|---|---|
| Variable | Definition | Value/units | Reference |
| $u$ | Eruption velocity | (Calculated, see below) | |
| $\Pi$ | Acoustic power | (Not calculated) | |
| $\rho_{air}$ | Air density | 1.4 kg $m^{-3}$ | |
| $c$ | Speed of sound | 320 m $s^{-1}$ | McNutt et al., 2013 |
| $\tau$ | Source duration | 2 s | |
| $K_d$ | Dipole source empirical constant | $10^{-2}$ | Woulff and McGetchin, 1976 |
| $R$ | Volcanic vent radius | 30 m | Wessels et al., 2013 |
| $r$ | Source-receiver distance | 12.2 km | McNutt et al., 2013 |
| **Plume modelling** | | | |
| | Parameter | Value/units | Reference |
| | Vent longitude and latitude | 60.48°, -152.74° | |
| | Vent elevation | 2400 m | |
| | Gas mass fraction | 0.03 | Mastin et al., 2013 |
| | Source temperature | 1173 K | Mastin et al., 2013 |
| | Solid pyroclastic density | 1200 kg $m^{-3}$ | Mastin et al., 2013 |
| | No-wind train coefficient | 0.09 | Woodhouse et al., 2013 |
| | Wind entrainment coefficient | 0.9 | Woodhouse et al., 2013 |
| | Calculated peak eruption velocities | Event 2: 315 m $s^{-1}$<br>Event 17: 251 m $s^{-1}$ | |

### 7.2.2 Plume rise model

We use the *PlumeRise* model of Woodhouse et al. (2013) to estimate the maximum plume height. This model provides a quantitative, 3-dimensional, description of the rise of volcanic ash columns in a moist and windy atmosphere, and is based on the fluid dynamics of turbulent buoyant plumes. The model includes a description of the thermodynamics of heat transfer between hot pyroclasts and the surrounding magmatic and atmospheric gases. *PlumeRise* allows assessing the effects of a variable atmosphere on volcanic plume

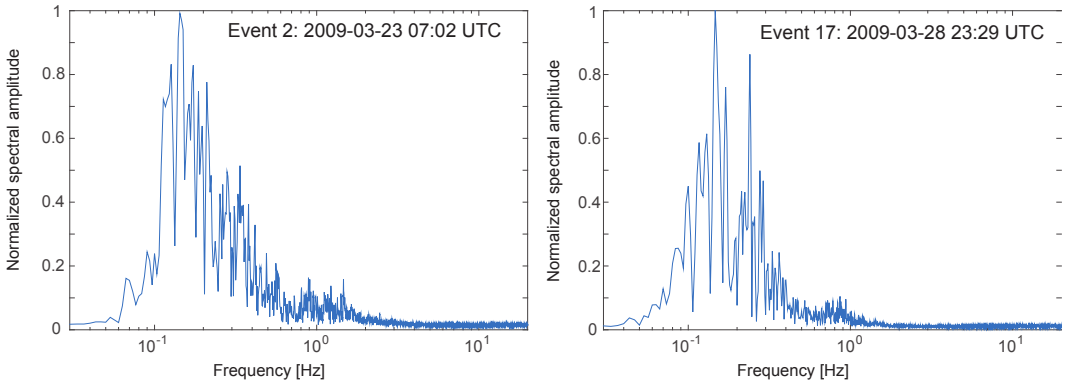


FIGURE 7.2: Frequency spectra of infrasound signals of explosions from Mt. Redoubt on March 23, 2009 07:02 UTC (left) and March 28, 2009 23:29 UTC (right).

rise and includes a description of the thermodynamics of phase changes of water. The effect of a cross wind on the plume ascent is accounted for, using the entrained formulation of Hewett et al. (1971). For atmospheric conditions, we used soundings measured above Anchorage, 168 km north-east of Mt. Redoubt, recorded at intervals of 6 or 12 hours (http://weather.uwyo.edu/upperair/sounding.html; last accessed 21/09/2015). For comparison, we also estimated the plumes using the US Standard Atmosphere (U.S. Standard Atmosphere, 1976, U.S. Government Printing Office, Washington, D.C., 1976), which is characterized by a piecewise linear temperature profile with height and hydrostatic pressure balance.

For each event analysed, we use the atmospheric sounding measurement taken nearest to the time of the event; additional parameters employed in the plume model along with their sources are listed in Table 7.1.

## 7.3 Results

We analysed infrasound signals for two explosive events during the eruption of Mt. Redoubt; events 2 and 17 (following the classification of Bull and Buurman, 2013, Figure 7.1a,c). Event 2 (7:02 UTC, 23 March) was the first large explosion in the crisis, accompanied by strong seismic and infrasound signals, and a measured plume height of 14 km (McNutt et al., 2013). From the infrasound signal, we calculated a peak mass velocity of 315 m $s^{-1}$ (Figure 7.1b). Event 17 (23:29 UTC, 28 March) was one of the largest explosions (plume height of 12.5 km) of a group characterised by short durations (3-4 mins). The calculated peak mass velocity for this event was 251 m $s^{-1}$ (Figure 7.1d).

The modelled plumes for events 2 and 17 are presented in Figure 7.3 and Figure 7.4, respectively. Accounting for local atmospheric conditions near the time of the events, including

cross-wind (see Section 2.2), the modelled plumes for event 2 and 17 propagate in the north-east and east directions and reach heights of 13,500 m and 12,000 m, respectively. These estimates are within 500 m of those obtained with the Doppler radar (Schneider and Hoblitt, 2013). Additionally, the direction of propagation (Figure 7.3a, 7.4a) is consistent with the distribution of tephra-fall deposits measured for these events (Figure 7.5; Wallace et al., 2013). Estimated plume distributions calculated using the US Standard Atmosphere remain fixed over the vent and overshoot the measured plume heights in excess of 1500 m.

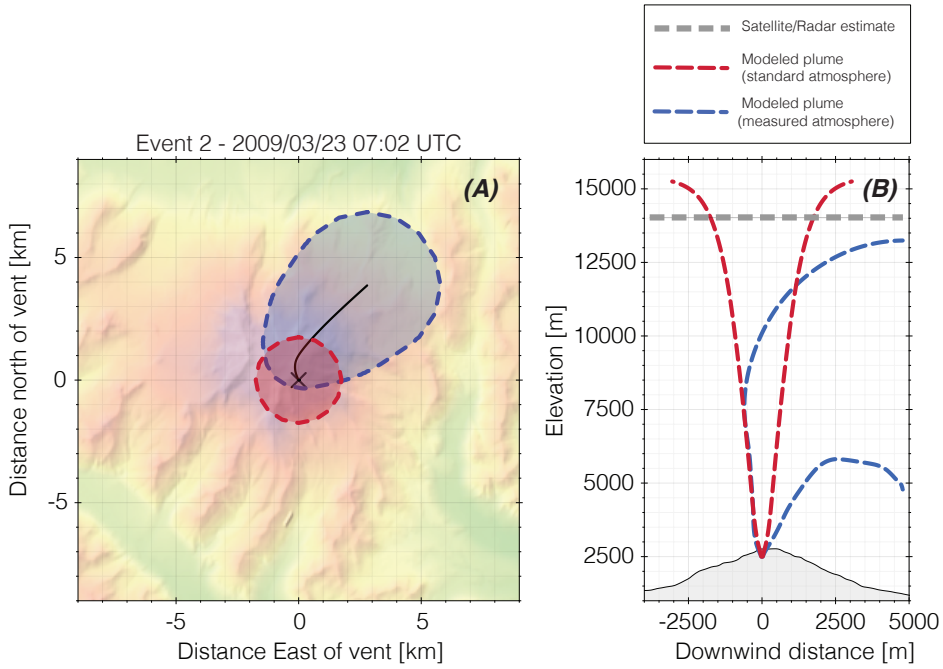


FIGURE 7.3: A plan view (A) and cross-sections (B) of the estimated plumes from event 2. Modelled plume heights in standard atmospheric conditions are plotted with red dashed lines, and those with measured atmospheric conditions are plotted with blue dashed lines. The plan view is plotted onto a digital elevation map of the Mt. Redoubt area. The cross-section is plotted along the black line in (A), that is the direction of the prevailing wind during the eruption. Observed plume heights (grey dashed line) were measured with satellite imagery (Webley et al., 2013) and Doppler radar (Schneider and Hoblitt, 2013).

## 7.4 Discussion

Numerical models of ash dispersion rely on estimates of initial plume height and mass eruption rates which remain, thus far, poorly constrained. The methods presented here provide a

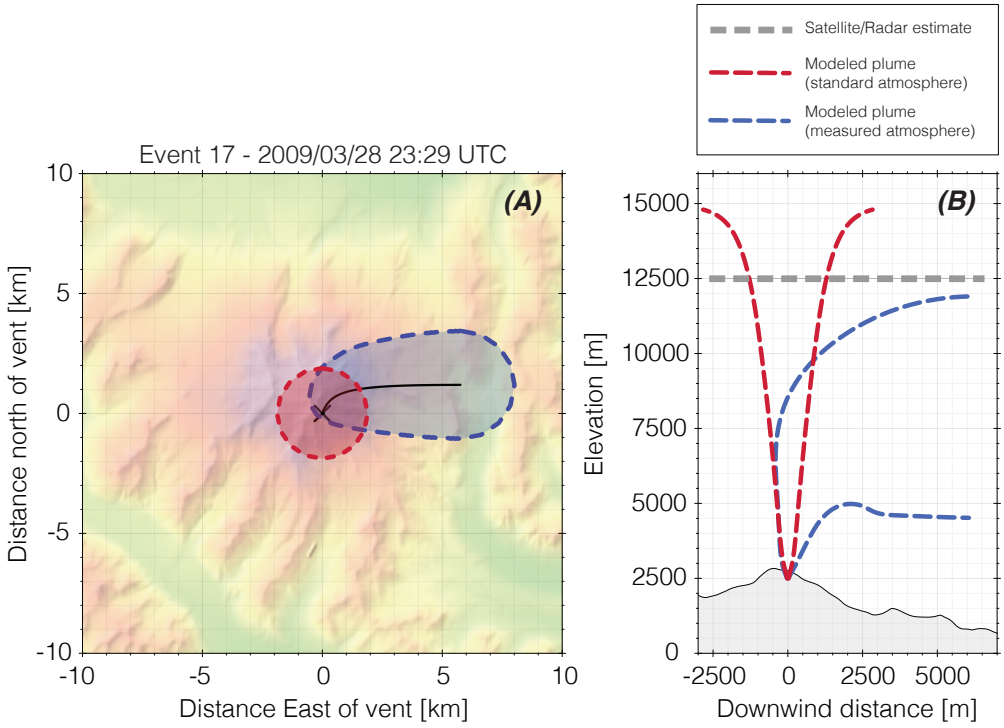


FIGURE 7.4: A plan view (A) and cross-sections (B) of the estimated plumes from event 17. Modelled plume heights in standard atmospheric conditions are plotted with red dashed lines, and those with measured atmospheric conditions are plotted with blue dashed lines. The plan view is plotted onto a digital elevation map of the Mt. Redoubt area. The cross-section is plotted along the black line in (A), that is the direction of the prevailing wind during the eruption. Observed plume heights (grey dashed line) were measured with satellite imagery (Webley et al., 2013) and Doppler radar (Schneider and Hoblitt, 2013).

means to infer eruption source parameters from acoustic measurements. Our plume height estimates at Mt. Redoubt expand on previous 1D modelling work by Mastin et al. (2013) for event 5 of the same eruption, who applied a 1D plume rise model assuming a velocity at the vent of 150 m $s^{-1}$. One fundamental difference between our model and previous work by Mastin et al. (2013) is the value used for mass velocity at the vent. They inferred a mass velocity using mapped erupted mass (Wallace et al., 2013) and measured eruption durations, whereas we used a value based on the analysis of infrasound data. Additionally, our model estimates 3D plume propagation with results in excellent agreement with the mapped distribution of tephra-fall deposits (Figure 7.5). Mastin et al. (2013) also successfully mapped the distribution of tephra from event 5, using a 3D tephra and ash dispersal model (Ash3d; Schwaiger et al., 2012). Ash3d parameters include the total erupted mass and the total grain size distribution, which may not be accurately constrained until after the end of an eruptive event.

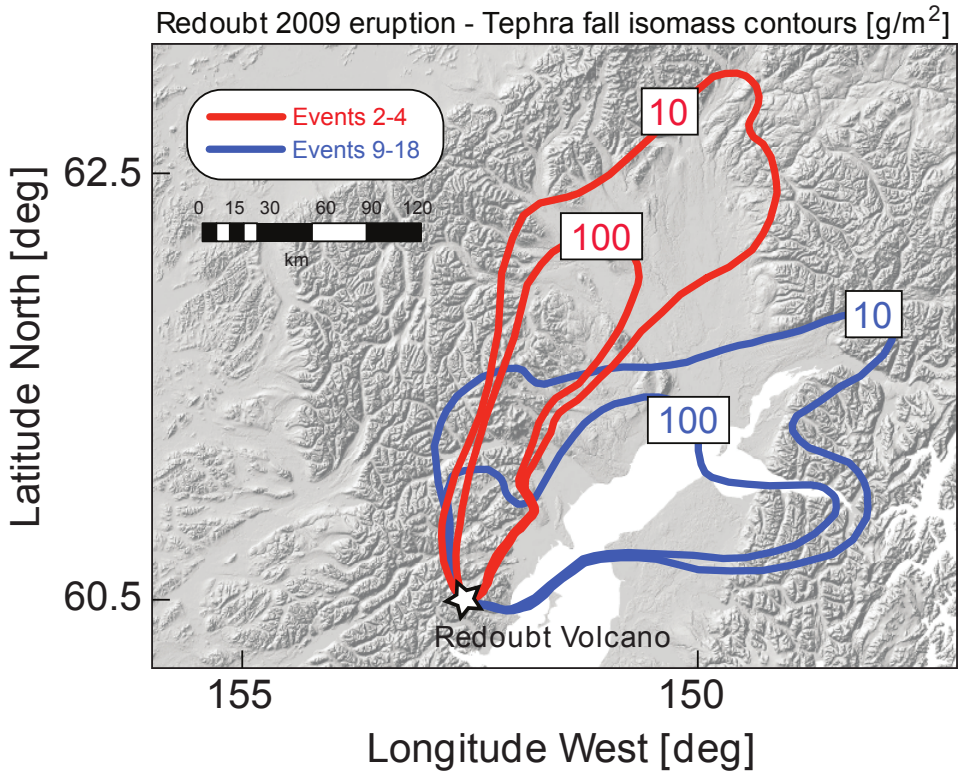


FIGURE 7.5: Regional map of the Cook Inlet area, Alaska, showing the distribution of tephra-fall deposits of the 2009 eruption of Mt. Redoubt. Contours show isomass in g $m^{-2}$. Modified with permission from Figure 1 of Wallace et al. (2013); digital contour data available from Schaefer and Wallace (2012).

Our model also differs from previous studies at other volcanoes such as Johnson (2007) and Matoza et al. (2009b). The former inferred that a monopole source best described pyroclastic explosions from Karymsky volcano, Russia. The explosions from Karymsky were smaller in time (a few seconds) and scale (plume heights <1 km), suggesting a significantly different source mechanism than at Mt. Redoubt. Matoza et al. (2009b) contended that sustained eruption noise has its source in large scale turbulence, favouring a quadrupole source. However, the eruptions described by Matoza et al. (2009b) generated infrasound signals with durations of hours whereas those at Mt. Redoubt only last for minutes. The vent for the 2009 activity at Mt. Redoubt lies inside a North-facing collapse scar (Bull and Buurman, 2013) which causes infrasound waves to interact with the wall around the vent during eruptions. For this reason a dipole source was deemed the most appropriate approximation for our calculations. Infrasound waveform inversion at Tunguruhua volcano, Ecuador, suggested a dipole source to explain the directivity of the acoustic wavefield (Kim et al., 2012).

One notable feature of the infrasound waveforms recorded at Mt. Redoubt in 2009, are their

unusually high amplitudes and relatively short rise times of the initial pulse. Whilst these observations support an explosion source mechanism rather than sustained jetting, they also pose questions on the nature of the flow at the vent. For example, for one event McNutt et al. (2013) showed clipped waveforms with a peak pressure of 173 Pa and estimated a full-scale pressure of 244 Pa at the DFR site (corresponding to >3000 Pa at the vent). Such high pressures may imply transonic to supersonic flow conditions at the vent, which would make equations (1-4) not applicable. A non-linear formulation should be considered instead (Marchetti et al., 2013). For instance, employing the Rankine-Hugoniot equations for 1D shock wave theory (e.g., Marchetti et al., 2013) and acoustic pressures between 50-200 Pa (i.e. within a range compatible with values measured at Mt. Redoubt), would result in velocities at the vent in excess of 1000 m $s^{-1}$. However, such high values are not supported by measurements of plume ascent at Mt. Redoubt using Doppler radar (see Figure 6 in Schneider and Hoblitt, 2013). Alternatively, McNutt et al. (2013) suggested that a highly directional flow may provide an explanation for the unusually high infrasound pressures. Furthermore, in the absence of clear observational evidence of supersonic flow, we assume that non-linear dynamics may be restricted to the near-vent region, and consider that the equations of linear acoustics represent a suitable first-order approximation for the purpose of our investigation.

Our calculations are dependent on the assumption that the infrasound source is best described by a pure dipole. To test this assumption, we repeated our workflow using monopole and quadrupole sources instead. The peak velocities for events 2 (107 and 620 m $s^{-1}$) and 17 (65 and 486 m $s^{-1}$) using monopole and quadrupole sources are too low or high when compared with values estimated from field observations (e.g. Doppler radar). We acknowledge that the ideal strategy to constrain eruption velocities would be inverting for a multipole source model where monopole, dipole, and quadrupole mechanisms contribute to the radiated acoustic wavefield. Kim et al. (2012) recently proposed a waveform inversion method that represents volcano acoustic sources as the combination of multipole terms (i.e. monopole and dipole) and employs analytical Green's functions in a half-space to model atmospheric sound propagation. Waveform inversion would allow an accurate estimate of time history of mass outflow at the vent and the systems of forces active at the source. However, this type of inversion requires data from multiple sensors, which were not available during the 2009 eruption at Mt. Redoubt. The most significant limitation of models used to characterise the propagation of volcanic infrasound is the use of equations (7.2, 7.3, 7.4) that are based on simplified Green's functions for a homogenous and isotropic free space. Calculations based on these relations rely on the implicit assumption that wave amplitude decays as an inverse function of distance from source. In this and previous studies, the effects of variable atmosphere, vent geometry, and the local topography on the propagation of infrasound are neglected. Numerical techniques such as finite-difference time-domain can be employed due to their ability to handle complicated phenomena in infrasound propagation, thus allowing inclusion of the effects of topography (Lacanna and Ripepe, 2013;

Lacanna et al., 2014; Kim et al., 2015).

Plume heights of the events in 2009 were assessed using satellite imagery (Webley et al., 2013) and Doppler radar measurements (Schneider and Hoblitt, 2013). Airborne ash was detected by satellites some time after each event. By tracking cloud top temperatures, Webley et al. (2013) were able to estimate plume heights. Their estimates generally fall below measured heights from radar and our estimates. As these measurements were taken some time after the eruptive event, the ash cloud had undoubtedly begun to disperse and cool, leading to apparently lower cloud-top heights. Our estimates fall close to Doppler radar measurements (Schneider and Hoblitt, 2013), demonstrating the strength of the *PlumeRise* model used. In our calculations, we used parameters calculated a-posteriori for each of the events (Table 1). If the proposed methodology is to be used for near real-time assessment of eruptive plumes during future volcanic crises, a number of parameters (e.g. vent radius, gas mass fraction, source temperature, pyroclast density) will need to be estimated based on previous eruptions.

At other volcanoes, eruptive plume heights have been estimated using other geophysical methods. Using data from Kasatochi and Augustine volcanoes, Alaska, Prejean and Brodsky (2011) demonstrated how the amplitude of explosion-sourced seismicity can be related to the mass ejection rate via force-balance equations. However, the method is limited to using a range of ejection rates and requires clear, noise-free signals from multiple stations located around the eruptive centre. Additionally, due to strong attenuation effects, the method is limited by the size of the explosion and the proximity of the seismometers. In Iceland, real-time GPS and tiltmeter measurements were demonstrated to correlate with plume heights during the 2011 eruption at Grímsvötn (Hreinsdóttir et al., 2014). Again, this method is limited by requiring instruments located close (<10 km) to the eruptive centre as deformation signals can degrade quickly with distance from the pressure source. At present, there is no methodology that provides alone a consistent solution to the problem of estimating mass eruption velocities, or ash plume heights. A multi-parameter, integrated approach should be employed to better constrain eruption dynamics.

A number of simplifying assumptions in our approach mean that we cannot fully replicate the complexity of a natural atmospheric system. However, a workflow based on this relatively simple proof-of-concept would require low computational resources, and results could be available in near real-time. The method proposed here requires few parameters to provide a rapid estimate of ash plume height. Furthermore, recent developments in both infrasound technology and numerical modelling mean that waveform inversion for more complex source mechanisms along with the use of more realistic Green's functions may soon be commonplace. We surmise that acoustic infrasound holds potential to provide accurate near-real time estimates of eruption source parameters such as mass flux rates and maximum plume height required in risk mitigation strategies.

## 7.5 Conclusions

Infrasound can provide detailed constraints on the timing, duration, and relative intensity of local and remote explosive volcanism, and can be used for early eruption warning. For the aviation industry, a timely issuing of airborne volcanic ash warnings is vital to avoid encounters between aircraft and ash clouds. Whilst numerical models can provide detailed forecasts of atmospheric ash dispersion patterns, they rely on accurate knowledge of key parameters such as initial plume height and mass eruption rates, which remain loosely constrained.

In this study we have presented a proof-of-concept which incorporates the analysis of infrasound data recorded during two explosive events during the 2009 eruption at Mt. Redoubt, USA. Using simple analytical models that describe infrasound radiation at the vent, we have calculated the flux of material ejected from the volcanic vent during each event. The flux measurements were then incorporated into an ash plume rise model, to calculate the maximum height of the eruptive column, and assess its atmospheric dispersal. By comparing the results of our calculations to Doppler radar and satellite measurements, we demonstrated the potential of this and similar methods to obtain accurate estimates of plume heights within seconds of a volcanic explosion. The main implication of our results is that key eruption source parameters can be quickly and accurately quantified. Incorporation of infrasound based eruption source parameters into ash transport modelling workflows holds the potential for more efficient forecasts of volcanic ash cloud dispersion.

# Chapter 8

# Conclusions

In this project I have shown how a multi-disciplinary approach can overcome individual method limitations to contribute to our understanding of dome-forming eruptions. This approach has allowed me to make insights into dynamics processes such as pre-eruptive seismicity, lava spine formation, changes in activity, and calculating ash plume heights. To conclude, I will outline how we have addressed the key aims and objectives as highlighted in section 1.2, before summarising potential future directions in research on these processes.

## 8.1 Response to project aims

In Chapter 4 I demonstrated how using a multi-disciplinary approach can produce more robust interpretations of sub-surface processes occurring during magma ascent. Seismic data recorded during the 1998 eruption of Volcán de Colima, Mexico, was analysed for repeating earthquakes and seismic velocity changes. Over 500 groups of repeating earthquakes were identified and a $\sim$0.2% decrease in velocity was calculated prior to the eruption on 20 November 1998. Similar features were detected from natural and artificial acoustic emissions during Brazil tensile tests on samples of andesite from Volcán de Colima. A decrease in elastic velocity, independent of sample porosity, is observed prior to complete failure. The occurrence of repeating acoustic emissions during a Brazil test appears to be related to the sample porosity. I demonstrate how this observation provides evidence for tensile failure as a viable mechanism for natural repeating earthquakes at volcanoes.

One major topic of debate within volcano-seismology centres on the source process for repetitive, shallow long-period earthquakes, such as those recorded at Mount St Helens during its 2004-2008 eruption (e.g. Iverson et al., 2006). Some investigations have inferred the cyclic collapse and recharge of pressurised hydrothermal cracks (e.g. Waite et al., 2008; Matoza et al., 2009a), whereas field, experimental and seismic studies have inferred repeated slow-rupture failure of volcanic materials along the margins of an ascending plug (e.g. Iverson et al., 2006; Iverson, 2008; Kendrick et al., 2012). At Unzen volcano, seismic data from the last phase of the 1991-1994 eruption recorded the ascent and extrusion of a lava spine.

In Chapter 5, two strong, cyclic groups of repeating earthquakes are identified from a catalogue of earthquakes, and interpreted as repeated fracturing events at the margin of the spine. Further analysis of the seismic data using coda wave interferometry and singular value decomposition, combined with previous field and experimental observations, helped produce a conceptual model that illustrates how late-stage densification of the spine can affect the repeating earthquake source locations.

Santiaguito dome complex is a persistently active lava dome located in western Guatemala. In Chapter 6, the first long-term seismo-acoustic dataset collected at the volcano is described and preliminary analysis is carried out. The dataset captures a major and unprecedented transition in activity at the volcano. Regular, gas-rich, and low-energy explosions are replaced by irregular, gas-rich, and highly energetic explosions which are often accompanied by pyroclastic density currents. Using the seismo-acoustic dataset, the rate and energies of the explosions can be tracked, providing insights into the source dynamics within the conduit. Furthermore, changes in the arrival times of the seismic and acoustic waves suggests that a small portion of the larger explosions originate at a greater depth in the conduit. Ultimately, this study highlights the importance of collecting long-term, multi-disciplinary datasets for understanding the dynamics of persistently active volcanoes.

For the aviation industry, timely warnings of airborne volcanic ash is vital for avoiding encounters between aircraft and ash clouds. Infrasound offers the potential to provide detailed constraints on the timing, duration, and relative intensity of local and remote volcanic explosions. In Chapter 7, I have presented a proof-of-concept which incorporates infrasound with numerical models to estimate ash plume heights during volcanic explosions. To illustrate the method, this study used data recorded during the 2009 eruption of Mt. Redoubt, USA. Using simple analytical models, we can estimate the flux of material ejected from the volcanic event during an explosion. The flux was then incorporated into a three dimensional ash plume rise model to calculate the maximum height of the eruptive column. Our estimations lie close to the heights measured via doppler radar and satellite images during each explosion. This study has demonstrated how infrasound and numerical models holds the potential for more efficient estimations of volcanic ash cloud heights and dispersal.

## 8.2 Study limitations and future directions

As detailed above, this project has highlighted some significant findings and implications for the monitoring of active lava dome volcanoes. However, due to the limitations of each study and the methods chosen, there are many possible further lines of investigation, as detailed below.

First, in Chapter 4 I have compared the results from seismic and experimental investigations to help interpret sub-surface processes occurring prior to an eruption at Volcán de

Colima in 1998. However, the interpretation was based on a qualitative comparison instead of a more robust quantitative one. Furthermore, the experiments were carried out at room temperature and ambient atmospheric pressure which are not representative of the higher temperature and pressure conditions found at shallow depth beneath a volcano. Further work is needed to generate a more unified model between the two sets of observations. For example, one can look for repeating acoustic emissions recorded during high temperature, triaxial compressive environments (e.g. Smith et al., 2009). For Volcán de Colima, the experiments only used andesitic lava as a representative for the whole volcanic edifice. Further experiments on a wider range of volcanic rock types from a variety of volcanoes would help to constrain the applicability of our observations.

The long-term seismo-acoustic dataset described and analysed in Chapter 6 demonstrated its value by helping to constrain what occurred during a period of unprecedented activity at the volcano in 2015-2016. However, there are several drawbacks to the collection and analysis of such long-term datasets. The deployment of the instrument network around Santiaguito was a technically challenging endeavour, requiring a large team of researchers and assistants to help out. Furthermore, due to the tropical environment and extremely rugged terrain, keeping remote stations running for more than a few months proved to be very difficult. These situations call for the construction of improved, lightweight, more compact instruments and equipment. A good example of the future direction for monitoring stations is the BENTO system, a highly-portable, low-cost, rapidly deployable and autonomous collection of instruments (Roman et al., 2014).

A common issue with analysing long-term datasets is how to efficiently and accurately pick out the relevant information, such as different types volcanic earthquakes. A number of automatic systems have been developed to resolve this issue (e.g. Beyreuther et al., 2008; Lara-Cueva et al., 2016) but these systems commonly have several drawbacks. Firstly, they often require a large amount of computing power which may not be affordable for many monitoring agencies. Secondly, the method used is often built and tested for a particular volcano and as such, it can be difficult to reapply it at another volcano. Furthermore, they are sometimes built to detect a particular type of earthquake which may not be useful for monitoring or general analysis purposes. Further work is needed to produce a cheap, efficient, and universal system that can be customised for any volcanic system and monitoring network around the world.

At Santiaguito dome complex and Mt. Redoubt (Chapter 7), acoustic data was used to study the source dynamics of volcanic explosions. A major limitation with each investigation was assuming that the effects of topography on the acoustic waveform were minimal. It has been shown that anomalous amplitudes of acoustic waveforms recorded around active craters is strongly influenced by the topography between the source and the receiver (e.g. Kim and Lees, 2011; Lacanna and Ripepe, 2013). At Mt. Redoubt, accounting for this effect may not alter our results dramatically because there was a direct line of sight between the

eruptive vent and the acoustic instrument. At Santiaguito however, the steep topography of the domes and the surrounding area will need to be accounted for before accurate source inversion of the acoustic data is carried out.

Using infrasound to calculate ash plume heights at Mt. Redoubt assumed that the explosion source can be best represented as a pure dipole source. As discussed in section 7.4, a more ideal and more accurate approach would be inverting for a multipole source model (e.g. Kim et al., 2012). However, this approach requires an extensive network or array of acoustic instruments deployed around the volcano, which was not possible at Mt. Redoubt but may be possible at Santiaguito dome complex. Future work should build on the Mt. Redoubt study by extending the workflow to include multipole source inversion. Furthermore, this workflow should be tested for small, repetitive explosions such as those at Santiaguito dome complex, or for infrasound recorded from far-field eruptions.

# Appendix A

# Overview of seismic and infrasound analytical methods

In this appendix, I will give an overview of the analytical methods used for the seismic and infrasound data in this project. A vast majority of the calculations were carried out within Matlab, using toolboxes tailed for large datasets: GISMO (Reyes and West, 2011) and CORAL (Creager, 1997).

## A.1 Seismic

Seismometers record the motion of the ground during an earthquake. Early designs employed a set-up where the motion of a magnet, attached to a mass and suspended by a spring, induces voltage in a coil; the recorded voltage is proportional to the velocity of the mass during Earth motion. Modern instruments use a more sophisticated set-up and are designed to achieve an even response to earth motions over a wide range of amplitudes and frequencies. The most commonly used instrument are dubbed broadband seismometers, which use a force-feedback mechanism. This is where a mass is maintained at a fixed position and the seismometer records the force required to keep this mass at rest; a force directly related to the Earth motion (Shearer, 2009).

### A.1.1 Event detection

During volcanic activity, thousands if not millions of earthquakes may be detected by seismometers purposely deployed around a volcano. Therefore, it is not always feasible to manually pick out each individual volcanic seismic event and classify them. A number of techniques have been developed to scan continuous seismic data and automatically detect individual earthquakes. The simplest method, the amplitude threshold trigger, scans the continuous data and records times when the ground motion rises above a chosen threshold (e.g. Roman et al., 2016). Nevertheless, simple methods can often under or overestimate the

number of seismic events present; e.g. noise from anthropogenic sources may be included. As a result, more complex methods have been developed to detect and/or classify real seismic signals and filter out spurious signals. This includes methods that use Continuous Hidden Markov Models (e.g. Beyreuther et al., 2008), principal component analysis (e.g. Unglert and Jellinek, 2017), or machine learning (e.g. Lara-Cueva et al., 2016). However, these more complex methods are often tailored for specific types of seismic events (e.g. Tremor; Unglert and Jellinek, 2017) and/or are computationally intensive. During this project, I used two relatively simple techniques: STA/LTA and envelope detection. Below, I have described how each technique works and discuss their advantages and limitations versus other methods.

**STA/LTA**

The short-term average/long-term average (STA/LTA) method is one of the most commonly used methods for detecting seismic events from continuous data (e.g. Matoza et al., 2009b; De Angelis et al., 2012a; Surono et al., 2012; Ketner and Power, 2013; Eyre et al., 2015). In this project, I use it to detect events at Volcán de Colima (Chapter 4) and Unzen volcano (Chapter 5). The method uses two moving windows, one longer than the other, to calculate the ratio of average amplitude in the shorter window over the longer. A seismic event is 'detected' when this ratio crosses a chosen threshold value. The values chosen for the window lengths and the threshold will decide how many events are 'picked' from the continuous record (Fig. A.1). For a ratio threshold of 2, a 1/5 short/long window length ratio successfully detects four seismic records from a sample waveform (Fig. A.1a), whereas a 5/15 ratio misses the smallest of the four earthquakes (Fig. A.1b). However, with a ratio threshold of 4, only the two largest events are detected for the 1/5 window ratio and no events are detected with a window ratio of 5/15. This highlights the importance of parameter choice when using the STA/LTA method for detecting events from a seismic record.

Two slightly different approaches with the STA/LTA method were used for the Volcán de Colima and Unzen studies. The former used a multi-station approach, whereas the latter detected events recorded at only one station. The multi-station technique runs a the STA/LTA method on seismic data from multiple stations and earthquakes are 'picked' when they are detected at a chosen number of stations, assuming a reasonable time window for waves to reach all stations. This improves the detection of earthquakes as it reduces the chance of 'picking' noise that may only be detected at one or two stations. However, the single-station approach can improve the chronology of earthquakes as it can include volcanic events that are not large enough to be detected at multiple stations. At Unzen, I used a multi-parametric filter to remove the false triggers that might otherwise have been filtered out by the multi-station approach (see section 5.2.2).

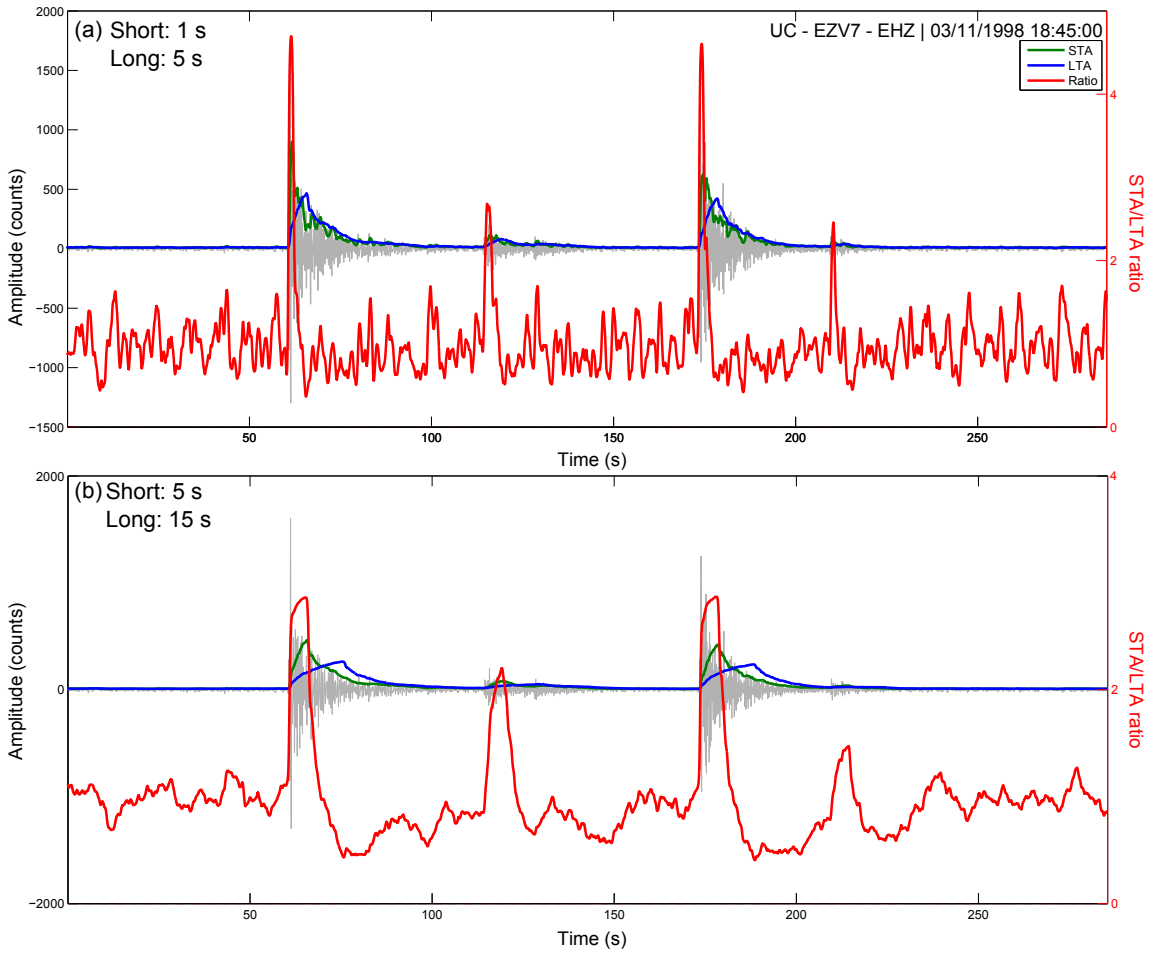


FIGURE A.1: The STA/LTA ratios (red) as calculated from seismic data (grey) recorded at Volcán de Colima on 3rd November 1998 for different window lengths. The average amplitudes calculated in the short (green) and long (blue) windows are also plotted. The lengths chosen for the short and long windows are indicated in each panel. See text for further discussion. For a clearer view of the seismic waveform, see Figure A.3.

### Envelope detection

Waveform envelopes were used to detect explosions in the seismic record at Santiaguito dome complex (Chapter 6). Instead of 'picking' all earthquakes recorded in the seismic data, this method simply looks for sequences of data that match a chosen waveform or shape. In principle, this is similar to how waveform correlation works (section A.1.3) but differs in two aspects. First, this technique matches the 'shape' of the waveform instead of the entire waveform (red line in Fig. A.2). Explosions at Santiaguito dome complex all produced slightly different waveforms due to the complexity of the upper conduit, but still generated the same sequence of energies, thus producing similar shapes. Second, we do not assign the most similar earthquakes into different groups of repeating earthquakes.

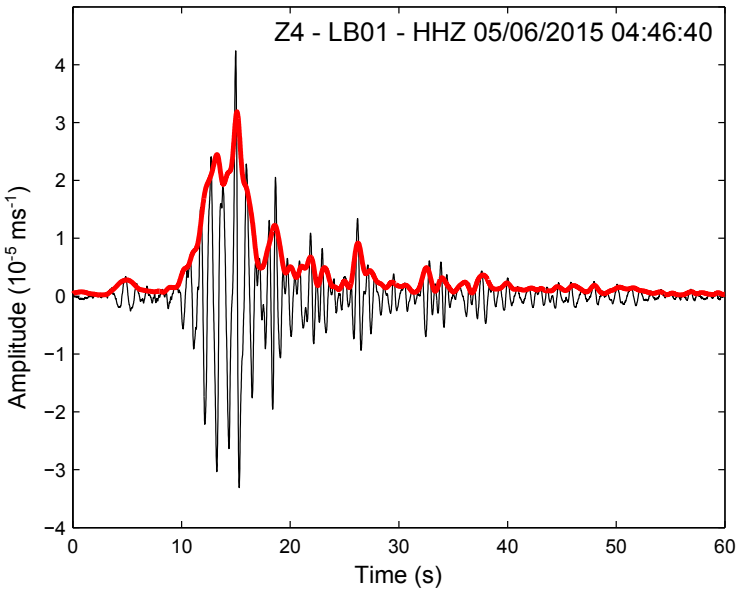


FIGURE A.2: Example of explosion waveform used for envelope detection at Santiaguito dome complex. Station name, channel code, and event date and time (UTC) are indicated.

### A.1.2 Pattern detection

All time-series, including seismic data, collected around volcanoes are inherently non-linear. Superposition of multiple cycles within the dataset can make it difficult to observe and interpret individual signals. The Fourier transform offers a mean of examining the characteristics of a time-series (Danielson and Lanczos, 1942) via the power spectral density (PSD) estimate, highlighting the strength of periodic components in the signal (Percival and Walden, 1993). However, the PSD requires statistical stationarity over the whole time-series; i.e. a relatively stable series that doesn't change in complexity. The Short-term Fourier Transform (STFT) offers a solution by using a series of overlapping PSD estimates from a moving window over the time-series, illustrating the results using spectrograms. An assumption of stationarity is only required within each individual window, making STFT spectrograms useful for tracking changes in frequency content of a time-series. In this project, these techniques have been used for two reasons: describing the frequency content of seismic (Chapters 5, 6) or infrasound waveforms (Chapter 6, 7), and statistical analysis of event counts (Chapter 5).

To produce a spectrogram from a time-series, it is critical to choose an appropriate window length and overlap (Fig. A.3). A window that is too long will not provide a sufficient temporal resolution of the time-series, but if it is too short then a robust calculation of the PSD in each window may not be achieved (Fig. A.3b,c). Too much overlap can risk smearing the spectrogram but too little will provide a poor representation of the frequency changes in the time-series, or even make smaller events invisible (Fig. A.3c - e).

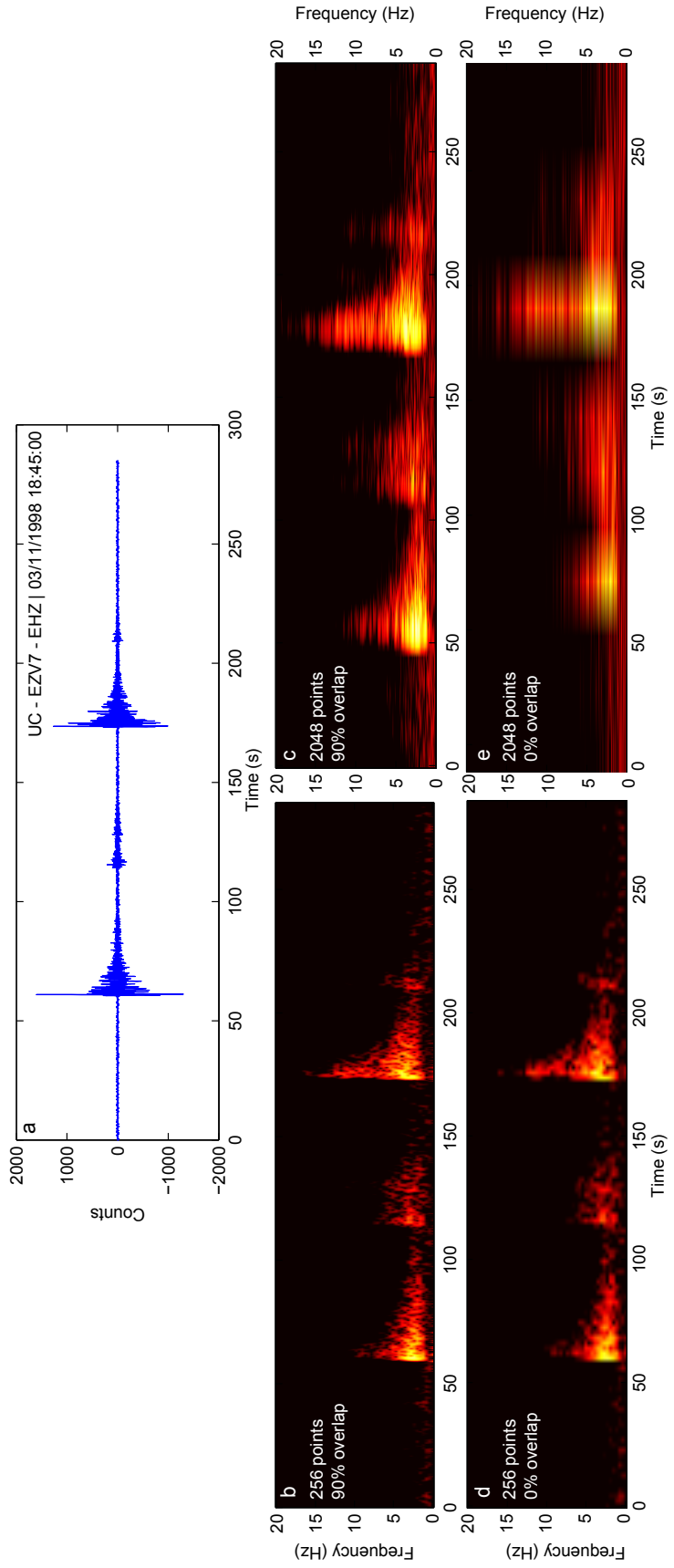


FIGURE A.3: Spectrograms calculated from seismic data recorded at Volcán de Colima on 3rd November 1998 (a); station name, channel code, and event date and time (UTC) are indicated. Each spectrogram (b - e) has been calculated with a different combination of window length (256 or 2048 samples) and overlap (0 or 90%). See text for further discussion.

### A.1.3 Repeating earthquakes

Within a catalogue of earthquakes, repeating events are significant because they represent the product of a repetitive, non-destructive source. They can be used to accurately describe sources of seismicity during volcanic activity, changes in properties of the source, and changes in rock properties between the source and the seismometer. In this project, we describe repeating earthquakes detected in seismic data from Volcán de Colima (Chapter 4) and Unzen volcano (Chapter 5). Unfortunately, as noted by Thelen et al. (2011), previous studies that have described repeating earthquakes (also called multiplets, clusters, or families) have used different methodologies and/or parameters to identify them from their earthquake catalogue. However, they generally use the same principle of cross-correlating pairs of waveforms to calculate their highest degree of similarity, or cross-correlation coefficient (CCC). The CCC is usually presented as a value between 0 and 1, where 0 is no degree of similarity and 1 is identical. Differences in methodology arise when choosing how to build the groups of repeating earthquakes, particularly when defining the CCC threshold for allocating two waveforms as matching, and when choosing the minimum waveforms needed to make a group. This is briefly discussed by Thelen et al. (2011) and in this project during my study at Unzen volcano (see Chapter 5, table 5.3, and Appendix C).

### A.1.4 Velocity changes

Seismic waves can provide crucial information on the temporal variation of the mechanical properties of volcanic edifices due to their velocity dependence on stress perturbations. Stress perturbations within a volcano can be caused through a variety of manners: magma movement (e.g. Wegler et al., 2006; Brenguier et al., 2008; Hotovec-Ellis et al., 2015), dynamic stresses from tectonic earthquakes (e.g. Battaglia et al., 2012; Hotovec-Ellis et al., 2014; Lesage et al., 2014; Taira and Brenguier, 2016), fluid saturation (e.g. Grêt et al., 2006; Sens-Schönfelder and Wegler, 2006), or surface-loading of snow (e.g. Hotovec-Ellis et al., 2014; Taira and Brenguier, 2016). There are two approaches for calculating velocity changes in the volcanic edifice: repeating earthquake coda (e.g. Hotovec-Ellis et al., 2014) and noise cross-correlation functions (CCF; e.g. Brenguier et al., 2008). Each method uses a similar principle by measuring differences on waveform coda from two different time periods. The former method uses natural, repeating earthquakes, and the latter uses CCFs built from natural ambient noise. The principle is summarised for noise CCFs by Brenguier et al. (2016) in Figure A.4. The top right waveform represents the symmetric CCF reconstructed from noise correlation. The top left figure represents the travel paths of coda arrivals that originate from scattering in the complex medium. If the medium (e.g. volcanic edifice) experiences a stress perturbation then the travel times are also disturbed ($\delta\tau$, red waveform in lower half of figure). The relative travel time perturbation ($^{\delta\tau}/_{\tau}$) is equal and opposite of the medium relative seismic velocity change between the normal and perturbed state ($^{\delta\tau}/_{\tau} = -^{\delta v}/_{v}$) for

small $\delta v$. By measuring $^{\delta\tau}/_{\tau}$ along the coda of repeating earthquakes or noise CCF, it is thus possible to assess the relative velocity change in the medium.

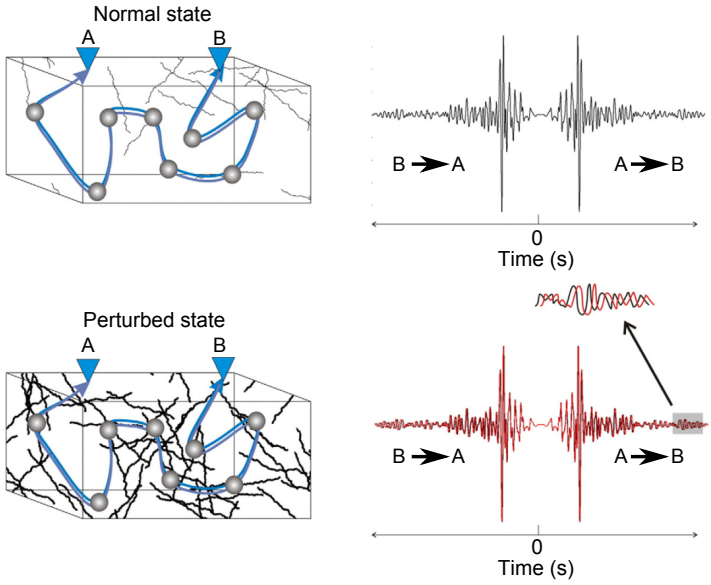


FIGURE A.4: Sketch illustrating the principle of seismic velocity change detection from travel time perturbations in the coda of noise correlation functions. For more details, see main text. Adapted from Brenguier et al. (2016).

## A.2 Infrasound

Specialised sensors are used to detect infrasound. These sensors measure changes in pressure relative to the ambient atmospheric pressure ($\sim 10^5$ Pa at sea level). The amplitude of recorded infrasound signals at volcanoes are generally in the range of 0.1 to 100 Pa (Fee and Matoza, 2013). The sensors and deployed as single sensors, an array, or as part of a wider network. An array is a group of sensors placed in a systematic configuration (<1 km wide) to detect coherent acoustic waves travelling across the set-up. A network consists of multiple sensors deployed around the source at various distances. A key advantage to the array set-up is that noise from wind becomes incoherent between sensors and thus can be filtered out. However, sensor site selection for arrays and networks in low-wind environments, such as dense forests, often prove to be a better solution (Fee and Matoza, 2013).

### A.2.1 Ejection velocities

In Chapter 7, infrasound recorded at Mt. Redoubt volcano in 2009 was used to calculate mass ejection velocity from the eruptive vent. This is based on a relation between the pressure fluctuations recorded by infrasound sensors at a distance and the acoustic power, which in turn depends on the ejection velocity at the vent (Woulff and McGetchin, 1976). However, the relation between eruptive flux and acoustic power is complicated by uncertainties in the dynamics of the sound source. The sound source can be divided into three types: monopole,

dipole and quadrupole (Woulff and McGetchin, 1976). A monopole can be envisioned as an isotropically expanding source (i.e. an explosion). A dipole is often described by a directional jet or gas flux that interacts with solid walls, much like if a sound speaker was set inside a tube. A quadrupole is best represented as a gas source that generates noise through turbulence (e.g. a jet engine).

For a source that radiates sound as an isotropous hemisphere of radius $r$ (i.e. source to receiver distance), the relation between recorded pressure $p$ and acoustic power $\Pi$ is given by:

$$\Pi = \frac{\pi r^2 \Delta p^2}{\rho_{air} c} \tag{A.1}$$

where $\rho_{air}$ is air density, $c$ is the speed of sound and $\Delta p$ is the pressure difference as recorded by the sensor. The modelled acoustic power depends strongly on the radiation mechanisms at the source (monopole: $\Pi_m$, dipole: $\Pi_d$, or quadrupole: $\Pi_q$) and is given by the following functions (Woulff and McGetchin, 1976):

$$\Pi_m = K_m \frac{4\pi R^2 u^4 \rho_{atm}}{c} \tag{A.2}$$

$$\Pi_d = K_d \frac{\pi R^2 u^6 \rho_{atm}}{c^3} \tag{A.3}$$

$$\Pi_q = K_q \frac{\pi R^2 u^8 \rho_{atm}}{c^5} \tag{A.4}$$

where $K_m$, $K_d$, and $K_q$ are empirically derived constants for specific radiation mechanisms (monopole, dipole, and quadrupole respectively), $R$ is the source radius (i.e. volcanic vent radius), $u$ is the velocity of the material at the source, and $c$ is the speed of sound in air. The value of $K_m$ is on the order of 1, while $K_d$ and $K_q$ are approximately $10^{-2}$ and $10^{-5}$, respectively (Woulff and McGetchin, 1976). Thus, despite the exponential effect of velocity, an acoustic sensor deployed at fixed distance from the source would record the same $\Delta p$ for a monopole source with low $u$ and a quadrupole source with high $u$ (Fig. A.5). Alternatively, for a given $\Delta p$ recorded by a sensor, the choice in source dynamics can have a dramatic effect on the calculated $u$.

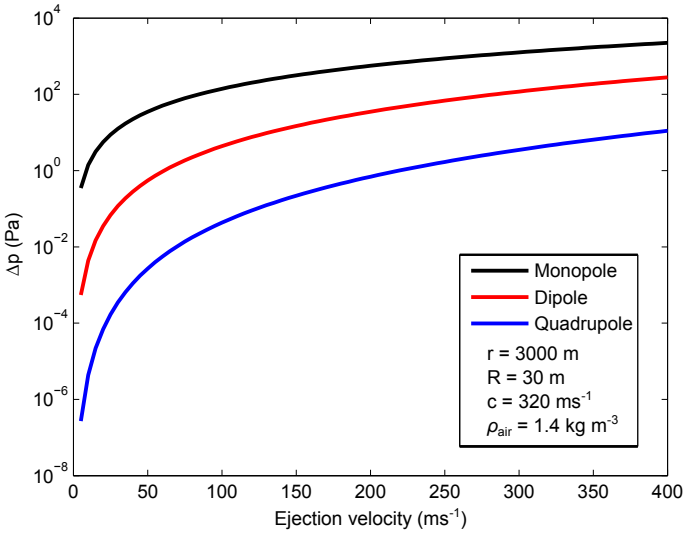


FIGURE A.5: Acoustic pressures as produced by various ejection velocities for monopole (black), dipole (red), and quadrupole (blue) sources. Calculated by inverting equations A.1 - A.4.

# Appendix B

# Seismic and experimental insights into eruption precursors at Volcán de Colima - Supplementary figures

This appendix contains the supplementary figures for Chapter 4 that were originally attached to *Seismic and experimental insights into eruption precursors at Volcán de Colima*, submitted for publication in *Geophysical Research Letters* in March 2017.

Figure B.1 plots the real-time seismic amplitude calculations from seismic data recorded at Volcán de Colima in 1998. Figure B.2 plots the detected clusters if a CCC of 0.7 was used instead of 0.8. Figure B.3 contains the output plots from the MSNoise software package used to produce the relative velocity change measurements at Volcán de Colima. Figure B.4 illustrates the set-up of the Brazil test experiments and figure B.5 contains a compilation of results from all the experiments. Finally, figure B.6 plots the changes in velocity in our Brazil text experiments but using the last pulse as a reference instead.

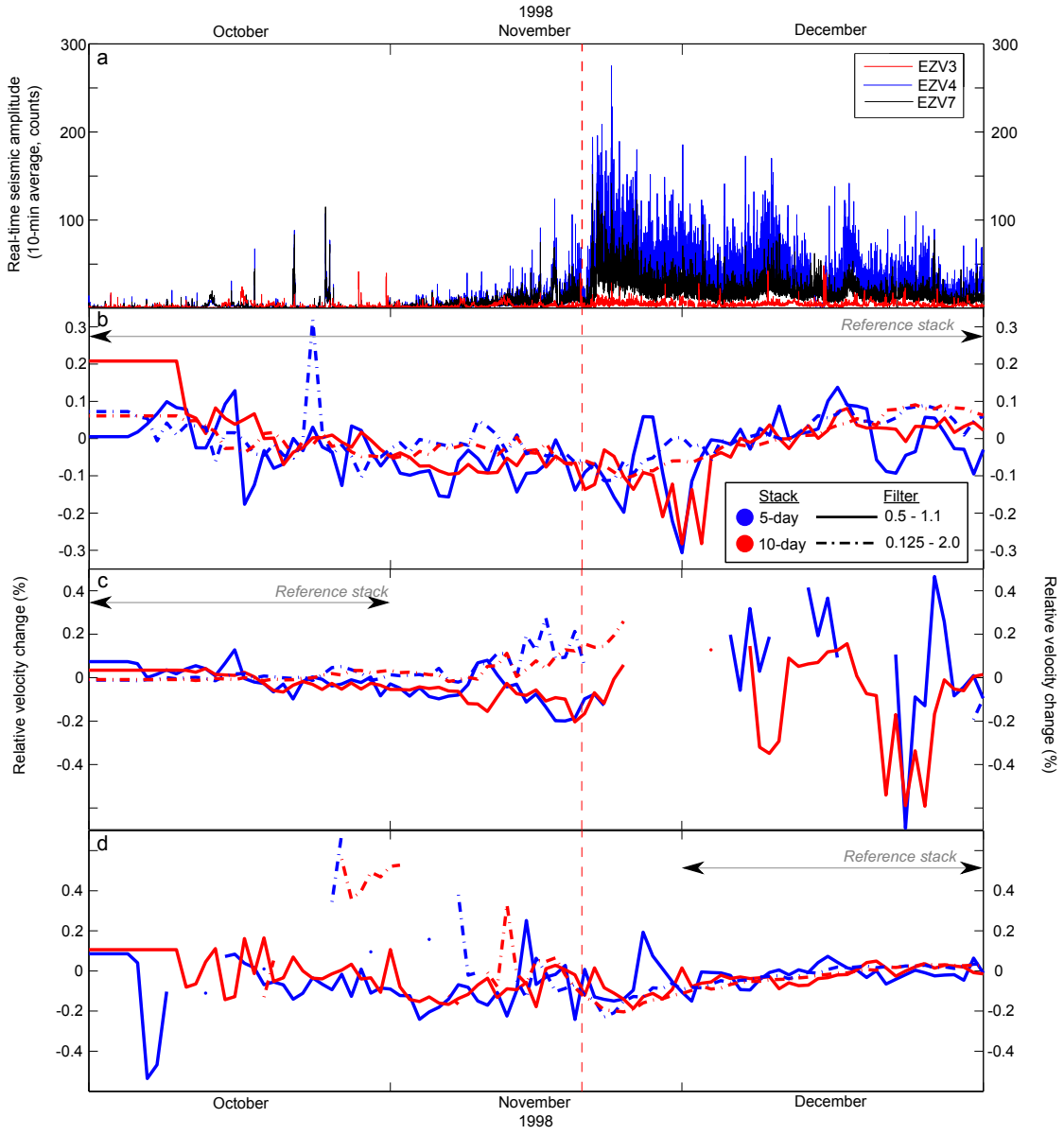


FIGURE B.1: (a) 10-min RSAM values calculated from stations EZV3 (red line), EZV4 (blue line) and EZV7 (black line). The dashed red line represents the beginning of the eruption at Volcán de Colima on 20 November 1998.(b-d) Variations seismic velocity calculated from 5-day (blue) and 10-day (red) moving windows at frequency bands of 0.5-1.1 Hz (solid lines) and 0.125-2 Hz (dot-dashed lines). Each plot represents the seismic velocities calculated using reference stacks built from (b) the whole period, (c) October, and (d) December.

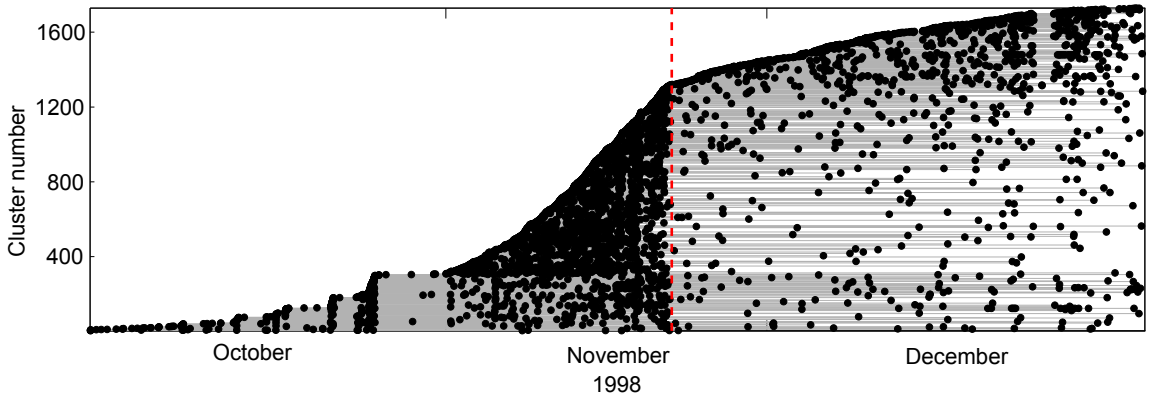


FIGURE B.2: Catalogue of repeating earthquakes (black dots and grey lines) in our dataset from 1 October to 31 December 1998, using a coefficient threshold of 0.7. Each plotted point represents an individual earthquake, and each line joins groups of repeating events. The red dashed line represents the beginning of the effusive eruption at VdC on 20 November 1998.

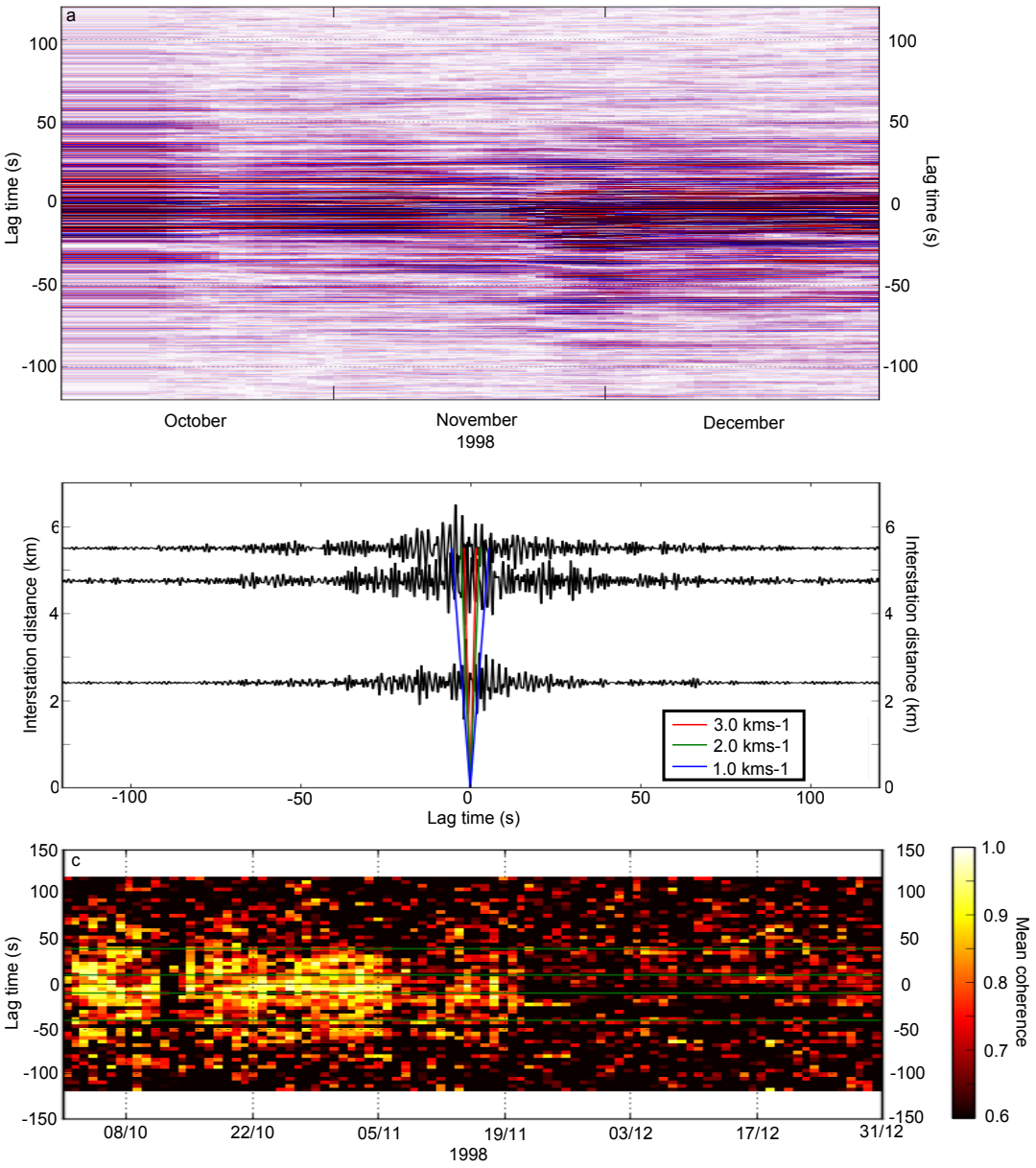


FIGURE B.3: MSNoise output plots at 0.5 to 1.1 Hz frequency. (a) Interferogram of calculated cross-correlation functions for station pair EZV3-EZV7 (b) Reference stacks for each station pair plotted against interstation distance. Blue, red and green lines plot rays travelling at 1, 2 and 3 km $s^{-1}$ respectively. (c) Mean coherence relative to the reference waveform for station pair EZV3-EZV7 for MWCS calculations. Selected time lags (10-40 s) for dt/t calculations are plotted as horizontal green lines.

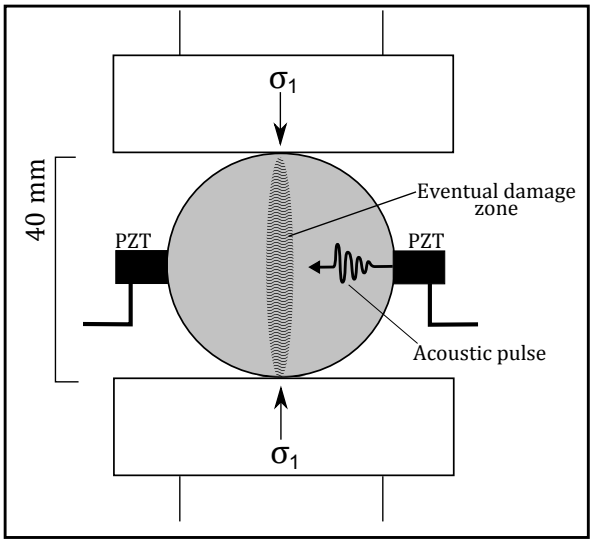


FIGURE B.4: Illustration of the set-up for the Brazil test experiments conducted during this research.

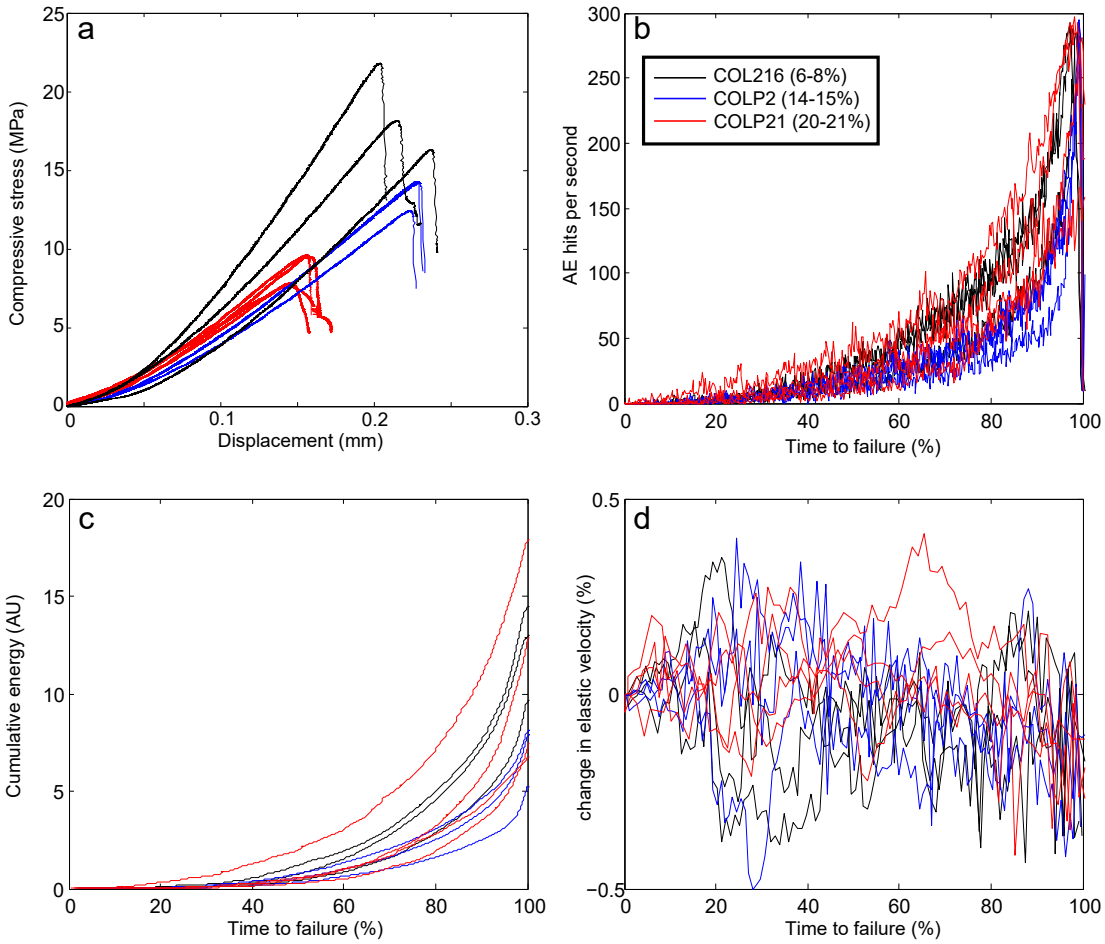


FIGURE B.5: A compilation of results from all experiments carried out on COL216 (black), COLP2 (blue) and COLP21 (red) samples. (a) Displacement vs. stress recorded during the experiment. (b) Number of AEs recorded per second. (c) Cumulative energy of all AEs recorded during the experiment. (d) Change in velocity during the experiments.

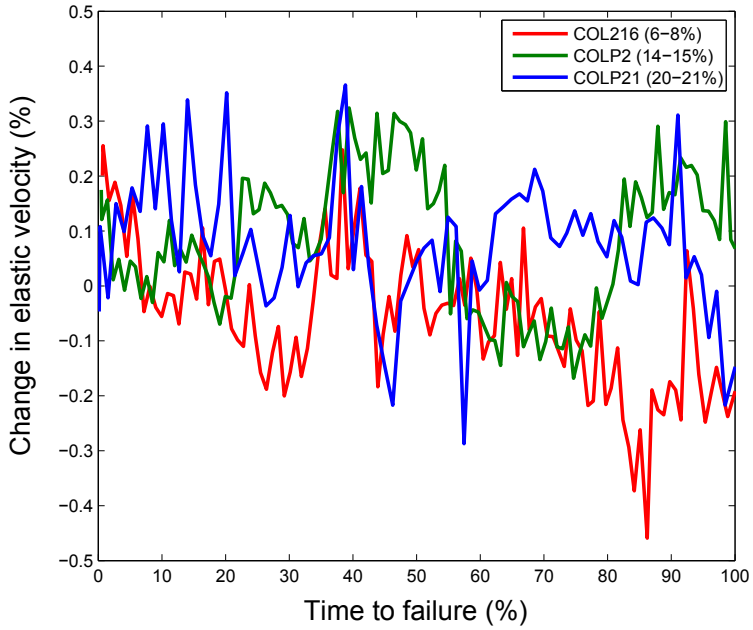


FIGURE B.6: Change in velocity during the experiments, using the last pulse as the reference waveform.

# Appendix C

# Repetitive fracturing during spine extrusion - Supplementary figures

This appendix contains the supplementary figures for Chapter 5 that were originally attached to *Repetitive fracturing during spine extrusion at Unzen volcano, Japan*, published in *Solid Earth* in December 2015.

Figures C.1 and C.2 plot results using different parameters for STFT and CWI methods, respectively. Figure C.3 plots the 10-min average RSAM for seismic data recorded at Unzen in late 1994. Figures C.4 to C.10 plot cluster lifespans resulting from different input parameters for waveform correlation; the parameters used are detailed in the top-left corner of each plot.

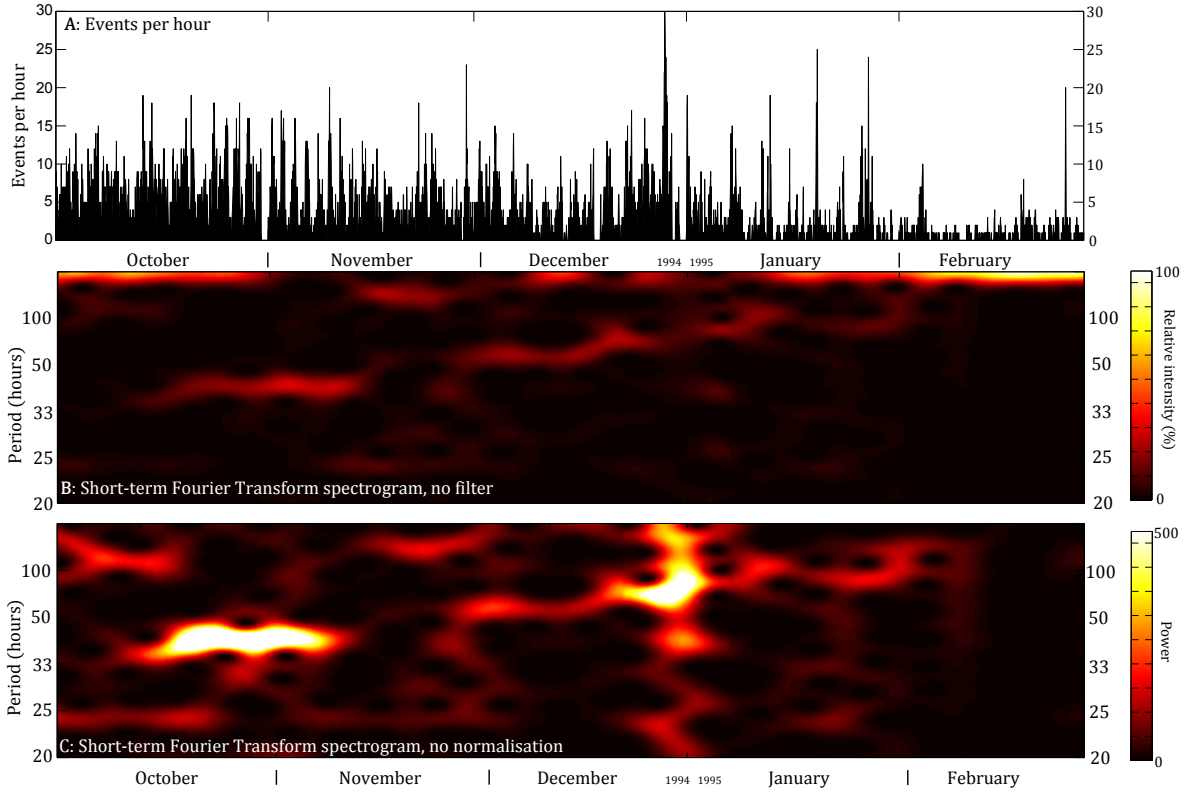


FIGURE C.1: (A) The hourly event record of events detected from continuous data recorded at station FG1 at Unzen from 1$^{th}$ October 1994 to 28$^{th}$ February 1995. (B) The STFT spectrogram for the hourly event count time-series plotted in (A), without any Butterworth filter applied to the time-series. (C) The STFT spectrogram of the hourly event count time-series plotted in (A), without any normalisation applied to each window.

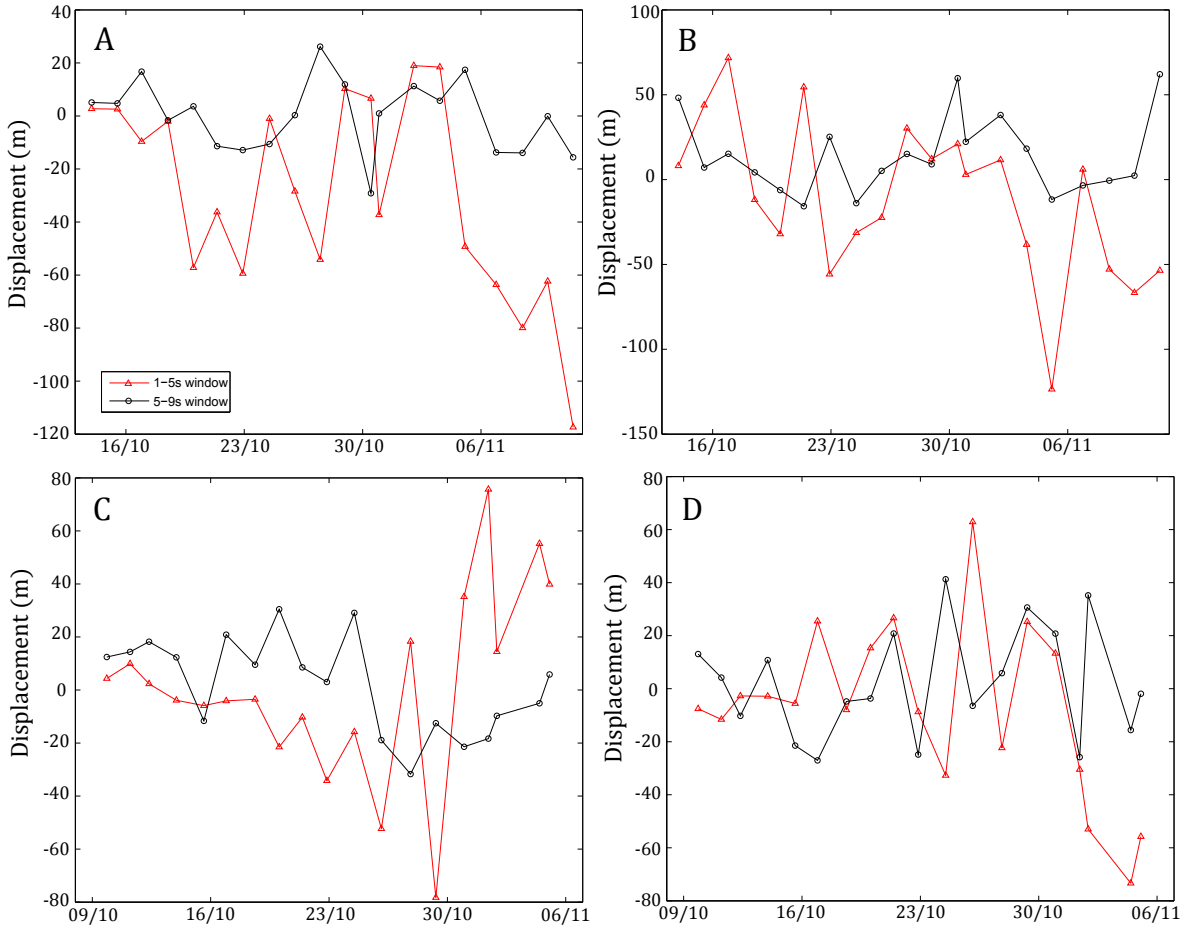


FIGURE C.2: Source displacements between the first stack and all other stacks for data bandpassed between 1-5 Hz (A and C) and 5-10 Hz (B and D) for cluster 1 (A and B) and cluster 2 (C and D).

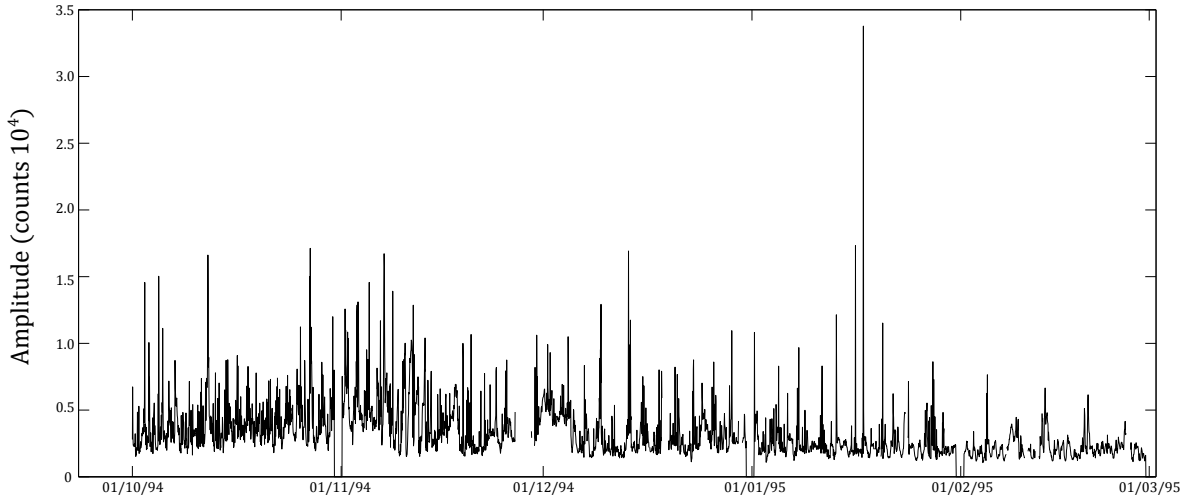


FIGURE C.3: 10-minute averaged Real-time Seismic Amplitude Measurements of the continuous data from station FG1.

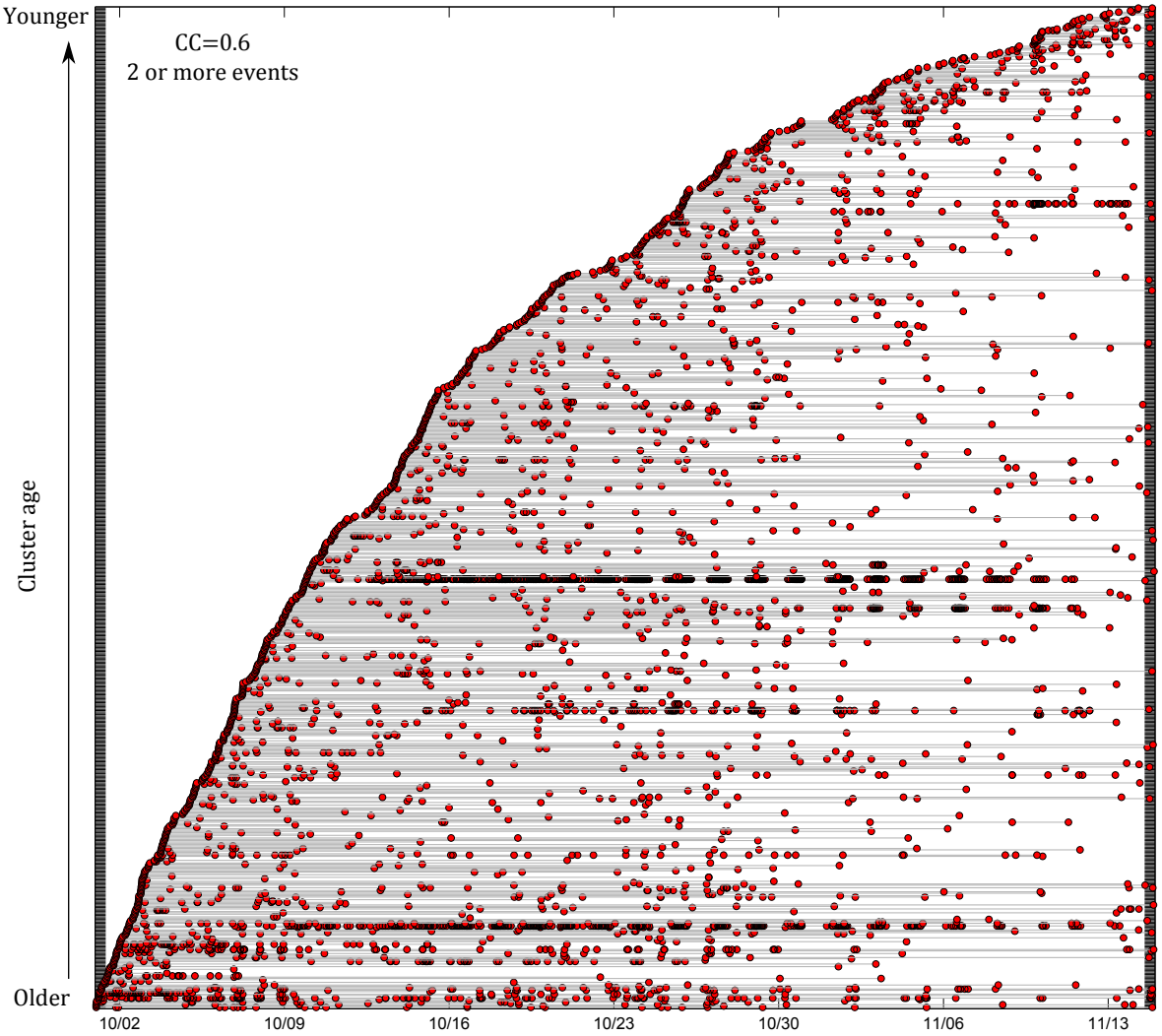


FIGURE C.4: Cluster lifespan plot for CC threshold of 0.6 and 2 or more events. Each line connects events within a single cluster. Clusters are plotted by age in ascending order.

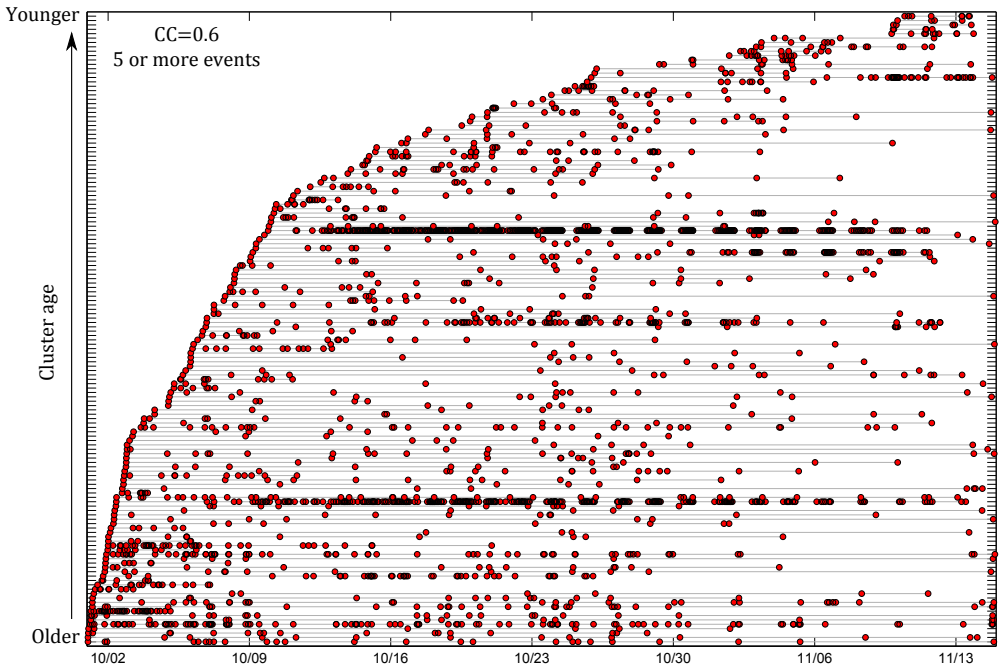


FIGURE C.5: Cluster lifespan plot for CC threshold of 0.6 and 5 or more events. Each line connects events within a single cluster. Clusters are plotted by age in ascending order.

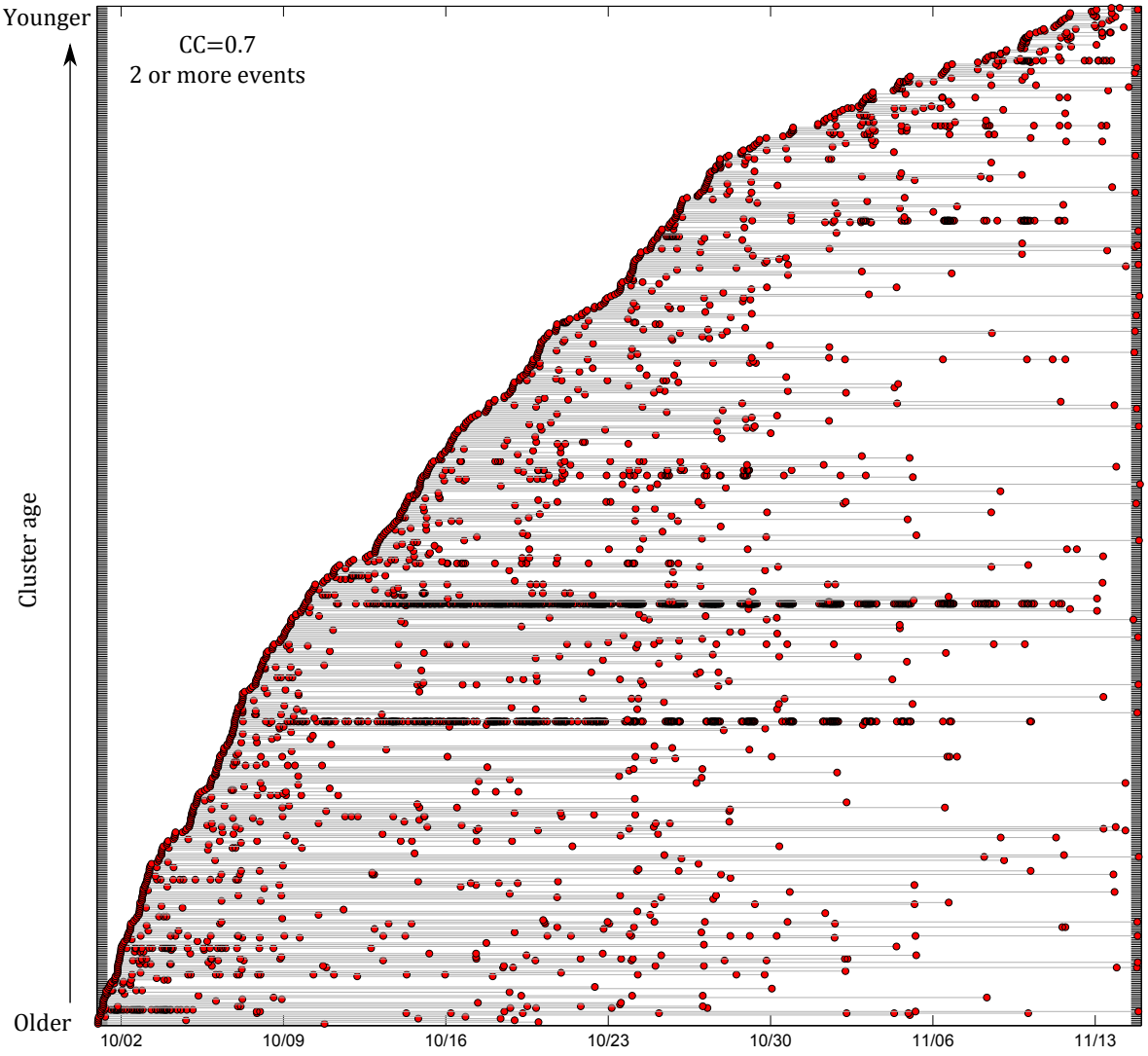


FIGURE C.6: Cluster lifespan plot for CC threshold of 0.7 and 2 or more events. Each line connects events within a single cluster. Clusters are plotted by age in ascending order.

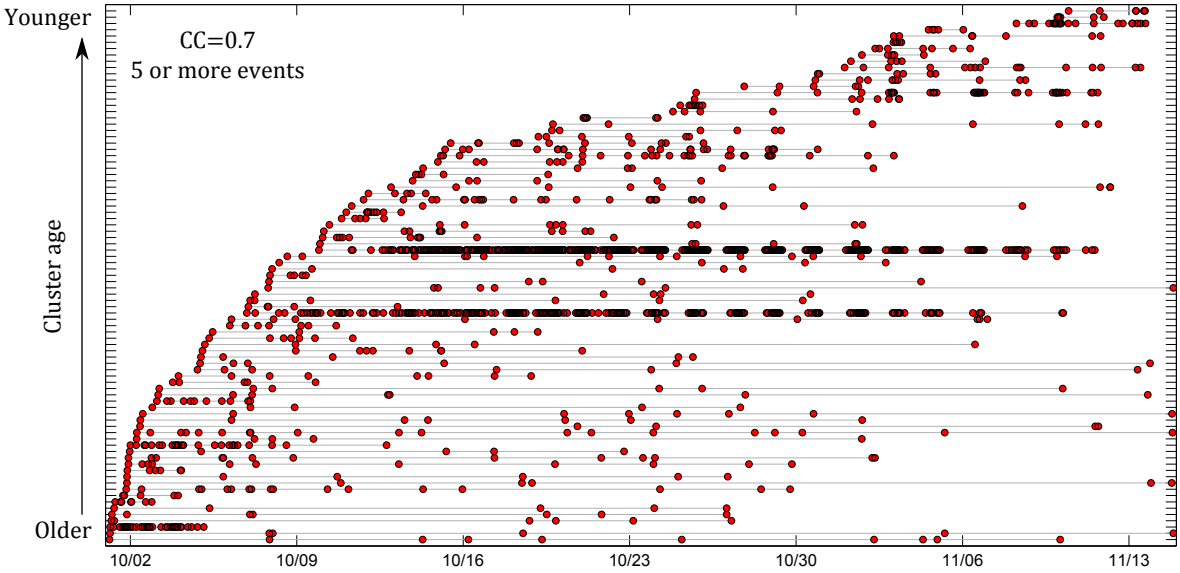


FIGURE C.7: Cluster lifespan plot for CC threshold of 0.7 and 5 or more events. Each line connects events within a single cluster. Clusters are plotted by age in ascending order.

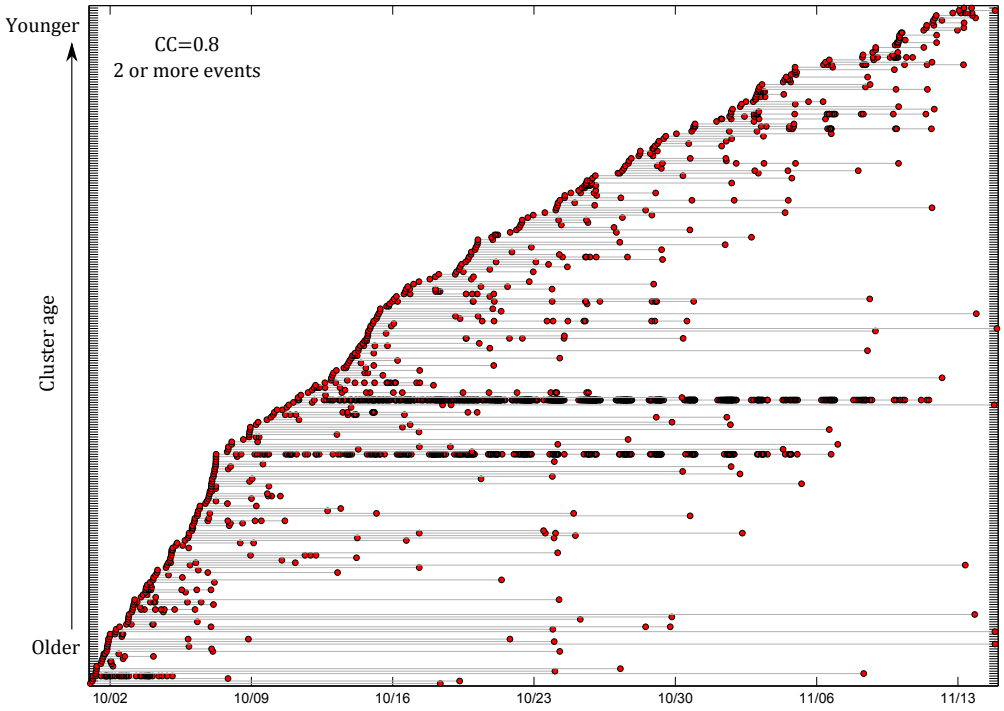


FIGURE C.8: Cluster lifespan plot for CC threshold of 0.8 and 2 or more events. Each line connects events within a single cluster. Clusters are plotted by age in ascending order.

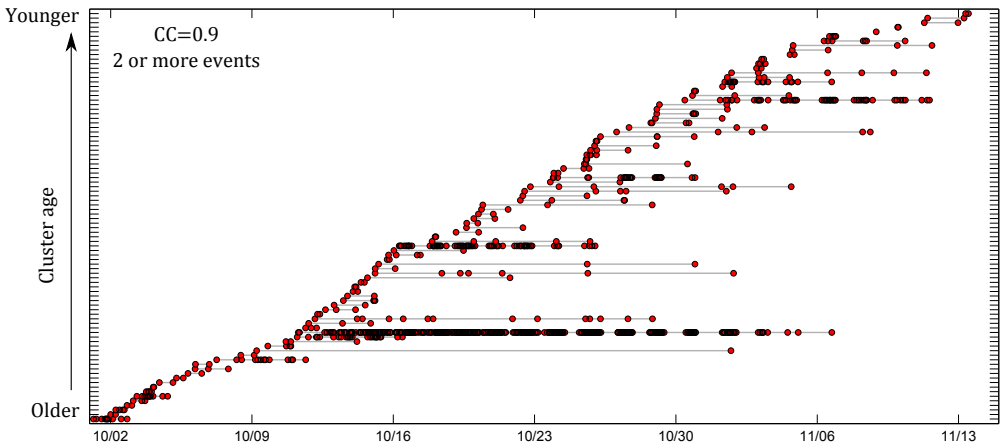


FIGURE C.9: Cluster lifespan plot for CC threshold of 0.9 and 2 or more events. Each line connects events within a single cluster. Clusters are plotted by age in ascending order.

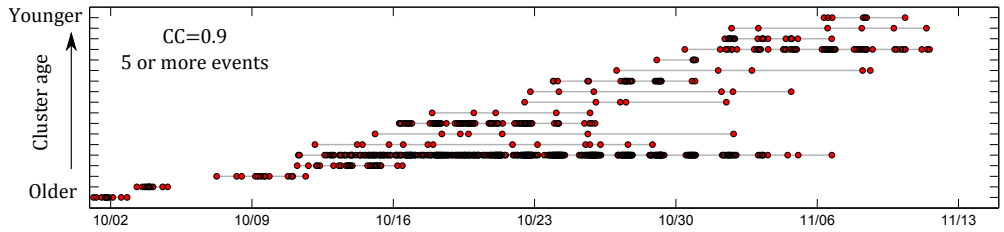


FIGURE C.10: Cluster lifespan plot for CC threshold of 0.9 and 5 or more events. Each line connects events within a single cluster. Clusters are plotted by age in ascending order.

# Appendix D

# Long-term variations in explosion dynamics at Santiaguito dome complex - Supplementary figures

This appendix contains the supplementary information for Chapter 6.

Figure D.1 plots the availability of data from each station deployed around the Santiaguito Dome Complex. Figures D.2 and D.3 plots the individual RSAM from each station used for constructing the network RSAM plotted in 6.3a.

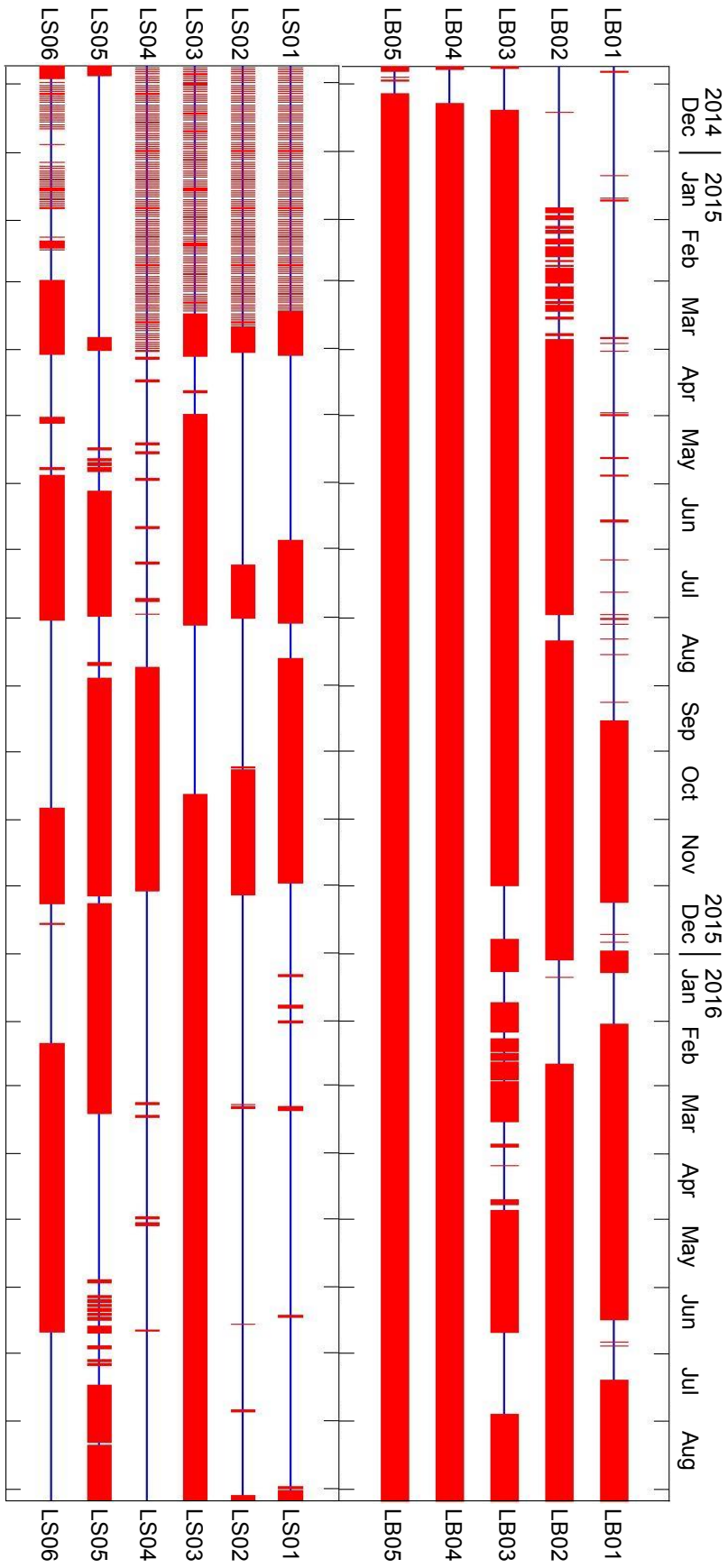


FIGURE D.1: The availability of data at each station deployed around Santiaguito dome complex. Each line corresponds to one station, and each individual red bar indicates a 10-min gap in the data.

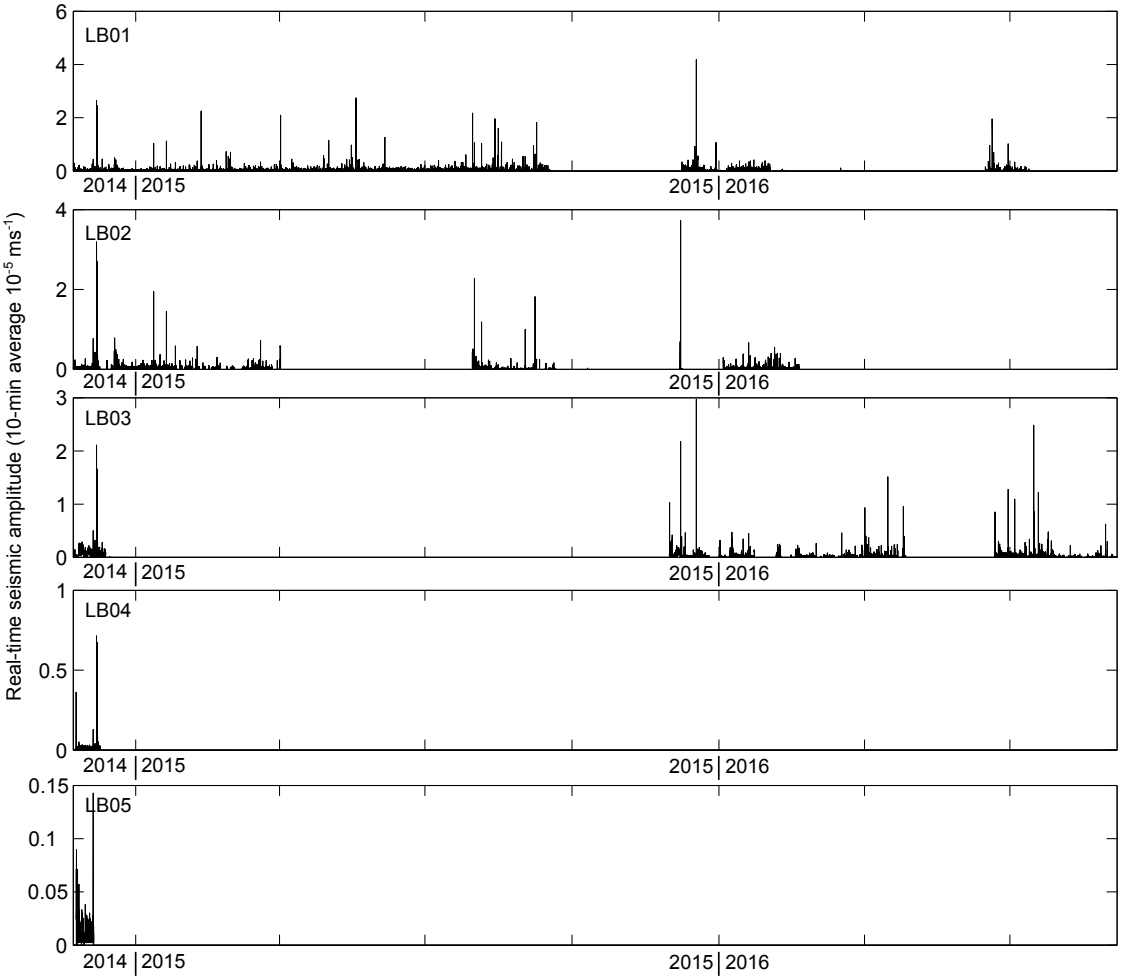


FIGURE D.2: Calculated RSAM from each broadband station at Santiaguito dome complex.

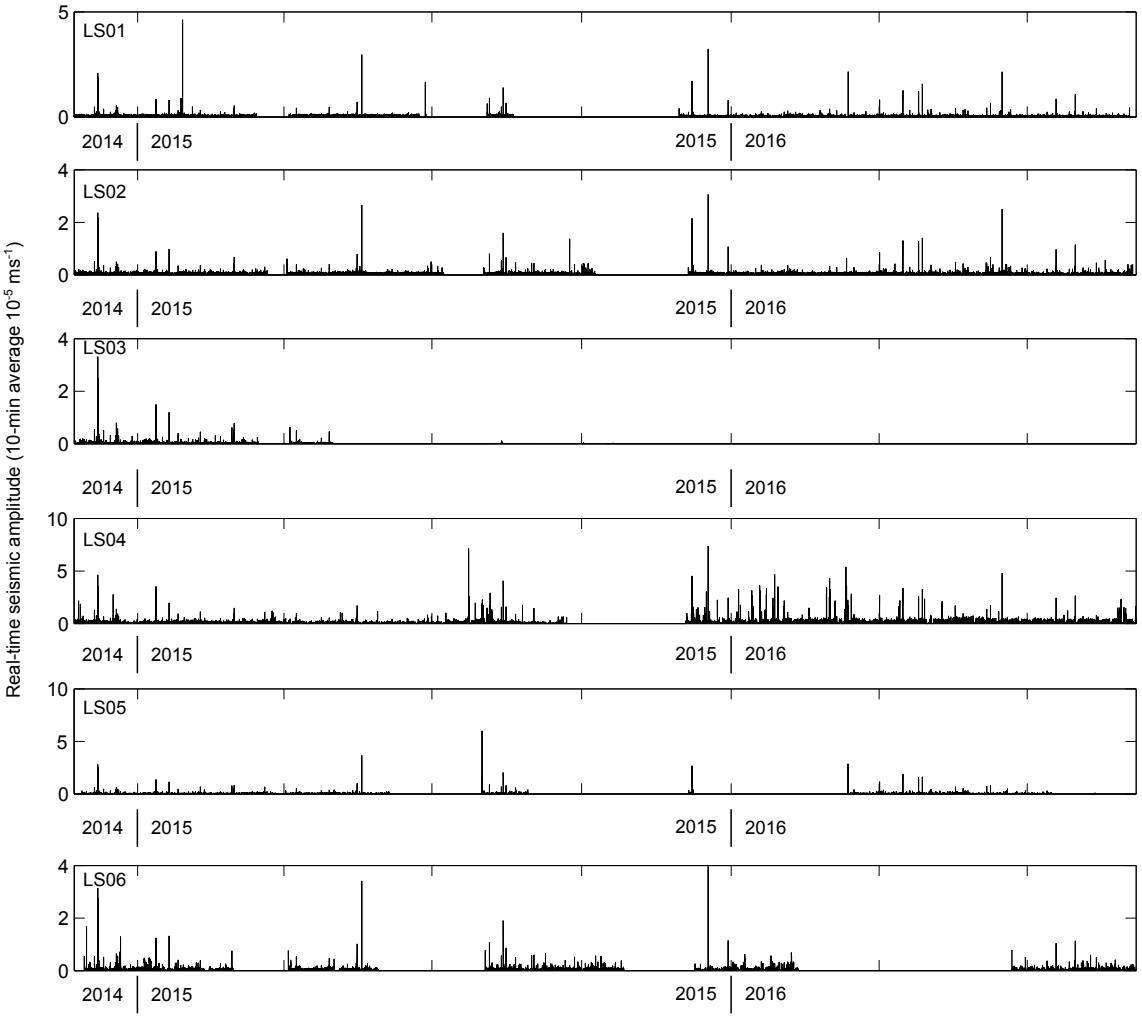


FIGURE D.3: Calculated RSAM from each short-period station at Santiaguito dome complex.

# Bibliography

Ágústsdóttir, T. et al. (2016). Strike-slip faulting during the 2014 Bárðarbunga-Holuhraun dike intrusion, central Iceland. *Geophysical Research Letters* 43, pp. 1495–1503. DOI: 10.1002/2013GL058740.

Aki, K.-i. and P. G. Richards (1980). *Quantitative seismology.* Sausalito, CA : University Science Books.

Allen, R. V. (1978). Automatic earthquake recognition and timing from single traces. *Bulletin of the Seismological Society of America* 68 (5), pp. 1521–1532.

Arciniega-Ceballos, A., P. Dawson, and B. A. Chouet (2012). Long period seismic source characterization at Popocatépetl volcano, Mexico. *Geophysical Research Letters* 39, p. L20307. DOI: 10.1029/2012GL053494.

Aster, R. et al. (2008). Moment tensor inversion of very long period seismic signals from Strombolian eruptions of Erebus Volcano. *Journal of Volcanology and Geothermal Research* 177 (3), pp. 635–647. DOI: 10.1016/j.jvolgeores.2008.08.013.

Barmin, A, O. Melnik, and R. S. J. Sparks (2002). Periodic behavior in lava dome eruptions. *Earth and Planetary Science Letters* 199 (1-2), pp. 173–184. DOI: 10.1016/S0012-821X(02)00557-5.

Battaglia, J., J. P. Métaxian, and E. Garaebiti (2012). Earthquake-volcano interaction imaged by coda wave interferometry. *Geophysical Research Letters* 39, p. L11309. DOI: 10.1029/2012GL052003.

Bean, C. J. et al. (2013). Long-period seismicity in the shallow volcanic edifice formed from slow-rupture earthquakes. *Nature Geoscience* 7 (1), pp. 71–75. DOI: 10.1038/ngeo2027.

Bell, A. F. et al. (2011). Challenges for forecasting based on accelerating rates of earthquakes at volcanoes and laboratory analogues. *Geophysical Journal International* 185 (2), pp. 718–723. DOI: 10.1111/j.1365-246X.2011.04982.x.

Ben-Zion, Y. and C. G. Sammis (2003). Characterization of Fault Zones. *Pure and Applied Geophysics* 160 (3), pp. 677–715. DOI: 10.1007/PL00012554.

Bennett, E. H. S., W. I. Rose, and F. M. Conway (1992). Santa María, Guatemala: A decade volcano. *Eos, Transactions American Geophysical Union* 73 (48), pp. 521–522. DOI: 10.1029/91EO00387.

Benson, P. M. et al. (2008). Laboratory simulation of volcano seismicity. *Science (New York, N.Y.)* 322 (5899), pp. 249–52. DOI: 10.1126/science.1161927.

Benson, P. M. et al. (2010). Spatio-temporal evolution of volcano seismicity: A laboratory study. *Earth and Planetary Science Letters* 297 (1-2), pp. 315–323. DOI: 10.1016/j.epsl.2010.06.033.

Benson, P. M. et al. (2014). Laboratory simulations of fluid/gas induced micro-earthquakes: application to volcano seismology. *Frontiers in Earth Science* 2, pp. 1–6. DOI: 10.3389/feart.2014.00032.

Beyreuther, M., R. Carniel, and J. Wassermann (2008). Continuous Hidden Markov Models: Application to automatic earthquake detection and classification at Las Canãdas caldera, Tenerife. *Journal of Volcanology and Geothermal Research* 176 (4), pp. 513–518. DOI: 10.1016/j.jvolgeores.2008.04.021.

Blake, O. O., D. R. Faulkner, and A. Rietbrock (2013). The Effect of Varying Damage History in Crystalline Rocks on the P- and S-Wave Velocity under Hydrostatic Confining Pressure. *Pure and Applied Geophysics* 170 (4), pp. 493–505. DOI: 10.1007/s00024-012-0550-0.

Boatwright, J. (1980). A spectral theory for circular seismic sources; simple estimates of source dimension, dynamic stress drop and radiated seismic energy. *Bulletin of the Seismological Society of America* 70 (1), pp. 1–27.

Bourbié, T. and B. Zinszner (1985). Hydraulic and acoustic properties as a function of porosity in Fontainebleau Sandstone. *Journal of Geophysical Research: Solid Earth* 90 (B13), pp. 11524–11532. DOI: 10.1029/JB090iB13p11524.

Brenguier, F. et al. (2008). Towards forecasting volcanic eruptions using seismic noise. *Nature Geoscience* 1 (2), pp. 126–130. DOI: 10.1038/ngeo104.

Brenguier, F. et al. (2016). 4-D noise-based seismology at volcanoes: Ongoing efforts and perspectives. *Journal of Volcanology and Geothermal Research* 321, pp. 182–195. DOI: 10.1016/j.jvolgeores.2016.04.036.

Breton Gonzalez, M., J. J. Ramirez, and C. Navarro (2002). Summary of the historical eruptive activity of Volcán De Colima, Mexico 1519 - 2000. *Journal of Volcanology and Geothermal Research* 117, pp. 21–46.

Brown, S., M. Auker, and R. Sparks (2015). Populations around Holocene volcanoes and development of a Population Exposure Index. *Global Volcanic Hazards and Risk*. Ed. by S. C. Loughlin et al. Cambridge: Cambridge University Press. DOI: 10.1017/CBO9781316276273.

Bull, K. F. and H. Buurman (2013). An overview of the 2009 eruption of Redoubt Volcano, Alaska. *Journal of Volcanology and Geothermal Research* 259, pp. 2–15. DOI: 10.1016/j.jvolgeores.2012.06.024.

Burlini, L. et al. (2007). Seismicity preceding volcanic eruptions: New experimental insights. *Geology* 35 (2), pp. 183–186. DOI: 10.1130/G23195A.1.

Buurman, H. and M. E. West (2010). Seismic Precursors to Volcanic Explosions During the 2006 Eruption of Augustine Volcano. *The 2006 eruption of Augustine volcano, Alaska: U.S. Geological Survey Professional Paper 1769*. Ed. by J. A. Power, M. L. Coombs, and J. T. Freymueller. Chap. 2, pp. 41–57.

Byerlee, J. (1978). Friction of rocks. *Pure and Applied Geophysics* 116 (4-5), pp. 615–626. DOI: 10.1007/BF00876528.

Calder, E. et al. (2015). Chapter 18; Lava Dome Eruptions. *Encyclopedia of Volcanoes 2nd Edition*. Ed. by H. Sigurdsson et al. Academic Press.

Calder, E. S. et al. (2002). Mechanisms of lava dome instability and generation of rockfalls and pyroclastic flows at Soufriere Hills Volcano, Montserrat. *Geological Society, London, Memoirs* 21 (1), pp. 173–190. DOI: 10.1144/GSL.MEM.2002.021.01.08.

Cannata, A. et al. (2011). Insights into explosive activity at closely-spaced eruptive vents using infrasound signals: Example of Mt. Etna 2008 eruption. *Journal of Volcanology and Geothermal Research* 208 (1–2), pp. 1 –11. DOI: 10.1016/j.jvolgeores.2011.09.003.

Caplan-Auerbach, J. and S. R. McNutt (2003). New insights into the 1999 eruption of Shishaldin volcano, Alaska, based on acoustic data. *Bulletin of Volcanology* 65 (6), pp. 405–417.

Caplan-Auerbach, J., A. Bellesiles, and J. K. Fernandes (2010). Estimates of eruption velocity and plume height from infrasonic recordings of the 2006 eruption of Augustine Volcano, Alaska. *Journal of Volcanology and Geothermal Research* 189 (1-2), pp. 12–18.

Caricchi, L. et al. (2007). Non-Newtonian rheology of crystal-bearing magmas and implications for magma ascent dynamics. *Earth and Planetary Science Letters* 264 (3-4), pp. 402–419. DOI: 10.1016/j.epsl.2007.09.032.

Casadevall, T. J. (1994). The 1989-1990 eruption of Redoubt Volcano, Alaska: impacts on aircraft operations. *Journal of Volcanology and Geothermal Research* 62, pp. 301–316. DOI: 10.1016/0377-0273(94)90038-8.

Cashman, K. and J. Blundy (2000). Degassing and crystallization of ascending andesite and dacite. *Philosophical Transactions of the Royal Society A: Mathematical, Physical and Engineering Sciences* 358 (1770), pp. 1487–1513. DOI: 10.1098/rsta.2000.0600.

Cashman, K. and R. S. J. Sparks (2013). How volcanoes work: A 25 year perspective. *Geological Society of America Bulletin* 125 (5-6), pp. 664–690. DOI: 10.1130/B30720.1.

Cashman, K., C. Thornber, and J. S. Pallister (2008). From Dome to Dust: Shallow Crystallisation and Fragmentation of Conduit Magma During the 2004-2006 Dome Extrusion of Mount St. Helens, Washington. *A Volcano Rekindled: The Renewed Eruption of Mount St. Helens, 2004-2006: US Geological Survey Professional Paper 1750*. Ed. by D. R. Sherrod, W. E. Scott, and P. Stauffer, pp. 387–413.

Castro, J. M. et al. (2012). The role of melt-fracture degassing in defusing explosive rhyolite eruptions at volcán Chaitén. *Earth and Planetary Science Letters* 333–334, pp. 63 –69. DOI: 10.1016/j.epsl.2012.04.024.

Caudron, C. et al. (2015a). Magma migration at the onset of the 2012-13 Tolbachik eruption revealed by Seismic Amplitude Ratio Analysis. *Journal of Volcanology and Geothermal Research* 307, pp. 60–67. DOI: 10.1016/j.jvolgeores.2015.09.010.

Caudron, C. et al. (2015b). On the use of remote infrasound and seismic stations to constrain the eruptive sequence and intensity for the 2014 Kelud eruption. *Geophysical Research Letters* 42, pp. 6614–6621. DOI: 10.1002/2015GL064885.

Chouet, B. et al. (2003). Source mechanisms of explosions at Stromboli Volcano, Italy, determined from moment-tensor inversions of very-long-period data. *Journal of Geophysical Research: Solid Earth* 108 (B1). DOI: 10.1029/2002JB001919.

Chouet, B., P. Dawson, and A. Arciniega-Ceballos (2005). Source mechanism of Vulcanian degassing at Popocatépetl Volcano, Mexico, determined from waveform inversions of very long period signals. *Journal of Geophysical Research* 110. DOI: 10.1029/2004JB003524.

Chouet, B. A. (1985). Excitation of a Buried Magmatic Pipe: A Seismic Source Model for Volcanic Tremor. *Journal of Geophysical Research* 90, pp. 1881–1893. DOI: 10.1029/JB090iB02p01881.

Chouet, B. A. (1996). Long-period volcano seismicity: its source and use in eruption forecasting. *Nature* 380, pp. 309–316.

Chouet, B. A. and R. S. Matoza (2013). A multi-decadal view of seismic methods for detecting precursors of magma movement and eruption. *Journal of Volcanology and Geothermal Research* 252, pp. 108–175. DOI: 10.1016/j.jvolgeores.2012.11.013.

Chouet, B. A. et al. (1994). Precursory swarms of long-period events at Redoubt Volcano (1989-1990), Alaska: Their origin and use as a forecasting tool. *Journal of Volcanology and Geothermal Research* 62, pp. 95–135.

Christopher, T. E. et al. (2015). Crustal-scale degassing due to magma system destablization and magma-gas decoupling at Soufrière Hills Volcano, Montserrat. *Geochemistry Geophysics Geosystems* 16, pp. 2797–2811. DOI: 10.1002/2015GC005791.

Collinson, A. S. D. and J. Neuberg (2012). Gas storage , transport and pressure changes in an evolving permeable volcanic edifice. *Journal of Volcanology and Geothermal Research* 243-244, pp. 1–13. DOI: 10.1016/j.jvolgeores.2012.06.027.

Cordonnier, B. et al. (2009). Rheological properties of dome lavas: Case study of Unzen volcano. *Earth and Planetary Science Letters* 279 (3-4), pp. 263–272. DOI: 10.1016/j.epsl.2009.01.014.

Cordonnier, B. et al. (2012). The viscous-brittle transition of crystal-bearing silicic melt: Direct observation of magma rupture and healing. *Geology* 40 (7), pp. 611–614. DOI: 10.1130/G3914.1.

Costa, A. et al. (2007a). Control of magma flow in dykes on cyclic lava dome extrusion. *Geophysical Research Letters* 34 (L02303). DOI: 10.1029/2006GL027466.

Costa, A., O. Melnik, and R. Sparks (2007b). Controls of conduit geometry and wallrock elasticity on lava dome eruptions. *Earth and Planetary Science Letters* 260 (1-2), pp. 137–151. DOI: 10.1016/j.epsl.2007.05.024.

Costa, A., G. Wadge, and O. Melnik (2012). Cyclic extrusion of a lava dome based on a stick-slip mechanism. *Earth and Planetary Science Letters* 337-338, pp. 39–46. DOI: 10.1016/j.epsl.2012.05.011.

Costa, A., L. Caricchi, and N. Bagdassarov (2009). A model for the rheology of particle-bearing suspensions and partially molten rocks. *Geochemistry, Geophysics, Geosystems* 10 (3). DOI: 10.1029/2008GC002138.

Creager, K. C. (1997). CORAL. *Seismological Research Letters* 68 (2), pp. 269–271.

Danielson, G. C. and C Lanczos (1942). Some improvements in practical fourier analysis and their application to x-ray scattering from liquids. *J. Franklin Institute* 233, pp. 365–380.

Dawson, P. B., B. A. Chouet, and J. Power (2011). Determining the seismic source mechanism and location for an explosive eruption with limited observational data: Augustine Volcano, Alaska. *Geophysical Research Letters* 38 (3). DOI: 10.1029/2010GL045977.

De Angelis, S. (2009). Seismic source displacement by coda wave interferometry at Soufriere Hills Volcano, Montserrat, WI. *Natural Hazards and Earth System Sciences* 9, pp. 1341–1347.

De Angelis, S. and S. M. Henton (2011). On the feasibility of magma fracture within volcanic conduits: Constraints from earthquake data and empirical modelling of magma viscosity. *Geophysical Research Letters* 38 (19), pp. 1–5. DOI: 10.1029/2011GL049297.

De Angelis, S. et al. (2012a). Detecting hidden volcanic explosions from Mt. Cleveland Volcano, Alaska with infrasound and ground-coupled airwaves. *Geophysical Research Letters* 39, p. L21312. DOI: 10.1029/2012GL053635.

De Angelis, S. et al. (2012b). Detecting hidden volcanic explosions from Mt. Cleveland Volcano, Alaska with infrasound and ground-coupled airwaves. *Geophysical Research Letters* 39 (21). DOI: 10.1029/2012GL053635.

De Angelis, S. et al. (2016). Characterization of moderate ash-and-gas explosions at Santiaguito volcano, Guatemala, from infrasound waveform inversion and thermal infrared. *Geophysical Research Letters* 43. DOI: 10.1002/2016GL069098.

Delle Donne, D. et al. (2014). Thermal, acoustic and seismic signals from pyroclastic density currents and Vulcanian explosions at Soufriere Hills Volcano, Montserrat. *Geological Society, London, Memoirs* 39 (1), pp. 169–178. DOI: 10.1144/M39.9.

Delle Donne, D. and M. Ripepe (2012). High-frame rate thermal imagery of Strombolian explosions: Implications for explosive and infrasonic source dynamics. *Journal of Geophysical Research* 117, B09206. DOI: 10.1029/2011JB008987.

Denlinger, R. P. and R. P. Hoblitt (1999). Cyclic eruptive behavior of silicic volcanoes. *Geology* 27, pp. 459–462.

Di Toro, G. et al. (2006). Natural and experimental evidence of melt lubrication of faults during earthquakes. *Science (New York, N.Y.)* 311 (5761), pp. 647–649. DOI: 10.1126/science.1121012.

Dieterich, J. H. (1979). Modeling of rock friction: 1. Experimental results and constituve equations. *Journal of geophysical research* 84 (9), pp. 2161–2168.

Dingwell, D. B. (1996). Volcanic Dilemma: Flow or Blow? *Science* 273 (5278), pp. 1054–1055.

Dingwell, D. B. and S. L. Webb (1989). Structural relaxation in silicate melts and non-Newtonian melt rheology in geologic processes. *Physics and Chemistry of Minerals* 16 (5), pp. 508–516. DOI: 10.1007/BF00197020.

Drexler, J. M. et al. (2011). Jet engine coatings for resisting volcanic ash damage. *Advanced Materials* 23, pp. 2419–2424. DOI: 10.1002/adma.201004783.

Duputel, Z. et al. (2009). Real time monitoring of relative velocity changes using ambient seismic noise at the Piton de la Fournaise volcano (La Réunion) from January 2006 to June 2007. *Journal of Volcanology and Geothermal Research* 184 (1-2), pp. 164–173. DOI: 10.1016/j.jvolgeores.2008.11.024.

Edmonds, M. (2008). New geochemical insights into volcanic degassing. 366 (1885), pp. 4559–79. DOI: 10.1098/rsta.2008.0185.

Elsworth, D. et al. (2008). Implications of Magma Transfer Between Multiple Reservoirs on Eruption Cycling. *Science* 322 (5899), pp. 246–248. DOI: 10.1126/science.1161297.

Eyre, T. S. et al. (2015). A brittle failure model for long-period seismic events recorded at Turrialba Volcano, Costa Rica. *Journal of Geophysical Research: Solid Earth* 120, pp. 1452–1472. DOI: 10.1002/2014JB011108.

Farquharson, J. et al. (2015). Permeability and porosity relationships of edifice-forming andesites: A combined field and laboratory study. *Journal of Volcanology and Geothermal Research* 297, pp. 52–68. DOI: 10.1016/j.jvolgeores.2015.03.016.

Farquharson, J. I. et al. (2016). Pore pressure embrittlement in a volcanic edifice. *Bulletin of Volcanology* 78 (6). DOI: 10.1007/s00445-015-0997-9.

Fazio, M., P. M. Benson, and S. Vinciguerra (2017). On the generation mechanisms of fluid-driven seismic signals related to volcano-tectonics. *Geophysical Research Letters*, pp. 1–9. DOI: 10.1002/2016GL070919.

Fee, D. and R. S. Matoza (2013). An overview of volcano infrasound: From hawaiian to plinian, local to global. *Journal of Volcanology and Geothermal Research* 249, pp. 123–139. DOI: 10.1016/j.jvolgeores.2012.09.002.

Fee, D. et al. (2011). Infrasound from the 2007 fissure eruptions of Kilauea Volcano, Hawai'i. *Geophysical Research Letters* 38 (6). L06309. DOI: 10.1029/2010GL046422.

Fee, D. et al. (2013). Infrasonic crackle and supersonic jet noise from the eruption of Nabro Volcano, Eritrea. *Geophysical Research Letters* 40, pp. 4199–4203. DOI: 10.1002/grl.50827.

Fee, D. et al. (2016). Seismic Envelope-Based Detection and Location of Ground-Coupled Airwaves from Volcanoes in Alaska. *Bulletin of the Seismological Society of America* 106 (3). DOI: 10.1785/0120150244.

Fee, D. et al. (2017). Volcanic tremor and plume height hysteresis from Pavlof Volcano, Alaska. *Science* 355 (6320), pp. 1–5.

Fink, J. H. and R. W. Griffiths (1998). Morphology, eruption rates, and rheology of lava domes: Insights from laboratory models. *Journal of Geophysical Research: Solid Earth* 103 (B1), pp. 527–545. DOI: 10.1029/97JB02838.

Firstov, P. and N. Kravchenko (1996). Estimation of the amount of explosive gas released in volcanic eruptions using air waves. *Volcanol. Seismol* 17, pp. 547–560.

Foroozan, R. et al. (2011). Magmatic-metering controls the stopping and restarting of eruptions. *Geophysical Research Letters* 38 (5), pp. 1–5. DOI: 10.1029/2010GL046591.

Gaunt, H. E. et al. (2014). Pathways for degassing during the lava dome eruption of Mount St. Helens 2004-2008. *Geology* 42 (11), pp. 947–950. DOI: 10.1130/G35940.1.

Geller, R. J. and C. S. Mueller (1980). Four similar earthquakes in Central California. *Geophysical Research Letters* 7 (10), pp. 821–824.

Gerst, A. et al. (2013). The first second of volcanic eruptions from the Erebus volcano lava lake, Antarctica - Energies, pressures, seismology, and infrasound. *Journal of Geophysical Research: Solid Earth* 118, pp. 3318–3340. DOI: 10.1002/jgrb.50234.

Ghil, M. et al. (2002). Advanced spectral methods for climatic time series. *Reviews of Geophysics* 40 (1), p. 1003. DOI: 10.1029/2000RG000092.

Global Volcanism Program (2015). Report on Santa Maria (Guatemala) — July 2015. *Bulletin of the Global Volcanism Network*. Ed. by E Venzke. Vol. 40. 7. Smithsonian Institution Press.

Global Volcanism Program (2016a). Report on Santa Maria (Guatemala) — February 2016. *Bulletin of the Global Volcanism Network*. Ed. by E Venzke. Vol. 41. 2. Smithsonian Institution Press.

Global Volcanism Program (2016b). Report on Santa Maria (Guatemala) — September 2016. *Bulletin of the Global Volcanism Network*. Ed. by E Venzke. Vol. 41. 9. Smithsonian Institution Press.

Gonnermann, H. M. and M. Manga (2007). The Fluid Mechanics Inside a Volcano. *Annual Review of Fluid Mechanics* 39 (1), pp. 321–356. DOI: 10.1146/annurev.fluid.39.050905.110207.

Goodfellow, S. D. and R. P. Young (2014). A laboratory acoustic emission experiment under in situ conditions. *Geophysical Research Letters* 41 (10), pp. 3422–3430. DOI: 10.1002/2014GL059965.

Goto, A. (1999). A new model for volcanic earthquake at Unzen Volcano: Melt Rupture Model. *Geophysical Research Letters* 26 (16), pp. 2541–2544. DOI: 10.1029/1999GL900569.

Gottsmann, J. et al. (2009). Magma-tectonic interaction and the eruption of silicic batholiths. *Earth and Planetary Science Letters* 284 (3-4), pp. 426–434. DOI: 10.1016/j.epsl.2009.05.008.

Green, D. N. and J. W. Neuberg (2006). Waveform classification of volcanic low-frequency earthquake swarms and its implication at Soufrière Hills Volcano, Montserrat. *Journal of Volcanology and Geothermal Research* 153 (1-2), pp. 51–63. DOI: 10.1016/j.jvolgeores.2005.08.003.

Grêt, A., R. Snieder, and J. Scales (2006). Time-lapse monitoring of rock properties with coda wave interferometry. *Journal of Geophysical Research: Solid Earth* 111 (3), pp. 1–11. DOI: 10.1029/2004JB003354.

Guffanti, M., T. J. Casadevall, and K. Budding (2010). Encounters of Aircraft with Volcanic Ash Clouds: A Compilation of Known Incidents, 1953 – 2009. *U.S. Geological Survey Data Series 545* 1, pp. 1–12.

Hale, A. J. and G. Wadge (2008). The transition from endogenous to exogenous growth of lava domes with the development of shear bands. *Journal of Volcanology and Geothermal Research* 171 (3-4), pp. 237–257. DOI: 10.1016/j.jvolgeores.2007.12.016.

Hammer, C. and J. Neuberg (2009). On the dynamical behaviour of low-frequency earthquake swarms prior to a dome collapse of Soufrière Hill volcano, Montserrat. *Geophysical Research Letters* 36 (6), pp. 10–12. DOI: 10.1029/2008GL036837.

Haney, M. M. et al. (2013). Source characterization for an explosion during the 2009 eruption of Redoubt Volcano from very-long-period seismic waves. *Journal of Volcanology and Geothermal Research* 259, pp. 77–88. DOI: 10.1016/j.jvolgeores.2012.04.018.

Harrington, R. M. and P. M. Benson (2011). Analysis of laboratory simulations of volcanic hybrid earthquakes using empirical Green's functions. *Journal of Geophysical Research* 116 (B11). DOI: 10.1029/2011JB008373.

Harrington, R. M. and E. E. Brodsky (2007). Volcanic hybrid earthquakes that are brittle-failure events. *Geophysical Research Letters* 34. DOI: 10.1029/2006GL028714.

Harris, A. J. L., W. I. Rose, and L. P. Flynn (2003). Temporal trends in lava dome extrusion at Santiaguito 1922 – 2000. *Bulletin of Volcanology* 65, pp. 77–89. DOI: 10.1007/s00445-002-0243-0.

Harris, A. J. L. et al. (2004). The evolution of an active silicic lava flow field: An ETM+ perspective. *Journal of Volcanology and Geothermal Research* 135 (1-2), pp. 147–168. DOI: 10.1016/j.jvolgeores.2003.12.011.

Hautmann, S. et al. (2009). Modelling ground deformation caused by oscillating overpressure in a dyke conduit at Soufrière Hills Volcano, Montserrat. *Tectonophysics* 471 (1-2), pp. 87–95. DOI: 10.1016/j.tecto.2008.10.021.

Heap, M. J., S. Vinciguerra, and P. G. Meredith (2009). The evolution of elastic moduli with increasing crack damage during cyclic stressing of a basalt from Mt. Etna volcano. *Tectonophysics* 471 (1-2), pp. 153–160. DOI: 10.1016/j.tecto.2008.10.004.

Heap, M. J. et al. (2010). Elastic moduli evolution and accompanying stress changes with increasing crack damage: Implications for stress changes around fault zones and volcanoes during deformation. *Geophysical Journal International* 183 (1), pp. 225–236. DOI: 10.1111/j.1365-246X.2010.04726.x.

Heap, M. J. et al. (2014). Mictrostructural controls on the physical and mechanical properties of edifice-forming andesites at Volcan de Colima, Mexico. *Journal of Geophysical Research: Solid Earth* 119, pp. 1–39. DOI: 10.1002/2013JB010521.

Heap, M. J. et al. (2015a). Fracture and compaction of andesite in a volcanic edifice. *Bulletin of Volcanology* 77 (6). DOI: 10.1007/s00445-015-0938-7.

Heap, M. J. et al. (2015b). Mechanical behaviour and failure modes in the Whakaari (White Island volcano) hydrothermal system, New Zealand. *Journal of Volcanology and Geothermal Research* 295, pp. 26–42. DOI: 10.1016/j.jvolgeores.2015.02.012.

Hess, K. U. and D. B. Dingwell (1996). Viscosities of hydrous leucogranitic melts: a non-Arrhenian model. *American Mineralogist* 81, pp. 1297–1300. DOI: 10.1016/0016-7037(82)90381-7.

Hewett, T., J. Fay, and D. Hoult (1971). Laboratory experiments of smokestack plumes in a stable atmosphere. *Atmospheric Environment (1967)* 5 (9), pp. 767–789.

Hill, D. P. (1996). Earthquakes and Carbon Dioxide beneath Mammoth Mountain, California. *Seismological Research Letters* 67 (1), pp. 8–15.

Hirabayashi, J.-I. et al. (1995). Discharge rate of SO2 from Unzen volcano, Kyushu, Japan. *Geophysical Research Letters* 22 (13), pp. 1709–1712.

Holland, A. P. et al. (2011). Degassing processes during lava dome growth: Insights from Santiaguito lava dome, Guatemala. *Journal of Volcanology and Geothermal Research* 202 (1-2), pp. 153–166. DOI: 10.1016/j.jvolgeores.2011.02.004.

Hornby, A. J. et al. (2015). Spine growth and seismogenic faulting at Mt. Unzen , Japan. *Journal of Geophysical Research: Solid Earth* 120. DOI: 10.1002/2014JB011660.

Horwell Claire J.and Williamson, B. J. et al. (2013). The nature and formation of cristobalite at the Soufrière Hills volcano, Montserrat: implications for the petrology and stability of silicic lava domes. *Bulletin of Volcanology* 75 (3), p. 696. DOI: 10.1007/s00445-013-0696-3.

Hotovec, A. J. et al. (2013). Strongly gliding harmonic tremor during the 2009 eruption of Redoubt Volcano. *Journal of Volcanology and Geothermal Research* 259, pp. 89–99. DOI: 10.1016/j.jvolgeores.2012.01.001.

Hotovec-Ellis, A. J. et al. (2014). A continuous record of intereruption velocity change at Mount St. Helens from coda wave interferometry. *Journal of Geophysical Research: Solid Earth* 119, pp. 2199–2214. DOI: 10.1002/2014JB011151.

Hotovec-Ellis, A. J. et al. (2015). Changes in seismic velocity during the first 14 months of the 2004-2008 eruption of Mount St. Helens, Washington. *Journal of Geophysical Research: Solid Earth* 120, pp. 1–15. DOI: 10.1002/2013JB010742.

Hreinsdóttir, S. et al. (2014). Volcanic plume height correlated with magma- pressure change at Grímsvötn Volcano, Iceland. *Nature Geoscience* 7 (12), pp. 1–5. DOI: 10.1038/ngeo2044.

Ikeda, R. et al. (2008). Physical rock properties in and around a conduit zone by well-logging in the Unzen Scientific Drilling Project, Japan. *Journal of Volcanology and Geothermal Research* 175 (1–2). Scientific drilling at Mount Unzen, pp. 13 –19. DOI: 10.1016/j.jvolgeores.2008.03.036.

Ishida, T. et al. (2017). ISRM Suggested Method for Laboratory Acoustic Emission Monitoring. *Rock Mechanics and Rock Engineering* (March). DOI: 10.1007/s00603-016-1165-z.

Iverson, R. M. (2008). Dynamics of Seismogenic Volcanic Extrusion Resisted by a Solid Surface Plug, Mount St. Helens, 2004-2005. *A Volcano Rekindled: The Renewed Eruption of Mount St. Helens, 2004-2006: US Geological Survey Professional Paper 1750*. Ed. by D. R. Sherrod, W. E. Scott, and P. H. Stauffer, pp. 425–460.

Iverson, R. M. et al. (2006). Dynamics of seismogenic volcanic extrusion at Mount St Helens in 2004-05. *Nature* 444 (7118), pp. 439–43. DOI: 10.1038/nature05322.

James, M. R., S. J. Lane, and B. A. Chouet (2006). Gas slug ascent through changes in conduit diameter: Laboratory insights into a volcano-seismic source process in low-viscosity magmas. *Journal of Geophysical Research: Solid Earth* 111 (B5). B05201, n/a–n/a. DOI: 10.1029/2005JB003718.

James, M. et al. (2004). Pressure changes associated with the ascent and bursting of gas slugs in liquid-filled vertical and inclined conduits. *Journal of Volcanology and Geothermal Research* 129 (1–3), pp. 61 –82. DOI: 10.1016/S0377-0273(03)00232-4.

Jaupart, C. (1998). Gas loss from magmas through conduit walls during eruption. *Geological Society, London, Special Publications* 145 (1), pp. 73–90. DOI: 10.1144/GSL.SP.1996.145.01.05.

Johnson, J. B. (2003). Generation and propagation of infrasonic airwaves from volcanic explosions. *Journal of Volcanology and Geothermal Research* 121 (1-2), pp. 1–14.

Johnson, J. B. and A. J. C. Miller (2014). Application of the Monopole Source to Quantify Explosive Flux during Vulcanian Explosions at Sakurajima Volcano (Japan). *Seismological Research Letters* 85 (6), pp. 1163–1176. DOI: 10.1785/0220140058.

Johnson, J. B. and R. C. Aster (2005). Relative partitioning of acoustic and seismic energy during Strombolian eruptions. *Journal of Volcanology and Geothermal Research* 148 (3-4), pp. 334–354. DOI: 10.1016/j.jvolgeores.2005.05.002.

Johnson, J. B. and J. L. Palma (2015). Lahar infrasound associated with Villarrica's March 3, 2015 eruption. *Geophysical Research Letters*, pp. 6324–6331. DOI: 10.1002/2015GL065024.

Johnson, J. B. and T. J. Ronan (2015). Infrasound from volcanic rockfalls. *Journal of Geophysical Research: Solid Earth* 120. DOI: 10.1002/2015JB012436.

Johnson, J. B. et al. (2009). Dissection of a composite volcanic earthquake at Santiaguito, Guatemala. *Geophysical Research Letters* 36 (16), p. L16308. DOI: 10.1029/2009GL039370.

Johnson, J. B. (2007). On the relation between infrasound, seismicity, and small pyroclastic explosions at Karymsky Volcano. *Journal of Geophysical Research* 112 (B8), B08203. DOI: 10.1029/2006JB004654.

Johnson, J. B. et al. (2008). Long-period earthquakes and co-eruptive dome inflation seen with particle image velocimetry. *Nature* 456, pp. 377–381. DOI: 10.1038/nature07429.

Johnson, J. B. et al. (2014). Explosive dome eruptions modulated by periodic gas-driven inflation. *Geophysical Research Letters* 41. DOI: 10.1002/2014GL061310.

Julian, B. R. (1994). Volcanic tremor: Nonlinear excitation by fluid flow. *Journal of Geophysical Research: Solid Earth* 99 (B6), pp. 11859–11877. DOI: 10.1029/93JB03129.

Kanamori, H. and J. W. Given (1983). Lamb pulse observed in nature. *Geophysical Research Letters* 10 (5), pp. 373–376. DOI: 10.1029/GL010i005p00373.

Kanamori, H., J. W. Given, and T. Lay (1984). Analysis of Seismic Body Waves Excited by the Mount St. Helens Eruption of May 18, 1980. *Journal of Geophysical Research* 89 (B3), pp. 1856–1866. DOI: 10.1029/JB089iB03p01856.

Kendrick, J. E. et al. (2012). Extreme frictional processes in the volcanic conduit of Mount St. Helens (USA) during the 2004-2008 eruption. *Journal of Structural Geology* 38, pp. 61–76. DOI: 10.1016/j.jsg.2011.10.003.

Kendrick, J. E. et al. (2013). The influence of thermal and cyclic stressing on the strength of rocks from Mount St. Helens, Washington. *Bulletin of Volcanology* 75 (7), p. 728. DOI: 10.1007/s00445-013-0728-z.

Kendrick, J. E. et al. (2014a). Seismogenic frictional melting in the magmatic column. *Solid Earth* 5 (1), pp. 199–208. DOI: 10.5194/se-5-199-2014.

Kendrick, J. E. et al. (2014b). Volcanic drumbeat seismicity caused by stick-slip motion and magmatic frictional melting. *Nature Geoscience* 7, pp. 438–442. DOI: 10.1038/NGEO2146.

Kendrick, J. E. et al. (2016). Blowing Off Steam: Tuffisite Formation As a Regulator for Lava Dome Eruptions. *Frontiers in Earth Science* 4 (41). DOI: 10.3389/feart.2016.00041.

Kennedy, L. A., J. K. Russell, and E. Nelles (2009). Origins of Mount St. Helens cataclasites: Experimental insights. *American Mineralogist* 94 (7), pp. 995–1004. DOI: 10.2138/am.2009.3129.

Kennedy, L. A. and J. K. Russell (2012). Cataclastic production of volcanic ash at Mount Saint Helens. *Physics and Chemistry of the Earth* 45-46, pp. 40–49. DOI: 10.1016/j.pce.2011.07.052.

Ketner, D. and J. Power (2013). Characterization of seismic events during the 2009 eruption of Redoubt Volcano, Alaska. *Journal of Volcanology and Geothermal Research* 259, pp. 45–62. DOI: 10.1016/j.jvolgeores.2012.10.007.

Kierfeld, J. and V. M. Vinokur (2006). Slow Crack Propagation in Heterogeneous Materials. *Phys. Rev. Lett.* 96 (17), p. 175502. DOI: 10.1103/PhysRevLett.96.175502.

Kim, K. and J. M. Lees (2011). Finite-difference time-domain modeling of transient infrasonic wavefields excited by volcanic explosions. *Geophysical Research Letters* 38 (6), pp. 2–6. DOI: 10.1029/2010GL046615.

Kim, K., J. M. Lees, and M. Ruiz (2012). Acoustic multipole source model for volcanic explosions and inversion for source parameters. *Geophysical Journal International* 191, pp. 1192–1204. DOI: 10.1111/j.1365-246X.2012.05696.x.

Kim, K. et al. (2015). Acoustic source inversion to estimate volume flux from volcanic explosions. *Geophysical Research Letters* 42 (13), pp. 5243–5249. DOI: 10.1002/2015GL064466.

Kohno, Y., T. Matsushima, and H. Shimizu (2008). Pressure sources beneath Unzen Volcano inferred from leveling and GPS data. *Journal of Volcanology and Geothermal Research* 175, pp. 100–109. DOI: 10.1016/j.jvolgeores.2008.03.022.

Kremers, S. et al. (2013). Inverting the source mechanism of Strombolian explosions at Mt. Yasur, Vanuatu, using a multi-parameter dataset. *Journal of Volcanology and Geothermal Research* 262, pp. 104–122. DOI: 10.1016/j.jvolgeores.2013.06.007.

Kueppers, U. et al. (2005). Field-based density measurements as tool to identify preeruption dome structure: Set-up and first results from Unzen volcano, Japan. *Journal of Volcanology and Geothermal Research* 141, pp. 65–75. DOI: 10.1016/j.jvolgeores.2004.09.005.

Kumagai, H. et al. (2009). Seismic tracking of lahars using tremor signals. *Journal of Volcanology and Geothermal Research* 183 (1-2), pp. 112–121. DOI: 10.1016/j.jvolgeores.2009.03.010.

Lacanna, G. and M. Ripepe (2013). Influence of near-source volcano topography on the acoustic wavefield and implication for source modeling. *Journal of Volcanology and Geothermal Research* 250, pp. 9–18. DOI: 10.1016/j.jvolgeores.2012.10.005.

Lacanna, G. et al. (2014). Influence of atmospheric structure and topography on infrasonic wave propagation. *Journal of Geophysical Research: Solid Earth* 119 (4), pp. 2988–3005. DOI: 10.1002/2013JB010827.

Lachowycz, S. M. et al. (2013). Long-range correlations identified in time-series of volcano seismicity during dome-forming eruptions using detrended fluctuation analysis. *Journal of Volcanology and Geothermal Research* 264, pp. 197–209. DOI: 10.1016/j.jvolgeores.2013.07.009.

Lahr, J. C. et al. (1994). Earthquake classification, location, and error analysis in a volcanic environment: implications for the magmatic system of the 1989-1990 eruptions at Redoubt Volcano, Alaska. *Journal of Volcanology and Geothermal Research* 62, pp. 137–151.

Lamb, O. D. et al. (2014). Multiple timescales of cyclical behaviour observed at two dome-forming eruptions. *Journal of Volcanology and Geothermal Research* 284, pp. 106–121. DOI: 10.1016/j.jvolgeores.2014.07.013.

Lamb, O. D. et al. (2015). Repetitive fracturing during spine extrusion at Unzen volcano, Japan. *Solid Earth* 6 (4), pp. 1277–1293. DOI: 10.5194/se-6-1277-2015.

Lane, S. J. et al. (2001). Experimental observations of pressure oscillations and flow regimes in an analogue volcanic system. *Journal of Geophysical Research: Solid Earth* 106 (B4), pp. 6461–6476. DOI: 10.1029/2000JB900376.

Lara-Cueva, R. et al. (2016). Feature Selection of Seismic Waveforms for Long Period Event Detection at Cotopaxi Volcano. *Journal of Volcanology and Geothermal Research* 316, pp. 34–49. DOI: 10.1016/j.jvolgeores.2016.02.022.

Latter, J. (1981). Volcanic earthquakes, and their relationship to eruptions at Ruapehu and Ngauruhoe volcanoes. *Journal of Volcanology and Geothermal Research* 9 (4), pp. 293–309. DOI: 10.1016/0377-0273(81)90041-X.

Lavallée, Y. et al. (2008). Seismogenic lavas and explosive eruption forecasting. *Nature* 453 (7194), pp. 507–10. DOI: 10.1038/nature06980.

Lavallée, Y. et al. (2012a). Magmatic architecture of dome-building eruptions at Volcán de Colima, Mexico. *Bulletin of Volcanology* 74, pp. 249–260. DOI: 10.1007/s00445-011-0518-4.

Lavallée, Y. et al. (2012b). Experimental generation of volcanic pseudotachylytes: Constraining rheology. *Journal of Structural Geology* 38, pp. 222–233. DOI: 10.1016/j.jsg.2012.02.001.

Lavallée, Y. et al. (2012c). Volcanic conduit failure as a trigger to magma fragmentation. *Bulletin of Volcanology* 74 (1), pp. 11–13. DOI: 10.1007/s00445-011-0544-2.

Lavallée, Y. et al. (2013). Reconstructing magma failure and the degassing network of dome-building eruptions. *Geology* 41 (4), pp. 515–518. DOI: 10.1130/G33948.1.

Lavallée, Y. et al. (2014). A frictional law for volcanic ash gouge. *Earth and Planetary Science Letters* 400, pp. 177–183. DOI: 10.1016/j.epsl.2014.05.023.

Lavallée, Y. et al. (2015a). Fault rheology beyond frictional melting. *Proceedings of the National Academy of Sciences*. DOI: 10.1073/pnas.1413608112.

Lavallée, Y. et al. (2015b). Thermal vesiculation during volcanic eruptions. *Nature* 528, pp. 544–547. DOI: 10.1038/nature16153.

Lavigne, F. et al. (2000). Instrumental lahar monitoring at Merapi Volcano, Central Java, Indonesia. *Journal of Volcanology and Geothermal Research* 100 (1–4), pp. 457 –478. DOI: 10.1016/S0377-0273(00)00151-7.

Lecocq, T., C. Caudron, and F. Brenguier (2014). MSNoise, a Python Package for Monitoring Seismic Velocity Changes Using Ambient Seismic Noise. *Seismological Research Letters* 85 (3), pp. 715–726. DOI: 10.1785/0220130073.

Lees, J. M. et al. (2008). Reventador Volcano 2005: Eruptive activity inferred from seismo-acoustic observation. *Journal of Volcanology and Geothermal Research* 176 (1), pp. 179–190. DOI: 10.1016/j.jvolgeores.2007.10.006.

Lejeune, A.-M. and P. Richet (1995). Rheology of crystal-bearing silicate melts: An experimental study at high viscosities. *Journal of Geophysical Research* 100 (B3), pp. 4215–4229. DOI: 10.1029/94JB02985.

Lensky, N. G. et al. (2008). Cyclic activity at Soufriere Hills Volcano, Montserrat: degassing-induced pressurization and stick-slip extrusion. *Geological Society, London, Special Publications* 307, pp. 169–188.

Lesage, P., G. Reyes-Dávila, and R. Arámbula-Mendoza (2014). Large tectonic earthquakes induce sharp temporary decreases in seismic velocity in Volcán de Colima, Mexico. *Journal of Geophysical Research: Solid Earth* 119, pp. 4360–4376. DOI: 10.1002/2013JB010884.

Li, D. and L. N. Y. Wong (2013). The brazilian disc test for rock mechanics applications: Review and new insights. *Rock Mechanics and Rock Engineering* 46, pp. 269–287. DOI: 10.1007/s00603-012-0257-7.

Llewellin, E. and M. Manga (2005). Bubble suspension rheology and implications for conduit flow. *Journal of Volcanology and Geothermal Research* 143 (1–3), pp. 205 –217. DOI: 10.1016/j.jvolgeores.2004.09.018.

Loughlin, S. C. et al. (2015). An introduction to global volcanic hazard and risk. *Global Volcanic Hazards and Risk*. Ed. by S. C. Loughlin et al. Cambridge: Cambridge University Press. DOI: 10.1017/CBO9781316276273.003.

Luhr, J. F. (2002). Petrology and geochemistry of the 1991 and 1998 - 1999 lava flows from Volcan de Colima, Mexico: implications for the end of the current eruptive cycle. *Journal of Volcanology and Geothermal Research* 117, pp. 169–194.

Luhr, J. F. and I. S. E. Carmichael (1990). Petrological monitoring of cyclical eruptive activity at Volcan Colima, Mexico. *Journal of Volcanology and Geothermal Research* 42, pp. 235–260.

Lyons, J. J. et al. (2016). Long period seismicity and very long period infrasound driven by shallow magmatic degassing at Mount Pagan, Mariana Islands. *Journal of Geophysical Research: Solid Earth* 121, pp. 188–209. DOI: 10.1002/2014JB011237.

Maeda, I. (2000). Nonlinear visco-elastic volcanic model and its application to the recent eruption of Mt. Unzen. *Journal of Volcanology and Geothermal Research* 95 (1-4), pp. 35–47. DOI: 10.1016/S0377-0273(99)00120-1.

Mann, M. E. and J. M. Lees (1996). Robust estimation of background noise and signal detection in climatic time series. *Climatic Change* 33 (3), pp. 409–445.

Marchetti, E. et al. (2013). Blast waves from violent explosive activity at Yasur Volcano, Vanuatu. *Geophysical Research Letters* 40 (22), pp. 5838–5843. DOI: 10.1002/2013GL057900.

Massol, H. and C. Jaupart (2009). Dynamics of magma flow near the vent: Implications for dome eruptions. *Earth and Planetary Science Letters* 279 (3-4), pp. 185–196. DOI: 10.1016/j.epsl.2008.12.041.

Mastin, L. G. et al. (2013). Injection, transport, and deposition of tephra during event 5 at Redoubt Volcano, 23 March, 2009. *Journal of Volcanology and Geothermal Research* 259, pp. 201–213.

Mastin, L. et al. (2009). A multidisciplinary effort to assign realistic source parameters to models of volcanic ash-cloud transport and dispersion during eruptions. *Journal of Volcanology and Geothermal Research* 186 (1-2), pp. 10–21.

Matoza, R. S. and B. A. Chouet (2010). Subevents of long-period seismicity: Implications for hydrothermal dynamics during the 2004–2008 eruption of Mount St. Helens. *Journal of Geophysical Research* 115 (B12), B12206. DOI: 10.1029/2010JB007839.

Matoza, R. S. and D. Fee (2014). Infrasonic component of volcano-seismic eruption tremor. *Geophysical Research Letters* 41, pp. 1964–1970. DOI: 10.1002/2014GL059301.

Matoza, R. S. et al. (2009a). Infrasonic jet noise from volcanic eruptions. *Geophysical Research Letters* 36 (L08303). DOI: 10.1029/2008GL036486.

Matoza, R. S. et al. (2009b). The source of infrasound associated with long period events at Mount St. Helens. *Journal of Geophysical Research* 114, B04305. DOI: 10.1029/2008JB006128.

Matsumoto, S. et al. (2012). Seismic reflection survey of the crustal structure beneath Unzen volcano, Kyushu, Japan. *Earth, Planets and Space* 64, pp. 405–414. DOI: 10.5047/eps.2011.11.006.

McLaskey, G. C. and B. D. Kilgore (2013). Foreshocks during the nucleation of stick-slip instability. *Journal of Geophysical Research: Solid Earth* 118 (6), pp. 2982–2997. DOI: 10.1002/jgrb.50232.

McNutt, S. et al. (2013). Local seismic and infrasound observations of the 2009 explosive eruptions of Redoubt Volcano, Alaska. *Journal of Volcanology and Geothermal Research* 259, pp. 63–76.

McNutt, S. R. (1992). Volcanic Tremor. *Encyclopedia of Earth System Science*. Ed. by W. A. Nierenberg. Vol. 4, pp. 417–425.

McNutt, S. R. and D. C. Roman (2015). *Volcanic Seismicity*. Second Edi, pp. 1011–1034. DOI: 10.1016/B978-0-12-385938-9.00059-6.

Michaut, C. et al. (2013). Eruption cyclicity at silicic volcanoes potentially caused by magmatic gas waves. *Nature Geoscience* 6, pp. 856–861. DOI: 10.1038/ngeo1928.

Moore, P. L., N. R. Iverson, and R. M. Iverson (2008). Frictional Properties of the Mount St . Helens Gouge. *A Volcano Rekindled: The Renewed Eruption of Mount St. Helens, 2004-2006: US Geological Survey Professional Paper 1750*. Ed. by D. R. Sherrod, W. E. Scott, and P. H. Stauffer, pp. 415–424.

Moran, S. C. et al. (2008). Seismic and acoustic recordings of an unusually large rockfall at Mount St. Helens, Washington. *Geophysical Research Letters* 35 (19). L19302. DOI: 10.1029/2008GL035176.

Morrissey, M. M. and B. A. Chouet (1997). Burst Conditions of Explosive Volcanic Eruptions Recorded on Microbarographs. *Science* 275 (5304), pp. 1290–1293. DOI: 10.1126/science.275.5304.1290.

Mueller, S. B. et al. (2013). Quantification of magma ascent rate through rockfall monitoring at the growing/collapsing lava dome of Volcán de Colima, Mexico. *Solid Earth* 4 (2), pp. 201–213. DOI: 10.5194/se-4-201-2013.

Mueller, S. et al. (2011). The porosity of pyroclasts as an indicator of volcanic explosivity. *Journal of Volcanology and Geothermal Research* 203 (3-4), pp. 168–174. DOI: 10.1016/j.jvolgeores.2011.04.006.

Murphy, M. D. et al. (2000). Remobilization of Andesite Magma by Intrusion of Mafic Magma at the Soufriere Hills Volcano, Montserrat, West Indies. *Journal of Petrology* 41 (1), p. 21. DOI: 10.1093/petrology/41.1.21.

Nakada, S., H. Shimizu, and K. Ohta (1999). Overview of the 1990-1995 eruption at Unzen Volcano. *Journal of Volcanology and Geothermal Research* 89 (May 1991), pp. 1–22.

Naranjo, J. L. et al. (1986). Eruption of the Nevado del Ruiz Volcano, Colombia, On 13 November 1985: Tephra Fall and Lahars. *Science* 233 (4767), pp. 961–963. DOI: 10.1126/science.233.4767.961.

Navarro-Ochoa, C., J. C. Gavilanes-Ruiz, and A. Cortes-Cortes (2002). Movement and emplacement of lava flows at Volcan de Colima, Mexico : November 1998 - February 1999. *Journal of Volcanology and Geothermal Research* 117, pp. 155–167.

Neuberg, J. et al. (1994). Highlights from a seismic broadband array on Stromboli Volcano. *Geophysical Research Letters* 21 (9), pp. 749–752. DOI: 10.1029/94GL00377.

Neuberg, J. W. (2000). Characteristics and causes of shallow seismicity in andesite volcanoes. *Philosophical transactions of the Royal Society A* 358, pp. 1533–1546.

Neuberg, J. W. (2011). Earthquakes, Volcanogenic. *Encyclopedia of Solid Earth Geophysics*. Ed. by H. K. Gupta. Springer, pp. 261 –269.

Neuberg, J. W. et al. (2006). The trigger mechanism of low-frequency earthquakes on Montserrat. *Journal of Volcanology and Geothermal Research* 153 (1-2), pp. 37–50. DOI: 10.1016/j.jvolgeores.2005.08.008.

Nicholson, E. et al. (2013). Cyclical patterns in volcanic degassing revealed by $SO_2$ flux time-series analysis: An application to Soufrière Hills Volcano, Montserrat. *Earth and Planetary Science Letters* 375, pp. 209–221. DOI: 10.1016/j.epsl.2013.05.032.

Nielsen, S. et al. (2010). On the transient behavior of frictional melt during seismic slip. *Journal of Geophysical Research: Solid Earth* 115 (10), pp. 1–17. DOI: 10.1029/2009JB007020.

Nishimura, T. et al. (2000). Source process of very long period seismic events associated with the 1998 activity of Iwate Volcano, northeastern Japan. *Journal of Geophysical Research* 105 (B8), pp. 19135–19147. DOI: 10.1029/2000JB900155.

Nunez-Cornu, F. J. et al. (2010). Comparison of Seismic Characteristics of Four Cycles of Dome Growth and Destruction at Colima Volcano, Mexico, from 1991 to 2004. *Bulletin of the Seismological Society of America* 100 (5A), pp. 1904–1927. DOI: 10.1785/0120080356.

O'Connell, R. J. and B. Budiansky (1974). Seismic Velocities in Dry and Saturated Cracked Solids. *Journal of Geophysical Research* 79 (35), pp. 5412–5426.

Odbert, H. M., R. C. Stewart, and G. Wadge (2014). Cyclic phenomena at the Soufriere Hills Volcano, Montserrat. *Geological Society, London, Memoirs* 39 (1), pp. 41–60. DOI: 10.1144/M39.2.

Odbert, H. and G. Wadge (2009). Time series analysis of lava flux. *Journal of Volcanology and Geothermal Research* 188 (4), pp. 305–314. DOI: 10.1016/j.jvolgeores.2009.09.005.

Ogiso, M., H. Matsubayashi, and T. Yamamoto (2015). Descent of tremor source locations before the 2014 phreatic eruption of Ontake volcano, Japan. *Earth, Planets and Space* 67 (206). DOI: 10.1186/s40623-015-0376-y.

Ohmi, S. and J. M. Lees (1995). Three-dimensional P- and S-wave velocity structure below Unzen volcano. *Journal of Volcanology and Geothermal Research* 65 (1-2), pp. 1–26. DOI: 10.1016/0377-0273(94)00091-T.

Okumura, S. et al. (2015). Rheological transitions in high-temperature volcanic fault zones. *Journal of Geophysical Research: Solid Earth* 120, pp. 2974–2987. DOI: 10.1002/2014JB011532.

Otsuki, K. (2003). Fluidization and melting of fault gouge during seismic slip: Identification in the Nojima fault zone and implications for focal earthquake mechanisms. *Journal of Geophysical Research* 108 (B4). DOI: 10.1029/2001JB001711.

Palacios, P. B. et al. (2016). Seismic-acoustic energy partitioning during a paroxysmal eruptive phase of Tungurahua volcano, Ecuador. *Geophysical Journal International* 205 (3), pp. 1900–1915. DOI: 10.1093/gji/ggw136.

Pallister, J. S. et al. (2008). Petrology of the 2004-2006 Mount St. Helens Lava Dome - Implications for Magmatic Plumbing and Eruption Triggering. *A Volcano Rekindled: The Renewed Eruption of Mount St. Helens, 2004-2006: U.S. Geological Survey Professional Paper 1750*. Ed. by D. R. Sherrod, W. E. Scott, and P. H. Stauffer. Chap. 30, pp. 647–702.

Pallister, J. S. et al. (2013). The Chaitén rhyolite lava dome: Eruption sequence, lava dome volumes, rapid effusion rates and source of the rhyolite magma. *Andean Geology* 40 (2), pp. 277–294. DOI: 10.5027/andgeoV40n2-a06.

Percival, D and W Walden (1993). Spectral Analysis for Physical Applications: Multitaper and Conventional Univariate Technique. Cambridge University Press.

Petersen, T. and S. R. McNutt (2007). Seismo-acoustic signals associated with degassing explosions recorded at Shishaldin Volcano, Alaska, 2003–2004. *Bulletin of Volcanology* 69 (5), pp. 527–536. DOI: 10.1007/s00445-006-0088-z.

Petersen, T. et al. (2006). Local infrasound observations of large ash explosions at Augustine Volcano, Alaska, during January 11–28, 2006. *Geophysical Research Letters* 33 (12). DOI: 10.1029/2006GL026491.

Pierce, A. D. (1981). *Acoustics: An Introduction to Its Physical Principles and Applications*. Vol. 34. 12. Acoustical Society of America, pp. 56–57. DOI: 10.1063/1.2914388.

Plail, M. et al. (2014). Geochemical evidence for relict degassing pathways preserved in andesite. *Earth and Planetary Science Letters* 386, pp. 21–33. DOI: 10.1016/j.epsl.2013.10.044.

Poupinet, G, W. L. Ellsworth, and J. Frechet (1984). Monitoring velocity variations in the crust using earthquake doublets: An application to the Calaveras Fault, California. *Journal of Geophysical Research* 89, pp. 5719–5731. DOI: 10.1029/JB089iB07p05719.

Power, J. A. and D. J. Lalla (2010). Seismic Observations of Augustine Volcano, 1970 – 2007. *The 2006 eruption of Augustine volcano, Alaska: U.S. Geological Survey Professional Paper 1769*. Ed. by J. A. Power, M. L. Coombs, and J. T. Freymueller. Chap. 1, pp. 3–40.

Prata, A. J. and A. Tupper (2009). Aviation hazards from volcanoes: The state of the science. *Natural Hazards* 51, pp. 239–244. DOI: 10.1007/s11069-009-9415-y.

Prejean, S. G. and E. E. Brodsky (2011). Volcanic plume height measured by seismic waves based on a mechanical model. *Journal of Geophysical Research* 116, B01306. DOI: 10.1029/2010JB007620.

Ramírez-Ruiz, J. J. et al. (2002). EDM deformation monitoring of the 1997-2000 activity at Volcán de Colima. *Journal of Volcanology and Geothermal Research* 117 (1-2), pp. 61–67. DOI: 10.1016/S0377-0273(02)00235-4.

Ramos, O. et al. (2013). Experimental Study of the Effect of Disorder on Subcritical Crack Growth Dynamics. *Phys. Rev. Lett.* 110 (16), p. 165506. DOI: 10.1103/PhysRevLett.110.165506.

Ratdomopurbo, A. and G. Poupinet (1995). Monitoring a temporal change of seismic velocity in a volcano: Application to the 1992 eruption of Mt. Merapi (Indonesia). *Geophysical Research Letters* 22 (7), pp. 775–778. DOI: 10.1029/95GL00302.

Reyes, C. G. and M. E. West (2011). The Waveform Suite: A Robust Platform for Manipulating Waveforms in MATLAB. *Seismological Research Letters* 82 (1), pp. 104–110.

Reyes-Dávila, G. A. et al. (2016). Volcán de Colima dome collapse of July, 2015 and associated pyroclastic density currents. *Journal of Volcanology and Geothermal Research* 320, pp. 100–106. DOI: 10.1016/j.jvolgeores.2016.04.015.

Ripepe, M. and E. Marchetti (2002). Array tracking of infrasonic sources at Stromboli volcano. *Geophysical Research Letters* 29 (22). 2076, pp. 33–1–33–4. DOI: 10.1029/2002GL015452.

Ripepe, M. et al. (1996). Infrasonic waves and volcanic tremor at Stromboli. *Geophysical Research Letters* 23 (2), pp. 181–184.

Ripepe, M. et al. (2013). Ash-plume dynamics and eruption source parameters by infrasound and thermal imagery: The 2010 Eyjafjallajökull eruption. *Earth and Planetary Science Letters* 366, pp. 112–121.

Rodgers, M. et al. (2013). Seismicity accompanying the 1999 eruptive episode at Telica Volcano, Nicaragua. *Journal of Volcanology and Geothermal Research* 265, pp. 39–51. DOI: 10.1016/j.jvolgeores.2013.08.010.

Rodgers, M., S. Rodgers, and D. C. Roman (2015a). Peakmatch: A Java Program for Multiplet Analysis of Large Seismic Datasets. *Seismological Research Letters* 86 (4), pp. 1–11. DOI: 10.1785/0220140160.

Rodgers, M. et al. (2015b). Stable and unstable phases of elevated seismic activity at the persistently restless Telica Volcano, Nicaragua. *Journal of Volcanology and Geothermal Research* 290, pp. 63–74. DOI: 10.1016/j.jvolgeores.2014.11.012.

Roman, D. C., A. Behar, and L. T. Elkins-Tanton (2014). The BENTO Box: Development and field-testing of a new satellite-linked data collection system for multiparameter volcano monitoring. *AGU Fall Meeting Abstracts*.

Roman, D. et al. (2008). Patterns of volcanotectonic seismicity and stress during the ongoing eruption of the Soufrière Hills Volcano, Montserrat (1995–2007). *Journal of Volcanology and Geothermal Research* 173 (3-4), pp. 230–244. DOI: 10.1016/j.jvolgeores.2008.01.014.

Roman, D. C. et al. (2016). Assessing the likelihood and magnitude of volcanic explosions based on seismic quiescence. *Earth and Planetary Science Letters* 450, pp. 20–28. DOI: 10.1016/j.epsl.2016.06.020.

Rose, W. I. (1973). Pattern and mechanism of volcanic activity at the Santiaguito Volcanic Dome, Guatemala. *Bulletin Volcanologique* 37 (1), pp. 73–94. DOI: 10.1007/BF02596881.

Rose, W. I. (1987). Volcanic activity at Santiaguito Volcano 1976-1984. *Geological Society of America Special Paper 212*, pp. 17–27. DOI: 10.1130/SPE212-p17.

Rowe, C. A. et al. (1998). Broadband recording of Strombolian explosions and associated very-long-period seismic signals on Mount Erebus Volcano, Ross Island, Antarctica. *Geophysical Research Letters* 25 (13), pp. 2297–2300. DOI: 10.1029/98GL01622.

Rubinstein, J. L. and W. L. Ellsworth (2010). Precise Estimation of Repeating Earthquake Moment: Example from Parkfield, California. *Bulletin of the Seismological Society of America* 100 (5A), pp. 1952–1961. DOI: 10.1785/0120100007.

Rust, A. C., K. V. Cashman, and P. J. Wallace (2004). Magma degassing buffered by vapor flow through brecciated conduit margins. *Geology* 32 (4), pp. 349–352. DOI: 10.1130/G20388.2.

Rust, A. C., N. J. Balmforth, and S. Mandre (2008). The feasibility of generating low-frequency volcano seismicity by flow through a deformable channel. *Geological Society, London, Special Publications* 307 (1), pp. 45–56. DOI: 10.1144/SP307.4.

Sahetapy-Engel, S. T., A. J. L. Harris, and E. Marchetti (2008). Thermal, seismic and infrasound observations of persistent explosive activity and conduit dynamics at Santiaguito lava dome, Guatemala. *Journal of Volcanology and Geothermal Research* 173 (1-2), pp. 1–14. DOI: 10.1016/j.jvolgeores.2007.11.026.

Saucedo, R. et al. (2002). Emplacement of pyroclastic flows during 1998-1999 eruption of Volcán de Colima, Mexico. *Journal of Volcanology and Geothermal Research* 117 (1-2), pp. 129–153. DOI: 10.1016/S0377-0273(02)00241-X.

Schaefer, J. R. and K. L. Wallace (2012). Ash fall contour map of the 2009 eruption of Redoubt Volcano, Alaska: Digital shapefiles of contours and sample locations. *Alaska Division of Geological and Geophysical Surveys Miscellaneous Publication 143*. DOI: 10.14509/23463.

Schaefer, L. N. et al. (2015). Geomechanical rock properties of a basaltic volcano. *Frontiers in Earth Science* 3 (29), pp. 1–15. DOI: 10.3389/feart.2015.00029.

Scharff, L, M Hort, and A Gerst (2014). The dynamics of the dome at Santiaguito volcano, Guatemala. *Geophysical Journal International* 197, pp. 926–942. DOI: 10.1093/gji/ggu069.

Scheu, B. et al. (2006). Temperature dependence of elastic P- and S-wave velocities in porous Mt. Unzen dacite. *Journal of Volcanology and Geothermal Research* 153 (1-2), pp. 136–147. DOI: 10.1016/j.jvolgeores.2005.08.007.

Schneider, D. J. and R. P. Hoblitt (2013). Doppler weather radar observations of the 2009 eruption of Redoubt Volcano, Alaska. *Journal of Volcanology and Geothermal Research* 259, pp. 133–144.

Schwaiger, H. F., R. P. Denlinger, and L. G. Mastin (2012). Ash3d: A finite-volume, conservative numerical model for ash transport and tephra deposition. *Journal of Geophysical Research* 117, B04204. DOI: 10.1029/2011JB008968.

Scott, J. A. et al. (2013). Geochemistry and evolution of the Santiaguito volcanic dome complex, Guatemala. *Journal of Volcanology and Geothermal Research* 252, pp. 92–107. DOI: 10.1016/j.jvolgeores.2012.11.011.

Segall, P. (2013). Volcano deformation and eruption forecasting. *Geological Society, London, Special Publications* 380. DOI: 10.1144/SP380.4.

Sens-Schönfelder, C. and U. Wegler (2006). Passive image interferemetry and seasonal variations of seismic velocities at Merapi Volcano, Indonesia. *Geophysical Research Letters* 33 (21), pp. 1–5. DOI: 10.1029/2006GL027797.

Shearer, P. M. (2009). *Introduction to Seismology*. 2nd edition. Cambridge: Cambridge University Press.

Shelly, D. R. et al. (2013). A fluid-driven earthquake swarm on the margin of the Yellowstone caldera. *Journal of Geophysical Research: Solid Earth* 118 (9), pp. 4872–4886. DOI: 10.1002/jgrb.50362.

Shimizu, H. et al. (1992). Seismological observations of Unzen Volcano before and during the 1990-1992 eruption. *Unzen Volcano, The 1990-1992 Eruption*. Ed. by T Yanagi, H Okada, and K Ohta. The Nishinippon and Kyushu University Press, pp. 38–43.

Sigmundsson, F. et al. (2010). Intrusion triggering of the 2010 Eyjafjallajökull explosive eruption. *Nature* 468 (7322), pp. 426–30. DOI: 10.1038/nature09558.

Sigmundsson, F. et al. (2015). Segmented lateral dyke growth in a rifting event at Bárðarbunga volcanic system, Iceland. *Nature* 517 (7533), p. 15. DOI: 10.1038/nature14111.

Smith, J., Y. Miyake, and T. Oikawa (2001). Interpretation of porosity in dacite lava domes as ductile-brittle failure textures. *Journal of Volcanology and Geothermal Research* 112 (1-4), pp. 25–35. DOI: 10.1016/S0377-0273(01)00232-3.

Smith, R., P. R. Sammonds, and C. R. Kilburn (2009). Fracturing of volcanic systems: Experimental insights into pre-eruptive conditions. *Earth and Planetary Science Letters* 280 (1-4), pp. 211–219. DOI: 10.1016/j.epsl.2009.01.032.

Smith, R. et al. (2011). Evolution of the mechanics of the 2004–2008 Mt. St. Helens lava dome with time and temperature. *Earth and Planetary Science Letters* 307 (1-2), pp. 191–200. DOI: 10.1016/j.epsl.2011.04.044.

Snieder, R. (2003). Constraining relative source locations with the seismic coda. *Project Review of the Consortium Project on Seismic Inverse Methods for Complex Structures*, pp. 207–216.

Snieder, R. and M. Vrijlandt (2005). Constraining the source separation with coda wave interferometry: Theory and application to earthquake doublets in the Hayward fault, California. *Journal of Geophysical Research* 110 (B4), pp. 2156–2202. DOI: 10.1029/2004JB003317.

Snieder, R. et al. (2002). Coda Wave Interferometry Estimating Nonlinear Behaviour in Seismic Velocity. *Science* 295, pp. 2253–2255. DOI: 10.1126/science.1070015.

Song, W. et al. (2014). Fusion characteristics of volcanic ash relevant to aviation hazards. *Geophysical Research Letters* 41, pp. 2326–2333. DOI: 10.1002/2013GL058954.

Spampinato, L. et al. (2011). Volcano surveillance using infrared cameras. *Earth-Science Reviews* 106 (1-2), pp. 63–91. DOI: 10.1016/j.earscirev.2011.01.003.

Sparks et al. (2000). Control on the emplacement of the andesite lava dome of the Soufriere Hills volcano, Montserrat by degassing-induced crystallization. *Terra Nova* 12 (1), pp. 14–20. DOI: 10.1046/j.1365-3121.2000.00267.x.

Sparks, R. S. J. (1997). Causes and consequences of pressurisation in lava dome eruptions. *Earth and Planetary Science Letters* 150 (3-4), pp. 177–189. DOI: 10.1016/S0012-821X(97)00109-X.

Strachey, R. (1888). On the air waves and sounds caused by the eruption of Krakatoa in August 1883. *Krakatau 1883 (published 1983)*. Ed. by T. Simkin and R. S. Fiske. Smithsonian Institution Press, pp. 368–374.

Surono et al. (2012). The 2010 explosive eruption of Java's Merapi volcano — A '100-year' event. *Journal of Volcanology and Geothermal Research* 241-242, pp. 121–135. DOI: 10.1016/j.jvolgeores.2012.06.018.

Symons, G. (1888). *The Eruption of Krakatoa and Subsequent Phenomena*. London: Royal Society of London, p. 627.

Taira, T. and F. Brenguier (2016). Response of hydrothermal system to stress transients at Lassen Volcanic Center, California, inferred from seismic interferometry with ambient noise. *Earth, Planets and Space* 68 (162). DOI: 10.1186/s40623-016-0538-6.

Tait, S., C. Jaupart, and S. Vergniolle (1989). Pressure, gas content and eruption periodicity of a shallow, crystallising magma chamber. *Earth and Planetary Science Letters* 92 (1), pp. 107–123. DOI: 10.1016/0012-821X(89)90025-3.

Tanguy, J.-C. (1994). The 1902–1905 eruptions of Montagne Pelée, Martinique: anatomy and retrospection. *Journal of Volcanology and Geothermal Research* 60 (2), pp. 87 –107. DOI: 10.1016/0377-0273(94)90064-7.

Thelen, W. A., M. West, and S. Senyukov (2010). Seismic characterization of the fall 2007 eruptive sequence at Bezymianny Volcano, Russia. *Journal of Volcanology and Geothermal Research* 194 (4), pp. 201–213. DOI: 10.1016/j.jvolgeores.2010.05.010.

Thelen, W. A., S. Malone, and M. E. West (2011). Multiplets: Their behavior and utility at dacitic and andesitic volcanic centers. *Journal of Geophysical Research* 116 (B08210). DOI: 10.1029/2010JB007924.

Thomas, M. E. and J. Neuberg (2012). What makes a volcano tick–A first explanation of deep multiple seismic sources in ascending magma. *Geology* 40 (4), pp. 351–354. DOI: 10.1130/G32868.1.

Thomson, D. J. (1982). Spectrum Estimation and Harmonic Analysis. *Proceedings of the IEEE* 70 (9), pp. 1055–1096.

Thun, J., I. Lokmer, and C. J. Bean (2015). New observations of displacement steps associated with volcano seismic long-period events, constrained by step table experiments. *Geophysical Research Letters* 42, pp. 3855–3862. DOI: 10.1002/2015GL063924.

Till, A. B., M. E. Yount, and M. L. Bevier (1994). The geologic history of Redoubt Volcano, Alaska. *Journal of Volcanology and Geothermal Research* 62 (1-4), pp. 11–30. DOI: 10.1016/0377-0273(94)90026-4.

Tuffen, H. and D. B. Dingwell (2005). Fault textures in volcanic conduits: evidence for seismic trigger mechanisms during silicic eruptions. *Bulletin of Volcanology* 67 (4), pp. 370–387. DOI: 10.1007/s00445-004-0383-5.

Tuffen, H., D. B. Dingwell, and H. Pinkerton (2003). Repeated fracture and healing of silicic magma generate flow banding and earthquakes? *Geology* 31 (12), p. 1089. DOI: 10.1130/G19777.1.

Tuffen, H., R. Smith, and P. R. Sammonds (2008). Evidence for seismogenic fracture of silicic magma. *Nature* 453 (7194), pp. 511–4. DOI: 10.1038/nature06989.

Umakoshi, K, H Shimizu, and N Matsuwo (2001). Volcano-tectonic seismicity at Unzen Volcano, Japan, 1985-1999. *Journal of Volcanology and Geothermal Research* 112, pp. 117–131.

Umakoshi, K. et al. (2008). Seismicity associated with the 1991-1995 dome growth at Unzen Volcano, Japan. *Journal of Volcanology and Geothermal Research* 175 (1-2), pp. 91–99. DOI: 10.1016/j.jvolgeores.2008.03.030.

Umakoshi, K., N. Itasaka, and H. Shimizu (2011). High-frequency earthquake swarm associated with the May 1991 dome extrusion at Unzen Volcano, Japan. *Journal of Volcanology and Geothermal Research* 206 (3-4), pp. 70–79. DOI: 10.1016/j.jvolgeores.2011.07.004.

Unglert, K. and A. Jellinek (2017). Feasibility study of spectral pattern recognition reveals distinct classes of volcanic tremor. *Journal of Volcanology and Geothermal Research*. DOI: 10.1016/j.jvolgeores.2017.03.006.

Unnþórsson, R. (2013). Hit Detection and Determination in AE Bursts. *Acoustic Emission - Research and Applications*. Ed. by W. Sikorski. InTech, pp. 1–20. DOI: 10.5772/54754.

Varley, N. R. et al. (2010). Generation of Vulcanian activity and long-period seismicity at Volcán de Colima, Mexico. *Journal of Volcanology and Geothermal Research* 198 (1-2), pp. 45–56. DOI: 10.1016/j.jvolgeores.2010.08.009.

Venzke, E (2013). *Global Volcanism Program*. DOI: 10.5479/si.GVP.VOTW4-2013.

Vergniolle, S. and J. Caplan-Auerbach (2006). Basaltic thermals and Subplinian plumes: Constraints from acoustic measurements at Shishaldin volcano, Alaska. *Bulletin of Volcanology* 68 (7-8), pp. 611–630.

Voight, B. et al. (1999). Magma Flow Instability and Cyclic Activity at Soufriere Hills Volcano, Montserrat, British West Indies. *Science* 283 (5405), pp. 1138–1142. DOI: 10.1126/science.283.5405.1138.

Voight, B. et al. (1998). Remarkable cyclic ground deformation monitored in real-time on Montserrat, and its use in eruption forecasting. *Geophysical Research Letters* 25 (18), pp. 3405–3408.

Wadge, G. et al. (2014). Chapter 1: An overview of the eruption of Soufrière Hills Volcano, Montserrat from 2000 to 2010. *Geological Society, London, Memoirs* 39 (1), pp. 1–40. DOI: 10.1144/M39.1.

Waite, G. P., B. A. Chouet, and P. B. Dawson (2008). Eruption dynamics at Mount St. Helens imaged from broadband seismic waveforms: Interaction of the shallow magmatic and hydrothermal systems. *Journal of Geophysical Research* 113 (B2), pp. 1–22. DOI: 10.1029/2007JB005259.

Wallace, K. L., J. R. Schaefer, and M. L. Coombs (2013). Character, mass, distribution, and origin of tephra-fall deposits from the 2009 eruption of Redoubt Volcano, Alaska—Highlighting the significance of particle aggregation. *Journal of Volcanology and Geothermal Research* 259, pp. 145–169.

Watts, R. B. et al. (2002). Growth patterns and emplacement of the andesitic lava dome at Soufriere Hills Volcano, Montserrat. *Geological Society, London, Memoirs* 21 (1), pp. 115–152. DOI: 10.1144/GSL.MEM.2002.021.01.06.

Webb, S. L. and D. B. Dingwell (1990). Non-Newtonian rheology of igneous melts at high stresses and strain rates: Experimental results for rhyolite, andesite, basalt, and nephelinite. *Journal of Geophysical Research* 95 (B10), p. 15695. DOI: 10.1029/JB095iB10p15695.

Webley, P. et al. (2013). Remote observations of eruptive clouds and surface thermal activity during the 2009 eruption of Redoubt volcano. *Journal of Volcanology and Geothermal Research* 259, pp. 185–200.

Wegler, U. et al. (2006). Increase of shear wave velocity before the 1998 eruption of Merapi volcano (Indonesia). *Geophysical Research Letters* 33 (9), pp. 4–7. DOI: 10.1029/2006GL025928.

Wessels, R. L. et al. (2013). High-resolution satellite and airborne thermal infrared imaging of precursory unrest and 2009 eruption at Redoubt Volcano , Alaska. *Journal of Volcanology and Geothermal Research* 259, pp. 248–269. DOI: j.jvolgeores.2012.04.014.

Wevers, M (1997). Listening to the sound of materials: acoustic emission for the analysis of material behaviour. *NDT & E International* 30 (2), pp. 99–106.

White, R. and W. McCausland (2016). Volcano-tectonic earthquakes: A new tool for estimating intrusive volumes and forecasting eruptions. *Journal of Volcanology and Geothermal Research* 309, pp. 139–155. DOI: 10.1016/j.jvolgeores.2015.10.020.

White, R. S. et al. (2011). Dynamics of dyke intrusion in the mid-crust of Iceland. *Earth and Planetary Science Letters* 304 (3–4), pp. 300 –312. DOI: 10.1016/j.epsl.2011.02.038.

Williams, S. N. and S. Self (1983). The October 1902 plinian eruption of Santa Maria volcano, Guatemala. *Journal of Volcanology and Geothermal Research* 16, pp. 33–56.

Wolfe, E. W. and R. P. Hoblitt (1996). Overview of the eruptions. *Fire and Mud: Eruptions and Lahars of Mount Pinatubo, Philippines*. Ed. by C. G. Newhall and R. S. Punongbayan. University of Washington Press.

Woodhouse, M. J. et al. (2013). Interaction between volcanic plumes and wind during the 2010 Eyjafjallajökull eruption, Iceland. *Journal of Geophysical Research: Solid Earth* 118 (1), pp. 92–109. DOI: 10.1029/2012JB009592.

Woulff, G. and T. R. McGetchin (1976). Acoustic Noise from Volcanoes: Theory and Experiment. *Geophysical Journal International* 45 (3), pp. 601–616.

Wright, T. J. et al. (2006). Magma-maintained rift segmentation at continental rupture in the 2005 Afar dyking episode. *Nature* 442, pp. 291–294. DOI: 10.1038/nature04978.

Yamada, T. et al. (2016). Initial phases of explosion earthquakes accompanying Vulcanian eruptions at Lokon-Empung volcano, Indonesia. *Journal of Volcanology and Geothermal Research* 327, pp. 310–327. DOI: 10.1016/j.jvolgeores.2016.08.011.

Yamamoto, H. et al. (2008). Rise dynamics and relative ash distribution in vulcanian eruption plumes at Santiaguito Volcano, Guatemala, revealed using an ultraviolet imaging camera. *Geophysical Research Letters* 35 (8), pp. 1–5. DOI: 10.1029/2007GL032008.

Yamashina, K. and H. Shimizu (1999). Crustal deformation in the mid-May 1991 crisis preceding the extrusion of a dacite lava dome at Unzen volcano, Japan. *Journal of Volcanology and Geothermal Research* 89 (1-4), pp. 43–55. DOI: 10.1016/S0377-0273(98)00121-8.

Yamashina, K., T. Matsishima, and S. Ohmi (1999). Volcanic deformation at Unzen, Japan, visualized by a time-differential stereoscopy. *Journal of Volcanology and Geothermal Research* 89, pp. 73–80.

Young, N. K. and J Gottsmann (2015). Shallow crustal mechanics from volumetric strain data: Insights from Soufrière Hills Volcano, Montserrat. *Journal of Geophysical Research: Solid Earth* 120, pp. 1559–1571. DOI: 10.1002/2014JB011551.

Zecevic, M. et al. (2013). Investigating the source characteristics of long-period (LP) seismic events recorded on Piton de la Fournaise volcano, La Réunion. *Journal of Volcanology and Geothermal Research* 258, pp. 1–11. DOI: 10.1016/j.jvolgeores.2013.04.009.

Zecevic, M. et al. (2016). Relocation of long-period (LP) seismic events reveals en echelon fractures in the upper edifice of Turrialba volcano, Costa Rica. *Geophysical Research Letters* 43 (19), pp. 10,105–10,114. DOI: 10.1002/2016GL070427.

Zobin, V. M. et al. (2002a). Comparative characteristics of the 1997-1998 seismic swarms preceding the November 1998 eruption of Volcan de Colima, Mexico. *Journal of Volcanology and Geothermal Research* 117, pp. 47–60.

Zobin, V. M. et al. (2002b). Overview of the 1997 - 2000 activity of Volcán de Colima, Mexico. *Journal of Volcanology and Geothermal Research* 117, pp. 1–19.